

# Dynamic mechanical behaviour of polymers and composite

19th Technical Meeting, 2010  
Strasbourg, France

## HIGH RATE THERMOMECHANICAL PROPERTIES OF GLASSY POLYMERS

D. Rittel  
*Faculty of Mechanical Engineering*  
*Technion*  
*32000 Haifa, Israel*

*merittel@technion.ac.il*

The dynamic response of polymers is of growing importance in many industrial applications, and thermomechanical data on their strength and failure behaviour is needed as an input to numerical simulations of polymeric structures. This talk will discuss commercial glassy polymers as generic materials, with emphasis on two specific issues.

The first topic to be discussed concerns the evolution of the specimen's temperature (*thermomechanical coupling*) when impact conditions are applied. We will present and discuss two experimental ways of measuring transient temperature changes, namely embedded thermocouples and non-contact infrared monitoring. It will be shown that the two techniques yield essentially identical results which can be subsequently processed to determine the rate of conversion of the mechanical energy into heat, as in Taylor and Quinney's work. These results can be incorporated in constitutive models of the high strain-rate response of polymers.

Another important issue relates to the *pressure-sensitivity of polymeric materials*, again related to the constitutive behaviour of these materials. We will present and discuss a simple methodology used to apply a constant confining pressure to a cylindrical specimen, under either quasi-static or dynamic loading conditions. It will be shown that the strain-rate and the pressure sensitivity of the investigated materials (commercial polycarbonate and polymethylmethacrylate) can actually be decoupled experimentally, so that the determination of the material's response over a large range of strain rates and pressures is greatly simplified. For the more "brittle" polymethylmethacrylate, we will report an interesting failure mode transition from brittle fragmentation to ductile adiabatic shear banding. Additional results will be shown for commercial polyetherimide (ULTEM).

# HIGH STRAIN RATE CHARACTERISATION OF UNIDIRECTIONAL CARBON-EPOXY IM7-8552 IN TRANSVERSE COMPRESSION AND IN-PLANE SHEAR VIA DIGITAL IMAGE CORRELATION

H. Koerber<sup>1</sup>, J. Xavier<sup>2</sup> and P. P. Camanho<sup>1</sup>

<sup>1</sup> *DEMec, Faculdade de Engenharia, Universidade do Porto, Rua Roberto Frias, 4200-465 Porto, Portugal*

<sup>2</sup> *CITAB/UTAD, Engenharias I, Apartado 1013, 5001-801 Vila Real, Portugal*

**Abstract.** This paper presents an experimental investigation of strain rate effects on polymer-based composite materials. Quasi-static and dynamic experiments at strain rates up to  $350\text{s}^{-1}$  were performed with end-loaded, rectangular off-axis compression and transverse compression specimens. The dynamic tests were performed on a split-Hopkinson pressure bar, where pulse shaping ensured early dynamic equilibrium and near constant strain rates for all specimen types. The in-plane strain field of the specimen was obtained via digital image correlation. With the high speed camera used for the dynamic tests, the failure process of the specimen was monitored and the fracture angle was measured. The effect of strain rate on the elastic modulus, ultimate strength and strain to failure was determined and the experimental failure envelope for combined transverse compression and in-plane shear loading was compared with the Puck failure criterion for matrix compression. Excellent correlation between experimental and predicted failure envelopes was observed for both strain rate regimes.

## 1. INTRODUCTION

The increasing applications of polymer-based composite materials in structures designed for crash and impact loading scenarios, and the related need to simulate the mechanical response under high strain rate deformation, requires a reliable identification of the strain rate effect on the in-plane material behaviour.

It is widely accepted that the longitudinal tensile properties of unidirectional (UD) carbon-epoxy composites are not strain rate sensitive, as demonstrated by Harding and Welsh [1] and confirmed by Zhou et al. [2] and Taniguchi et al. [3]. For transverse tension, a small increase of modulus and strength under dynamic loading was reported by Taniguchi et al. [3].

For the longitudinal compressive properties, conflicting results are found in the literature [4, 5] and a further investigation was carried out to clearly identify the effects of strain rate on the longitudinal compressive modulus and on the longitudinal compressive strength of carbon-epoxy composites [6].

In addition to the dynamic material characterisation for the principal material directions, a detailed knowledge of the compressive behaviour under combined loading conditions, such as transverse compression and in-plane shear is required to validate and further develop existing composite constitutive and failure models. In particular for physically based failure criteria, such as the one proposed by Puck and Schürmann [7], an understanding of the failure mode at high strain rate is of great importance.

Low and high speed photography in combination with the digital image correlation (DIC) technique [8, 9] provides an excellent opportunity to study the complex orthotropic material behaviour and failure modes of composites under quasi-static and dynamic loading.

The high strain rate tests in the present work were performed on split-Hopkinson pressure bars (SHPBs) at near constant strain rates and under dynamic equilibrium throughout the test.

A constant strain rate tests allows a direct comparison of the quasi-static and dynamic results and can be achieved by using shaped incident pulses, which must be chosen in accordance with the specimen stress-strain behaviour [10]. The pulse shaping analysis proposed by Nemat-Nasser et al. [11] was adopted to systematically obtain suited incident-pulse shapes. If the specimen is loaded under dynamic equilibrium, the entire dynamic specimen stress-strain curve can be used and the dynamic modulus can be measured with confidence. The relevance of DIC for SHPB experiments was recently demonstrated by Gilat et al. [12]. A more detailed description of the present work can be found in [13].

## 2. EXPERIMENTAL SETUP

In the present study a  $\varnothing 16\text{mm}$  steel SHPB was used for the high strain rate experiments ( $\dot{\epsilon}_{dyn} = 90\text{s}^{-1}$  to  $350\text{s}^{-1}$ ) and a screw-driven INSTRON test machine was used for the quasi-static reference tests ( $\dot{\epsilon}_{qs} = 4 \times 10^{-4}\text{s}^{-1}$ ). End-loaded rectangular off-axis compression and transverse compression specimens ( $15^\circ$ ,  $30^\circ$ ,  $45^\circ$ ,  $60^\circ$ ,  $75^\circ$  and  $90^\circ$ ) with nominal dimensions of  $20 \times 10 \times 4\text{mm}^3$  (length  $\times$  width  $\times$  thickness) were cut from a 32-ply UD panel. The specimens were prepared for DIC measurement by applying a random black-on-white speckle pattern to the specimen surface using aerosol spray painting. A fine speckle pattern was applied to the quasi-static specimens whereas a slightly coarser pattern was used for the dynamic specimens.

The dynamic test setup is shown schematically in Figure 1a, consisting of a striker-, incident- and transmission-bar with lengths of 0.6m, 2.6m and 1.6m, respectively. The specimen is placed directly between the incident- and transmission-bar and friction is reduced by applying a thin layer of  $\text{MoS}_2$ -paste at the interfaces. Copper pulse shapers were used to generate trapezoidal-shaped incident-pulses due to the elastic-plastic specimen stress-strain behaviour. A PHOTRON SA5 high speed camera was used to capture the deformation of the random speckle pattern at a frame rate of 100000fps and a resolution of  $320 \times 192$  pixels. The in-plane specimen strain field was calculated via the DIC software ARAMIS. For illumination two units of the DEDOLIGHT 400D daylight lightning system were used. To avoid reflections from the shiny bar-surface, the ends of the incident- and transmission-bar were covered with black insulation tape (Figure 1b).

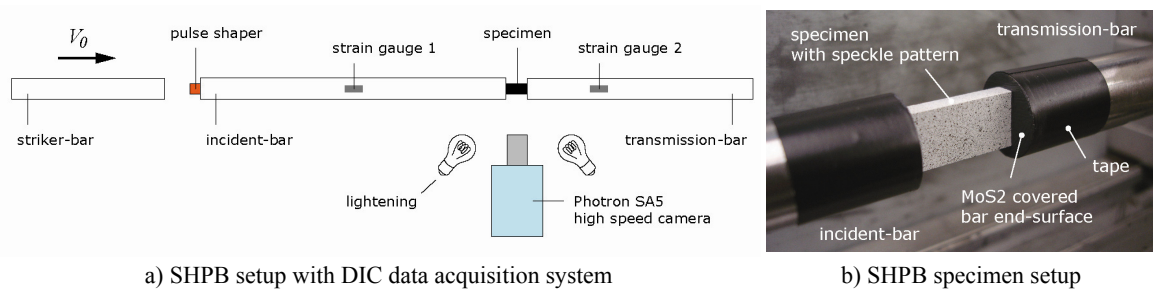


**Figure 1.** Dynamic experimental setup.

The quasi-static test setup is shown in Figure 2. Due to the low material strength of the load adapters, Tungsten-Carbide (TC) inserts were placed at both specimen ends. For the quasi-static tests a BAUMER FWX20 low speed camera was used to capture the specimen deformation at a frame rate of 1fps and a resolution of  $1624 \times 1236$  pixels. For lightning, two standard halogen lamps were used. Friction at the specimen ends was reduced by applying a thin layer of  $\text{MoS}_2$ -paste.

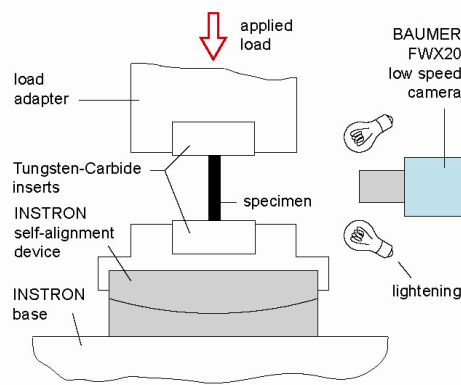


**Figure 2.** Quasi-static experimental setup.

Three tests were performed for each specimen type and load regime, with the exception of the 15° off-axis test, where 12 quasi-static and 5 dynamic tests were performed. More tests were necessary since two different failure modes were observed for the 15° specimen type.

### 3. RESULTS

#### 3.1 Off-Axis and Transverse Compression

A comparison of the quasi-static and dynamic axial compressive stress-strain response for all tested off-axis angles and for transverse compression is shown in Figure 3. The axial stress-time response and the specimen strain rate were calculated via SHPB analysis [14], while the axial compressive strain-time curve was obtained from the DIC software ARAMIS. An example for the in-plane axial compressive strain field  $\epsilon_{xx}$ , calculated via DIC, is shown for a dynamic 45° off-axis test in Figure 4. To obtain the strain-time curve for each specimen, the strain field was averaged over a virtual strain gauge at the specimen centre with an areal extension of  $6 \times 6 \text{ mm}^2$  for the dynamic case and  $3 \times 3 \text{ mm}^2$  for the quasi-static case. The virtual strain gauge area sizes represent typical grid sizes of conventional foil strain gauges and were chosen in accordance with the available camera resolution.

Quite different axial stress-strain behaviours were observed for the various specimen types (Figure 3). The highest strength and smallest failure-strain was observed for the 15° off-axis tests. Significant plasticity with high failure strains were observed for the 30°, 45° and 60° off-axis tests. The 75° and 90° specimens show the highest extent of linearity, particularly at high strain rates. Stiffening of the axial stress-strain response was observed for all specimen types under dynamic loading. For the 15°, 30° and 45° off-axis specimens, maximum fibre rotations of about 1.9°, 2.2° and 1.4° were observed at both load regimes, respectively. The fibre rotation is caused by the extension-shear coupling effect occurring for the off-axis specimen type (Figure 4c). Average values for the axial compressive modulus  $E_x$ , the axial compressive strength  $\sigma_{xx}^{\max}$  and the average strain rates measured for the SHPB tests are presented in Table 1.

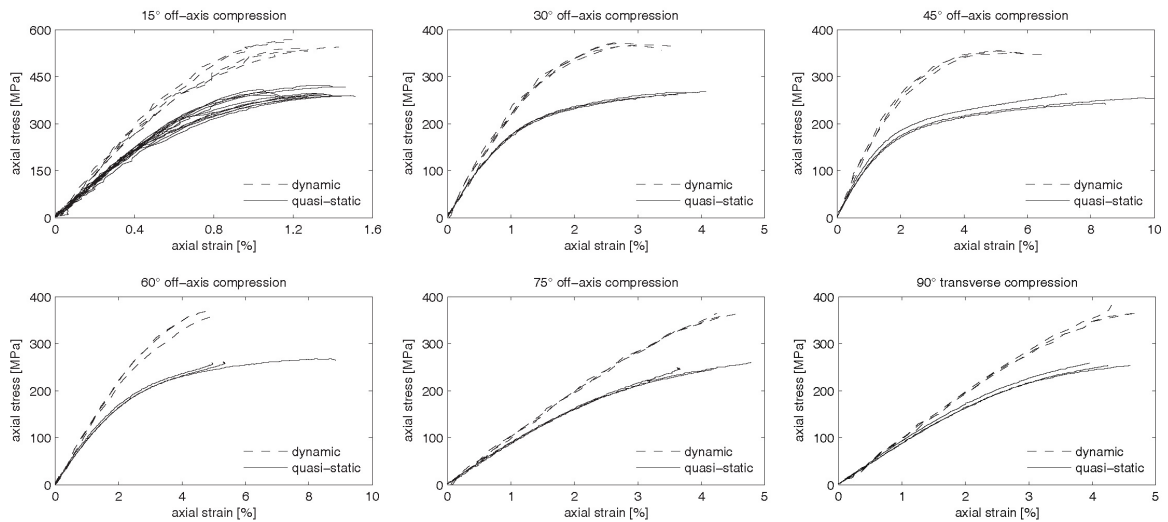


**Figure 3.** Static and dynamic axial stress-strain responses from off-axis and transverse compression tests.

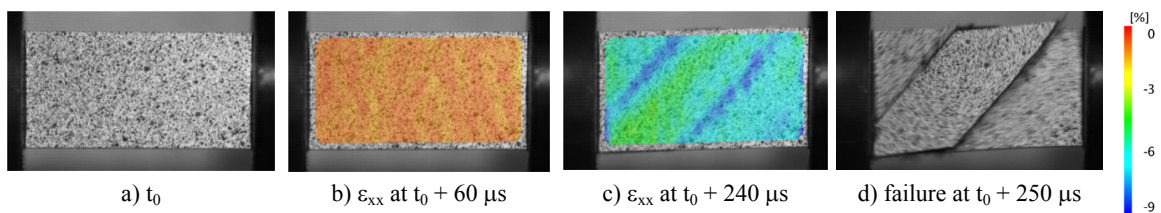


**Figure 4.** Dynamic 45° off-axis compression test and superimposed in-plane axial compressive strain  $\epsilon_{xx}$ .

**Table 1.** Off-axis and transverse compression results.

	15°		30°		45°		60°		75°		90°	
	<i>qs</i>	<i>dyn</i>										
$E_x$ [GPa]	55.3	73.9	21.7	24.0	13.1	15.8	9.8	11.7	8.8	10.0	8.9	10.0
$\sigma_{yy}^{\max}$ [MPa]	399	549	266	370	254	354	263	365	252	363	255	371
$\dot{\epsilon}$ [ $s^{-1}$ ]	-	93	-	233	-	290	-	346	-	300	-	258

The quasi-static and dynamic failure modes for the off-axis and transverse compression specimens are shown in Figures 5 and 6, respectively. Overall, similar failure modes were observed for both load regimes with in-plane shear (IPS) dominated failure in case of the 15° and 30° off-axis specimens and transverse compression-dominated failure for the 45°, 60°, 75° and 90° specimens. In case of the quasi-static 15° specimen, a distinct kink-band failure mode was also observed (Figure 5a). Under dynamic loading, the 15° specimen failed with the initiation of a kink-band, which was immediately followed by IPS failure with multiple cracks (Figure 6a,b). The number of IPS cracks increased for both 15° and 30° off-axis specimens under dynamic loading.

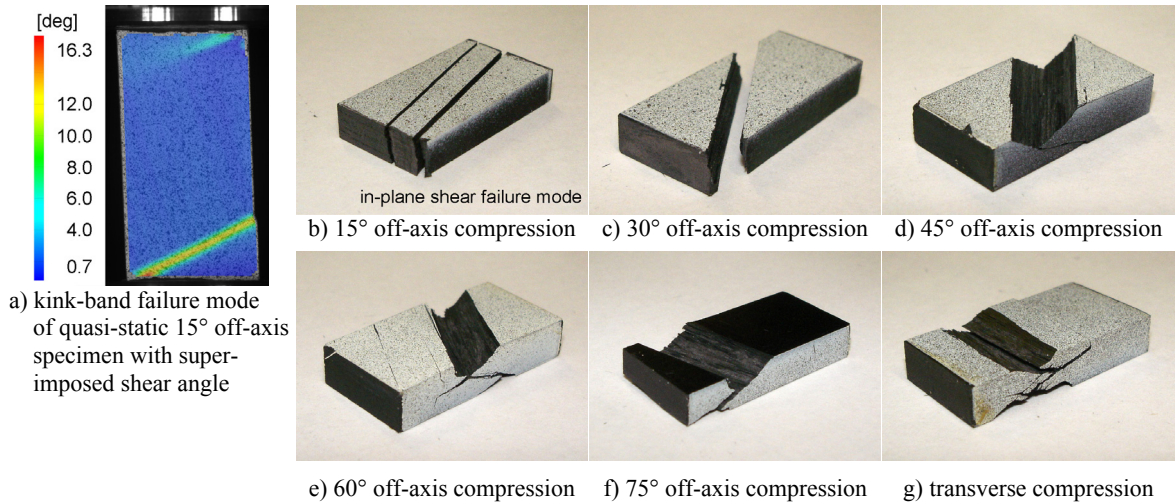


**Figure 5.** Quasi-static failure modes.

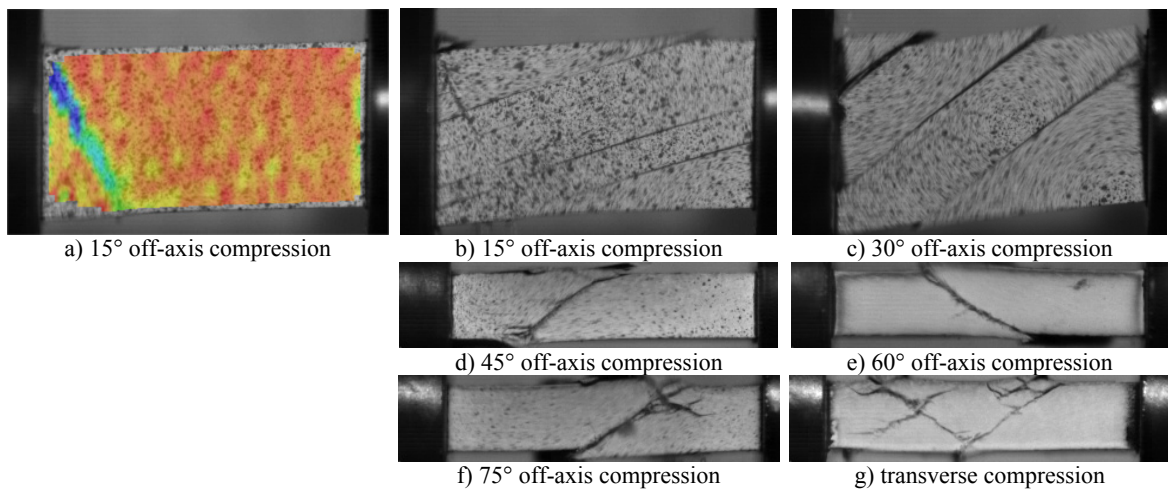


**Figure 6.** Dynamic failure modes.

It is noted that a different camera configuration was used for the tests performed to capture the failure mode of the 45°, 60°, 75° off-axis and transverse compression under high strain rate loading (Figure 6d-g). For these tests the specimen was filmed from the side at a frame rate of 232500fps and an image resolution of 320×70pixels.

### 3.2. In-Plane Shear

The quasi-static and dynamic in-plane shear (IPS) response was obtained by decomposing the axial stress  $\sigma_{xx}$  and the axial strain  $\varepsilon_{xx}$  (Figure 3) into the IPS stress and strain components  $\tau_{12}$  and  $\gamma_{12}$  and into the transverse compressive stress and strain components  $\sigma_{22}$  and  $\varepsilon_{22}$ , using classic laminate theory transformation. The transformation angle consists of the initial off-axis angle and the additional fibre-rotation angle, which was also measured during the test.

Figure 7a shows the quasi-static and dynamic IPS stress-strain response, obtained from the off-axis compression tests. It is seen that whereas the initial part of the quasi-static and dynamic shear curves is very similar for the different off-axis specimen types, the strength depends on the specimen type and thus on the ratio of transverse compressive and in-plane shear. Therefore, only the IPS modulus can be obtained from Figure 7a. Using the shear stress-strain curve of the 45° off-axis specimen type, the quasi-static and dynamic IPS moduli are  $G_{12}^{qs} = 5.1$  GPa and  $G_{12}^{dyn} = 6.3$  GPa, respectively.

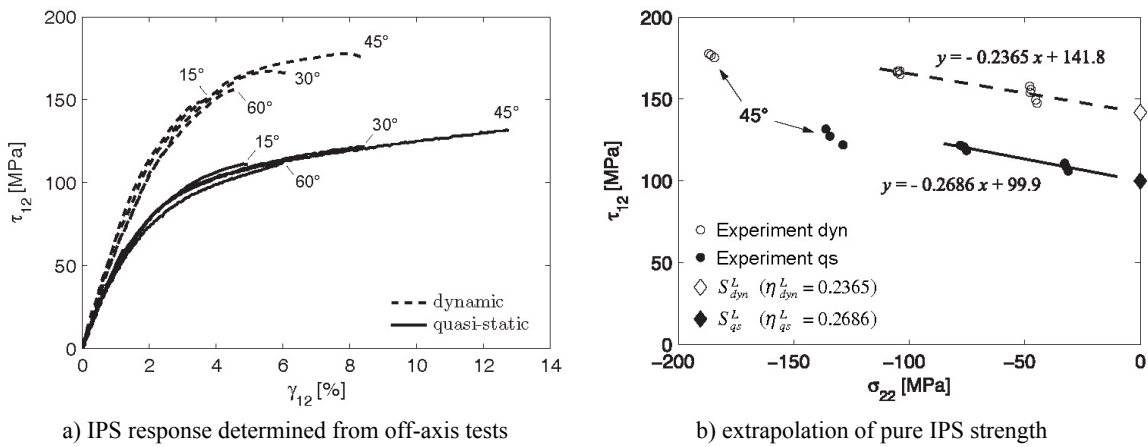


**Figure 7.** In-plane shear (IPS) response and extrapolation of pure IPS strength.

The IPS strength was determined via a linear extrapolation method proposed by Tsai and Sun [15], using the 15° and 30° off-axis specimens with IPS failure mode. Figure 7b shows the failure strengths of the quasi-static and dynamic 15°, 30° and 45° off-axis tests in the combined  $\sigma_{22} - \tau_{12}$  stress space, obtained from the respective axial strengths (Table 1) by applying the stress decomposition described at the beginning of this section. Pure quasi-static and dynamic IPS strengths of  $S_L^{qs} = 99.9$  MPa and  $S_L^{dyn} = 141.8$  MPa were determined, respectively.

## 4. DISCUSSION

The quasi-static and dynamic moduli for longitudinal [6], off-axis and transverse compression are summarized in Figure 8a. A small modulus increase under dynamic loading was observed for the off-axis and transverse compression tests. No rate effect on the modulus was however found for longitudinal compression [6]. Considering the high ratio between longitudinal and transverse compressive modulus, the increase of the elastic modulus for the off-axis and transverse compression specimens (approximately 20%) is hardly noticeable at the strain rates considered in this study.

For the longitudinal, off-axis and transverse compressive strengths a very uniform increase of about 40% was observed (Figure 8b). This suggests that despite the very different stress-strain responses observed for

the respective specimen types, the strength increase under dynamic loading is dominated by the viscoplastic behaviour of the polymer matrix.

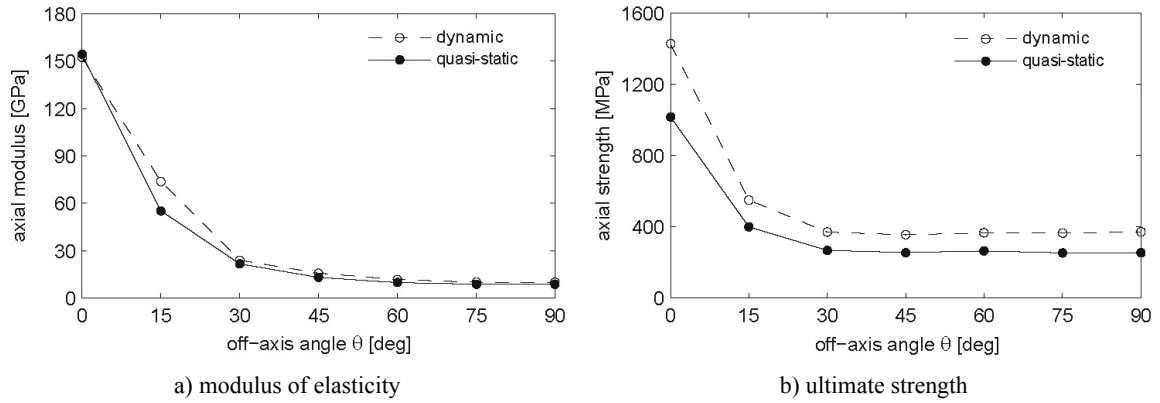


**Figure 8.** Strain rate effect on the axial modulus of elasticity and on the axial strength.

The quasi-static and dynamic failure envelopes for combined transverse compression and IPS loading are shown in Figure 9a, where the experimental results from the off-axis and transverse compression tests, and the extrapolated quasi-static and dynamic IPS strengths are shown together with the Puck failure criterion for matrix failure under transverse compression [7]:

$$\left( \frac{\tau^T}{S^T - \eta^T \sigma_n} \right)^2 + \left( \frac{\tau^L}{S^L - \eta^L \sigma_n} \right)^2 = 1 \quad (1)$$

The stresses  $\tau^T$ ,  $\tau^L$  and  $\sigma_n$  are the shear and normal stresses acting on the fracture plane. The transverse friction coefficient  $\eta^T$  and the transverse friction strength  $S^T$  were calculated according to the formulations given by Dávila et al. [16]. The longitudinal friction coefficient  $\eta^L$  and the longitudinal shear strength  $S^L$  (IPS strength) were obtained from Figure 7b as the coefficients of the linear extrapolation equations. For both load regimes, a very good correlation is found for the experimental and predicted failure envelopes. It is noted that the predicted failure envelopes shown in Figure 9a are functions of the fracture surface angle  $\alpha$  and are found by searching for the angle which maximises Equation (1) within a range of possible angles ( $0 < \alpha < \alpha_0$ ) [16]. A comparison between the fracture angle  $\alpha$  obtained from the SHPB experiments and the predicted fracture angle [17] is shown in Figure 9b.

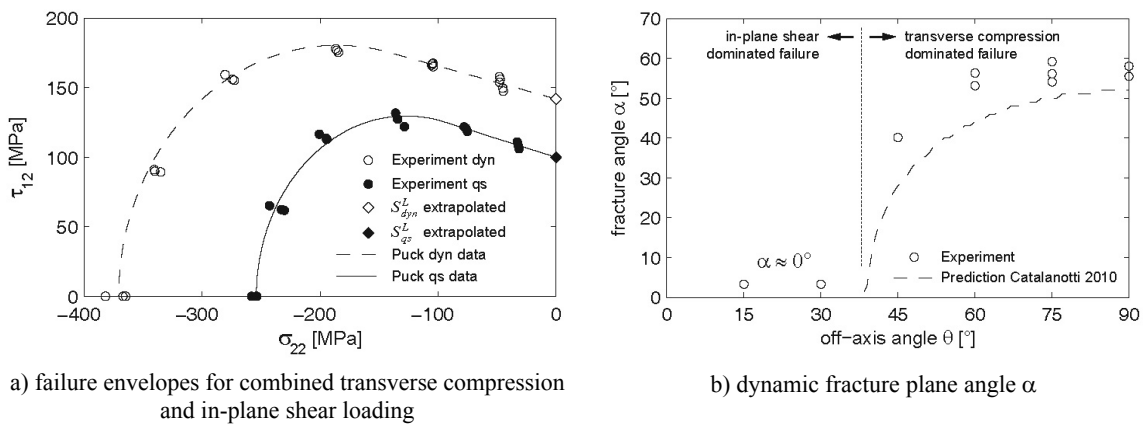


**Figure 9.** Quasi-static and dynamic failure envelopes and dynamic fracture angle.

## 5. CONCLUSION

It is concluded that end-loaded specimens, together with the pulse shaping and data reduction techniques presented in this work, are well suited to determine the off-axis, transverse compressive and in-plane shear properties of unidirectional polymer composites.

The following conclusions were drawn for the strain rate effect on the transverse compressive, off-axis compressive and in-plane shear response of unidirectional carbon-epoxy IM7-8552, considering the strain rates applied in the present study:

- The transverse compressive modulus of elasticity  $E_{2c}$  increases by 14% under dynamic loading.
- The off-axis compressive moduli  $E_x$  for 15°, 30°, 45°, 60° and 75° off-axis angles increase by about 32%, 10%, 21%, 19% and 14%, respectively under dynamic loading (average increase: 19%).
- The in-plane shear modulus  $G_{12}$  increases by about 24% under dynamic loading.
- The transverse, off-axis and in-plane shear strengths,  $Y_C$ ,  $\sigma_{xx}^{\max}$  and  $S_L$ , respectively, increase evenly by about 40% under dynamic loading.
- This very uniform strength increase suggests that despite the very different stress-strain responses observed for the respective specimen types, the strength increase under dynamic loading is dominated by the viscoplastic behaviour of the matrix.
- The failure mode of all specimen types does not change significantly with strain rate.
- The Puck failure criteria for matrix compression can be applied to both load regimes if the respective transverse compressive strength  $Y_C$ , the in-plane shear strength  $S_L$  and the longitudinal friction parameter  $\eta^L$  are known.

## Acknowledgments

The authors thank Tim Nicholls, PHOTRON UK, and Hagen Berger, GOM Germany, for providing the high speed camera and the Aramis DIC analysis software. The advice of Nik Petrinic, Clive Siviour and Richard Froud, University of Oxford, Department of Engineering Science, during the setup of the SHPB is acknowledged. The work described in this article was sponsored by the Portuguese Foundation for Science and Technology (FCT) under the project PTDC/EMEPME/64984/2006.

## References

- [1] Harding J. and Welsh L. M., *J Mater Sci.*, 18 (1983) 1810-1826.
- [2] Zhou Y., Wang Y., Jeelani S. and Xia Y., *Appl Compos Mater.*, 14 (2007) 17-31.
- [3] Taniguchi N., Nishiwaki T. and Kawada H., *Adv Composite Mater.*, 16 (2007) 167-180.
- [4] Hsiao H. M. and Daniel I. M., *Composites Part B.*, 29B (1998) 521-533.
- [5] Hosur M. V., Alexander J., Vaidya U. K. and Jeelani S., *Compos Struct.*, 52 (2001) 405-417.
- [6] Koerber H. and Camanho P. P., (submitted to) *Composites Part A.*, (2010).
- [7] Puck A. and Schürmann H., *Compos Sci Technol.*, 58 (1998) 1045-1067.
- [8] Sutton M. A., McNeill S. R., Helm J. D. and Chao Y. J., *In: Photomechanics.*, Springer 77/2000 (2000) 323-372.
- [9] Pan B., Qian K., Xie H. and Asundi A., *Meas Sci Technol.*, 20 (2009) 062001pp.
- [10] Subash G. and Ravicandran G., *In: ASM Handbook Vol 8.*, (2000) 497-504.
- [11] Nemat-Nasser S. Isaacs J. B. and Starret J. E., *Proc R Soc London Ser A.*, 435 (1991) 371-391.
- [12] Gilat A. Schmidt T. E. and Walker A. L., *Exp Mech.*, 49 (2009) 291-302.
- [13] Koerber H., Xavier J. and Camanho P.P., *Int J Mech Mater.*, (2010) doi: 10.1016/j.mechmat.2010.09.003.
- [14] Gray III G. T., *In: ASM Handbook Vol 8.*, (2000) 462-476.
- [15] Tsai J. L. and Sun C. T., *Compos Sci Technol.*, 65 (2005) 1941-1947
- [16] Dávila C. G., Camanho P. P. And Rose C. A., *J Compos Mater.*, 39 (2005) 323-345.
- [17] Catalanotti G., *PhD Thesis, University of Porto, Faculty of Engineering.*, (2010).

# EXPERIMENTAL STUDY OF THE CONFINED BEHAVIOUR OF PMMA UNDER QUASI-STATIC AND DYNAMIC CONDITIONS

P. Forquin<sup>1</sup>, M. Nasraoui<sup>1,2</sup>, A. Rusinek<sup>3</sup>, L. Siad<sup>2</sup>

<sup>1</sup>Laboratory of Physics and Mechanics of Materials, Université Paul Verlaine - Metz, Ile du Saulcy, 57045 Metz Cedex 1, France

<sup>2</sup>URCA/GRESPI/LMN, Université de Reims, BP 1039, 51687 Reims cedex 2, France

<sup>3</sup>Laboratory of mechanics, Biomechanics, Polymers and Structures (LABPS), Ecole Nationale d'Ingénieur de Metz (ENIM), Ile du Saulcy, 57000 Metz, France

**Abstract.** A testing device is presented for the experimental study of the confined behaviour of PMMA under quasi-static loading or at high strain-rates. The constitutive law for the metal of the ring being known, transverse gauges glued on its lateral surface allow for the measurement of the lateral confining pressure. The hydrostatic pressure and the Mises stress can be computed. Quasi-static and dynamic tests performed in a strain-rate range of  $1e-3/s$  -  $1e3/s$  are processed with the method and compared to results of unconfined compression tests. Finally, the compressive behaviour of PMMA is seen to be weakly influenced by the level of pressure and much more sensitive to strain-rate: an elastic brittle behaviour is observed at high strain-rates in unconfined or confined conditions whereas an elastoplastic behaviour is noted under quasi-static loading.

## 1. INTRODUCTION

PMMA (Poly methyl methacrylate) is a thermoplastic polymer widely used as protective structure in aeronautics, nuclear industry, and machinery equipment, against shocks or ballistic impacts. To improve the design of such structures by using numerical simulation the mechanical behaviour of PMMA under high confining pressure and high strain-rates must be investigated [1]. The behaviour of PMMA has been widely studied in the last decades through unconfined compression tests as function of temperature and strain-rate [2-4]. In quasi-static conditions a cylindrical specimen is placed in-between parallel platens and loaded through a hydraulic press. The authors have observed a continuous increase of the compressive yield stress with strain-rate and negative temperature sensitivity in the explored range from  $-120^{\circ}\text{C}$  to the glass temperature transition ( $T_g = 105^{\circ}\text{C}$ ) [5]. Split Hopkinson Pressure Bar device is generally used to reach strain-rates of few thousands per second [3, 6, 7]. Whereas the yield stress is tripled in the range [ $1e-3/s$  –  $1e3/s$ ] a strong softening is observed in dynamic conditions [2-3]. Brittleness of PMMA at high strain-rates has been also observed in puncture tests by impact [4]. During an impact, the target is subjected to compressive stresses and high pressures in the vicinity of the impact point and tensile stresses further down that may induce cracking and breaking of the target. Therefore, the response of PMMA under high confining pressure is a key-parameter to be considered for simulating numerically the behaviour of PMMA structures subjected to impact loading [1]. In this work, quasi-static and dynamic quasi-oedometric compression tests have been developed and performed. The processing method and some results are described below.

## 2. DESCRIPTION OF THE CONFINED COMPRESSION TESTS

### 2.1. Principle

Primarily, Quasi-Oedometric Compression (QOC) tests have been developed to test geomaterials as concretes, rocks or soils under high confining pressures. The principle is the following: a cylindrical specimen tightly enclosed in a confinement vessel is axially compressed. As it tends to expand, both radial and axial stresses increase in the specimen. The test provides a reading of the strength of the material at different levels of the pressure. Several experimental devices for quasi-oedometric compression were proposed by Bažant et al. [8], Burlion [9] and Gatuingt [10]. Burlion et al. [11], for instance, developed an instrumented elastic steel vessel. Forquin et al. [12-14] proposed a new analysis of experimental data taking account of the shortening of specimen and of a possible plastic deformation of the confining cell. More

---

<sup>1</sup> e-mail : pascal.forquin@univ-metz.fr

recently, dynamic QOC tests have been performed with a split-Hopkinson pressure bar device in the range of strain-rates from 80 to 200/s applying the previous methodology [15, 16]. The accuracy of the method and the influence of friction were specially discussed. The steel ring allows for exploring the behaviour of concrete under levels of lateral pressure up to 800 MPa. In particular, these tests revealed a huge influence of free water on the dynamic strength of concrete under high confining pressures [16].

In the present study, cylindrical specimen of PMMA 10 mm in diameter and 14 mm in length enclosed in a confinement vessel is subjected to axial compression through a universal testing machine and compression plugs made of high strength steel (Fig. 1b). The brass confinement vessel is a crown of 10 mm as inner diameter, 22 mm as outer diameter and 16 mm in length. The axial stress in the specimen is calculated from the load cell. LVDTs are attached to compression platen to measure the axial strain. The radial strain and stress in the specimen are deduced from the hoop micro-strain measured through  $G_1$  strain gauge attached on the outer surface of the vessel (Fig. 1a). Hoop strain gauges  $G_2$  and  $G_3$  are located at a distance from the middle equal to  $\frac{3}{4}$  of the half-length of the ring. As axial strain gauge  $G_2$ ,  $G_3$  and  $G_4$  are used to evaluate the barrelling of the ring, by comparison with the central gauges  $G_1$ . They also indirectly provide an evaluation of the difference in axial displacement between the specimen and the ring.

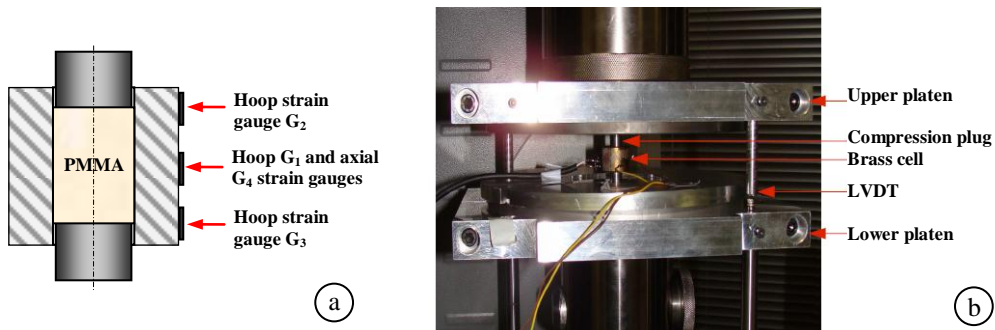


**Figure 1.** Device and instrumentation used for quasi-static quasi-oedometric compression tests

## 2.2. Processing method

With the aim to evaluate from  $G_1$  strain measurement the average contact pressure between the vessel and the specimen, a series of numerical simulations have been performed that takes into account the elasto-plastic behaviour of the vessel material [12, 15]. First, the constitutive law of brass has been identified from a quasi-static tensile test (Fig. 2).

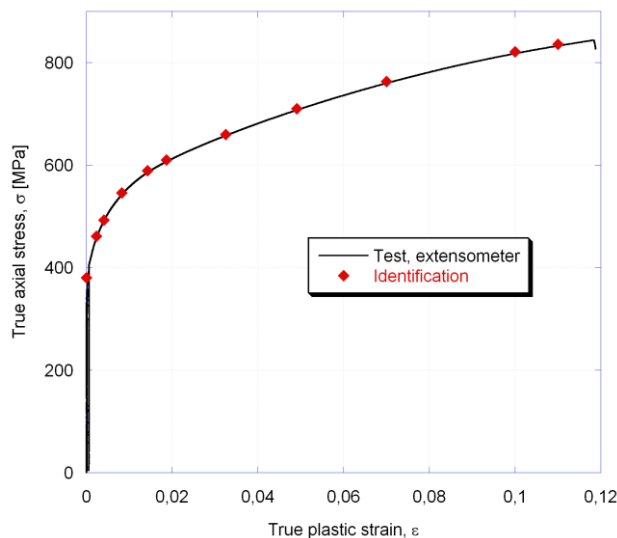


**Figure 2.** Identification of the constitutive law of brass from a tensile test

Next, three computations have been performed using 4-nodes axisymmetric elements and Abaqus-standard FE code. For the first simulation, a radial compression is applied on the inner cylindrical surface of the vessel through a length of 14 mm (the initial length of the specimen). The computation provides a relation between the external hoop strain and the internal radial stress (Fig. 3). For the second and third simulations, 12 mm and 10 mm are considered.

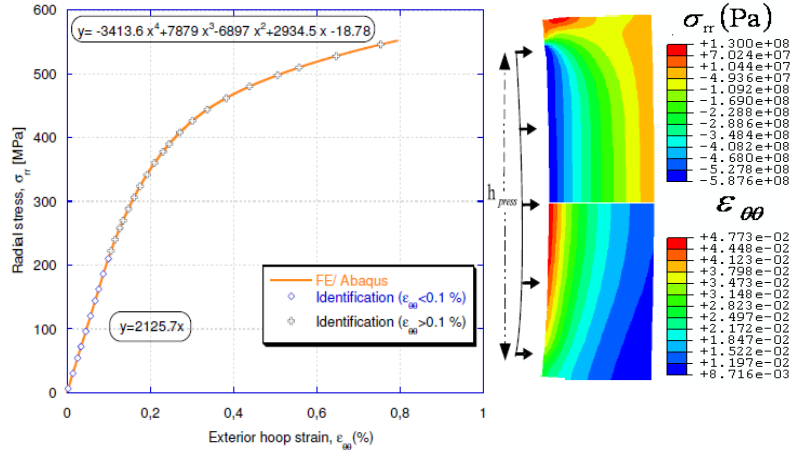


**Figure 3.** Relation between the external hoop strain and the internal radial stress applied on 14 mm

Using simple interpolation of the results provided by the three numerical simulations, the change of specimen length is accounted for in the processing of data (Equation 1).

$$\begin{cases} \text{if } 14 \text{ mm} \geq h_{press} \geq 12 \text{ mm}, & -\bar{\sigma}_{radial}(h, \varepsilon_{\theta\theta}^{(z=0,ex)}) = \left( \frac{h-h_{12}}{h_{14}-h_{12}} \right) f_{14}(\varepsilon_{\theta\theta}^{z=0,ex}) + \left( \frac{h_{14}-h}{h_{14}-h_{12}} \right) f_{12}(\varepsilon_{\theta\theta}^{z=0,ex}) \\ \text{if } 12 \text{ mm} \geq h_{press} \geq 10 \text{ mm}, & -\bar{\sigma}_{radial}(h, \varepsilon_{\theta\theta}^{(z=0,ex)}) = \left( \frac{h-h_{10}}{h_{12}-h_{10}} \right) f_{12}(\varepsilon_{\theta\theta}^{z=0,ex}) + \left( \frac{h_{12}-h}{h_{12}-h_{10}} \right) f_{10}(\varepsilon_{\theta\theta}^{z=0,ex}) \end{cases} \quad (1)$$

where functions ( $f_{14}$ ,  $f_{12}$  and  $f_{10}$ ) are identified from numerical simulations. In a similar way, the average radial strain ( $\bar{\varepsilon}_{radial}$ ) of the specimen is deduced from data of gauges  $G_1$ ,  $G_2$  and  $G_3$ . Next, the axial load being known, the average axial stress may be also computed:

$$\bar{\sigma}_{axial} = \frac{F_{axial}}{\pi r_0^2 (1 + \bar{\varepsilon}_{radial})^2}, \quad (2)$$

Knowing the mean axial stress and radial stress, the von Mises stress and the hydrostatic pressure are deduced:

$$\bar{\sigma}_{vonMises} = |\bar{\sigma}_{axial} - \bar{\sigma}_{radial}|, \quad P_{hydrostat} = -\frac{1}{3}(\bar{\sigma}_{axial} + 2\bar{\sigma}_{radial}) \quad (3, 4)$$

Now, the Mises stress may be plotted as function of axial strain and hydrostatic pressure. This methodology is applied herein to quasi-static and dynamic quasi-oedometric compression tests.

### 3. RESULTS OF QUASI-OEDOMETRIC COMPRESSION TESTS

#### 3.1. Quasi-static tests

A series of quasi-static quasi-oedometric compression tests have been carried out. The change of radial stress, axial stress, hydrostatic pressure and Mises stress is plotted as function of axial strain on Fig. 4 for one test performed at 0.001/s. The hydrostatic pressure increases to roughly 550 MPa during the experiments. Under such confining pressures, PMMA exhibits an elastic perfectly plastic behaviour with a maximum strength about 160 MPa (Fig. 4), to be compared to unconfined strength measured in uniaxial compression test (about 130 MPa). Moreover, the level of friction at specimen-vessel interface has been

evaluated by comparing the change of hoop strains ratio  $(G_2+G_3)/2G_1$  with numerical data (Fig. 5). Indeed, the higher the friction between the specimen and the vessel, the more marked the barrelling deformation of the vessel, the lower this ratio. Thus, numerical simulations of a vessel subjected to an internal pressure through 12 mm and tangential stresses corresponding to 0, 10% or 20% of the internal pressure have been performed. Comparison of experimental data and numerical data allows estimating that friction coefficient is lower than 0.1 (Fig. 5).

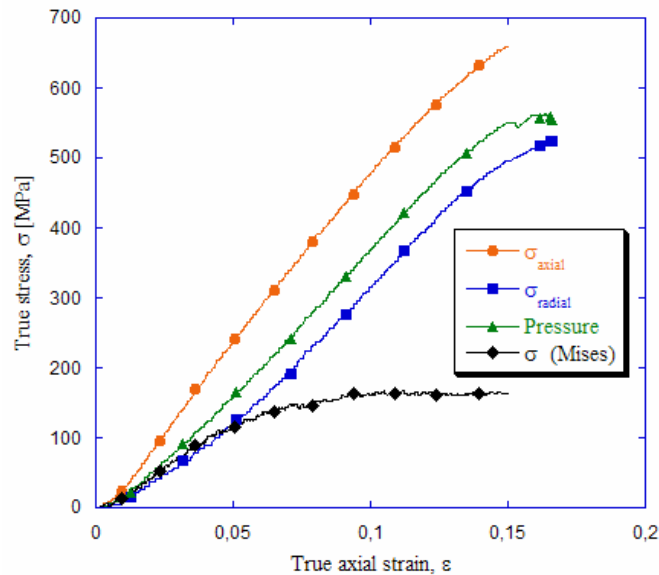


**Figure 4.** Quasi-static quasi-oedometric compression test (brass vessel, strain rate: 0.001/s).

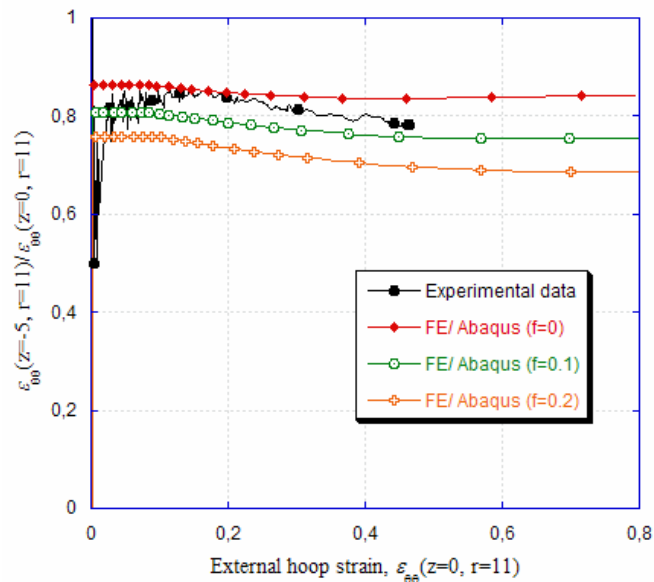


**Figure 5.** Ratio of external hoop strains  $(G_2+G_3)/2G_1$  as function of  $G_1$ . Comparison of experimental data to numerical simulation of a vessel subjected to an internal pressure through 12 mm and tangential stresses corresponding to 0, 10% or 20% of the internal pressure.

### 3.2. Dynamic tests

In parallel, a Split-Hopkinson-Pressure-Bar device (SHPB) has been used to identify the unconfined and confined strength of PMMA at high strain-rates (2000-4000/s). This experimental set-up, widely used today, was pioneered by Kolsky [17]. In this work, a device composed of two high strength steel bars (input and output bars, 1.5 m in length, 20 mm in diameter) and projectiles of length 400 or 600 mm has been used. Gauges glued on the input and output bars allows for the knowledge of forces and particle velocities at both faces of the specimen. Forces provide the change of axial stress in the specimen whereas particle velocities are integrated to deduce the change of axial strain as function of time. Next, the processing method described previously is applied (equations 3, 4). Moreover, brass is assumed to be insensitive to strain-rate and relation (1) is used again.

The evolution of stresses is shown for a quasi-oedometric compression test performed with brass vessel. The average strain-rate is about 1430/s. When the maximum Mises stress is reached (about 330 MPa), the hydrostatic pressure is equal to 400 MPa. One may also observe that the lateral pressure applied by the specimen on the ring (Equation (1)) is not constant during the test but is continuously increasing. After time  $t = 80 \mu\text{s}$  axial stress show a sharp fall whereas the radial stress is accelerating. The resulting fall of Mises stress is supposedly due to a breakage within the specimen. Indeed, inclined planes are clearly visible on the failure pattern after the test. Thus, the residual strength observed afterward (100-250  $\mu\text{s}$ ) is certainly the consequence of rubbing failure planes maintained in contact because of the confinement.

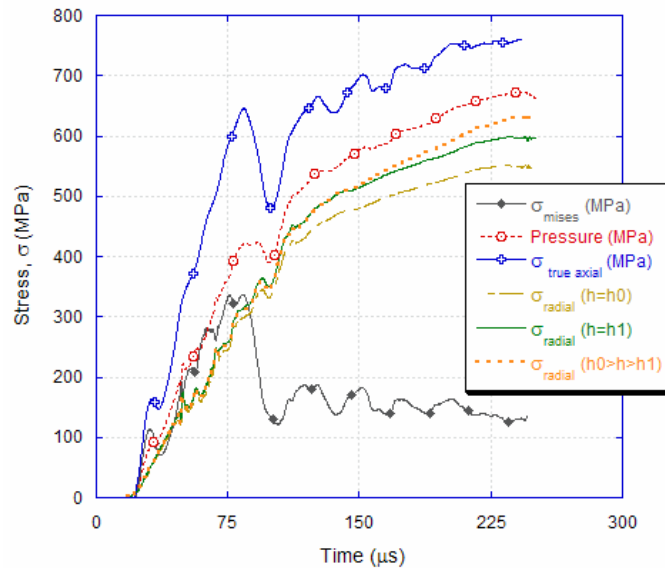


**Figure 6.** Change of axial stress, radial stress, Mises stress and Pressure as function of time in a dynamic QOC test (brass cell).

The change of Mises stress is plotted as function of axial strain in Fig. 7 for the previous test. A elastic-brittle behaviour is clearly noticed despite the high level of hydrostatic pressure reached during the test. Moreover, the quasi-oedometric compression test is compared has been compared to two dynamic unconfined compression tests performed with the same apparatus (SHPB device). Elastic modulus and yield strain are almost identical, a confirmation of the low influence of the confining pressure on the dynamic strength of PMMA. On the other hand, strain-rate has a strong influence on the dynamic confined strength of PMMA as shown by Fig. 8, on which both quasi-static and dynamic quasi-oedometric compression tests are compared. According to these results, the brittleness of PMMA under high strain-rate is a key-parameter to be considered for simulating numerically the behaviour of PMMA structures subjected to impact loading.

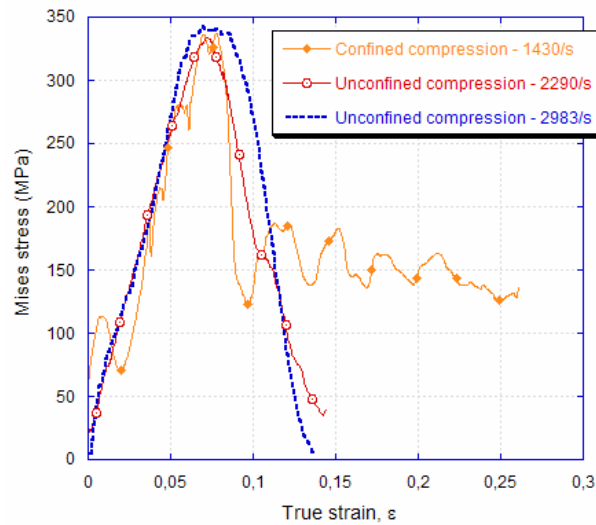


**Figure 7.** Comparison between unconfined and quasi-oedometric dynamic compression tests

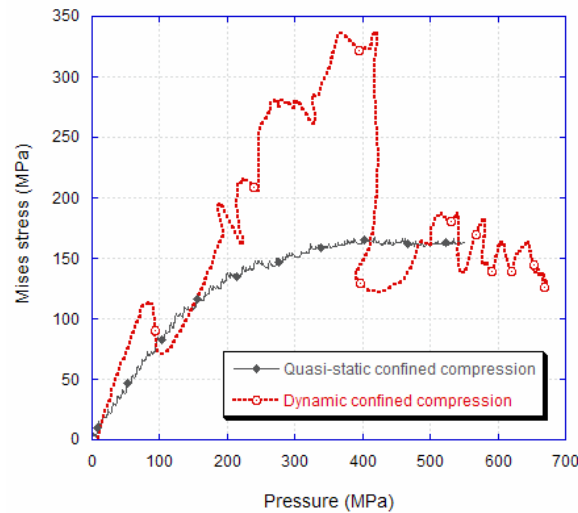


**Figure 8.** Comparison between quasi-static and dynamic quasi-oedometric compression tests

#### 4. CONCLUSION

Quasi-Oedometric Compression (QOC) tests have been developed to test PMMA in quasi-static or dynamic conditions. Cylindrical specimens of PMMA enclosed in a brass confinement vessel have been subjected to axial compression through a universal testing machine or Split-Hopkinson Pressure Bar device. A processing method has been developed based on numerical simulations of the confining ring loaded by an internal pressure. It allows taking into account the shortening of the specimen and the elasto-plastic behaviour of brass that composed the vessel. Due to the thickness of the ring, hydrostatic pressures as high as 400 MPa have been obtained both in quasi-static and dynamic experiments. According to quasi-static tests, the maximum strength is weakly affected by a confining pressure as the increase of strength is limited to few tens of MPa for the considered level of pressure (few hundreds of MPa). On the other hand, an elastic-brittle response is pointed out in dynamic testing with or without confinement and the yield stress is almost unchanged (about 330 MPa). Finally, this work shows that the level of confining pressure seems to have a limited influence on the quasi-static and dynamic behaviour of PMMA polymer.

## References

- [1] A. Dorogoy, D. Rittel, A. Brill (2010). "A study of inclined impact in polymethylmethacrylate plates" *Int J Impact Eng*, **37** 285-294.
- [2] E.M. Arruda, M.C Boyce, et R. Jayachandran (1995). "Effects of strain rate, temperature and thermomechanical coupling on the finite strain deformation of glassy polymers" *Mechanics of Materials*, **19**, 193-215.
- [3] J. Richeton, S. Ahzi, K.S. Vecchio, F.C. Jiang, R.R. Adharapurapu (2006). "Influence of temperature and strain rate on the mechanical behavior of three amorphous polymers: Characterization and modelling of the compressive yield stress" *Int J Solids Struct*, **43**, 2318–2335.
- [4] M. Segreti, A. Rusinek, et J.R. Klepaczko. (2004) "Experimental study on puncture of PMMA at low and high velocities, effect on the failure mode" *Polymer Testing*, **23**, 703–718
- [5] J. Richeton, S. Ahzi, L. Daridon, Y. Rémond (2005). "A formulation of the cooperative model for the yield stress of amorphous polymers for a wide range of strain rates and temperatures" *Polymer*, **46** 6035–6043.
- [6] Z.H. Li, J. Lambros (2001) "Strain rate effects on the thermomechanical behavior of polymers." *Int. J. Solids Struct.* **38** (20), 3549–3562.
- [7] D. Rittel, A. Brill (2008) "Dynamic flow and failure of confined polymethylmethacrylate" *J. Mech. Phys. Solids*, **56** (4), 1401-1416.
- [8] Z.P. Bazant, F.C. Bishop, T.P. Chang (1986) "Confined compression tests of cement paste and concrete up to 300 ksi" *ACI J.* **33**, 553-560.
- [9] N. Burlion. (1997) "Compaction des bétons: éléments de modélisation et caractérisation expérimentale" PhD thesis. ENS Cachan.
- [10] F. Gatingt. (1999) "Prévision de la rupture des ouvrages en béton sollicités en dynamique rapide" PhD thesis, ENS Cachan.
- [11] N. Burlion, G. Pijaudier-Cabot, N. Dahan (2001). "Experimental analysis of compaction of concrete and mortar" *Int. J. Numer. Anal. Meth. Geomec.* **25**, 467-1486.
- [12] P. Forquin, A.A. Arias, R. Zaera (2007). "An experimental method of measuring the confined compression strength of geomaterials" *Int. J. Solids Struct.* **44**, 4291-4317.
- [13] P. Forquin, A.A. Arias, R. Zaera (2008a). "Role of porosity in controlling the mechanical and impact behaviours of cement-based materials" *Int J Imp Eng.* **35**(3), 133-146.
- [14] P. Forquin, A.A. Arias, R. Zaera (2008b). "Relationship Between Mesostructure, Mechanical Behaviour and Damage of Cement Composites Under High-Pressure Confinement" *Exp. Mechanics.* **49**, 613–625.
- [15] P. Forquin, G. Gary, F. Gatingt (2008c). "A testing technique for concrete under confinement at high rates of strain" *Int J Imp Eng.* **35**(6), 425-446.
- [16] P. Forquin, K. Safa, G. Gary (2010). "Influence of free water on the quasi-static and dynamic strength of concrete in confined compression tests" *Cem. Concr. Res.* **40**(2), 321-333.
- [17] Kolsky H. (1949) "An investigation of mechanical properties of materials at very high rates of loading" *Proceedings of the Physical Society London; B* **62**, 676-700.

# Bioinspired polymeric foam-lattice composite: Towards superior energy absorption capability

R.G. Rinaldi<sup>1</sup>, C. Hammett<sup>2</sup>, J. Bernal-Ostos<sup>1</sup>, B. Kanungo<sup>1</sup>, A.J. Jacobsen<sup>3</sup>, R. Mc Meeking<sup>2</sup>,  
F.W. Zok<sup>1</sup>

<sup>1</sup>University of California, Materials department, Santa Barbara, CA, 93106,

[rrinaldi@engineering.ucsb.edu](mailto:rrinaldi@engineering.ucsb.edu)

<sup>2</sup>University of California, Mechanical Engineering department, Santa Barbara, CA, 93106,

<sup>3</sup>HRL Laboratories, LLC, Malibu, CA 90265

## Abstract

Many systems found in nature are hierarchical multi-scale materials in which periodicity and porosity are prominent features<sup>[1]</sup>. Such hierarchy suggests that different mechanisms are operative at distinct length-scales, potentially enhancing mechanical performance beyond that which could be obtained in simpler systems. Inspired by examples provided by nature, we aim to develop, characterize and understand hierarchical composites for force protection by combining periodic lattices with stochastic foams.

The system of present interest combines a periodic polymer lattice at the mm scale with a stochastic foam at the  $\mu\text{m}$  scale, yielding a hierarchical co-continuous composite. The lattice is produced via a self-propagating polymerization process<sup>[2]</sup> and is then filled with polyurethane foam. The study focuses specifically on the efficacy of this composite structure on energy absorption capability. To this end, experimental measurements have been made of the compressive stress-strain response from low (quasi-static) to high (dynamic) strain rates, within a range in which polymeric materials exhibit strong rate sensitivity<sup>[3]</sup>. Comparisons between the rate sensitivities of the constituent materials and the composite structures have been used to glean insights into the synergism that occurs as a result of the hierarchical nature of the composite design. Parametric numerical studies using finite element analysis have been instrumental in clarifying the key design parameters and in guiding the optimization process.

[1] Chen P-Y. et al., *Structure and Mechanical Properties of Selected biological materials*, *J. of the Mech. Behav. of Biomed. Mat. I* (2008) 208-226.

[2] Jacobsen A.J. et al., *Compression behavior of micro-scale truss structures formed from self-propagating polymer waveguides* *Act. Mat.* (2007) 6724-6733.

[3] Mulliken, A.D., Boyce, M.C., *Mechanics of the rate-dependent elastic-plastic deformation of glassy polymers from low to high strain rates* *Int. J. of Sol. & Struct.*(2006) 1331-1356.

**Key-words:** composite, periodic lattice, stochastic foam, energy absorption

- > Final printed area will be of 15 cm x 23 cm. The proceedings will be made of A4 colour prints.
- > Publication limited to 8 pages.
- > **Submit 2 electronic files, a .doc file and a .pdf file, along with the copyright agreement form, p. 3 of this file, by October 15, 2010 : bahlouli@unistra.fr**

3,7 cm



## "ON BOUNDED RATE CONSTITUTIVE MODEL: MOTIVATION AND APPLICATION TO DYNAMIC LOCALIZATION AND FAILURE"

O. Allix <sup>1</sup>

*1LMT/ENS Cachan/CNRS/Université Paris 6/PRES UniverSud Paris*

**Abstract.** This paper deals with the objective prediction of damage localization and failure within the framework of local constitutive model. One of the main limitations of such model with respect to failure prediction is that the results are mesh dependent. In order to overcome this problem, spatial localization limiters have been proposed and widely studied. In this paper an alternative approach based on bounded rate internal variables is explored. Several questions are addressed from modelling issues to identification ones. To illustrate the advantages and limitations of the approach the paper will make use of several examples as:

- spalling of 3D composites
- dynamic delamination of composites
- localization by necking in ductile metallic material
- objective prediction of erosion of laminated structures submitted to ballistic impact.

### 1. INTRODUCTION

Today, numerical simulations are widely used in industry in order to ensure the capability of a structure to support a given load, the later being some time quite complex like in the case of bird strikes. If the possible failure scenarios needs to be analyzed precisely, refined modelling should be used which allow to predict the failure in a robust manner. In today industrial environment, due to the lack of robustness of failure model [1], important numerical parametrs such as the mesh density, are fixed in order to calibrate the model with respect to some reference test. Industry involved in such calculation are more and more aware of the problem and seek for adapted solutions.

This fundamental problem has been studied since more of thirty years now and is well understood and analyzed. The more widespread approach to overcome the lack of consistency of material model with respect to failure is the one of non-local approach.

An huge litterature has been devoted to non-local model with variantes from non-local integral approaches to explicit and implicit gradient approaches or Cosserat models [2-10]. Despite of all this studies the development of these approaches in an industrial context is still seldom, a counter example can be found in [11]. The main reason is probably the fact that non-locality implies many and non obvious code developments, identification practices is also an issue.

That is why we have seek for another, even if maybe less general, possibility, to overcome the difficulty, the use of rate dependent models. Needleman was possibly the first to discuss how, in statics, the use of viscosity can help to conserve the elliptic property of the incremental equilibrium equations and, thus, eliminate pathological mesh-sensitivity [12]. Several models have been proposed in order to control localization through viscosity or rate-dependence, particularly for ductile materials with negative hardening Nevertheless several experimentations have led to deceptive results especially in dynamics. The study of Comi & Perego does perfectly illustrate the fact that the use of viscous damage model does not necessarily provide a way to regularize the problem in dynamics [13]. More recently a rate-dependent model of the Johnson-Cook type has been carefully studied in [14]. Here again it is concluded that the uniqueness of the simulation results until failure because the maximum cumulated plastic strain rate in the process zone increases without bounds when the mesh size decreases.

This seems in conflicts with theoretical studies which show that the use of viscosity allows the problem to remain hyperbolic, even in the presence of damage because the higher order terms of the equation do not involve the damage anymore. In a non published work by motivated by the description of damage and rupture of composites, we have concluded that such an analysis to be mathematically founded would require the damage rate to be bounded ; the fact that the problem remains hyperbolic [15] is connected to the fact that the highest derivatives become the dominant part of the solution for decreasing wave lengths. Such an analysis is correct indeed if lower terms can really be neglected, which can not be ensured if the

damage rate is not bounded. In statics this is always the case, the rate of the damage being directly linked to the external loading rate.

That is why we have proposed in [16-17] the concept of bounded damage rate model. A physical interpretation of the model is that a continuous damage variable results from a complex averaging process of micro flaws each of which having a finite propagation velocity, leading thus to a bounded damage rate. This idea is to be related with the concept of incubation time introduced in some failure criteria for dynamic loading [18-19]. A drawback, but in our opinion an inevitable one if one wish to conduct realistic simulations, is that the incubation rupture time is typically of the order of the microsecond, leading to very narrow localized zone in order to mimic a crack surrounded by the deteriorated area. Such model has to not to be interpreted as distinguished classical model used for viscosity, the introduction of the maximal damage rate intervenes only during the localisation phase (i. e. unstable phase) when the damage rate becomes close to its maximal value. If the material exhibits viscous effects apart during localization, they should to be incorporated in addition.

In [20] a broad identification making use of plate experiments on 3D C/C has been conducted. It has been concluded that the characteristic time of the model is comparable with the meso length scale divided by the celerity. In [21] experiments on mode II dynamic delamination have allowed the identification of the model for interlaminar interfacial damages, in addition associated rate dependent fracture mechanics criteria has been obtained. In recent work in cooperation with DGA Gramat the idea has been extended to the objective prediction of erosion in the case of high velocity impact on laminated plate, quite correct comparison with experiment have been obtained.

Those studies were conducted within the infinitesimal strain theory in the case where localization and instability were induced by damage only.

In the work of Suffis and Combescure [2000], a first attempt has been made to apply the bounded rate damage model in order to described in an objective manner the ductile failure of metallic plates inducing finite strains. Even if interesting results have been obtained, in particular with respects to the identification procedure, the proposed extension was not fully satisfying because in order to avoid localisation problem a critical damage value was introduced, in order to prevent spurious localization. In the context of the deterioration of metallic parts subjected to bird impact (Airbus-France) we have analyze the reason of the difficulty described herein. For finite plasticity and damage two sources of instability are encountered, only one being controlled by the use of a bounded rate damage model. A modification of the model has been proposed motivated by the fact that, at the material level, the failure is induced by intensive inelastic strain. The appearance of local necking or shear banding giving rise to the initiation and coalescence of microvoids and micro cracks up to the formation of a macro-crack. To mimic this process we rely on a continuous model in the finite strain setting where a damage variable governed by an equivalent plastic strain whose rate is bounded and governs the damage evolution. The proposed model prevents from mesh dependency while leading to standard code developments. The model has been identified and 2D simulations are compared with test results for several failure scenarios of aluminum structures.

In a study case of ductile failure of metallic material conducted with Airbus France

## References

- [1] Bazant, Z.P., 1976. Instability, ductility and size effect in strain softening concrete. In: Journal of engineering mechanics, 102, 331-344.
- [2] Triantafyllidis, N., Aifantis, E.C., 1986. A gradient approach to localization of deformation: I. Hyperelastic materials. In: Journal of Elasticity, 16, 225-237.
- [3] Lasry, D., Belytschko, T., 1988. Localization limiters in transient problems. In: International Journal of Solids and Structures, 24, (6), 581-597.
- [4] De Borst, R., 1991. Simulation of strain localization: A reappraisal of the Cosserat continuum. In: Engineering Computations, 8, 317-332.
- [5] Mühlhaus, H.B., De Borst, R., Aifantis, E.C., 1991. Constitutive models and numerical analysis for inelastic materials with microstructure. In: Computer Methods and Advances in Geomechanics. (Eds. G. Beer, J.R. Booker and J.P. Carter), Balkema, Rotterdam and Boston, 337-386.
- [6] De Borst, R., Sluys, L.J., Mühlhaus, H.-B., Pamin, J., 1993. Fundamental issues in finite element analysis of localization of deformation. In: Engineering Computations, 10, 99-121.
- [7] Pijaudier-Cabot, G., Bazant, Z.P., 1987. Non local damage theory. In: Journal of Engineering Mechanics, 113, 1512-1533.
- [8] Lasry, D., Belytschko, T., 1989. A study of localization limiters for strain softening in statics, dynamics. In: Computers and Structures, 33, (3), 707- 715.

- [9] Peerlings, R.H.J., Geers, M.G.D., De Borst, R., Brekelmans, W.A.M., 2001. A critical comparison of non-local, gradient enhanced softening continua. In: *International Journal of Solids and Structures*, 38, 7723-7746.
- [10] E. Lorentz, S. Andrieux, 2003 Analysis of nonlocal models through energetic formulations in: *Int. J. Solids and Structures*, vol 40/12, pp 2905-2936
- [11] Needleman, A., 1988. Material rate dependence, mesh sensitivity in localization problems. In: *Computer Methods in Applied Mechanics and Engineering*, 63, 69-85.
- [12] Loret, B., Prevost, J.H., 1990. Dynamic strain localization in elasto-viscoplastic solids, Part I. General formulation, one-dimensional examples. In: *Computer Methods in Applied Mechanics and Engineering*, 83, 247-273.
- [13] Comi, C., Perego, U., 1997. On visco-damage models for concrete at high strain rates. In: *Computational Plasticity, Fundamentals and applications*, CIMNE, 113, 1552-1556.
- [14] Flatten, A., Klingbeil, D., Svendsen, B., 2007 Non-local modelling of thermomechanical localization in metals. *Proc. of CFRAC 2007 - 1st International Conference on Computational Fracture and Failure of Materials and Structures*.
- [15] R. Dautray, J-L Lions *Mathematical Analysis and Numerical Method for Science and Technology*, Springer 2000
- [16] Allix, O., Deü, J.F., 1997. Delay damage modelling for fracture prediction of laminated composites under dynamic loading. In: *Engineering transactions*, 45, 29-46.
- [17] Allix, O., Feissel, P., Thevenet, P., 2003. A delay damage mesomodel of laminates under dynamic loading: basic aspects, identification issues. In: *Computers and Structures*, 81, 1177-1191.
- [18] Morozov, N.F., Petrov, Y.V., 2006. Incubation time based testing of materials. In: *European Journal of Mechanics and Solids*, 25, 670-676.
- [19] Curran, D.R., Seaman, L., Shockey, D.A., 1987. Dynamic failure of solids. In: *Physics Report (Review Section of Physics Letters)*, 147, 253-388.
- [20] Sen-Gupta, J., Allix, O., Boucard, P.A., Fanget, A., Hérel, P. Fracture prediction of a 3D C/C material under impact. *Composites Science & Technology*. Vol 65. Num 3/4. Pages 375-386. 2005
- [21] Guimard, J.M., Allix, O., Pechnick, N., Thevenet, P. Characterization and modeling of rate effects in the dynamic propagation of Mode-II delamination in composite laminates. *Int J of Fracture*. Vol 160. Num 1. Pages 55-71. 2009
- [22] Suffis, A., Combescure, A., Lubrecht, A., 2003. Damage model with delayed effect: Analytical, numerical studies of the evolution of the characteristic length. In: *International Journal of Solids and Structures*, 40, 3463-3476.

# MICROMECHANICAL MODELLING OF FINITE DEFORMATION OF THERMOPLASTIC MATRIX COMPOSITES

M. I. Okereke<sup>1</sup>, C. P. Buckley<sup>2</sup>

<sup>1</sup> *School of Engineering, University of Greenwich, Chatham Maritime, Kent, ME4 4TB.*

<sup>2</sup> *Department of Engineering Science, University of Oxford, 17 Parks Road, Oxford, OX1 3PJ.*

Emails: [m.i.okereke@gre.ac.uk](mailto:m.i.okereke@gre.ac.uk), [paul.buckley@eng.ox.ac.uk](mailto:paul.buckley@eng.ox.ac.uk)

**Abstract.** The prediction of the constitutive behavior of thermoplastic matrix composites from quasi-static up to impact rates demands a detailed understanding of the behavior of the polymeric constituents of these materials. This is due to the pronounced rate dependence of the polymeric matrix. This paper is an attempt at approaching the prediction of finite deformation of thermoplastic matrix composites using a multi-scale approach in which the fibre and the matrix are separately modelled and combined within a finite element scheme to determine the constitutive response of the test composite. A micromechanical model comprising a finite element implementation of constitutive laws for the fibre and matrix constituents are presented. Robust formulation for predicting the behavior of the matrix – a semicrystalline polymer, has been developed and described in this work. The techniques of generating 3D representative volume element (RVE) of the composite as well as prescribing periodic boundary conditions on the 3D RVE are described here. Validation studies for predicting the elastic properties of the composite using the FE methods are shown, while the effect of spatial arrangement of the fibre inclusions within the matrix at finite strains is illustrated.

## 1. INTRODUCTION

Continuous fibre, thermoplastic matrix, composite materials are attractive for high volume products because they combine manufacturing economics with some of the stiffness, strength and density advantages of the more widely used thermoset matrix composites. They have potential, for example, in components of light-weight cars of the future. However, these materials offer new challenges for the prediction of their properties in-use, arising from the pronounced viscoelasticity and plasticity of the matrix polymer, and its sensitivity to thermal and mechanical history during processing. The test composite used in this work is Plytron – a glass fibre polypropylene matrix composite. This talk is aimed at prediction the finite deformation of thermoplastic matrix composites.

The modelling approach involves a multi-scale modelling of the composite by tracking deformation from very small strains (where linear viscoelasticity conditions apply) to finite strains (dominated by nonlinear viscoelasticity effects). The modelling strategy is divided into *microscale* and *mesoscale* levels of analyses. The former deals with a microscale representation of constitutive models for semicrystalline polymers (i.e. the matrix) and the fibre while the later considers the lamina-level representation and modelling of the composite. A finite element implementation of the proposed micromechanical model, at lamina-level is presented.

Therefore, the key topics of the talk include: (a) development of robust matrix model for semicrystalline polymers; (b) design of novel method of generating 3D representative volume element (RVE) of continuous fibre composites; (c) implementation of periodic boundary conditions and application of single load cases to the 3D RVE; (d) and FE implementation of chosen homogenization strategy at lamina-level to predict nonlinear finite deformation of the composite.

## 2. DEVELOPMENT OF MATRIX MODEL FOR TEST COMPOSITE

The test matrix used in this work is polypropylene – a semicrystalline polymer. A robust physically-based constitutive model has been developed for modelling experimentally observed constitutive response for polypropylene. The 1D mechanical analogue for the model is shown in Figure 1 while Figure 2 shows the comparison between model and experimental data for compression tests on polypropylene. The

model prediction is thought to capture accurately the observed experimental response. The matrix modelling principle is an extension to two-process viscoelastic relaxation of a single-mode glass-rubber constitutive model for amorphous polymers[1-3]

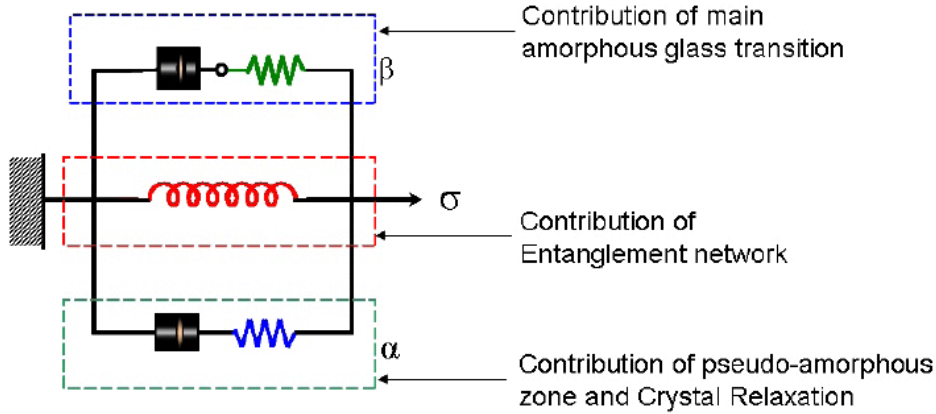


**Figure 1.** 1D Mechanical Analogue for modelling of semicrystalline polymers

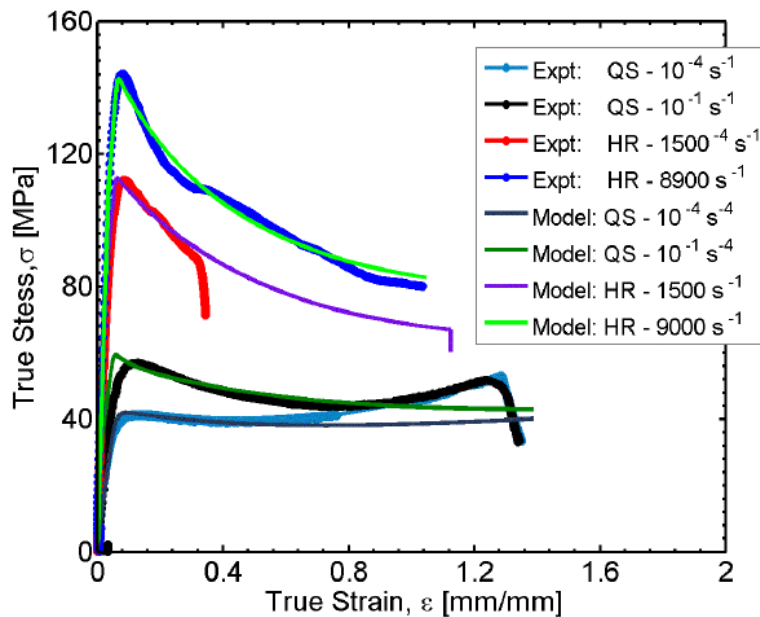


**Figure 2.** Comparison of experiments with model prediction for compression tests on polypropylene

### 3. A NEW ALGORITHM FOR GENERATING 3D REPRESENTATIVE VOLUME ELEMENTS

Having developed a robust matrix model, the next stage of the micromechanical modelling approach is the development of a Representative Volume Element (RVE) for the test material. A MATLAB algorithm has been developed based on the Monte Carlo Method or Hard Core model[4-6] in which a defined 2D RVE window is populated randomly until a defined volume fraction is achieved. An extra constraint of *periodicity of material* was applied on the generated RVE. For every fibre inclusion that is cut by a boundary wall, the corresponding half of the inclusion is replicated at a corresponding opposite and parallel wall. Typical RVEs generated using the above approach is shown in Figure 3 while Figure 4 shows the strategy for creating a 3D RVE for use in the micromechanical modelling.

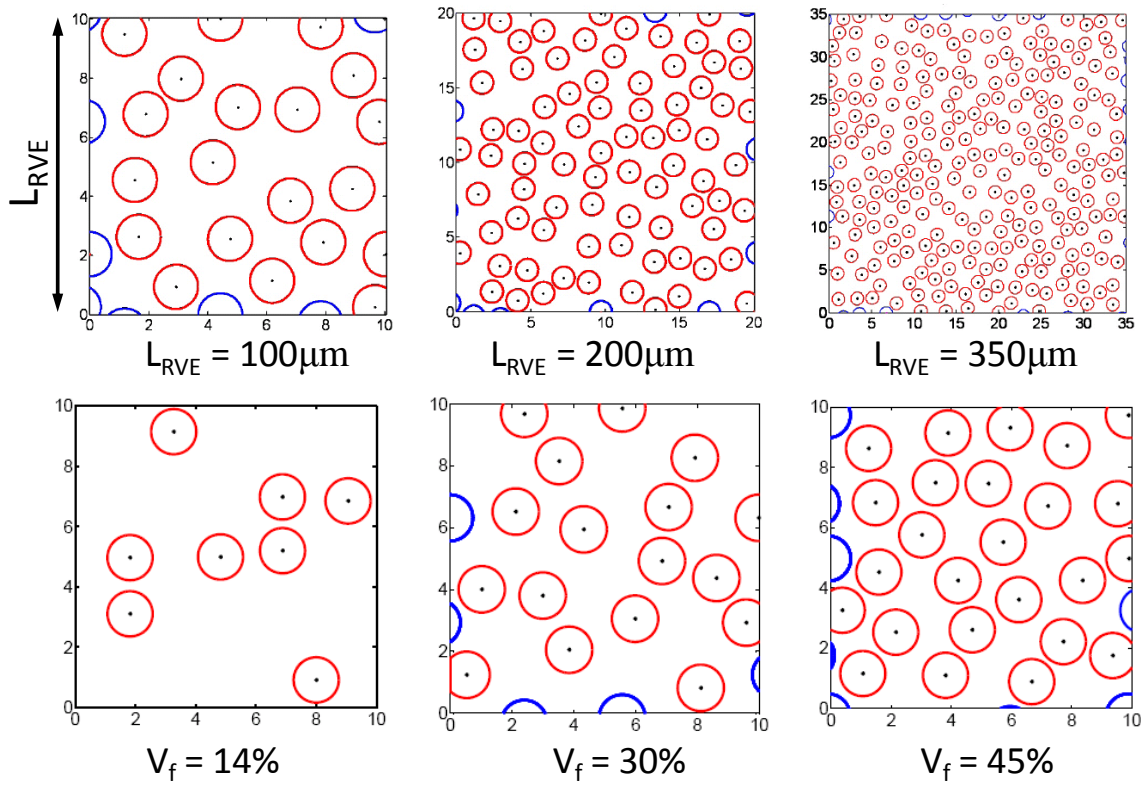


**Figure 3.** Typical 2D RVEs generated using the Monte Carlo Algorithm for different RVE window sizes ( $L_{RVE}$ ) and different volume fractions ( $V_f$ ).

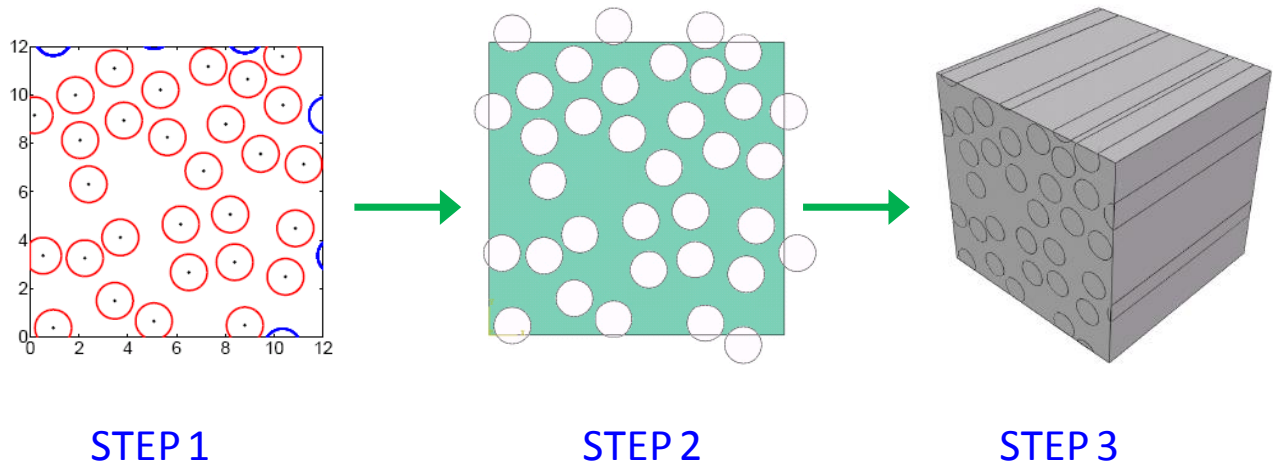


**Figure 4.** A three step implementation for creating 3D RVEs where Step 1: 2D RVE generated using Monte Carlo Algorithm, Step 2: Use of Python script within ABAQUS to convert 2D RVE to ABAQUS assembly model where white circles (fibres) and green region (matrix) and Step 3: Extrusion of 2D model to create 3D RVE.

#### 4. IMPLEMENTATION OF PERIODIC BOUNDARY CONDITION ON 3D RVES

Traditionally, periodic boundary conditions have generally been applied to 2D RVEs such that homogeneous deformation is enforced on boundary nodes of a given 2D RVE as shown in Figure 5. This work serves as the first instance where periodic boundary conditions (PBCs) have been applied to 3D RVEs with random spatial arrangement of inclusions. This implies applying homogeneous deformation equations shown in Figure 6, to all six surface nodes, 8 corner nodes and 12 edge nodes of a 3D RVE.

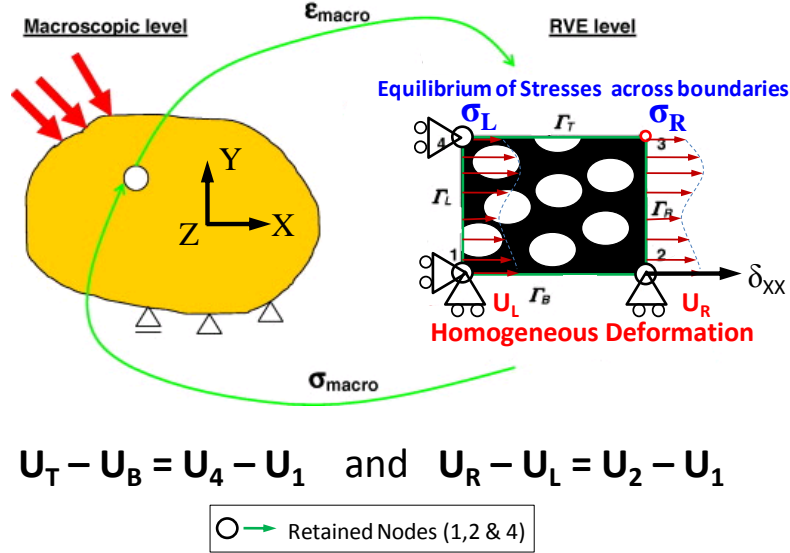


**Figure 5.** Strategy for applying Periodic Boundary Conditions (PBCs) on 2D RVEs.

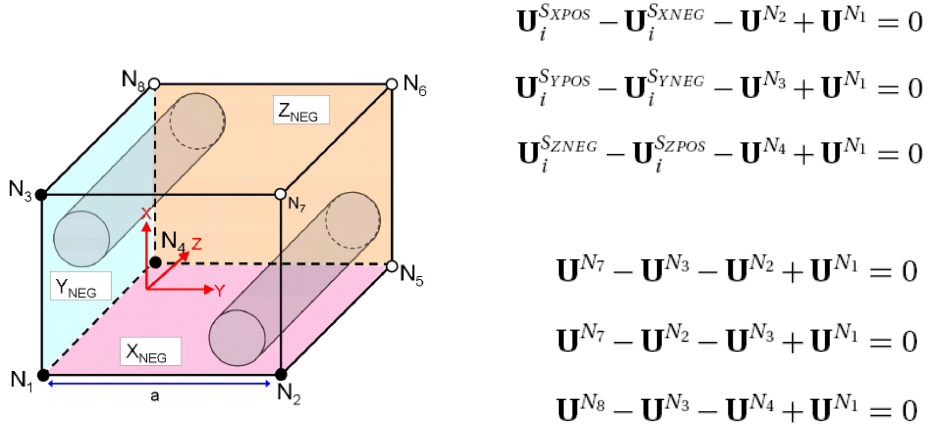


**Figure 6.** Strategy for applying Periodic Boundary Conditions (PBCs) on 3D RVEs and list of applicable homogeneous deformation equations for the given 3D RVE domain.

The following show examples of simulations based on 3D RVEs of polypropylene-glass fibre composite where the z-axis corresponds with the fibre direction. Figure 7 shows the logarithmic strain for compression tests along the x- and y-axes. Figure 8 shows von mises stress in the z-axis and out-of-plane shear deformation (xy) while Figure 9 shows logarithmic strain for out-of-plane (xz) and in-plane (yz) shear deformations.

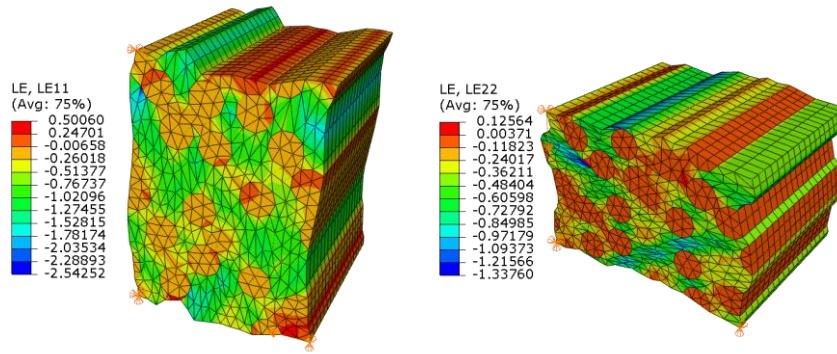


Figure 7: In-plane uniaxial compression along x/11- and y/22-axes

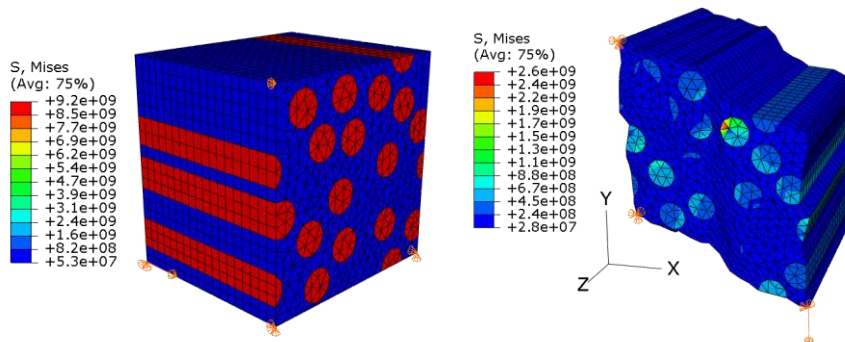


Figure 8: Fibre axis compression and out-of-plane (xy) shear deformation

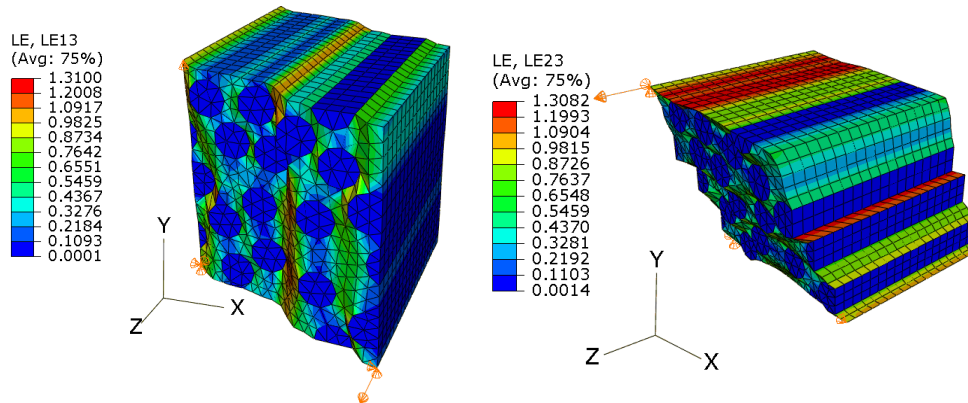


Figure 9: Out-of-plane (xz/13) or In-plane (yz/23) shear deformations

## 5. HOMOGENIZATION STRATEGY

In order to derive constitutive properties of the test composites, the generated 3D RVE implemented with periodic boundary conditions has to be used to determine homogenized properties. A homogenization strategy based on the Direct macro-micro relationship[7-11] has been adopted in this work. The previous works have adopted a 2D RVE where three retained nodes (for the RVE) are used to prescribe any desired load case. This work has extended the homogenization strategy above for a 3D RVE such that four retained nodes are used to prescribe 3D homogeneous deformation for the given RVE.

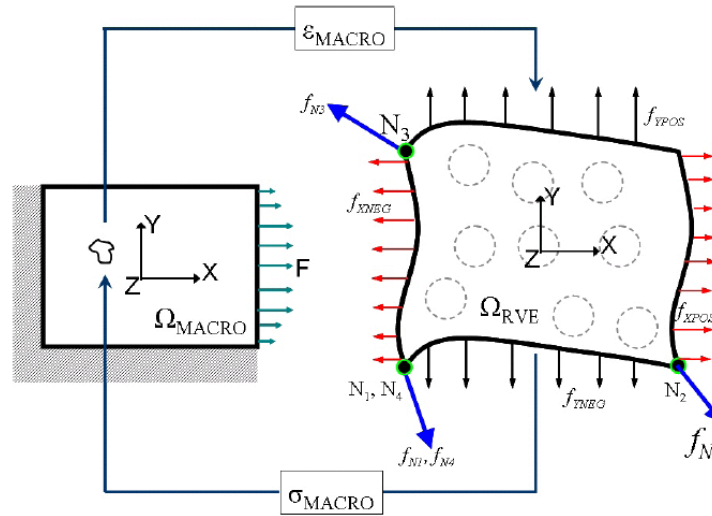


Figure 10: Macro-micro links for an RVE subjected to periodic boundary conditions

Consider a typical 3D RVE domain ( $\Omega_{RVE}$ ) such that there exist four retained nodes ( $N_1, N_2, N_3$  and  $N_4$ ). The coordinate positions for these nodes become:  $\mathbf{x}_1, \mathbf{x}_2, \mathbf{x}_3$ , and  $\mathbf{x}_4$ ). The corresponding reactions forces (in 3D) for the four nodes include:  $\mathbf{f}_{N1}, \mathbf{f}_{N2}, \mathbf{f}_{N3}$ , and  $\mathbf{f}_{N4}$ . The formulations for determining the overall stresses and strains at macroscale based on reaction forces and coordinate positions of chosen retained nodes are shown below:

$$\sigma_{macro} = \langle \boldsymbol{\sigma} \rangle = \frac{1}{V} \left\{ \mathbf{x}_1 \otimes \mathbf{f}_{N1} + \mathbf{x}_2 \otimes \mathbf{f}_{N2} + \mathbf{x}_3 \otimes \mathbf{f}_{N3} + \mathbf{x}_4 \otimes \mathbf{f}_{N4} \right\}$$

$$\mathbf{u}_2 = \boldsymbol{\epsilon}_{macro}(\mathbf{x}_2 - \mathbf{x}_1), \quad \mathbf{u}_3 = \boldsymbol{\epsilon}_{macro}(\mathbf{x}_3 - \mathbf{x}_1), \quad \text{and} \quad \mathbf{u}_4 = \boldsymbol{\epsilon}_{macro}(\mathbf{x}_4 - \mathbf{x}_1),$$

## 6. MODEL PREDICTIONS

In order to validate the modelling strategy, a boron-aluminium composite of volume fraction 47% was simulated using the above strategy. Experimental data on tests carried out on the boron-aluminium composite [12] and predictions from several prediction approaches were compared with predictions based on this work. One of the other approaches include that attributed to Sun and Vaidya [13] which is an FEM approach using a single-fibre square fibre array 3D RVE. Other approaches are Hashin-Rosen analytical approach based on energy variational principles[14-16], as well as semi-empirical classical laminate theory[17, 18]. This work used two 3D RVEs consisting of (a) one fibre (FEM Small) and size  $30\mu\text{m}^2$  and (b) 27 fibres (FEM Big) and size  $100\mu\text{m}^2$ . Table 1 shows the results of comparison between the two approaches.

In order to determine elastic properties using the above approach, an optimal RVE window size need to be determined for the test composite. This is the RVE window size at which there is a convergence of all elastic properties for the given RVE window. Figure 11 shows the graph of elastic properties against the RVE window size for Young Modulus.

Also, model predictions of rate-dependent transverse compression for polypropylene-glass fibre composite are shown in Figure 12 using the above homogenization approach. Again, the effect of spatial fibre arrangement at nonlinear finite deformation is illustrated in Figure 13. This shows the transverse strain ( $\epsilon_{22}$ ) contour plots for six different realizations of a  $90 \times 90\mu\text{m}^2$  RVE window tested at  $25^\circ\text{C}$ .

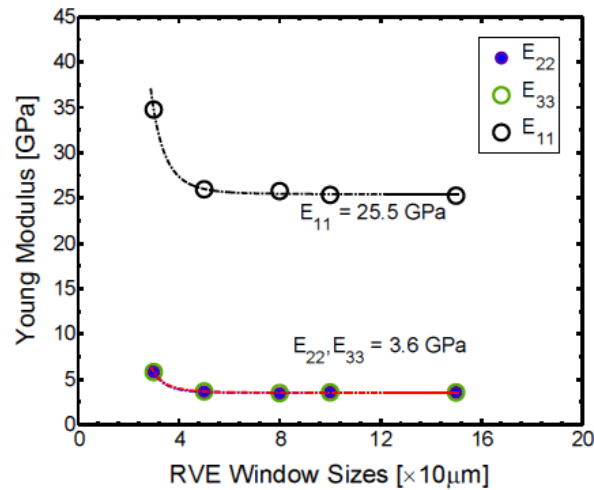


**Figure 11.** Variation of predictions of Young Modulus with RVE Window sizes

**Table 1:** Comparison of Elastic properties of boron-aluminium composite ( $v_f=47\%$ ) based on different approaches. Fibre axis is along 1-axis and transverse directions are 2- and 3-axes. Unit: GPa

Properties	Expt	FEM Big	FEM Small	FEM Sun	Analyt.	Empi.
$E_{11}$	216	208.7	213.4	214	215	214
$E_{22}$	140	134.3	141.0	135	139.1 {131.4}	156
$E_{33}$	-	135.2	141.0	-	-	-
$G_{12}$	52	52.9	51.9	51.1	53.9	62.6
$G_{13}$	-	52.8	52.0	-	-	-
$G_{23}$	-	49.4	45.0	-	54.6 {50.0}	43.6
$\nu_{12}$	0.29	0.299	0.300	0.19	0.195	0.20
$\nu_{13}$	-	0.299	0.300	-	-	-
$\nu_{23}$	-	0.193	0.198	-	0.31 {0.280}	0.31

## 7. CONCLUSIONS

A Finite Element Modelling (FEM) micromechanical model for prediction of finite deformation of a polypropylene-glass fibre composite is presented. The modelling overview include development of robust matrix model, generation of 3D RVE, implementation of PBCs on 3D RVEs, definition of micro-macro homogenization relationships and finally the model predictions for elastic and finite deformations. The effect of spatial arrangement at finite deformation suggests that in order to obtain homogenized responses at such large strains, a large RVE window is required. This presents opportunities for further work.

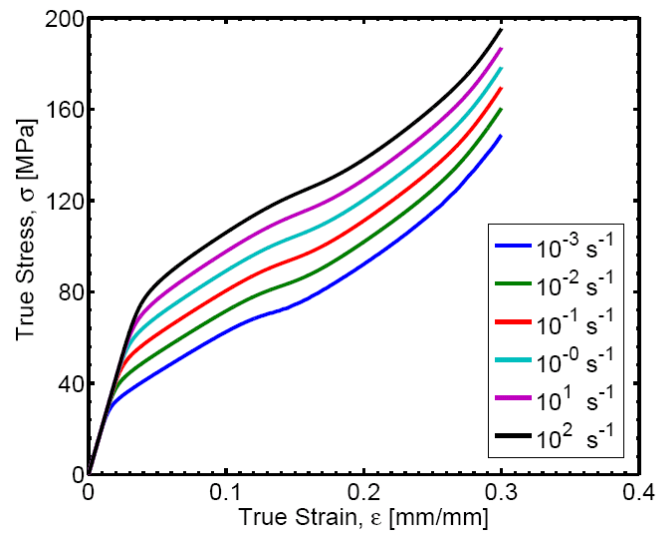


**Figure 12.** Prediction of rate-dependent transverse compression of test composite

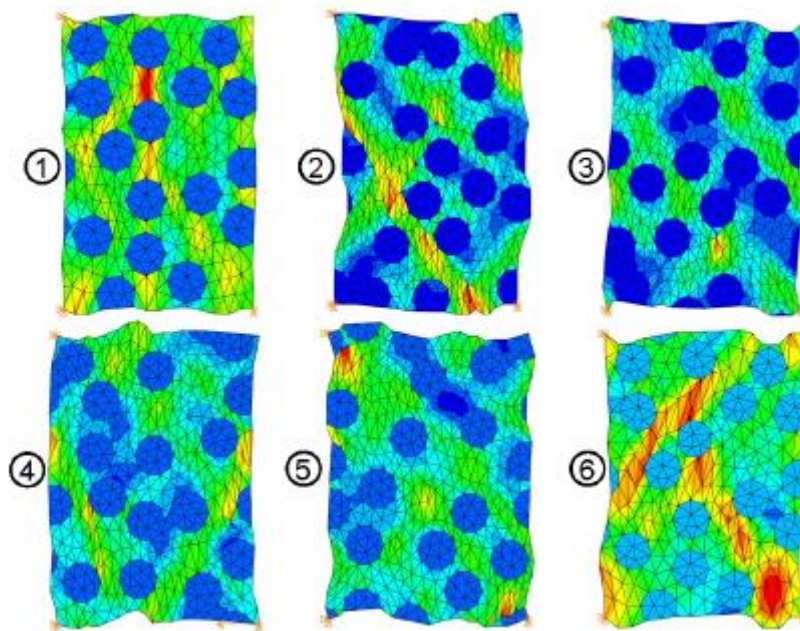


**Figure 13.** Transverse compression ( $\epsilon_{22}$ ) contour plots for 6 different spatial arrangements of the test composite.

## REFERENCES

1. Buckley, C.P., et al., *Deformation of thermosetting resins at impact rates of strain. Part 2: constitutive model with rejuvenation*. Journal of the Mechanics and Physics of Solids, 2004. **52**(10): p. 2355.
2. Buckley, C.P. and D.C. Jones, *Glass-rubber constitutive model for amorphous polymers near the glass transition*. Polymer, 1995. **36**(17): p. 3301.
3. Buckley, C.P., D.C. Jones, and D.P. Jones, *Hot-drawing of poly(ethylene terephthalate) under biaxial stress: Application of a three-dimensional glass-rubber constitutive model*. Polymer, 1996. **37**(12): p. 2403.
4. Buryachenko, V.A., et al., *Quantitative description and numerical simulation of random microstructures of composites and their effective elastic moduli*. International Journal of Solids and Structures, 2003. **40**(1): p. 47.
5. Melro, A.R., P.P. Camanho, and S.T. Pinho, *Generation of random distribution of fibres in long-fibre reinforced composites*. Composites Science and Technology, 2008. **68**(9): p. 2092.
6. Wongsto, A. and S. Li, *Micromechanical FE analysis of UD fibre-reinforced composites with fibres distributed at random over the transverse cross-section*. Composites Part A: Applied Science and Manufacturing, 2005. **36**(9): p. 1246.
7. van der Sluis, O., et al., *Overall behaviour of heterogeneous elastoviscoplastic materials: effect of microstructural modelling*. Mechanics of Materials, 2000. **32**(8): p. 449.
8. van der Sluis, O., P.J.G. Schreurs, and H.E.H. Meijer, *Homogenisation of structured elastoviscoplastic solids at finite strains*. Mechanics of Materials, 2001. **33**(9): p. 499.
9. van der Sluis, O., P.J.G. Schreurs, and H.E.H. Meijer, *Effective properties of a viscoplastic constitutive model obtained by homogenisation*. Mechanics of Materials, 1999. **31**(11): p. 743.
10. Kouznetsova, V., W.A.M. Brekelmans, and F.P.T. Baaijens, *Approach to micro-macro modeling of heterogeneous materials*. Computational Mechanics, 2001. **27**(1): p. 37.
11. Kouznetsova, V.G., M.G.D. Geers, and W.A.M. Brekelmans, *Multi-scale second-order computational homogenization of multi-phase materials: a nested finite element solution strategy*. Advances in Computational Plasticity, 2004. **193**(48-51): p. 5525.
12. Kenaga, D., J.F. Doyle, and C.T. Sun, *The Characterization of Boron/Aluminum Composite in the Nonlinear Range as an Orthotropic Elastic-Plastic Material*. Journal of Composite Materials, 1987. **21**(6): p. 516.
13. Sun, C.T. and R.S. Vaidya, *Prediction of composite properties from a representative volume element*. Composites Science and Technology, 1996. **56**(2): p. 171.
14. Hashin, Z., *Analysis of Composite Materials - A Survey*, in *Journal of Applied Mechanics, Transactions ASME*. 1983. p. 481.
15. Hashin, Z. and S. Shtrikman, *A variational approach to the theory of the elastic behaviour of multiphase materials*. Journal of the Mechanics and Physics of Solids, 1963. **11**(2): p. 127.
16. Hashin, Z. and Cr, *Theory of Fibre Reinforced Materials*, in *NASA Contractor Reports*. 1972.
17. Chamis, C.C., *Simplified Composite Micromechanics Equation for Hygral, Thermal, and Mechanical Properties*. S.A.M.P.E. quarterly, 1984. **15**(3): p. 14.
18. Chamis, C., *Simplified Composite Micromechanics Equations for Hygral, Thermal and Mechanical Properties*. 1983.

## TRANSFER OF COPYRIGHT AGREEMENT

Copyright to the article entitled: *Micromechanical modelling of finite deformation of thermoplastic matrix composites.*

By : M. I. Okereke, C. P. Buckley  
All Authors

is hereby transferred to the

**DYMAT Association**

effective when the article is accepted for publication in :

**19<sup>th</sup> DYMAT Technical Meeting**  
(electronic or hardcopy format)

However, the authors reserve the following:

- (1) All proprietary rights other than copyright, such as patent rights.
- (2) The right to use all or part of this article in future works of their own, such as lectures, press releases, reviews, textbooks, or reprint books.

*Third party requests to reprint all or part of the article must be directed to the publisher in order to obtain publisher's written permission.*

To be signed by at least one of the authors (who agrees to inform the others, if any) or, in the case of a "work made for hire", by the employer.

<u>Okereke</u> Signature	_____ Signature
MICHAEL I. OKEREKE Print Name	_____ Print Name
_____ Title, if not Author	_____ Title, if not Author
UNIVERSITY OF GREENWICH Institution or Company	_____ Institution or Company
23 <sup>RD</sup> SEPTEMBER, 2010 Date	_____ Date

The signed statement must be received before  
the manuscript can be accepted for publication.

Return to DYMAT before July 18, 2010 :

DYMAT 19<sup>th</sup> TM 2010 Nexter Munitions / 7 route de Guerry / 18023 Bourges Cedex /  
France Fax: 00 33 (0) 2 48 21 94 06      Email: 18dymat@nexter-group.fr

# INFLUENCE OF STRAIN RATE ON THE VISCOELASTIC RESPONSE OF ELASTOMERS

Jean-Christophe Petiteau<sup>1</sup>, Erwan Verron<sup>1</sup>, Hervé Le Sourne<sup>2</sup>, Ramzi Othman<sup>1</sup>, Bernard Auroire<sup>3</sup>, Jean-François Sigrist<sup>4</sup>

<sup>1</sup>Institut de Recherche en Génie Civil et Mécanique (GeM), UMR CNRS 6183, Ecole Centrale Nantes, BP 92101, 44321 Nantes Cedex 3, France

<sup>2</sup>Laboratoire Energétique Mécanique et Matériaux (LE2M), Institut Catholique d'Arts et Métiers (ICAM), 35 avenue du champ de Manoeuvres, 44470 Carquefou, France

<sup>3</sup>DGA Techniques Navales, Avenue de la Tour Royale, BP 40915, 83050 Toulon Cedex, France

<sup>4</sup>DCNS BU Propulsion, Indret, 44620 La Montagne, France

**Abstract.** Elastomers are widely used in industry because of their remarkable damping properties, e.g. antivibration mounts... Indeed, they can undergo severe mechanical loading conditions, i.e. large strain and large strain rates. In the case of dynamic loading conditions, the mechanical response of these materials can vary from a purely rubber-like behaviour to a glassy behaviour depending on the strain rate undergone.

The aim of the present work is to propose relevant constitutive equations for rubber-like materials subjected to intermediate strain rates loading conditions (from 1 to 100 s<sup>-1</sup>). In order to take into account the change of response (from rubber-like to glassy) of the polymers and to investigate their damping properties, two different incompressible and isotropic hyper-viscoelastic models proposed by Huber and Tsakmakis (Finite deformation viscoelasticity laws, *MECHANICS OF MATERIALS*, **32**, 1-18, 2000) are studied.

Uniaxial tension-compression cycles at different strain rates are studied. For finite strain, the models lead to different responses for the same loading conditions. Nevertheless, their responses evolve similarly with the strain rate: (i) the stress/strain curves exhibit the strengthening of rubber with the increase of the strain rate and (ii) the size of the hysteresis loop, i.e. the dissipative part of the response, first increases with strain rate and then decreases as the strain rate tends to infinity. The limiting properties of the models are analysed and we show that the parallel constitutive model is more relevant to predict the change of stiffness with respect to strain rate.

## INTRODUCTION

Because of their remarkable dissipation properties, elastomers are more and more used as damping parts in industry. There are especially used to absorb shock loading. Indeed, they can undergo severe mechanical loading conditions, i.e. large strain and strain rates. Nevertheless, the mechanical response of these materials can vary from a purely rubber-like behaviour to a glassy behaviour depending on the strain rate undergone, as shown by Yi *et al.* [2005] or Sarva *et al.* [2007]. In case of a shock, a rubber part can experience moderate to high strain rates; but the response of the material for this large range of strain rates is not well-known.

As other polymers, elastomers exhibit different types of behaviour depending on the temperature: these materials admit a glassy or a rubbery behaviour. These two different types of mechanical response are separated by a transition zone around the glass transition temperature  $T_g$ . However, it should be noticed that this definition of the glass transition depends on the characteristic time of the experience. More precisely,  $T_g$  is defined as the temperature for which the relaxation time of the material becomes very small as compared to the experience duration, i.e. the Deborah number  $D_e = t_c/t_p$  becomes greater than one,  $t_c$  being the relaxation time of the material and  $t_p$  the characteristic duration of the experience. So, as the strain rate increases, i.e.  $t_p$  decreases and  $D_e$  increases for a given temperature, and the glass transition temperature increases with the strain rate: rubber behaves as a glassy material for low temperature or high strain rate. For intermediate strain rate (10-100 s<sup>-1</sup>), the behaviour is in the transition zone (nor glassy neither rubbery). For this range of rates, very few experiments have been made: Fatt and Bekar [2004] can be cited for their experience using a modified Charpy pendulum to perform tension tests that highlight the material strengthening for increasing strain rate.

Here, we study the influence of the strain rate on the behaviour of a rubbery material and propose an appropriate constitutive model for large strain and intermediate strain rates. In fact, this type of materials is classically considered as large strain elastic solids and the constitutive equations are hyperelastic with more or less complicated free energy densities (see for example Fatt and Bekar [2004] and Renaud *et al.*

[2008]). Nevertheless, in order to predict the damping properties of the material, we take into account the viscoelastic nature of these materials in the model. Numerous different hyper-viscoelastic models have been previously proposed, but numbers of them are more or less based on the two basic phenomenological models developed by Huber and Tsakmakis [2000]. These constitutive equations can be seen as (non-linear) large strain counterparts of simple rheological models often used to describe linear viscoelasticity. The first one consists in a spring parallel to a Maxwell element also called Zener element, and the second one is composed by a Kelvin-Voigt element in series with a spring, also called Poynting-Thomson element, as shown in Fig. 1. The aim of the present work is to compare these two different models under dynamic loading conditions, and more precisely to study how the strain rate can influence the behaviour of each model.

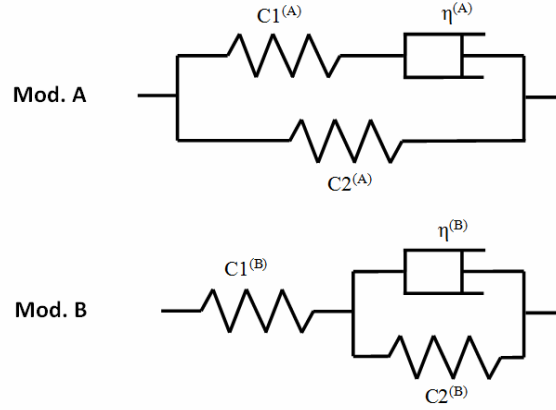


**Figure 1:** Simple rheological models A and B

## 1. DETERMINATION OF THE MOST APPROPRIATE MODEL FOR HIGH STRAIN RATES

### 1.1. Governing equations

The mechanical responses of the two models are identical for small strain problems. Here, they are extended to large strain by considering the springs as non-linear hyperelastic solids and the dashpots as Newtonian fluids of viscosity  $\eta$ . Classically, the deformation gradient is multiplicatively decomposed into elastic and inelastic parts:

$$\mathbf{F} = \mathbf{F}_e \mathbf{F}_i \quad (1)$$

Here we adopt the classical assumption of rubber incompressibility, and we consider that both parts of the deformation gradient are incompressible:

$$\det(\mathbf{F}) = \det(\mathbf{F}_e) = \det(\mathbf{F}_i) = 1 \quad (2)$$

The second principle of thermodynamics states that the intrinsic dissipation has to be positive:

$$J\boldsymbol{\sigma} : \mathbf{D} - \dot{\Psi} = \boldsymbol{\sigma}_E : \mathbf{D} - \dot{\Psi} \geq 0 \quad (3)$$

where the Cauchy stress tensor is separated into the spherical stress, which involves the hydrostatic pressure due to incompressibility, and the deviatoric stress, i.e.  $\boldsymbol{\sigma} = -p\mathbf{I} + \boldsymbol{\sigma}_E$ , where  $\Psi$  is the free energy density of the model and  $\mathbf{D} = \frac{1}{2}(\mathbf{L} + \mathbf{L}^T)$  is the strain rate tensor with  $\mathbf{L} = \dot{\mathbf{F}}\mathbf{F}^{-1}$ . This equation is satisfied for all incompressible transformation, i.e. transformations with  $\text{tr}\mathbf{D} = 0$ .

For the model A, the free energy is written as:

$$\Psi = \Psi_1^{(A)}(\mathbf{E}) + \Psi_2^{(A)}(\mathbf{E}_e) \quad (4)$$

where  $\mathbf{E} = \frac{1}{2}(\mathbf{F}^T\mathbf{F} - \mathbf{I})$  and  $\mathbf{E}_e = \frac{1}{2}(\mathbf{F}_e^T\mathbf{F}_e - \mathbf{I})$  are the total and the elastic Green Lagrange strain tensors,  $\Psi_1^{(A)}(\mathbf{E})$  is the free energy of the first spring and  $\Psi_2^{(A)}(\mathbf{E}_e)$  the free energy of the second one. For isotropic materials, these free energy densities can be expressed in terms of the two first invariants of their respective strain tensor:

$$\Psi_1^{(A)}(\mathbf{E}) = \chi_1^{(A)}(\mathbf{I}_B, \mathbf{II}_B) \quad (5)$$

and

$$\Psi_2^{(A)}(\mathbf{E}_e) = \chi_2^{(A)}(\mathbf{I}_{B_e}, \mathbf{II}_{B_e}) \quad (6)$$

Finally, the model A is governed by the following set of equations (see Hüber and Tsakmakis for details)

$$\begin{cases} \boldsymbol{\sigma} = -p\mathbf{I} + \boldsymbol{\sigma}_E \\ \boldsymbol{\sigma}_E = \boldsymbol{\sigma}_E^{(E)} + 2\frac{\partial\chi_2^{(A)}}{\partial\mathbf{I}_{B_e}}\mathbf{B}_e + 2\frac{\partial\chi_2^{(A)}}{\partial\mathbf{II}_{B_e}}\mathbf{B}_e^{-1} \text{ with } \mathbf{B}_e = \mathbf{F}_e\mathbf{F}_e^T \\ \boldsymbol{\sigma}_E^{(E)} = 2\frac{\partial\chi_1^{(A)}}{\partial\mathbf{I}_B}\mathbf{B} + 2\frac{\partial\chi_1^{(A)}}{\partial\mathbf{II}_B}\mathbf{B}^{-1} \text{ with } \mathbf{B} = \mathbf{F}\mathbf{F}^T \\ \dot{\mathbf{B}}_e = \mathbf{B}_e\mathbf{L}^T + \mathbf{L}\mathbf{B}_e - \frac{2}{\eta^{(A)}}\mathbf{B}_e \left( \boldsymbol{\sigma}_E - \boldsymbol{\sigma}_E^{(E)} \right)^D \end{cases} \quad (7)$$

In these equations,  $\eta^{(B)}$  is the viscosity (of the dashpot) and the last equation is the evolution equation of the internal variable  $\mathbf{B}_e$ .

The free energy density of the model B depends on both the elastic and viscous deformation gradients:

$$\Psi = \Psi_1^{(B)}(\mathbf{E}_e) + \Psi_2^{(B)}(\mathbf{E}_i) \quad (8)$$

in which  $\Psi_1^{(B)}(\mathbf{E}_e)$  is the free energy of the first spring and  $\Psi_2^{(B)}(\mathbf{E}_i)$  is the free energy of the second spring in terms of the inelastic deformation:

$$\Psi_1^{(B)}(\mathbf{E}_e) = \chi_1^{(B)}(\mathbf{I}_{B_e}, \mathbf{II}_{B_e}) \quad (9)$$

and

$$\Psi_2^{(B)}(\mathbf{E}_i) = \chi_2^{(B)}(\mathbf{I}_{B_i}, \mathbf{II}_{B_i}) \quad (10)$$

and the corresponding set of equations is

$$\begin{cases} \boldsymbol{\sigma} = -p\mathbf{I} + \boldsymbol{\sigma}_E \\ \boldsymbol{\sigma}_E = 2\frac{\partial\chi_1^{(B)}}{\partial\mathbf{I}_{B_e}}\mathbf{B}_e + 2\frac{\partial\chi_1^{(B)}}{\partial\mathbf{II}_{B_e}}\mathbf{B}_e^{-1} \\ \boldsymbol{\sigma}_E^{(s)} = 2\frac{\partial\chi_2^{(B)}}{\partial\mathbf{I}_{B_i}}\mathbf{B}_i + 2\frac{\partial\chi_2^{(B)}}{\partial\mathbf{II}_{B_i}}\mathbf{B}_i^{-1} \text{ with } \mathbf{B}_i = \mathbf{F}_i\mathbf{F}_i^T \\ \dot{\mathbf{B}}_e = \mathbf{B}_e\mathbf{L}^T + \mathbf{L}\mathbf{B}_e + 2\mathbf{F}_e\mathbf{D}_i\mathbf{F}_e^T \\ \mathbf{F}_e\mathbf{D}_i\mathbf{F}_e^T = \frac{1}{\eta^{(B)}} \left\{ \mathbf{B}_e (\boldsymbol{\sigma}_E)^D - \mathbf{F}_e \left( \boldsymbol{\sigma}_E^{(s)} \right)^D \mathbf{F}_e^T \right\} \end{cases} \quad (11)$$

in which  $\eta^{(B)}$  is the viscosity of the dashpot. The two last equations are the evolution equations for the internal variable  $\mathbf{B}_e$ .

## 1.2. Results

To investigate the influence of the strain rate on the response of each model, we consider a series of uniaxial loading and unloading stretch. We set the strain rate tensor  $\mathbf{D}$  constant throughout the deformation process:

$$\mathbf{D} = \begin{pmatrix} \dot{\zeta} & 0 & 0 \\ 0 & -\frac{\dot{\zeta}}{2} & 0 \\ 0 & 0 & -\frac{\dot{\zeta}}{2} \end{pmatrix} \quad (12)$$

during loading and

$$\mathbf{D} = \begin{pmatrix} -\dot{\zeta} & 0 & 0 \\ 0 & \frac{\dot{\zeta}}{2} & 0 \\ 0 & 0 & \frac{\dot{\zeta}}{2} \end{pmatrix} \quad (13)$$

during the unloading where  $\dot{\zeta}$  is constant and denoted  $\alpha$  in the following. Thus,

$$\mathbf{F} = \begin{pmatrix} e^\zeta & 0 & 0 \\ 0 & e^{-(\zeta/2)} & 0 \\ 0 & 0 & e^{-(\zeta/2)} \end{pmatrix} \quad (14)$$

The corresponding strain-time curve is shown in Figure 2, using  $\lambda = 1 + \epsilon = e^\zeta$  as the dilatation.

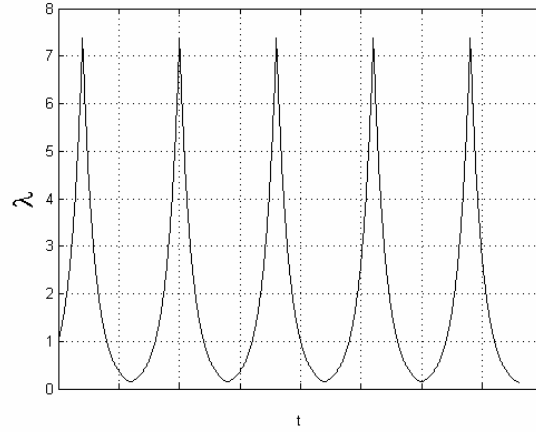


**Figure 2:** Loading strain/time curve

To simplify the following discussion, we choose the neo-Hookean strain energy density for all springs in both models A and B ( $\sigma = -p\mathbf{I} + c\mathbf{B}$  with  $c$  the material parameter). The corresponding material parameters are given in Table 1.

Model A		Model B	
$CI^{(A)}$ (MPa)	10	$CI^{(B)}$ (MPa)	20
$C2^{(A)}$ (MPa)	10	$C2^{(B)}$ (MPa)	20
$\eta^{(A)}$ (MPa.s)	1	$\eta^{(B)}$ (MPa.s)	1

**Table 1:** Material parameters

For small strain problems, there exists an explicit relationship between the material parameters of the two models that renders identical their responses. For large strain problems, if the same relationship is considered, the true stress/true strain curves are not identical as shown in Figure 3. We will further study the differences between the two models while increasing the strain rate.

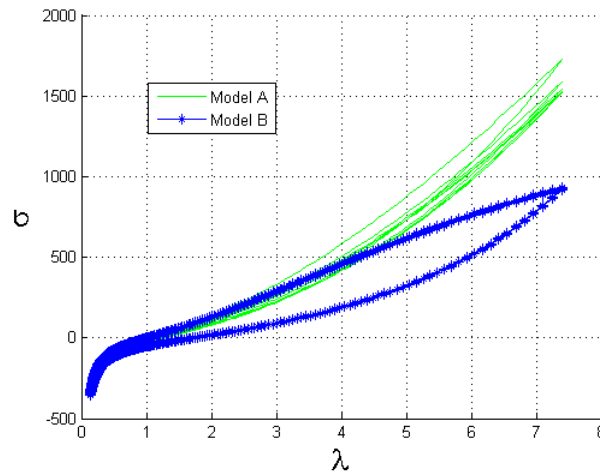
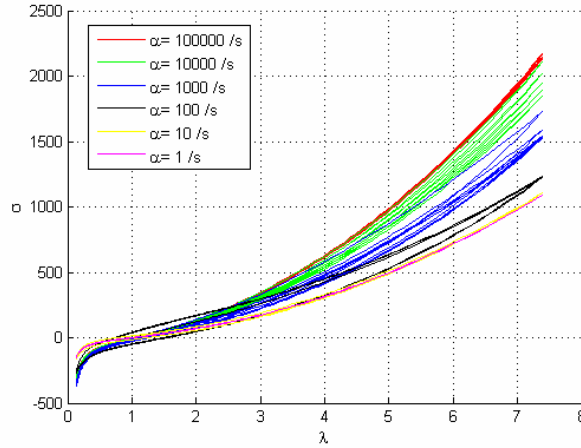
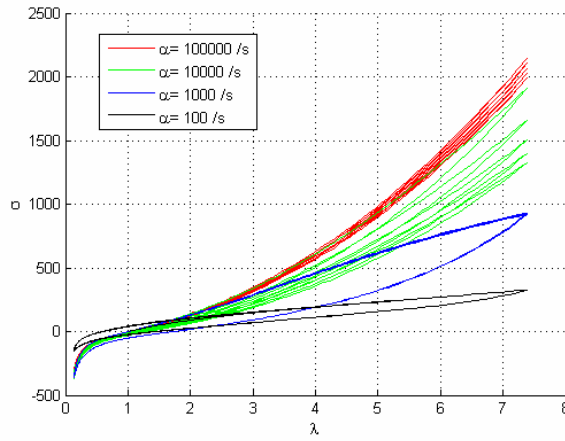


**Figure 3:** Stress/strain curve of model A and B assuming the small strain relationship between the material parameters



a) Model A



b) Model B

**Figure 4:** Stress/strain curves for different strain rates

As the value of the strain rate  $\alpha$  increases, Figure 4 shows that the stress-strain curves of both models exhibit a strengthening and a significant change in the hysteresis loop. Strengthening was expected for this kind of experiment and both models exhibit it, while keeping constant the three parameters (one parameter for each of the spring and one for the dashpot). So, the models do not need a change of the parameters to reproduce strengthening as it is the case for hyperelastic constitutive equations: non-linear hyper-viscoelastic constitutive equations intrinsically contains this characteristic. The size of the hysteresis loop first increases while increasing the strain rate and then decreases as shown in Figure 4.

### 1.3. Discussion

Even if the two model present different responses for the same loading conditions, it is difficult to argue that a model is better than the other one; because both responses seem realistic. In order to further study their differences and to determine which model is the most appropriate for high strain rates, we will determine their respective limits as the strain rate tends to zero and infinity.

If the strain rate tends to infinity,  $\mathbf{F}_e$  tends to  $\mathbf{F}$  (so  $\mathbf{B}_e$  tends to  $\mathbf{B}$ ) and  $\mathbf{F}_i$  tends to zero. Then, the “infinity-limit” for model A reduces to:

$$\boldsymbol{\sigma} = -p\mathbf{I} + 2 \left( \frac{\partial \chi_1^{(A)}}{\partial \mathbf{I}_B} + \frac{\partial \chi_2^{(A)}}{\partial \mathbf{I}_B} \right) \mathbf{B} + 2 \left( \frac{\partial \chi_1^{(A)}}{\partial \mathbf{II}_B} + \frac{\partial \chi_2^{(A)}}{\partial \mathbf{II}_B} \right) \mathbf{B}^{-1} \quad (15)$$

and for model B to

$$\boldsymbol{\sigma} = -p\mathbf{I} + 2\frac{\partial\chi_1^{(B)}}{\partial\mathbf{I}_B}\mathbf{B} + 2\frac{\partial\chi_1^{(B)}}{\partial\mathbf{II}_B}\mathbf{B}^{-1} \quad (16)$$

Then, both models are simply hyperelastic and it confirms that the size of the hysteresis loop decreases and tends to zero for high strain rates.

For quasi static experiments, i.e. when the strain rate tends to zero, it can be shown that

$$\dot{\mathbf{F}} = \dot{\mathbf{F}}_e\mathbf{F}_i + \mathbf{F}_e\dot{\mathbf{F}}_i \rightarrow 0 \quad (17)$$

for both models, but  $\mathbf{F}$  is not equal to zero and so,  $\mathbf{F}_e$  and  $\mathbf{F}_i$  are not null. So, all strain rate tensors ( $\dot{\mathbf{F}}_e, \dot{\mathbf{F}}_i, \mathbf{D}_e, \mathbf{D}_i$ ) tend to zero. Then, for model A, we have the deviatoric part:

$$\left(\boldsymbol{\sigma}_E - \boldsymbol{\sigma}_E^{(E)}\right)^D \rightarrow 0 \quad (18)$$

or similarly

$$\boldsymbol{\sigma}_E - \boldsymbol{\sigma}_E^{(E)} \rightarrow u\mathbf{I} \quad (19)$$

and finally the “zero-limit” model A reduces to:

$$\boldsymbol{\sigma} = -(p+u)\mathbf{I} + 2\frac{\partial\chi_1^{(A)}}{\partial\mathbf{I}_B}\mathbf{B} + 2\frac{\partial\chi_1^{(A)}}{\partial\mathbf{II}_B}\mathbf{B}^{-1} \quad (20)$$

For model B, if  $\mathbf{D}_i \rightarrow 0$ ,  $(c_e\sigma_E - \sigma_E^{(s)})^D \rightarrow 0$  ( $\eta$  is finite), and we find:

$$2\frac{\partial\chi_1^{(B)}}{\partial\mathbf{I}_{B_e}}\mathbf{C}_e - 2\frac{\partial\chi_1^{(B)}}{\partial\mathbf{II}_{B_e}}\mathbf{C}_e^{-1} - 2\frac{\partial\chi_2^{(B)}}{\partial\mathbf{I}_{B_i}}\mathbf{B}_i + 2\frac{\partial\chi_2^{(B)}}{\partial\mathbf{II}_{B_i}}\mathbf{B}_i^{-1} \rightarrow u\mathbf{I} \quad (21)$$

This relation links the movement of the elastic and the inelastic part but no simple general model can be found using this relation.

Finally, both models admit simple limits as the strain rate tends to infinity; this limit is a simple hyperelastic model in both cases. When the strain rate tends to zero, i.e. for quasi-static loading conditions, we also obtain a simple hyperelastic limit model for model A, but for model B, we only derived a relationship between the elastic and the inelastic parts of the deformation. This relation does not lead to a simple constitutive equation. As we know that for quasi-static loading conditions, elastomers are elastic (Treloar [1975]), it is more relevant to choose model A to carry on our study: as it admits a well-defined hyperelastic model as “zero-limit”, it will be easier to determine some of its material parameters with the help of quasi-static experiments.

## 2. STUDY OF MODEL A UNDER DYNAMIC LOADING CONDITIONS

### 2.1. Equations of the model

Considering neo-Hookean strain energy densities, model A only depends on three material parameters ( $C_1, C_2$  associated with the springs and  $\eta^{(A)}$  with the dashpot) and the constitutive equation of model A reduces to

$$\begin{cases} \boldsymbol{\sigma} = -p\mathbf{I} + \boldsymbol{\sigma}_E \\ \boldsymbol{\sigma}_E = \boldsymbol{\sigma}_E^{(E)} + 2C_2\mathbf{B}_e \\ \boldsymbol{\sigma}_E^{(E)} = 2C_1\mathbf{B} \text{ with } \mathbf{B} = \mathbf{F}\mathbf{F}^T \\ \dot{\mathbf{B}}_e = \mathbf{B}_e\mathbf{L}^T + \mathbf{L}\mathbf{B}_e - \frac{2}{\eta^{(A)}}\mathbf{B}_e \left(\boldsymbol{\sigma}_E - \boldsymbol{\sigma}_E^{(E)}\right)^D \end{cases} \quad (22)$$

### 2.2. Analysis of the model

It can be shown that, for  $C_1$  and  $C_2$  set constant, keeping the product  $\alpha\eta^{(A)}$  constant leads to identical true stress/true strain curves. Thus, in order to study the response of the model for different material parameters, we can set  $\eta^{(A)}$  constant and only change the strain rate  $\alpha$ . As the parameter  $C_1$  defines the elastic response of the model, it gives the stiffness of the model for low strain rates. The parameter  $C_2$

drives the stiffness change between low and high strain rates. Thus, as  $C_2$  increases, both the strengthening of the stress-strain response and the size of the hysteresis loop increase.

Nevertheless, explaining the role of each model parameter is not sufficient to understand how the model “works”. So, in the following, we study the evolution of each strain (elastic, inelastic and total) during loading and unloading. Time evolutions of the strain measures during the cycles are presented in Figure 5 for different strain rates  $\alpha$ . Even if the total strain presents the same shape for the three strain rates, elastic and inelastic parts do not act similarly in the three cases. Firstly, elastic strain is nearly equal to zero for very low strain rates; it increases with the strain rate and finally reach the total strain when the strain rate tends to infinity. Inelastic strain evolves in the opposite way: it decreases as the strain rate increases.

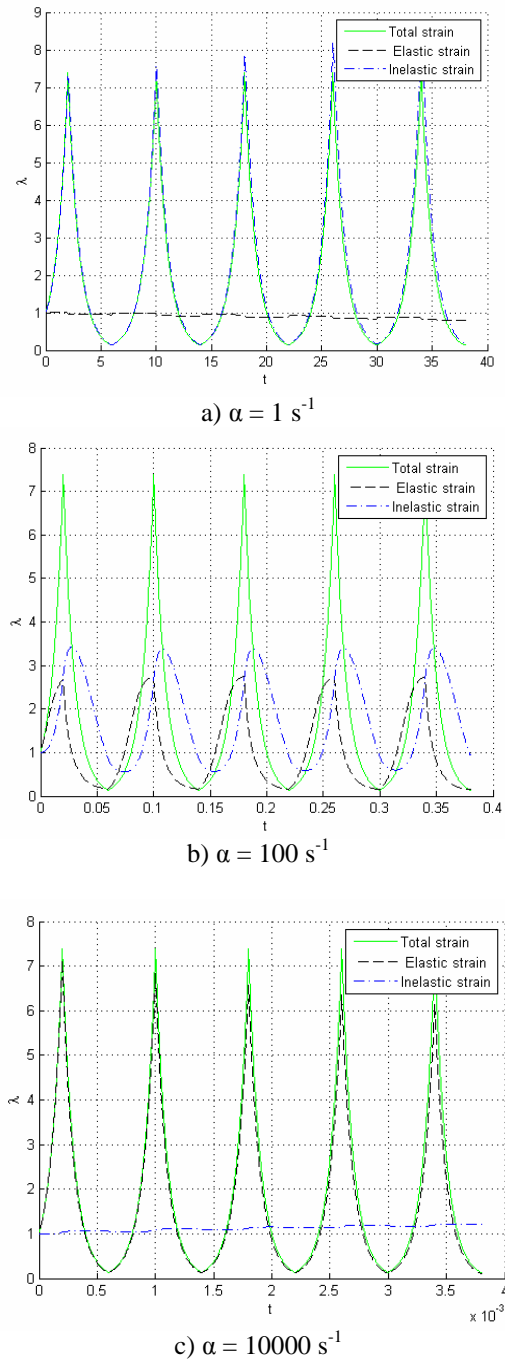


**Figure 5:** Elastic, inelastic and total strain vs. time for different strain rates

Second, strengthening of the model for high strain rates is directly related to the increase of the ratio between the elastic and the total strains. In fact, for low strain rates, the stress is only due to the spring subjected to the total strain, as the dashpot stretch. As the strain rate increases, the spring subjected to the elastic strain renders the response more and more rigid, because the dashpot does not have sufficient time to stretch.

Obviously, the elastic strain remains in phase with the total one, whereas the inelastic one is not. As the strain rate increased, the dephasing between the inelastic strain and the total one increases, because the viscosity prevents stress to increase; and the more the strain rate increases, the more it is difficult for the dashpot to reach the prescribed velocity. Thus, the elastic part of the strain must rise instantly while the model is loaded and then reach a plateau when the dashpot reaches the rate imposed by loading conditions. This dephasing explains why the size of the hysteresis loop increased at first. The decrease of the size of the hysteresis loop is related to the decrease of the ratio between the inelastic and the total strain. We have also noticed that the inelastic strain continues to increase while stopping the loading or starting the unloading. We are not sure that this effect is realistic; it appears as an artefact of the constitutive equation.

## CONCLUSION

In this paper, we have studied two different hyper-viscoelastic constitutive equations at different strain rates. As expected, the strengthening of both models is experienced for increasing strain rates as well as the change in the size of the hysteresis loop, i.e. the amount of dissipated energy. The limit properties of the models (for very low and high strain rates) have been studied and model A has been retained as the most appropriate for further studies because of its ability to exhibit a simple hyperelastic response for quasi-static experiments. The role of each parameter is now better understood: the parameters of the spring that experiences the total strain  $\mathbf{F}$  drives the stiffness for low strain rates and the ones of the spring that experiences the elastic strain  $\mathbf{F}_e$  drives the change in stiffness between low and high strain rates. The viscosity leads the model to strengthen for a given range of strain rates. To continue this study, we will carry out experiments on rubber parts at intermediate strain rates in order to determine if it is possible to model rubber response over a range of intermediate strain rates ( $1-100 \text{ s}^{-1}$ ) with model A.

## References

- [1] Fatt and Bekar, High-speed testing and material modeling of unfilled styrene butadiene vulcanizates at impact rates, *JOURNAL OF MATERIALS SCIENCE* 39 (2004) 6885 – 6899, 2004.
- [2] Hüber and Tsakmakis, Finite deformation viscoelasticity laws, *MECHANICS OF MATERIALS* 32 (2000) 1±18, 2000.
- [3] Renaud, The Yeoh model applied to the modeling of large deformation contact/impact problems, *INTERNATIONAL JOURNAL OF IMPACT ENGINEERING* 36 (2009) 659–666, 2008.
- [4] Sarva, Stress-strain behavior of a polyurea and a polyurethane from low to high strain rates, *POLYMER*, 48 (8): 2208-2213 , 2007.
- [5] Yi, Large deformation rate-dependent stress-strain behavior of polyurea and polyurethanes, *POLYMER*, 47 (1): 319-329, 2005.
- [6] Treloar, *The Physics of Rubber Elasticity*. (3rd ed.), Oxford University Press, 1975

# IDENTIFICATION OF ELASTIC STIFFNESSES OF COMPOSITES FROM FULL-FIELD MEASUREMENTS USING AN ULTRA HIGH SPEED CAMERA

F. Pierron<sup>1</sup>, R. Moulart<sup>1</sup>, S.R. Hallett<sup>2</sup> and M.R. Wisnom<sup>2</sup>

<sup>1</sup> LMPF, Arts et Métiers ParisTech, Rue St Dominique, BP 508, Châlons-en-Champagne, France

<sup>2</sup> ACCIS, University of Bristol, Queen's building, University Walk, Bristol BS8 1TR, UK

**Abstract.** The present paper deals with full-field strain measurement on unnotched and open-hole tensile specimens submitted to high strain rate loading through a Hopkinson bar device. After having briefly explained the methodology (using an Ultra-High speed camera), the displacement, strain and acceleration maps are given and discussed. Then, a first attempt to identify stiffnesses on this dynamic case only from the actual strain and acceleration maps using the Virtual Fields Method (VFM) is introduced. The results are extremely promising considering the limited quality of the measurements. Finally, the impact force is reconstructed with a variant of the VFM and compared with the measured impact force. The match between the two is discussed.

## 1. INTRODUCTION

The identification of the mechanical behaviour of materials at high strain rates is still an open problem. One of the reasons is that at such strain rates, homogeneous stress and strain states are extremely difficult to obtain so that the usual identification procedures do not apply [1]. In particular, loads are very challenging to measure because of inertia effects causing ringing in standard load cells. This is the reason of the use of the very well established split Hopkinson pressure bar (SHPB) which enables to extract global stress strain curves under very restrictive assumptions.

Thanks to the recent development of ultra-high speed imaging systems [2,3], it should now be possible to study the strain distribution in high-rate applications by adapting the full-field measurement methods used in quasi-static load states. This work proposes a first attempt to draw strain fields at speeds up to 300,000 frames per second (fps) with the grid method

## 2. EXPERIMENTAL PROCEDURE

The specimens were 16 mm wide,  $[45_2/90_2/-45_2/0_2]_s$  quasi-isotropic glass laminated composite coupons, one with a 3.2 mm diameter open circular hole and one without a hole. On these specimens, a cross-grid of 200  $\mu\text{m}$  pitch was bonded. This grid constitutes the pattern necessary to measure the full-field displacement maps. The grid method was used [4] to process the grid images. It is based on the calculation of the phase of a periodic pattern (the grid) deposited onto the surface to study. The in-plane displacement maps can thus be obtained and, by numerical differentiation, the in-plane strain fields.

These specimens were tested in tension using a Hopkinson bar device. They were attached to two bars. A projectile was shot onto the input bar, creating a strain wave that will be partially transmitted through the sample.

To record the pictures of the grid during the mechanical test, an ultra-high speed camera was used. This one, a Cordin 550-62, is based on a rotating mirror that directs the light successively to 62 multiplexed CCD sensors that record the different states of loading. The frame rate of recording is given by the rotation speed of the mirror. With this device, one can obtain a maximum of 4,000,000 fps acquisition. In this study, due to light and triggering issues, the acquisition was limited to 300,000 fps. Figure 1 gives a general overview of the device.

In order to overcome the problems of image distortions that can occur when correlating images from one CCD sensor to another (misalignment of the sensors, rotations, variations of light intensity, etc.), the displacement maps were calculated sensor by sensor. To do so, a first set of still images was taken before performing the mechanical test. A second set of images was taken during the loading and the displacement between the initial (still) and the actual states have thus been calculated sensor by sensor from these two sets. This approach is only possible if the global strain remains low and by using some phase unwrapping algorithm in order to get "absolute" values of the displacements [5]. With this approach, one can obtain a displacement resolution between 0.5 and 1.8 % of the grid pitch. With each grid line sampled by 9 pixels,

this translates into a resolution between 0.05 and 0.16 pixels for a spatial resolution of 9 pixels. For comparison purposes to image correlation with a 32 pixels subset, it corresponds to an equivalent resolution between 0.01 and 0.05 pixels. This is worse than what can be obtained in quasi-static tests but not so bad considering the frame rate. A view of the displacement fields for the unnotched specimen is given in Figure 2.

It is also necessary to compute strains from displacements by spatial differentiation. A smoothing procedure is essential here in order to reach the required strain resolution since the strain levels before damage are every small. Here, a local smoothing technique known as ‘diffuse approximation’ is used [6] with a radius of 10, providing a strain resolution around  $10^{-3}$ . Strain maps are represented in Figure 3. Finally, acceleration maps can be obtained by double temporal differentiation of the displacements. Since this is an operation that will be very sensitive to noise, some temporal smoothing is required as well. The smoothed displacements maps were processed and at each pixel, a fourth order polynomial in time was fitted over a sliding window of 9 points centered on the active pixel. The resulting resolution in acceleration was found to be around  $2.10^5 \text{m.s}^{-2}$ . Acceleration maps are given in Figure 4. Figure 5 represents the average acceleration as a function of time for the open-hole specimen (the data is very similar for the unnotched one). One can see the noise occurring before the stress waves hits the specimen and then a sharp rise of the acceleration that lasts about  $30 \mu\text{s}$ . This is the time interval where inertial forces will be sufficiently high to identify the stiffnesses as detailed in Section 3.

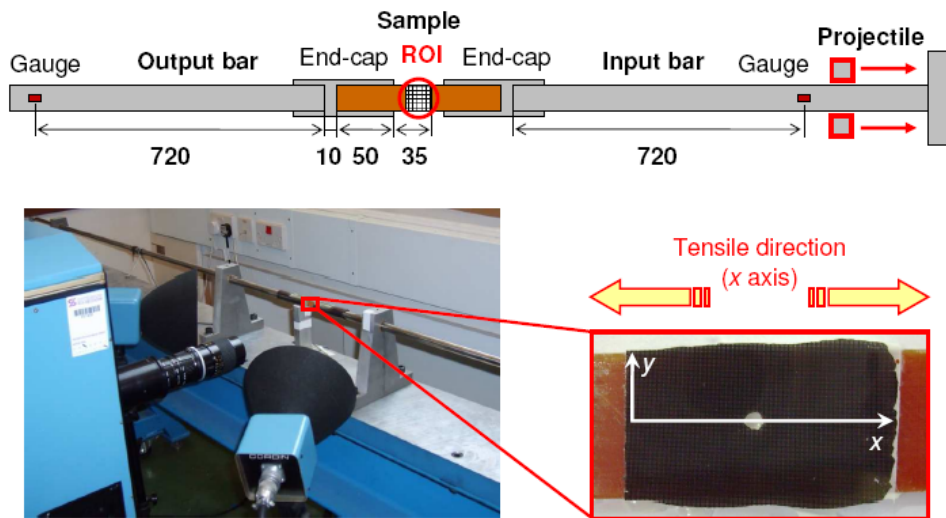


Figure 1. Experimental set-up (open-hole specimen here).

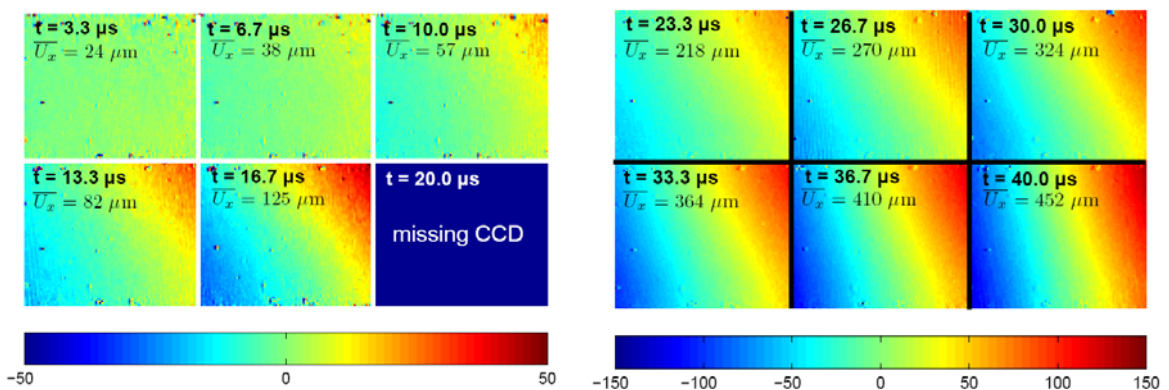


Figure 2. Displacement maps, with average subtracted (colorbar in  $\mu\text{m}$ ).

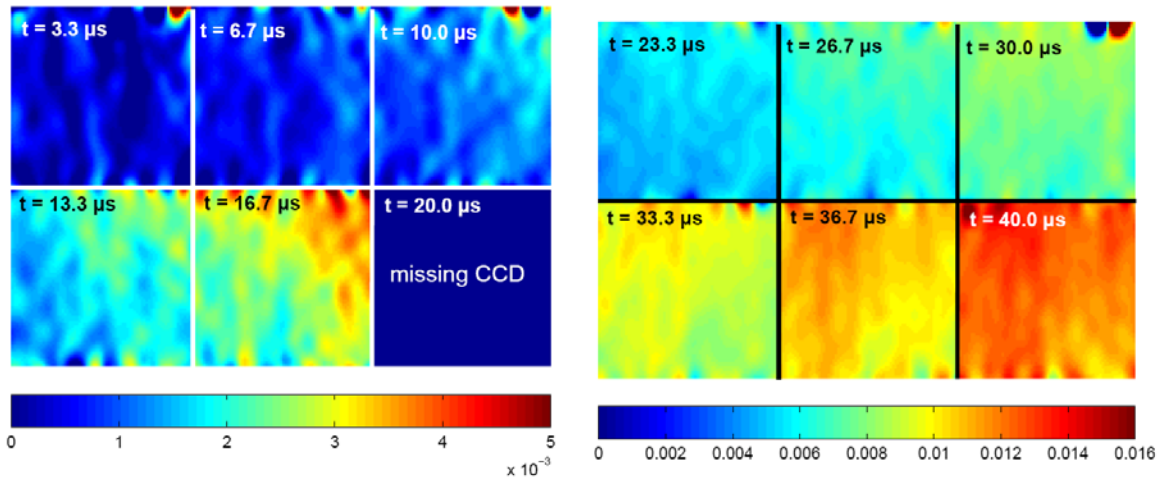


Figure 3. Strain maps.

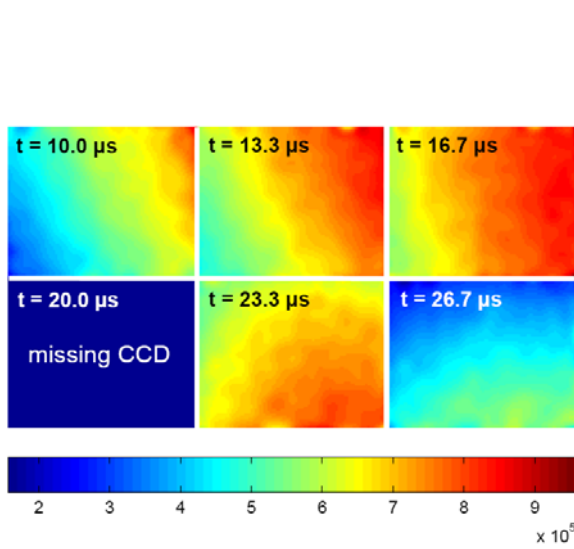


Figure 4. Acceleration maps (colorbar in  $\text{m}\cdot\text{s}^{-2}$ ).

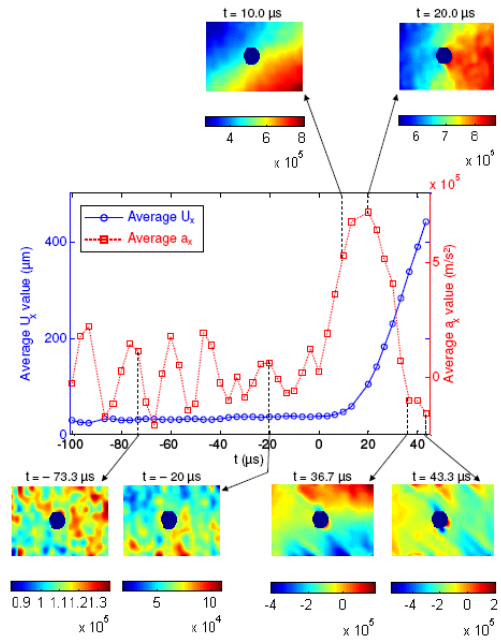


Figure 5. Average acceleration with maps (colorbar in  $\text{m}\cdot\text{s}^{-2}$ ), open hole specimen.

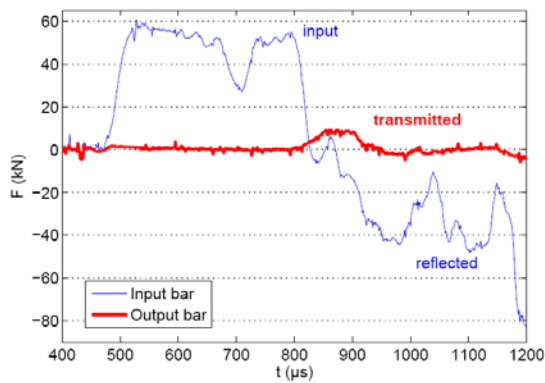


Figure 6. Force measured from the input and output bars.

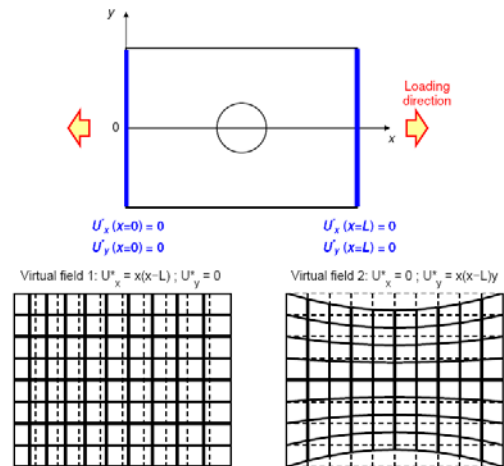


Figure 7. Virtual fields for stiffness identification.

### 3. THE VIRTUAL FIELDS METHOD

#### 3.1. The Virtual Fields Method in dynamics

The Virtual Fields Method (VFM) relies on the use of the principle of virtual work that describes the global dynamic equilibrium of the solid:

$$-\int_V \sigma : \varepsilon^* dV + \int_{\partial V} T \cdot u^* dS = \int_V \rho a \cdot u^* dV \quad (1)$$

where  $\sigma$  is the actual stress tensor,  $u^*$  is a virtual displacement field and  $\varepsilon^*$  the virtual strain field associated,  $V$  is the volume of the region of interest,  $T$  is the actual loading imposed at the boundary of the considered region  $\partial V$ ,  $a$  is the actual acceleration field and  $\rho$  is the density of the material. The double points indicate the contracted product between two second order tensors and the single dot represents the dot product between two vectors. The idea of the VFM is to write this equation with different virtual fields in order to identify the constitutive parameters hidden in the stress components. This has been applied to many types of problems and a review can be found in [7]. In linear isotropic elasticity, and considering that the material is homogeneous, the previous equation can be written as:

$$\begin{aligned} -Q_{xx} \int_V (\varepsilon_{xx} \varepsilon_{xx}^* + \varepsilon_{yy} \varepsilon_{yy}^* + 2\varepsilon_{xy} \varepsilon_{xy}^*) dV - Q_{xy} \int_V (\varepsilon_{yy} \varepsilon_{xx}^* + \varepsilon_{xx} \varepsilon_{yy}^* - 2\varepsilon_{xy} \varepsilon_{xy}^*) dV \\ + \int_{\partial V} (T_x u_x^* + T_y u_y^*) dS = \int_V \rho (a_x u_x^* + a_y u_y^*) dV \end{aligned} \quad (2)$$

In quasi-static conditions where the right hand-side term can be neglected, then it is necessary to involved  $T$  in the equation in order to identify the stiffness components. If the load is not measured, it is possible to cancel out its contribution from Eq. 2 but the, only equations of the type  $aQ_{xx} + bQ_{xy} = 0$  can be obtained, leading to the identification of stiffness ratios only, such as Poisson's ratio (see [8] for an example of this). Fortunately, in dynamics, it is possible to cancel out the force term if the virtual work of the inertia forces is significant enough. The measurement of displacement maps at different times enables to calculate the acceleration maps by double temporal differentiation (see previous section). Therefore, the right hand-side term of Eq. 2 can be calculated provided that the density of the material is known. In a way, the inertia forces act as a volume distributed load cell with the density being the gauge factor! This property of the VFM has already been used in vibrations where the inertia term is very easy to calculate (harmonic loading), [9,10]. A similar use of the inertia forces is made in the so-called Magnetic Resonance Elastography to identify properties of tissues in-vivo [11]. It should also be noted that a similar though simplified idea of using the inertia forces has recently appeared in [12] where it is used to calculate the forces in any section of a unidirectionally loaded rectangular specimen. Another example of the use of the acceleration term in the VFM can be found in [13] (application to a three point bending impact test on an aluminium bar). The next section explains how to identify the stiffnesses from the full-field measurements.

#### 3.2. Stiffness identification

Using Eq. 2 to identify the stiffness components to identify, one has to define at least two virtual fields to obtain a linear system to invert. It should be noted that the hypothesis of isotropic behaviour holds here because of the specific composite lay-up (quasi-isotropic). The two following virtual fields are defined (see Figure 7 for a graphical representation):

$$\begin{aligned} \{u_x^1 = x(x-L), u_y^1 = 0\} \Rightarrow \{\varepsilon_{xx}^{(1)*} = 2x-L, \varepsilon_{yy}^{(1)*} = 0, \varepsilon_{xy}^{(1)*} = 0\} \\ \{u_x^2 = 0, u_y^2 = x(x-L)y\} \Rightarrow \{\varepsilon_{xx}^{(2)*} = 0, \varepsilon_{yy}^{(2)*} = x(x-L), \varepsilon_{xy}^{(2)*} = 0.5(2x-L)y\} \end{aligned} \quad (3)$$

It can be seen that both virtual fields are such that the virtual displacements are zero for both  $x=0$  and  $x=L$ . Therefore, the term  $\int_{\partial V} \mathbf{T} \cdot \mathbf{u}^* d\mathbf{S}$  reduces to zero, as required. The integrals in Eq. 2 can then be approximated by discrete sums and by introducing the spatial average function (indicated with an over script bar), the following linear system is obtained (neglecting the contribution of  $a_y$  which is very small):

$$\begin{bmatrix} \overline{(2x-L)\varepsilon_{xx}} & \overline{(2x-L)\varepsilon_{yy}} \\ \overline{x(x-L)\varepsilon_{yy} + 2(x-L)y\varepsilon_{xy}} & \overline{x(x-L)\varepsilon_{xx} - 2(x-L)y\varepsilon_{xy}} \end{bmatrix} \begin{pmatrix} Q_{xx} \\ Q_{xy} \end{pmatrix} = \begin{pmatrix} \overline{\rho a_x(x(x-L))} \\ 0 \end{pmatrix} \quad (4)$$

From this system, the stiffness components can be obtained by simple inversion.

### 3.3. Force reconstruction

While in the previous section, the virtual fields zeroed the contribution of the external load, it is now possible to reconstruct the impact load with another virtual field now that the stiffnesses are known from the previous section. To do so, the following virtual field is used:

$$\{\mathbf{u}_x^{3*} = x, \mathbf{u}_y^{3*} = 0\} \Rightarrow \{\varepsilon_{xx}^{(3)*} = 1, \varepsilon_{yy}^{(3)*} = 0, \varepsilon_{xy}^{(3)*} = 0\} \quad (5)$$

The resulting equation is:

$$-Q_{xx} \int_V \varepsilon_{xx} dV - Q_{xy} \int_V \varepsilon_{yy} dV + FL = \int_V \rho x a_x dV \quad (6)$$

The force applied to the right hand-side boundary of the specimen can then be expressed as:

$$F = wt(\overline{\rho x a_x} + Q_{xx} \overline{\varepsilon_{xx}} + Q_{xy} \overline{\varepsilon_{yy}}) \quad (7)$$

where  $w$  and  $t$  are respectively the width and thickness of the specimen. It can be seen that this force consists in an inertial term ( $F_i$ ) and in a strain term ( $F_d$ ) composed of the last two quantities in Eq. 7. With the values of  $Q_{xx}$  and  $Q_{xy}$  identified in Section 3.2, it is possible to calculate  $F$  and compare it to the force measured from the strain gauge on the output bar (Figure 6, red curve). These two signals have to be synchronized using the speed of wave propagation in the bar and the composite.

## 4. RESULTS AND DISCUSSION

### 4.1. Stiffness identification

The two stiffness components of the quasi-isotropic composite specimens (unnotched and open-hole) were identified using Eq. 4. They were then converted into Young's modulus and Poisson's ratio using the standard plane stress formulae. The results are reported in Tables 1 and 2. Since Eq. 4 is valid at any time of the test, elastic constants are obtained at each instant were an image is captured. However, this can only be done when sufficient acceleration in the  $x$  direction is present, ie, in the first 30  $\mu\text{s}$  (see Figure 5). The results show very good agreement between the identified values and the quasi-static reference for the unnotched specimen (Table 1). The last value at 26.7  $\mu\text{s}$  is deviating more than the others because the acceleration is probably already too low at that stage. Poisson's ratio is very stable and very close to the reference. There is no problem at 26.7  $\mu\text{s}$  because Poisson's ratio is obtained directly from the second line of Eq. 4 and therefore, does not depend on the acceleration. The results are less convincing for the open-hole specimen even though the right order of magnitude for  $E$  is obtained and the identification of Poisson's ratio is reasonable. This is not surprising however since in the open-hole specimen, steep strain gradients

are present around the hole and the performance of the camera does not enable the correct capturing of these details. This shows that moving to more complex test geometries with strain gradients will require better camera performances and rigorous design of the test configuration. This is among the plans for the future development of this methodology.

**Table 1.** Identification results (unnotched specimen)

Young's modulus in GPa (Reference value: $E = 23.2$ GPa)					
Time ( $\mu s$ )					Average
10.0	13.3	16.7	23.3	26.7	
22.6	31.8	23.8	22.0	42.2	28.5
Poisson's ratio (Reference value: $\nu = 0.34$ )					
Time ( $\mu s$ )					Average
10.0	13.3	16.7	23.3	26.7	
0.46	0.31	0.34	0.31	0.32	0.35

**Table 2.** Identification results (open-hole specimen)

Young's modulus in GPa (Reference value: $E = 23.2$ GPa)					
Time ( $\mu s$ )					Average
6.7	10.0	13.3	20.0	23.3	
20.4	21.1	15.8	15.7	16.6	13.6
Poisson's ratio (Reference value: $\nu = 0.34$ )					
Time ( $\mu s$ )					Average
6.7	10.0	13.3	20.0	23.3	
0.28	0.22	0.32	0.27	0.29	0.30

#### 4.2. Force reconstruction

From the average stiffness values in Table 1, the impact force was reconstructed using Eq. 7. The results are plotted in Figure 8. One can see that the reconstructed force matches reasonably well the measured force even though at the beginning of the curves, the difference is rather large. Part of this difference may come from the synchronization. The dotted curve corresponds to the measured load synchronized with the reconstructed force using slightly different modulus and density values for the titanium and the composite. The error is significantly reduced. Moreover, the output bar signal is very small because of the impedance mismatch between the titanium input bar and the composite specimen. Therefore, the measured load is not the most reliable experimental information here. The reconstructed load is much smoother thanks to the redundancy of the full-field measurements. In any case, this comparison gives extra confidence in the methodology introduced in the present paper even though such validation will have to be confirmed with better output load measurements.

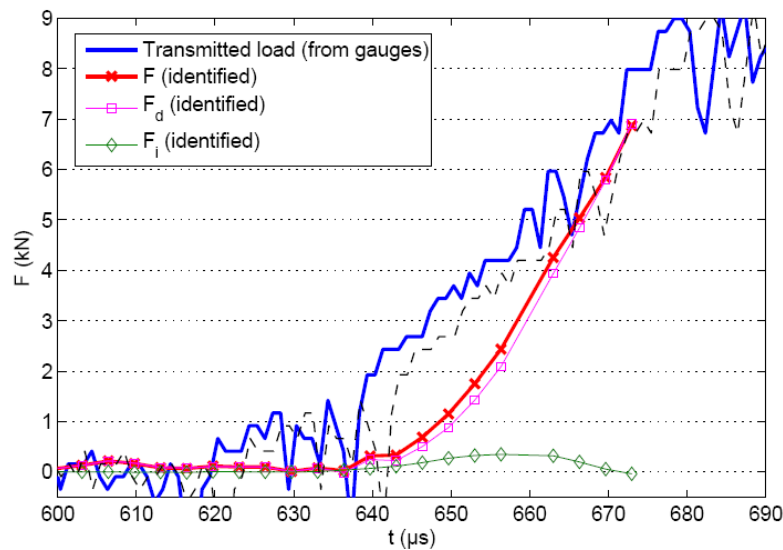


**Figure 8.** Comparison between measured and reconstructed forces.

## 5. CONCLUSION

In this paper, a first attempt at full-field measurements on unnotched and open-hole composite tensile specimens tested at high strain rates has been introduced. The methodology using a UHS camera has been exposed. Regarding the multi-sensor nature of the camera, this method involves the computation of displacement maps from initial and actual stages sensor by sensor (and not incrementally from one sensor to another) to be able to get relevant displacement values by limiting the effects of the sensor to sensor discrepancies.

The strain maps have been deduced from the displacements using a diffuse approximation algorithm. These maps have shown spatial distributions of strain compatible with the ones obtained for the same geometry in quasi-static. Nevertheless, some asymmetry in these fields suggested that the loading was not exactly homogeneous and unidirectional; some bending effects, probably due to how the coupons are attached to the fixture, were superimposed to the tensile loading.

Finally, a first attempt of identification of mechanical properties from strain and acceleration using the Virtual Field Method has been performed. Although the measurements are rather noisy, this identification procedure has yielded very reasonable values of the equivalent isotropic Young's modulus and Poisson's ratio of the tested laminate, which is quite interesting and encouraging as this is the first time that such an approach is used.

Some further experiments using the same experimental device and the same procedure should be performed in the future to try to obtain better results (in terms of strain and acceleration resolutions) and thus consolidate the first identification result obtained. Contrast of the grid pattern and lighting are two tracks to follow to improve the quality of the measurements.

## Acknowledgments

The authors would like to express their gratitude to the UK Engineering and Physical Sciences Research Council for their financial support to this project (Grant n°: EP/G001715/1) and the loan of the ultra high speed Cordin camera through the Engineering Instrument Pool.

## References

- [1] Field J.E., Walley S.M., Proud W.G., Goldrein H.T. and Siviour C.R., *Int. J. Impact Eng.*, 30 (2004) 725-775.
- [2] Kirugulige M.S., Tippur H.V. and Denney T.S., *Applied Optics*, 46 (2007) 5083-5096.
- [3] Tiwari V., Sutton M.A. and McNeill S.R., *Exp. Mech.*, 47 (2007) 561-579.
- [4] Surrel Y., Moiré and grid methods: a signal processing approach, *Interferometry '94 : Photomechanics*, SPIE vol. 2342 (1994).
- [5] Bioucas-Dias J. and Valadao G., Phase unwrapping via graph cuts, *IEEE Trans. Image Proc.*, 16 (2007) 696-709.
- [6] Avril S., Feissel P., Pierron F. and Villon P., *Eur. J. Comp. Mech.*, 17 (2008)857-868.
- [7] Grédiac M., Pierron F., Avril S. and Toussaint E., *Strain*, 42 (2006) 233-253.
- [8] Pierron F., *J. Strain Anal. Des.*, 45 (2010) 233-253.
- [9] Grédiac M., Fournier N., Paris P.-A. and Surrel Y., *J. Sound & Vib.*, 210 (1998) 643-659.
- [10] Giraudeau A., Pierron F. and Guo B., *J. Sound & Vib.*, 329 (2010) 1653-1672.
- [11] Sinkus R., Tanter M., Xydeas T., Catheline S., Bercoff J. and Fink M., *Magn. Res. Imag.*, 23 (2005) 159-165.
- [12] Othman R., Aloui S. and Poitou A., *Polymer Testing*, 29 (2010) 616-623.
- [13] Pierron F., Sutton M. and Tiwari V., *Exp. Mech.*, in press, DOI 10.1007/s11340-010-9402-y, 2010.

# Impact analysis of a turbomachine with composite blades

L. Idoux<sup>1</sup>, P. Cartraud<sup>2</sup>, P. Rozycki<sup>2</sup>, J-C Guldner<sup>2</sup>

<sup>1</sup> EDF, 1 Avenue du Général de Gaulle, 92140 Clamart, France.

<sup>2</sup> Gem, Ecole Centrale de Nantes, 1 rue de la Noë, 44321 Nantes, France.

**ABSTRACT.** This study is about the development of a material law taking in account the strain rate effect. The aim is to get finite element simulations that could better predict the behaviour of composites blades under impact. The context of the study is the development of new jet engine composite fan blades that will have to withstand bird or ice strikes and fan blade off tests.

SNECMA and General Electrics are developing together the successor of the CFM56 engine, and aim to use a specific composite material for fan blades. It handles with a woven carbon fibre preform which is moulded by using RTM (Resin Transfer Moulding) process. The composite is considered as having two fibre directions. In order to meet the conditions for the airworthiness certification, the authorities such as the Federal Aviation Administration in the U.S. impose the engine to withstand to bird or ice strike and fan blade off. In this framework Snecma needs to rely on simulation tools, efficient and reliable, which will be used during the design process. This paper describes the methodology developed in order to achieve this goal. It comprises several steps: the material characterization through experimental tests, the modeling of its behavior using continuum damage mechanics, its numerical implementation in a commercial finite element software, and lastly the structural computations performed on the engine.

Through loading/unloading quasistatic tests on composite specimens in each fiber direction, both curves being similar to the one shown figure 1, two main non-linear mechanisms have been underlined: the simultaneous growth of damage, due to stiffness loss, and the presence of inelastic strain. Another feature to take into account is the microcrack closure effect which enables the material to recover its undamaged elastic properties during compressive loads. A model developed by the French Aerospace Lab (ONERA) [1] is dedicated to the modelling of such composite materials. It gives a good correlation between simulation and experiment. We also developed a simplified model that includes the same non-linear effects. Damage acts only on the Young's modulus in the diagonal terms. Upgrades are possible by adding damage on the shear modulus, as soon as some tests will be performed. Damage is calculated from the thermodynamic forces (see [2], [3], [4]) and a delay damage model is available [5] to avoid mesh dependency. Besides, a fast identification process is proposed for the new model. Both models were implemented in the commercial finite element software LS-Dyna, and their strengths and limitations are discussed by comparing the simulation results to the quasistatic test results.

Then both models are used to perform two bird strike and one fan blade off calculations, corresponding to industrial tests. The first bird strike calculation handles with a static composite panel standing for a composite blade. This experimental test shows different damage levels all over the panel, which allows us to associate the numerical damage level with experimental observations. Two areas are especially pointed out: one with widespread and small damage, and one with higher damage level where failure occurs. Even if fracture and crack propagation are not included in our damage models, a good agreement was found between the calculation and the test. The second bird strike calculation aims at simulating a test on rotating composite blades. Only three blades are modelled, one being used as a timeline reference and the two other blades being stroken. Only qualitative results can be pointed out, especially for the position of the peak of damage compared to the zones where failure occurs during the test.

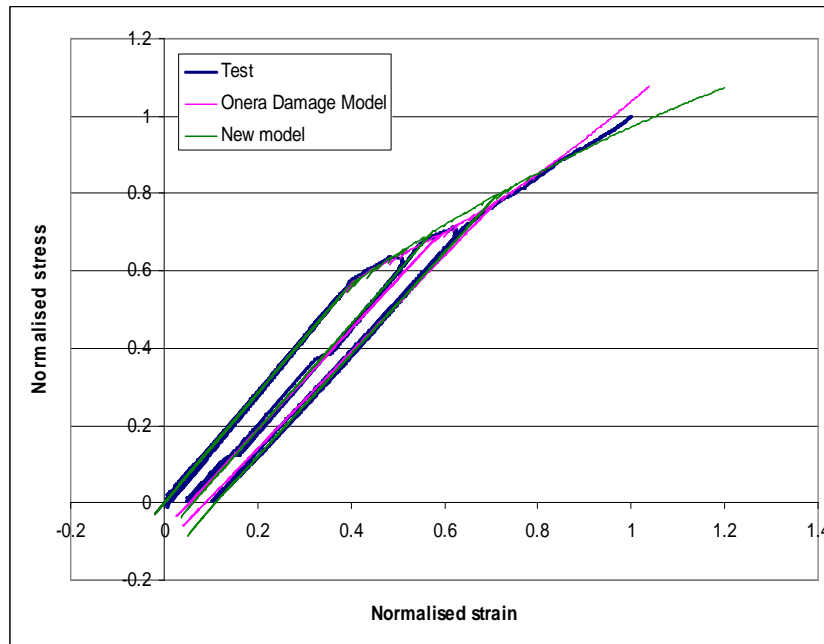


Figure 1: Load/unload test and simulation in the warp direction

Finally, both damage models are used to calculate a fan blade off. This kind of calculation shows clearly the limitations of the models, as failure occurs and leads to break the blades in several fragments which impact the casing simultaneously. The size of the fragments, and therefore their mass, is an important data to know in order to be able to predict the damage level on the casing, in term of cumulated plastic strain. Our models don't include crack initiation or propagation, so the only tool we can use is the automatic erosion of the elements where a failure criterion (based on damage or strain) is reached.

To conclude, the behaviour of a woven-composite used for designing fan blade has been characterized through different tests. These tests show that damage occurs in the material as well as inelastic strain. Thus, a constitutive law is proposed, in order to describe accurately the material behaviour. The model chosen is as simple as possible, in order to save computational cost, and to make easy the calibration of the material parameters. The first results obtained for structural applications are encouraging.

## References

- [1] J.-F. Maire, J.-L. Chaboche, A new formulation of Continuum Damage Mechanics (CDM) for Composite Materials. *Aerospace Science and Technology*, 247-257, 1997.
- [2] O. Allix, A composite damage meso-model for impact problems. *Composites Science and Technology*, **61**, 2193-2205, 2001.
- [3] C. Hochard, P.-A. Aubourg, J.-P. Charles, Modelling of the mechanical behaviour of woven-fabric CFRP laminates up to failure. *Composites Science and Technology*, **61**, 221-230, 2001.
- [4] A.F. Johnson, Modelling fabric reinforced composites under impact loads. *Composites: Part A*, **32**, 1197-1206, 2001.
- [5] P. Ladevèze, A damage computational approach for composites: Basic aspects and micromechanical relations. *Computational Mechanics*, **17**, 142-150, 1995.

# INVESTIGATION OF THE SELF-HEALING BEHAVIOR OF AN IONOMER AT PROJECTILE VELOCITIES UP TO 6 KM/S

T. Haase<sup>1</sup>, I. Rohr<sup>1</sup> and K. Thoma<sup>1</sup>

<sup>1</sup> *Fraunhofer-Institute for High-Speed Dynamics, Ernst-Mach-Institut, Eckerstr. 4, 79104 Freiburg, Germany*

**Abstract.** The self-healing behavior of partially neutralized poly(ethylene-co-methacrylic acid) was investigated at different impact velocities ranging from quasi-static tests up to hypervelocity impact at 6 km/s. Our experiments show that there exists a certain self-healing range. Only for projectile velocities within this range, self-healing of the material can be observed. By analyzing the experimental results, it was possible to explain why such a distinct self-healing range exists.

## 1. INTRODUCTION

Self-healing materials are materials with the built-in ability to heal certain kinds of damage. Some of them can do this autonomously and others need external help, e.g. by adding heat. Many different approaches for such materials have been developed, especially for self-healing polymers [1]. Those include for example embedding microcapsules [2] or hollow glass fibers [3] filled with a liquid healing agent which is able to seal cracks in the material. There are also ways to produce self-healing coatings containing microcapsules to heal scratches on surfaces [4]. Other materials use certain chemical reactions (e.g. Diels-Alder reactions [5]) or hydrogen bonds (supramolecular polymers [6]) to repair broken bonds across fracture surfaces after bringing them back into contact with each other.

Most self-healing polymers can only heal small damaged areas like cracks or scratches, or they can heal fracture surfaces only after those are brought back into contact. And those materials often need several hours to complete the healing process. The polymer investigated in this study is completely different. It is able to self-heal the damage caused by an impacting projectile [7-9]. The healing process takes place autonomously and immediately after the impact. No prior modification of the polymer is necessary. In this study, the self-healing ability of this polymer was investigated over a wide range of projectile velocities from quasi-static tests up to hypervelocity impact.

## 2. THE SELF-HEALING MATERIAL

The polymer used is poly(ethylene-co-methacrylic acid) which has some of its acid groups neutralized with sodium. It is also known as Surlyn® 8940 from DuPont. The neutralized groups contain oppositely charged ions and because of its ionic content the material is called an ionomer. The ionic groups can attract each other and form so called multiplets and ionic clusters in the material which act as physical crosslinks between the polymer chains. Those physical crosslinks can break at higher temperatures and allow the material to melt like a thermoplastic [10]. At lower temperatures the material behaves like an elastomer. It therefore combines the properties of a thermoplastic and an elastomer in one material and belongs to the group of so called thermoplastic elastomers.

The polymer resin was compression molded into approximately 1.8 mm thick plates used for this study. The manufacturing process of the plates is crucial, since anisotropic mechanical properties as a result of, for instance, an extrusion process prevent a successful self-healing of the material [11].

The self-healing process of this material when it is shot at with a projectile takes place in three steps as shown in Figure 1. In the first step, the penetrating projectile causes the ionomer plate to fail by petaling. This means that starting from the impact point several cracks propagate radially outwards. In a second step, immediately after the projectile has penetrated the material, the petals fold back elastically, whereby the edges of the cracks come back into contact. During the impact process, the material around the impact point

has been heated up to its melting point. As a last step, this molten material seals the cracks and the self-healing process is completed. The fact that the material melts during the impact process was verified using differential scanning calorimetry measurements in [8]. The first two steps of this self-healing process are only possible because the material has properties of an elastomer, whereas the last step can only take place because of its thermoplastic properties.

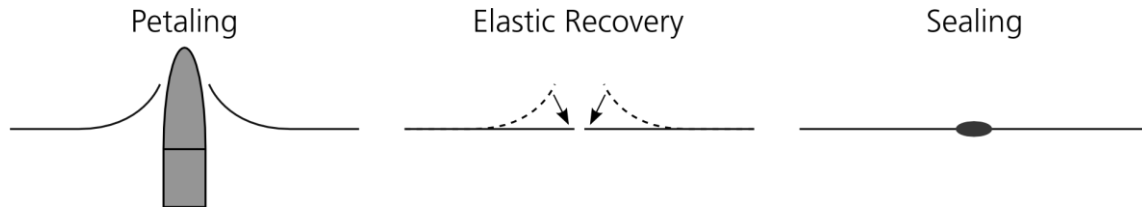


**Figure 1.** Schematic representation of the self-healing process.

### 3. EXPERIMENTAL METHODS

The self-healing behavior of the ionomer plates was studied at three different projectile velocities. In the quasi-static range, a sharp metal rod with a diameter of 2.5 mm was slowly pressed through the polymer plate. For impact velocities in an intermediate velocity range, a single stage gun operated with compressed air was used. The projectiles employed with this gun were .22 caliber ogive shaped projectiles (mass 3.6 g) with an impact velocity of about 300 m/s and steel spheres (diameter 3 mm, mass 110 mg) at about 500 m/s. Further tests were done at projectile velocities around 6000 m/s using a two stage light gas gun with lighter aluminum spheres as projectiles (diameter 2 mm, mass 12 mg). All projectiles used in this study are shown in Figure 2.

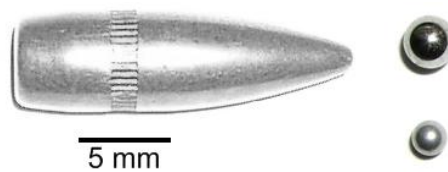


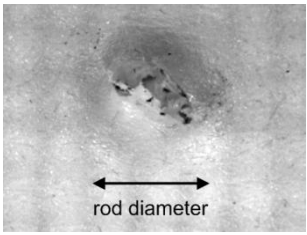
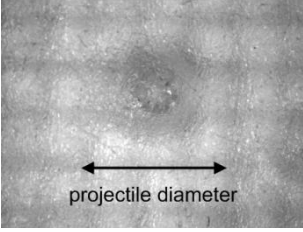
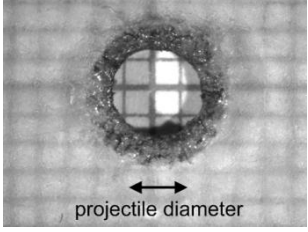
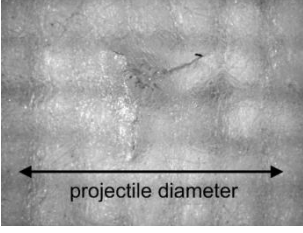
**Figure 2.** Different projectiles used for the experiments around 400 m/s (top) and 6000 m/s (bottom).

The tests have been recorded with a high-speed camera with a frame rate of up to 100,000 fps for subsequent analysis.

#### 4. RESULTS & DISCUSSION

The results of the experiments are summarized in Table 1. It shows the back sides of the ionomer plates after impact of the different projectiles in the three velocity ranges examined in this study. The front side is the side facing the approaching projectile and the back side is the opposite one.

**Table 1.** Experimental results. The gridlines in the background of the pictures have a distance of 1 mm.

	Quasi-static	300-500 m/s	6000 m/s
2.5 mm rod 		-	-
2 mm resp. 3 mm sphere 	-		
5.6 mm ogive shaped 	-		-

Obviously, no self-healing of the material took place at an impact velocity of 6000 m/s, as there is still a hole in the plate with a diameter of 3 mm. Also in the quasi-static case, no self-healing could be observed. Although the material seems to have closed the hole, there are still cracks which open up immediately if the plate is bent. Only at intermediate velocities around 300-500 m/s, the material was able to self-heal the damage. There are no more holes and also the cracks are healed. This was verified by a leak test, where compressed air was applied to the front side of the ionomer plate and no escaping air was detected on the back side.

To understand why the material is only able to self-heal the impact damage at intermediate projectile velocities, one has to keep in mind the three steps of the self-healing process described in section 2. In the quasi-static case, were a metal rod was pushed through the ionomer plate, the material was able to fold back and close the hole due to its elastomeric properties. However, for the last step of the self-healing process to take place, it is necessary for the material to melt around the impact point in order to seal the cracks. But during the quasi-static test, no melting of the material was observed. The temperature rise was not large enough to reach the melting point and therefore no self-healing could take place.

At a projectile velocity of 6000 m/s, the material did melt around the impact point as can be seen by inspecting the damaged ionomer plate. But at such high impact velocities, the first two steps of the self-healing process could not take place. This can be seen at the high-speed video of the experiment (see Figure 3). Instead of failing by petaling and elastically folding back the petals, the material splintered into many pieces. There are two reasons for this behavior. Firstly, the material becomes more brittle at such high strain rates that occur during the impact, which is a common property of polymers. Secondly, there is no possibility for the material to globally deform during the impact process. At lower velocities, bending

waves could be observed with a velocity of roughly 500 m/s. If the projectile travels much faster than these bending waves propagate, there is no time for the material to react on a global scale. Instead, the impact process is localized to a small area around the impact point. As a result of these two effects, the projectile at 6000 m/s just cut a hole in the plate and no self-healing was possible any more.

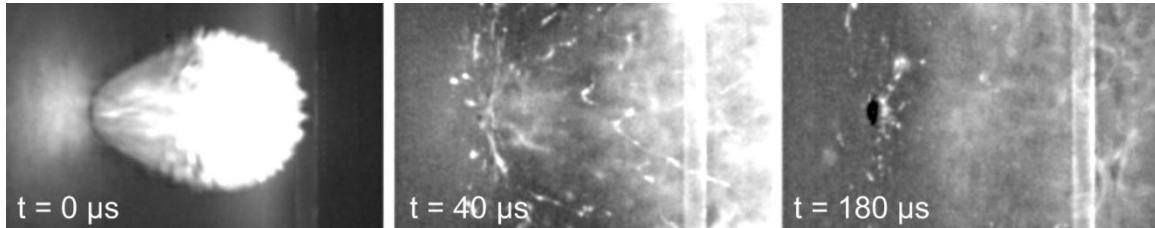


**Figure 3.** High-speed images of a 2 mm aluminum sphere impacting a 1.8 mm ionomer plate at 6000 m/s.

At intermediate projectile velocities around 400 m/s, all steps of the self-healing process occurred. After the projectile has penetrated the plate, it elastically folded back within about 50 μs as could be observed from the high-speed videos (see Figure 4). Afterwards, the molten material around the impact point sealed the cracks and the self-healing process was completed.



**Figure 4.** High-speed images of a .22 caliber ogive shaped projectile impacting a 1.8 mm ionomer plate at 300 m/s.

## 5. SUMMARY

The self-healing ability of partially neutralized poly(ethylene-co-methacrylic acid) was investigated over a wide range of projectile velocities from quasi-static loading up to hypervelocity impact using approximately 1.8 mm thick compression molded plates. While at intermediate velocities of 300-500 m/s the material was able to self-heal the damage caused by the penetrating projectile, no self-healing was observed at quasi-static loading or at 6000 m/s impact velocity. Obviously there exists a certain self-healing range of projectile velocities as shown in Figure 5.

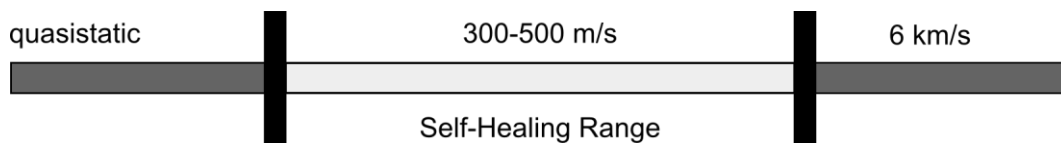


**Figure 5.** Self-healing range of projectile velocities.

At too low velocities, the temperature rise during impact is not large enough to melt the material around the impact point and therefore the cracks cannot be sealed. The higher limit of the self-healing range exists because bending waves can only propagate at a certain finite velocity and the material becomes more brittle at higher strain rates, which leads to less global deformation at increasing projectile velocities. In this case, the projectile cuts a hole in the ionomer plate which prevents self-healing at such high velocities. Only if the projectile velocity lies within the self-healing range, the material is able to heal the impact damage.

## References

- [1] Wu D.Y., Meure S. and Solomon D., *Prog. Polym. Sci.*, 33 (2008) 479-522.
- [2] White S.R. et al., *Nature*, 409 (2001) 794-797.
- [3] Trask R.S., Williams G.J. and Bond I.P., *J. R. Soc. Interface*, 4 (2007) 363-371.
- [4] Suryanarayana C., Rao Chowdoji K. and Kumar D., *Progress in Organic Coatings*, 63 (2008) 72-78.
- [5] Chen X. et al., *Macromolecules*, 36 (2003) 1802-1807.
- [6] Cordier P. et al., *Nature*, 451 (2008) 977-980.
- [7] Fall R., "Puncture Reversal of Ethylene Ionomers – Mechanistic Studies", Master Thesis (2001), Virginia Polytechnic Institute and State University.
- [8] Kalista S.J. and Ward T.C., *J. R. Soc. Interface*, 4 (2007) 405-411.
- [9] Varley R.J. and van der Zwaag S., *Acta Mater*, 56 (2008) 5737-5750.
- [10] Tant M.R. and Wilkes G.L., *Polymer Reviews*, 28 (1988) 1-63.
- [11] Haase T., Wicklein M. and Thoma K., "Influence of the manufacturing process on the self-healing behavior of ionomers", *DYMAT 2009* cf., *DYMAT 2009* (2009) 765-770.

# MODELING HIGH-SPEED IMPACT ON CFRPS WITH AN ENERGY BALANCE EQUATION

J. López-Puente, D. Varas, J.A. Loya, C. Navarro, R. Zaera

*Department of Continuum Mechanics and Structural Analysis, University Carlos III of Madrid,  
28911 Leganés, Madrid, Spain*

**Abstract.** In this work an analytical model has been developed in order to predict the residual velocity of a spherical or cylindrical steel projectile, after impacting into a woven carbon/epoxy thin laminate. The model is based in an energy balance, in which the kinetic projectile energy is absorbed by the laminate through three different mechanisms: linear momentum transfer, fiber failure and laminate crushing. This last mechanism needs the quantification of the through-thickness compressive strength, which has been evaluated by means of quasi-static punch tests. Finally, high velocity impact tests have been accomplished in a wide range of velocities, to validate the model.

## 1. INTRODUCTION

New requirements of strength, stiffness and lightness in structural components have brought an upsurge in the sphere of composite materials. The technical development of these components has come mainly from the aeronautical and aerospace industries which impose very strict criteria in the material selection, particularly with regard to their density since any slight reduction of the total mass of the structure means a saving of power and of fuel. The composite materials most used for structural applications in these sectors are of laminated carbon fiber in an epoxy matrix which combines good mechanical properties, high resistance to corrosion and fatigue, and low density. CFRP applications in commercial aircraft have been steadily increasing [1] as raw material costs are reduced, automation of manufacturing processes evolves and experience in design technology is increased. At least 50% of the next generation of military and civil aircraft structures are likely to be made mainly from composites [2]. Vulnerability against high velocity impact loads is becoming an increasingly critical issue for the design of CFRP aircraft and aerospace structures in recent years. Bird strikes and hailstones are the most critical situations because of its high probability of occurrence and its disastrous consequences, especially when ingested by the engine. Also the ice released from the edge of a propeller blade may impact the nacelle of the twin engine or the fuselage, and runway debris may impact the underside of wing structures. Other kinds of projectiles that may impact aircraft structures are small and medium calibre bullets and fragments due to a blast, both of them could cause hydrodynamic ram effects when impacting the fuel tank of an airplane or a helicopter [3,4]. The aeroengine turbine blade may also fail due to fatigue and may penetrate the wall of the containment cell, damaging oil tanks and airframes. The near-earth space environment, where satellites, the International Space Station, and the Space Shuttle orbit the earth, is jumbled with both artificial and natural debris [5,6]. This debris is too small and numerous to be individually tracked and there are many satellites in orbit, so that the average time between destructive collisions is about 10 years. CFRPs are well known to be particularly vulnerable to impact of foreign objects, especially because of the brittleness of the polymeric phase, giving rise to a multiplicity of failure modes and leading to significant strength reduction in post-damage performance. Therefore understanding its response to a range of potential impact loadings and resulting damage mechanisms is essential for the successful use of these materials.

The response of CFRP panels to low or to high velocity impacts is quite different [7]. The response of CFRPs to low velocity impact damage -few meters per second- has been widely studied, using experimental test methods such as pendulum Charpy or drop tower. However, the number of papers concerned with the impact response of carbon fiber laminates under impact at hundreds of meters per second is relatively small. Experimental results of projectiles impacting CFRPs at high speed velocities can be found in [6-21]. These authors described the impact of a projectile onto the composite plate in different phases: initial contact and stress wave propagation, compression and local punch, plug formation under shear and compression, fiber breakage at the rear layers, and final perforation. During the penetration process the initial energy of the projectile is totally (in case of arrest) or partially (in case of perforation) absorbed by the laminate by kinetic energy, strain energy or damage mechanisms, namely matrix cracking, delamination, fiber shear, or tensile fiber failure. In high velocity impacts, the main feature of these energy dissipation phenomena is the local response of the material, because of the small mass which impacts and the short contact duration so that

available kinetic energy of the projectile is likely distributed over a small volume surrounding the contact point.

Quite complex numerical or analytical simulation models have been developed by several authors to predict the entire impact process. Beyond the predictive interest of these tools, simulation models can aid in the detailed understanding of the behavior of a CFRP laminate to a range of threats, providing detailed information about the penetration loads, absorbed energies and the damage evolution processes. This paper *reviews different analytical models* proposed by the authors to predict the residual velocity of a spherical or a cylindrical projectile after impacting at ballistic velocity regime against carbon/epoxy plain woven laminates. This simulation tool is formulated from an energy balance. The models were validated with impacts at velocities between 100 and 500 m/s. The models predict with accuracy the residual velocity and estimate the minimum impact velocity of the projectile needed to perforate the laminate. Moreover, their formulation in terms of non-dimensional parameters facilitates an analysis of influence of the different energy absorption mechanisms during the impact process.

## 2. DESCRIPTION OF THE MODEL

The analytical model is formulated in terms of energy balance. In this type of carbon/epoxy reinforcement it is considered that the kinetic energy of the projectile  $E_k$  will be absorbed by the laminate by three different processes: laminate breakage due to crushing  $E_c$ , linear momentum transferred from the projectile to the detached part of laminate  $E_m$ , and tensile fiber failure  $E_f$ .

$$-dE_k = dE_c + dE_m + dE_f \quad (1)$$

The energy absorbed by delamination neither was considered due to the low extension of this type of damage in plain woven laminates and its low specific energy [22]. Plastic deformation of the projectile has also been neglected, because it has been experimentally observed for this type of materials that it does not suffer any permanent strains. A spatial rather than temporal integration will be chosen because the expressions get considerably simplified. The terms that appear in Eq. (1) could be expressed as follows:

### 2.1. Kinetic energy of the projectile

The variable  $x$  represents the projectile position from the impact side of the composite laminate (Fig. 1). In a differential change of position it loses a quantity of energy given by

$$dE_k = \frac{1}{2} m_p d(v(x)^2) \quad (2)$$

where  $m_p$  is the projectile mass and  $v$  its velocity.

### 2.2. Energy absorbed by linear momentum transfer

The differential laminate volume detached from the laminate is accelerated from the rest to the current projectile velocity, and it is assumed to remain attached to the projectile during the penetration. The associated amount of energy is written as:

$$dE_m = \frac{1}{2} A(x) dx \rho_l v(x)^2 \quad (3)$$

where  $\rho_l$  is the laminate density and  $A(x)$  is the frontal projectile area that contacts the non-crushed laminate. In the case of a cylindrical projectile  $A(x)$  is constant whereas for spherical projectile this value varies with the depth of penetration according to the following piecewise function

$$A(x) = \begin{cases} \pi(r^2 - (r-x)^2) & 0 \leq x \leq h \\ \pi((r-x+h)^2 r^2 - (r-x)^2) & h \leq x \leq r \\ \pi(r-x+h)^2 & r \leq x \leq r+h \\ 0 & x \geq r+h \end{cases} \quad (4)$$

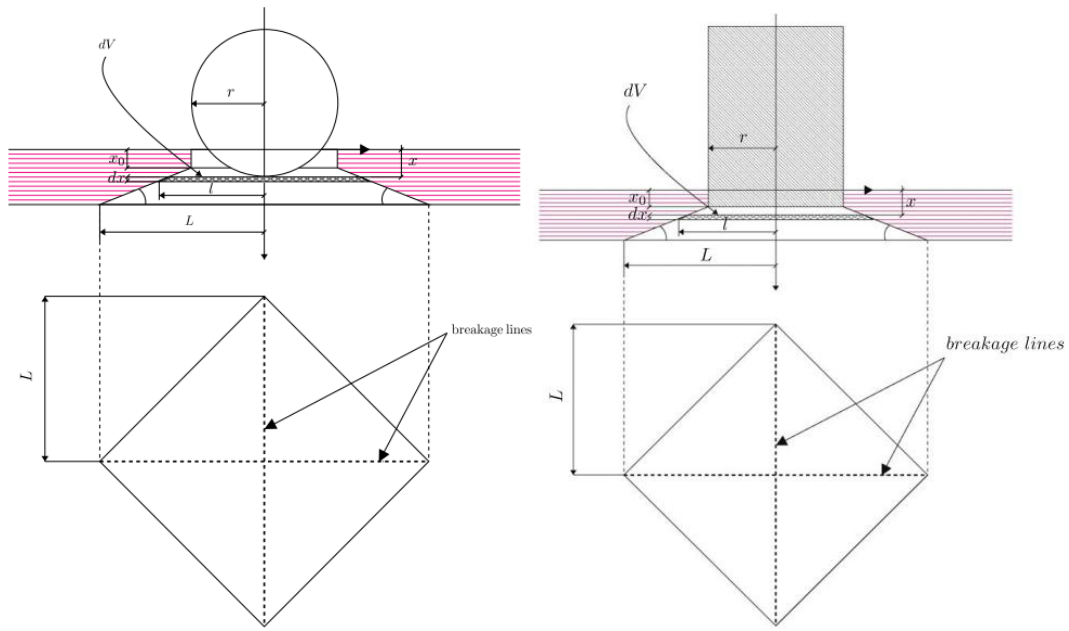


**Figure 1.** Fiber failure breakage scheme for spherical (left) and cylindrical (right) projectile.

### 2.3. Energy absorbed by laminate crushing

When the projectile contacts the laminate it breaks the composite material in front of it by compression. In a differential displacement of the projectile, the energy dissipated by this mechanism was estimated as the product of the out-of-plane compressive strength of the laminate  $\sigma_c(x)$ , the contact area  $A(x)$  and the distance covered by the projectile. The corresponding energetic term may be written as

$$dE_c = \sigma_c(x)A(x)dx \quad (5)$$

In order to quantify the value of the compressive strength of the laminate in the through-thickness direction as a function of the penetration depth  $x$ , quasi-static punch shear tests were performed. These test were performed on a Universal Testing Machine, where the puncture on the laminate sample was applied through a 5.5 mm diameter cylinder with flat tip,

### 2.4. Energy absorbed by fiber failure

This mechanism becomes relevant mainly at velocities close to those required to perforate the laminate (ballistic limit). Figure 2 shows an optical microscope image of the transverse plane of a CFRP woven laminate impacted at 100 m/s, which is a velocity slightly below the ballistic limit. A crushing breakage was observed in the first plies, while the rest failed through tensile failure in the impact axis. This last zone finally collapsed, creating a 65° troncoconic volume. This kind of breakage appears only when the projectile velocity is slow, otherwise the non-penetrated plies would not have enough time to break by fiber failure. Numerical simulations of the impact process investigated by López-Puente et al. [23] shows very good correlation with experimental data; using these results was found that the time  $t_0$  to tensile failure is approximately equal to that needed by the elastic wave to reach the lower face of the laminate and reverse through the total thickness of the plate:

$$t_0 = 2h/\sqrt{E_3/\rho_l} \quad (6)$$

$E_3$  being the through-thickness elastic modulus. The differential energy associated with this failure mechanism is written as:

$$dE_f = \omega_f dV \quad (7)$$

where  $\omega_f$  is the specific energy and  $dV$  the volume of material affected at any  $dx$ . Assuming that the fiber behavior is linear elastic up to failure,  $\omega_f$  is estimated as

$$\omega_f = 2\left(\frac{1}{2}X_t\varepsilon_f\right) \quad (8)$$

$X_t$  is the tensile strength in direction 1 or 2, and  $\varepsilon_f$  the ultimate strain. The fiber breakage is located in a truncated pyramid, with a semiangle  $\alpha = 65^\circ$  and its diagonals aligned in the fiber directions. The length of the upper base semidiagonal is  $r$  and that of the lower base semidiagonal is  $L = r + (h - x_0)\tan\alpha$ , with  $x_0$  the position of the projectile at  $t = t_0$  (Figure 1). The affected volume for any  $dx$  was described as

$$dV = 2l^2 dx = 2(r + (x - x_0)\tan\alpha)^2 dx \quad (9)$$

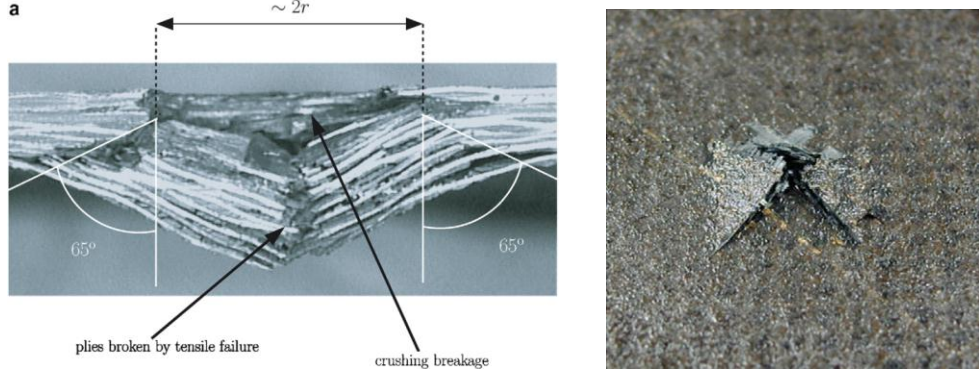


**Figure 2.** Left: cross section of a woven laminate impacted by a spherical projectile at 100 m/s. Right: image of the laminate lower face.

Since this term participates in the impact process exclusively under certain conditions, it must be multiplied by a cutdown function  $c_r(x)$

$$c_r(x) = \begin{cases} 0 & 0 < x < x_0 \\ 1 & x_0 \leq x < h \\ 0 & x \geq h \end{cases} \quad (10)$$

and the value of  $x_0$  may be determined by

$$\int_0^{x_0} \frac{d\chi}{v(\chi)} = \frac{2H}{\sqrt{E_3/\rho_l}} \quad (11)$$

### 3. SOLUTION OF THE DIFFERENTIAL EQUATION

The four terms in the energy balance equation lead to a non-linear differential equation in the variable  $x$ :

$$-\frac{1}{2}m_p d(v(x)^2) = \sigma_c(x)A(x)dx + \frac{1}{2}A(x)dx\rho_l v(x)^2 + 2X_t\varepsilon_f(r + (x - x_0)\tan\alpha)^2 c_r(x)dx \quad (12)$$

Converting the velocity and the projectile displacement into dimensionless variables ( $v^* = v/v_i$ ,  $x^* = x/h$ ,  $\sigma_c^* = \sigma_c/\sigma_0$ ,  $A^* = A/A_0$ , where  $\sigma_0$  is the strength in the through-thickness direction as supplied by the manufacturer and  $A_0 = \pi r^2$ ), and applying the following change of variable for the sake of simplicity

$$w^* = (v^*)^2 \quad (13)$$

we can rewrite the energy equation with the initial condition

$$-\frac{dw^*}{dx^*} = R_{ck}\sigma_c^* + R_m w^* + R_{fk} \left(1 + \left(x^* \frac{h}{r} - \frac{x_0}{r}\right)\tan\alpha\right)^2 c_r(x^*) \quad (14)$$

$$w^*(0) = 1$$

where three constants have been introduced, whose order of magnitude may be estimated to analyse the relative importance of each term in the energy equation

$$R_{ck} = \frac{2h\sigma_0 A_0}{m_p v_i^2} \square \frac{10^3}{v_i^2}, \quad R_m = \frac{hA\rho_l}{m_p} \square 10^{-2}, \quad R_{fk} = \frac{4h\varepsilon_f X_t r^2}{m_p v_i^2} \square \frac{10}{v_i^2}$$

$R_{ck}$  estimates the importance of the energy absorbed by laminate crushing as compared with the projectile initial kinetic energy.  $R_m$  is the ratio between the laminate mass affected directly by the impact, as compared with the projectile weight, and  $R_{fk}$  estimates the energy absorbed by tensile fiber failure, again

compared with the projectile initial kinetic energy. The last ratio is always lower than the others at any impact velocity (within the velocity range considered). The general energy equation admits different solutions according to the following hypothesis.

### 3.1. Solution 1. Cylindrical projectile

In this case  $A(x)$  is constant and the equation has an exact solution in the form

$$w(x) = c_1 \exp(R_m x) + c_2 x^2 + c_3 x + c_4 \quad (15)$$

However, due to the mathematic complexity of this solution, a numerical integration is preferred to calculate the results.

### 3.2. Solution 2. Constant through-thickness strength

In this case  $\sigma_c(x)$  is assumed as constant (mean value of the curve), the solution of the equation may be obtained using a regular perturbation analysis through the correction  $\varepsilon = R_{fk}$ . The solution of the equation may be obtained by the expansion (from now on, asterisks are going to be omitted)

$$w = w_{(0)} + \varepsilon w_{(1)} + O(\varepsilon^2) \quad (16)$$

The differential equation for zero order leads to

$$\begin{cases} -w'_{(0)} = R_{ck} A + R_m A w_{(0)} \\ w_{(0)}(0) = 1 \end{cases} \quad (17)$$

having a simple closed-form solution

$$w_{(0)}(x) = -\frac{R_{ck}}{R_m} + \left(1 + \frac{R_{ck}}{R_m}\right) \exp(-R_m \hat{A}) \quad (18)$$

where  $\hat{A}$  is the primitive of  $A$ . An interesting result of this solution is the closed-form expression for the residual velocity, as a function of geometric parameters, material properties and, of course, impact velocity. The residual velocity is easily determined taking from the zero order

$$w_{(0)}(\infty) = \exp(R_m) \left(1 - \frac{2\sigma_c R_{ck}}{\rho_l v_i^2} (\exp(R_m) - 1)\right) \quad (19)$$

and equaling to zero we get the ballistic limit

$$v_{bl} = \sqrt{\frac{2\sigma_c}{\rho_l} \left( \exp\left(\frac{hA\pi r^2}{m_p}\right) - 1 \right)} \quad (20)$$

The differential equation for first order also leads to a closed form solution

$$w_{(1)}(x) = -\exp(-R_m \hat{A}) \left( \int_0^x c_r \left(1 + \frac{h\kappa - x_0}{r} \tan \alpha\right)^2 \exp(R_m \hat{A}) d\kappa \right) \quad (21)$$

## 4. EXPERIMENTAL TESTING FOR MODEL VALIDATION

To validate the analytical model above described, experimental tests were carried out with woven AGP-193-PW/8552 (AS4 fiber) with 10 plies and a total thickness of 2.2 mm. This configuration is widely used in aeronautic and aerospace applications to manufacture structural elements subjected to torsion or shear forces. Its weak delamination under impact loads makes it a good choice when these are expected in service conditions. The material was provided by SACESA (Spain) from prepregs manufactured by HEXCEL with a volumetric content of fibers of 60%. The elastic and the strength properties of the composite are shown in Table 1. The specimen size was 80x80 mm<sup>2</sup>. Tempered steel projectiles (sphere 7.5 mm in diameter and 1.73 g of mass; cylinder with 5.5 mm diameter, 6.0 mm length and 1.1 g of mass) were used. The tempered steel is hard enough to ensure that no plastic deformation will occur during penetration and this simplifies the analysis because the entire energy projectile lost is due to the decrement of its kinetic energy. A Photron Ultima APX digital high speed camera was used to measure the residual velocity. The selected frame rate was 15.000 per second, so that a picture is taken every 67 μs. The resolution was 1024x128 pixels and the

shutter was set to 11  $\mu$ s. These settings were selected based on early testing and represent an optimal trade-off between available lighting and the minimization of blur in the images. With this set-up the trajectory of the projectile after penetration is accurately determined, for a good measurement of its residual velocity.

**Table 1.** Properties of AGP-193-PW/8552as provided by Hexcel.

Property	Value
$E_3$ (GPa)	9.0
$X_t$ (MPa)	860
$\rho_l$ (kg/m <sup>3</sup> )	1430
$\epsilon_f$	0.02
$\sigma_0$ (MPa)	60

## 5. RESULTS OF THE MODEL

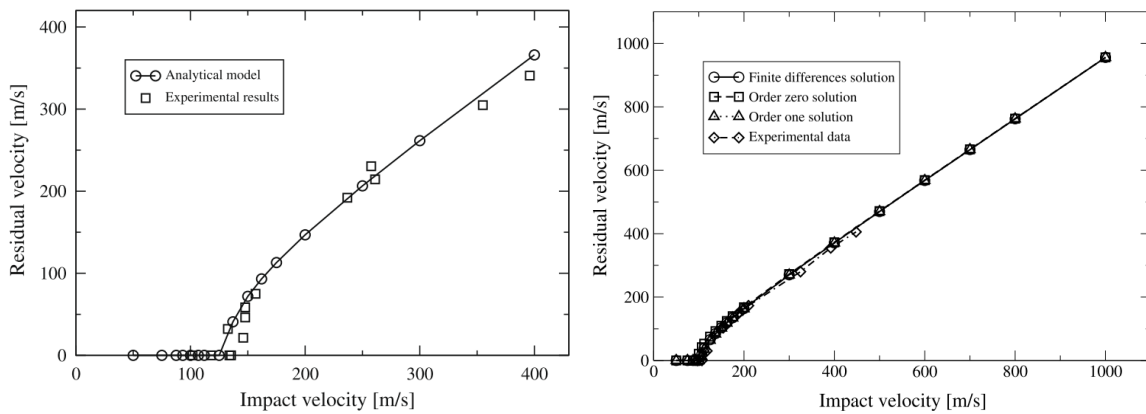
The residual velocity after penetration is the variable used to validate the model. Figure 4 shows the residual velocity versus the impact velocity, from the experimental data and from results taken from the analytical models. The model predicts with accuracy the residual velocity and estimates the minimum impact velocity of the projectile needed to perforate the laminate. As the impact velocity increases, the curve tends to a straight line, which is the expected result.

Figure 5 shows the relative importance of each absorption mechanism as a function of the impact velocity. As the impact velocity increases, the term related to the linear momentum transfer increases its relative importance, reaching the 60% of the total energy absorbed by the laminate when the projectile impact velocity is 600 m/s. The trend of the other two energy absorption mechanisms (tensile fiber failure and laminate crushing) is almost the same for velocities above the ballistic limit (around 130 m/s): its importance decreases as the impact velocity increases because both mechanisms do not vary significantly with impact velocity. However, below ballistic limit its trends are different. Laminate crushing increases with impact velocity because more thickness of the laminate is involved in the penetration process. Tensile fiber failure decreases, because it starts to play a role only after  $t = t_0$ ; then, at low velocities this mechanism initiates when the projectile is closer to the impact face and involves more plies of the laminate.

Last analysis summarizes the influence of two most important dimensionless parameters ( $R_m$  and  $R_{ck}$ ) in only one graph (Figure 6 left). Here, the ratio between the residual velocity  $v_r$  and the impact velocity  $v_i$  is plotted in the vertical axes, and the mass ratio parameter  $R_m$  in the horizontal axes; the different curves correspond to different values of the crushing–kinetic ratio parameter. It is clear that as  $R_m$  increases (lighter projectile or heavier laminates), the velocity ratio decreases for a constant value of  $R_{ck}$ . The figure benefits of the dimensionless approach and gathers the information for any impact case consistent with the hypothesis of the model. This way it is possible to obtain  $v_i - v_r$  curves (Figure 6 right), frequently used for predesign analysis, by keeping constant  $R_m$  – and considering that  $R_{ck}$  is inversely proportional to the square of the impact velocity. The family of curves in Figure 6 left smoothly approaches to the one corresponding to  $R_{ck} = 0$ . This limit value is reached asymptotically when the impact velocity is much higher than the ballistic limit, consequently leading to a proportionality between  $v_r$  and  $v_i$  at high impact velocity. The asymptotic behavior of the  $v_i - v_r$  curve given by the model is also observed experimentally on any projectile-plate impact process. Figure 6 also shows how the slope of the asymptote of the  $v_i - v_r$  curve increases as  $R_m$  decreases or, in other words, as the mass of the projectile predominates over the mass of the laminate affected by the impact. In the limit case that  $R_m$  becomes zero, the residual velocity equals the impact velocity.

## 6. CONCLUSIONS

An analytical model to predict residual velocity of spherical or cylindrical projectiles after impacting onto a thin carbon/epoxy woven laminate has been developed. The model considers three different energy absorption mechanisms for the laminate. Experimental impact tests were carried out to validate the model, showing a very good correlation between the results obtained both experimental and numerically, and also demonstrating that the model predicts faithfully the residual velocity of the projectile.



**Figure 4.** Residual velocity vs impact velocity; analytical and experimental results. Left: cylindrical projectile. Right: spherical projectile.

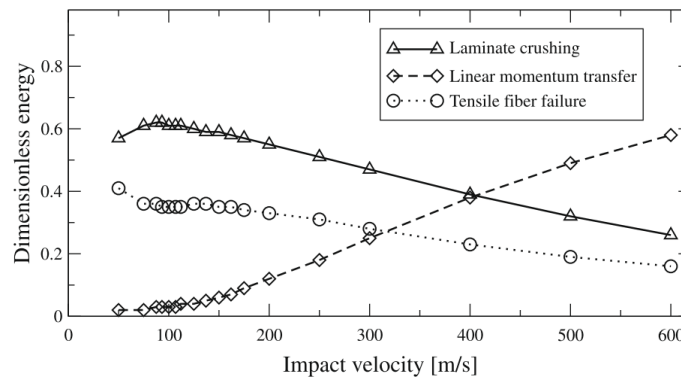


**Figure 5.** Dimensionless energy vs impact energy. Cylindrical projectile.

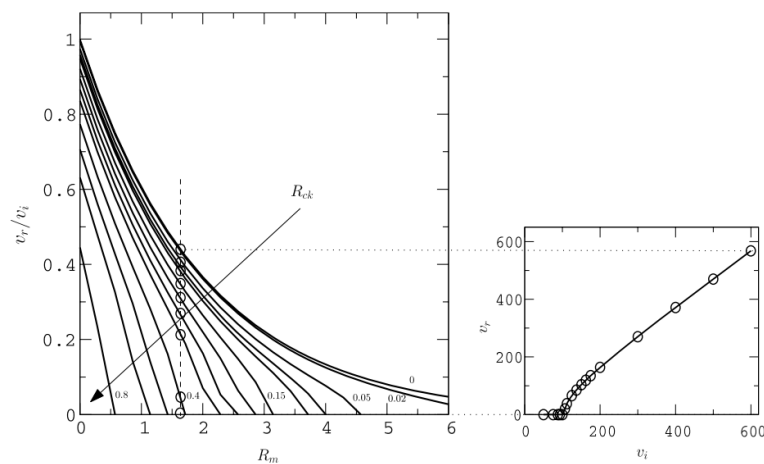


**Figure 6.** Left: influence of  $R_m$  and  $R_{ck}$  on dimensionless residual velocity. Right: residual velocity vs impact velocity for a given value of  $R_m$ . Spherical projectile.

## ACKNOWLEDGEMENTS

Authors would like to acknowledge to the Center for the Development of Industrial Technology (CDTI) of Spain and to the company AERNNOVA Aerospace for the financial support of this research.

## References

- [1] Tennyson R. C., Composites in space – challenges and opportunities. Proc ICCM-10, 1 (1995) 35–56.
- [2] David-West O.S., Nash D.H., Banks W.M., “An experimental study of damage accumulation in balanced CFRP laminates due to repeated impact”, *Compos Struct*, 83 (2008) 247–58.
- [3] Varas D., López-Puente J., Zaera R., “Experimental analysis of fluid-filled aluminium tubes subjected to high-velocity impact”, *Int J Impact Eng*, 36 (2009) 81–91.
- [4] Varas D., Zaera R., López-Puente J., “Numerical modelling of the hydrodynamic ram phenomenon”, *Int J Impact Eng*, 36 (2009) 363–74.
- [5] Schonberg W.P., “Hole size and crack length models for spacecrafts walls under oblique hypervelocity projectile impact”, *Aerospace Sci Technol*, 3 (1999) 461–71.
- [6] Farenthold E.P., Hernandez R.J., “Simulation of orbital debris impact on the space shuttle wing leading edge”, *Int J Impact Eng*, 33 (2006) 231–43.
- [7] Cantwell W.J., Morton J., “Comparison of low and high velocity impact response of CFRP”, *Composites*, 20 (1989) 545–51.
- [8] Sun C.T., Potti V., “A simple model to predict residual velocities of thick composite laminates subjected to high velocity impact”, *Int J Impact Eng*, 18 (1996) 339–53.
- [9] Larsson F., “Damage tolerance of a stitched carbon/epoxy laminate”, *Composites Part A: Appl Sci Manufact*, 28 (1997) 923–34.
- [10] Bland P.W., Dear J.P., “Observations on the impact behaviour of carbon-fibre reinforced polymers for the qualitative validation of models”, *Composites Part A: Appl Sci Manufact*, 32 (2001) 1217–27.
- [11] Will M.A., Franz T., Nurick G.N., “The effect of laminate stacking sequence of CFRP filament wound tubes subjected to projectile impact”, *Compos Struct*, 58 (2002) 259–70.
- [12] Tanabe Y., Aoki M., Fujii K., Kasano H., Yasuda E., “Fracture behavior of CFRPs impacted by relatively high-velocity steel sphere”, *Int J Impact Eng*, 28 (2003) 627–42.
- [13] Tanabe Y., Aoki M., “Stress and strain measurements in carbon-related materials impacted by a high-velocity steel sphere”, *Int J Impact Eng*, 28 (2003) 1045–59.
- [14] Hammond R.I., Proud W.G., Goldrein H.T., Field J.E., “High-resolution optical study of the impact of carbon-fibre reinforced polymers with different lay-ups”, *Int J Impact Eng*, 30 (2004) 69–86.
- [15] Hosur M.V., Vaidya U.K., Ulven C., Jeelani S., “Performance of stitched/unstitched woven carbon/epoxy composites under high velocity impact loading”, *Compos Struct*, 64 (2004) 455–66.
- [16] Herzsberg I., Weller T., “Impact damage resistance of buckled carbon/epoxy panels”, *Compos Struct* 73 (2006) 130–7.
- [17] Caprino G., Lopresto V., Santoro D., “Ballistic impact behaviour of stitched graphite/epoxy laminates”, *Compos Sci Technol* 67 (2007) 325–35.
- [18] Hazell P.J., Kister G., Stennett C., Bourque P., Cooper G., “Normal and oblique penetration of woven CFRP laminates by a high velocity steel sphere”, *Composites: Part A*, 39 (2008) 866–74.
- [19] Kim H., Welch D.A., Kedward K.T., “Experimental investigation of high velocity ice impacts on woven carbon/epoxy composite panels”, *Composites Part A: Appl Sci Manufact*, 34 (2003) 25–41.
- [20] Chambers A.R., Mowlem M.C., Dokos L., “Evaluating impact damage in CFRP using fibre optic sensors”, *Compos Sci Technol*, 67 (2007) 1235–42.
- [21] Asp L.E., Juntikka R., “High velocity impact on NCF reinforced composites”, *Compos Sci Technol*, 69 (2009) 1478–82.
- [22] López-Puente J., Zaera R., Navarro C., “The effect of low temperatures on the intermediate and high velocity impact response of CFRPs”, *Compos Part B: Eng*. 33 (2002) 559–566.
- [23] López-Puente, J., Zaera, R., Navarro, C., “High energy impact on woven laminates”, *J. Phys. IV* 110 (2003), 639–644.

# EFFECTS OF THE MECHANICAL TRANSVERSE PROPERTIES OF BUNDLES ON THE BALLISTIC IMPACT ONTO TEXTILE FABRIC: NUMERICAL MODELING

C. Ha-Minh<sup>1,2</sup>, F. Boussu<sup>2</sup>, T. Kanit<sup>1</sup>, D. Crepin<sup>2</sup>, A. Imad<sup>1</sup>

<sup>1</sup> Univ. Lille Nord de France, Cité Scientifique, 59655 Villeneuve d'Ascq Cedex, France

<sup>2</sup> ENSAIT-GEMTEX, 2 allée Louise et Victor Champier BP 30329, 59056 ROUBAIX Cedex, France

**Abstract.** A numerical model performed on Radioss, finite element code, was done to study a ballistic impact on a 2D Kevlar KM2 plain-woven fabric. A good agreement between numerical and experiment results show the validation of the numerical model constructed. This paper focused on studying the effect of Poisson's ratio and transverse modulus of bundle on impact behaviors of a single bundle and a complete fabric. This study indicates that when the Poisson's ratio diminishes, the fragility of a single bundle increases. However, globally, the effect of the Poisson's ratio is negligible in both impact cases on a single bundle and a complete fabric. In the range from 0.01 GPa to 0.62 GPa, transverse modulus decreases, single bundles are softened, and the ballistic performance of the fabric is very low. At the values superior to 1.34 GPa (experimental value), the effect of transverse modulus does not seem to exist anymore. In this work, the failure criterion FLD (Forming Limited Diagram) is suggested for bundle failure. Damage phenomena of yarns during impact are also discussed.

## 1. INTRODUCTION

Textile fabrics are widely used for various industrial and army applications due to a high performance onto impact [1-5]. Several authors investigated numerically ballistic impact on plain-woven fabrics [6-13]. Rao et al. [8] studied the effect of longitudinal Young's modulus and strength yarns on ballistic performance of woven-plain fabrics. In this paper, a numerical model is created and validated with experience results in the literature. Using this model, we focused on numerical studying the effects of the transverse properties of bundles in the case of a 2D Kevlar KM2® plain-woven fabric subjected to ballistic impact. This study indicates that when the Poisson's ratio diminishes, the fragility of a single bundle increases. However, globally, the effect of the Poisson's ratio is negligible in both impact cases on a single bundle and a complete fabric. In the range from 0.01 GPa to 0.62 GPa, transverse modulus decreases, single bundles are softened, and the ballistic performance of the fabric is very low. At the values superior to 1.34 GPa (experimental value), the effect of transverse modulus seems not to exist anymore. In this work, the failure criterion FLD (Forming Limited Diagram) is suggested for bundle failure. Damage phenomena of yarns during impact are also discussed.

## 2. COMPUTATION CONDITIONS

The material used is a Kevlar KM2 plain-woven fabric 50.6x50.6mm. The warp density is 13.4 ends/cm, which is equivalent to a distance of 1.49mm between bundles (Fig. 1). The fabric is fixed only at the two edges (Fig. 2). In order to reduce computation time, only a quarter of the complete model is calculated due to the symmetry of the impact system (Fig. 2b). At the symmetric plans, displacement of nodes in corresponding normal directions and their out-of-plane rotations are considered as fixed (Fig. 2b). It is assumed that the contact point between the fabric and the projectile is the crossover point at the fabric centre. The projectile has a spherical form with a diameter of 5.35 mm and a mass of  $6.25 \times 10^{-4}$  kg. In the case of a single layer plain-woven fabric, projectile deformation after impact is very small, thus, this spherical projectile is assumed infinitely rigid. For simplification, the friction between individual bundles, fabric and the projectile can be taken into account by unique Coulomb coefficients;  $\mu=0.23$  and  $\mu=0.20$  respectively.

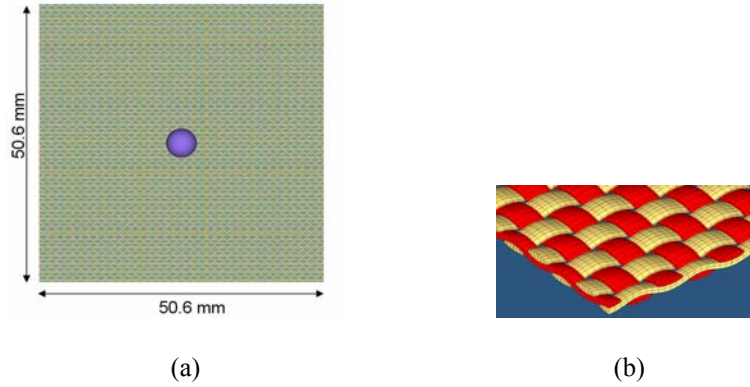


**Figure 1:** a) The initial configuration of the ballistic impact system simulated in the present study; (b) Detailed illustration of Kevlar KM2 plain-woven fabric

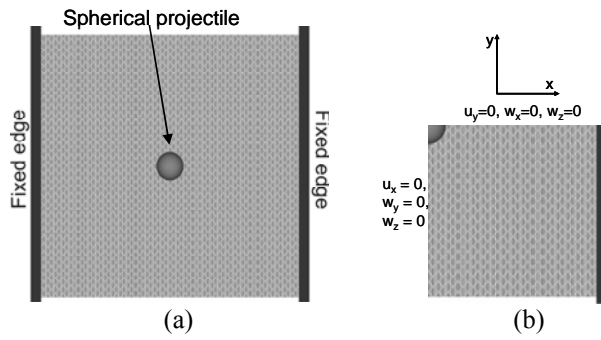


**Figure 2:** Boundary conditions of the model: (a) full model, (b) a quart of the model

Kevlar KM2 bundles in this study have a volume density of  $1310 \text{ kg/m}^3$ . The mechanical properties of each bundle can be assumed elastic and orthotropic along bundle central line because of the symmetry (Fig. 3). The behavior of this orthotropic material (the relation between the strains  $(\varepsilon_{11}, \varepsilon_{22}, \varepsilon_{12}, \varepsilon_{23}, \varepsilon_{31})$  and stresses  $(\sigma_{11}, \sigma_{22}, \sigma_{12}, \sigma_{23}, \sigma_{31})$  of a bundle) is formulated by a compliant matrix:

$$\begin{pmatrix} \varepsilon_{11} \\ \varepsilon_{22} \\ 2\varepsilon_{12} \\ 2\varepsilon_{23} \\ 2\varepsilon_{31} \end{pmatrix} = \begin{pmatrix} \frac{1}{E_{11}} & \frac{-\nu_{21}}{E_{22}} & 0 & 0 & 0 \\ \frac{-\nu_{12}}{E_{11}} & \frac{1}{E_{22}} & 0 & 0 & 0 \\ 0 & 0 & \frac{1}{G_{12}} & 0 & 0 \\ 0 & 0 & 0 & \frac{1}{G_{23}} & 0 \\ 0 & 0 & 0 & 0 & \frac{1}{G_{31}} \end{pmatrix} \begin{pmatrix} \sigma_{11} \\ \sigma_{22} \\ \sigma_{12} \\ \sigma_{23} \\ \sigma_{31} \end{pmatrix}$$

Where  $E_{11}$  is the longitudinal Young's modulus of a bundle;  $E_{22}$  is the transversal Young's modulus of a bundle;  $\nu_{12}, \nu_{21}$  are Poisson's ratios of a bundle;  $G_{12}, G_{23}, G_{31}$  are the shear moduli of a bundle.

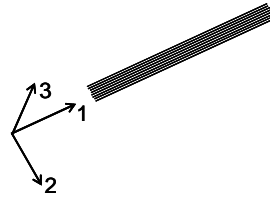


**Figure 3:** Directions of a fibers bundle

In this formulation, we excluded the strain and stress in yarn cross section height  $\epsilon_{33}$ ,  $\sigma_{33}$  due to a very small ratio between the height and the width of yarn cross section. For a simplification, we can assume  $G_{12} = G_{31}$  (shearing in the direction perpendicular to the bundle). Moreover, we can consider  $G_{23} \approx 0$  (shearing in the direction parallel to the bundle) because a bundle is composed of thousands separated single fibers (Fig.3). Moreover, we knew that the compliant matrix is symmetric, then  $\nu_{12}/E_{11} = \nu_{21}/E_{22}$ . In general, we need 4 experimental values for material elastic constants of a bundle:  $E_{11}$ ,  $E_{22}$ ,  $\nu_{12}$ ,  $G_{12}$ . Assuming that the behavior of single fibers does not change in a bundle, we can apply the correspondent values of single fibers measured experimentally by Cheng et al. 2005 [14] for a bundle. The table 1 presents the values of 4 necessary mechanical constants in this study (Tab. 1).

**Table 1:** Material constants of Kevlar KM2 single fibers (Cheng et al. 2005 [14])

$E_{11}$ (GPa)	$E_{22}$ (GPa)	$G_{12}$ (GPa)	$\nu_{12}$
84.62	1.34	24.4	0.6

A textile fabric is woven by two systems of orthogonal warp and weft yarns. The impact behavior of a single yarn is the one of the important elements that decides the response of a plain-woven fabric onto projectile impact. In this study, impact tests on a single yarn were also modeled to understand better impact phenomena (Fig. 4). In order to reduce computation time, only a quarter of the complete model is calculated due to the symmetry of the impact system (Figs. 4b, 4d). At the symmetry planes, the displacement of nodes in corresponding normal directions and their out-of-plane rotations are considered as fixed (Figs. 4b, 4d).

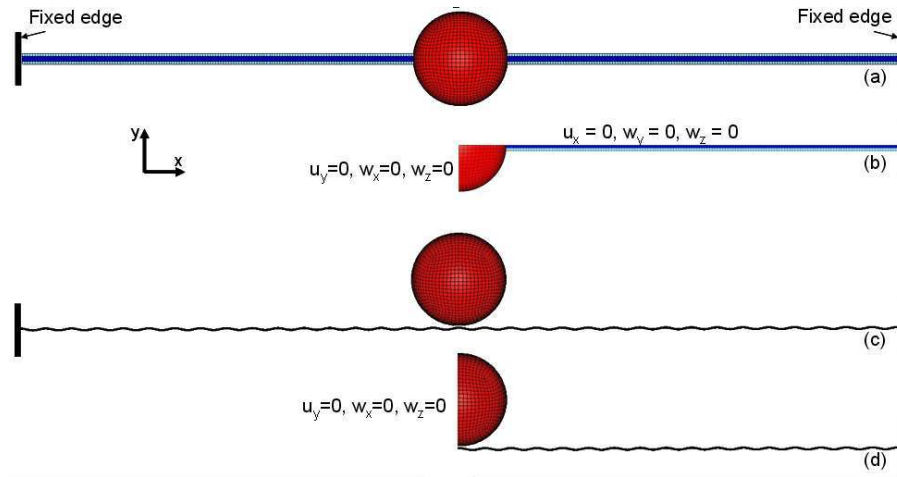


**Figure 4:** Configuration of numerical impact model on a single bundle: a) Vertical view of the model; b) Vertical view of a quart of the model; c) Horizontal view of the model; d) Horizontal view of a quart of the model

Most of the authors [6-14] agree with this hypothesis that bundles are elastic to failure. Thus, we can suggest the FLD criterion (Forming Limit Diagram) where the failure zone is defined in the plane of principal strains (Fig. 5) [15]. Failure zone in FLD criteria needs to be defined by the evolution of the maximum principal strain in term of the minimum one. Figure 5 shows a simple method to determine the FLD criterion. Indeed, in our case, the experiment value of the dynamic failure strain of a KM2® single

fiber is equal to 4.58% [14]. We can use this value as the dynamic failure strain of KM2® bundles of the fabric in the FLD failure criterion of the numerical models.

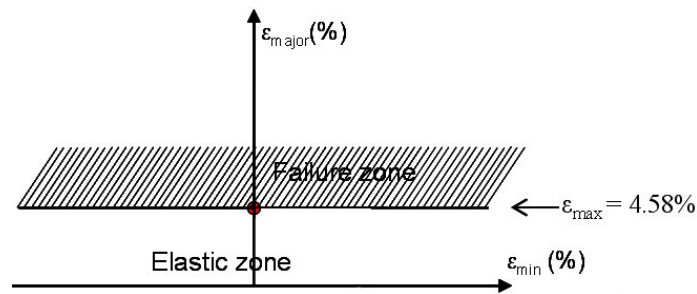


**Figure 5:** Schematization of a forming limit diagram (FLD)

### 3. RESULTS AND DISCUSSIONS

#### 3.1. Validation of the numerical model

Figure 6 shows experiment and numerical results on the dynamic behavior of the studied woven-plain fabric subjected to the projectile with a velocity of 245 m/s. Penetration of the projectile causes damage phases on the fabric. The fabric zone that contacts with the projectile submits a large concentrated force. Therefore, yarns are damaged and failed in this zone. These yarns that pass this zone are called primary yarns. However, only vertical primary yarns fixed at two edges of fabric are failed because they are tensed during impact event. With exception of the central yarn, horizontal yarns in perpendicular direction only slip on the projectile and do not fail because they are free at two ends. We can observe in this direction that the central yarn does not fail, but it is pulled out from the fabric (Fig. 6). In the zone far from impact point, yarns seem not to be affected hence, they are not damaged. The fabric in this zone displaces following primary yarns due to the weave interlacement among yarns but woven structure still seems to remain intact. However, at the free edge of the fabric, a few yarns are burst out of the fabric. The reason is that the fabric is shrunk due to projectile penetration, only a few horizontal yarns fixed at two ends are retained, and therefore, they are out of the fabric (Fig. 6).

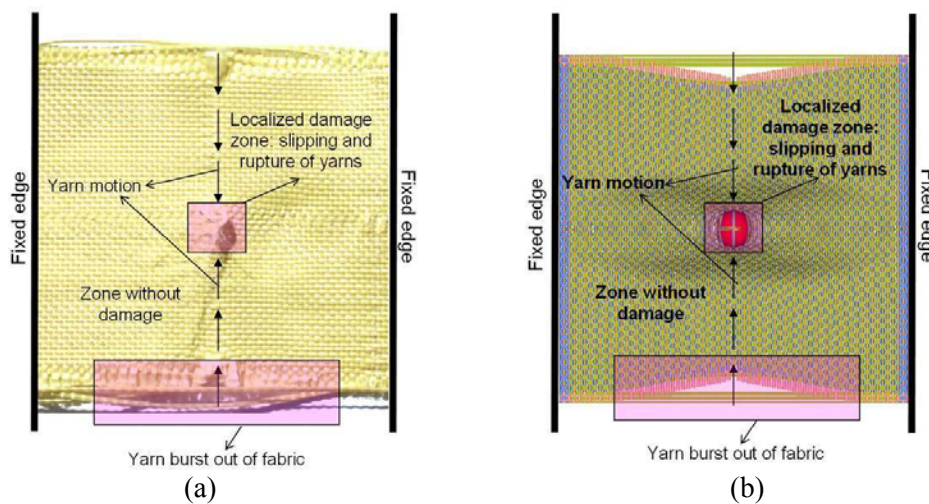


**Figure 6:** Comparison on a 245m/s ballistic impact onto a plain-woven fabric between: a) Experiment test; b) Numerical result

Globally, we can estimate that there is a good agreement between numerical and experiment results in the figure 6. Moreover, the residual velocity (projectile velocity after perforation) of the numerical model is equal to 222.4 m/s. This result is close to experimental value equal to 207 m/s [6]. Again, it indicates a good validation of the numerical model.

### 3.2. Effect of the Poisson's ratio

Figures 7 and 8 show projectile velocity evolution versus time when Poisson's ratio is varied for both impact cases on a single bundle and on a complete fabric. In this paper, we vary the Poisson's ratio from 0.001 to 0.99 to study the effect of the Poisson's ratio in the numerical model. We can observe that all curves in the impact case on a single bundle seem be the one. Projectile velocity diminishes slowly in the first 10  $\mu\text{s}$  because it corresponds to the bundle de-crimping period. After this time, projectile velocity decreases more strongly with yarns at the tense state. Globally, at 32.5  $\mu\text{s}$ , all curves are horizontal, projectile velocity does not change anymore. It is the time when the single bundle is failed. In general, we can found that the effect of Poisson's coefficient is not significant on the numerical result of a ballistic impact on a single bundle. However, it is noted that there is a slight difference among curves. In the figure 7, when Poisson's ratio increases, projectile velocity diminishes more slowly and fails later. It indicates that fragility of a single bundle decreases with the growth of Poisson's ratio.

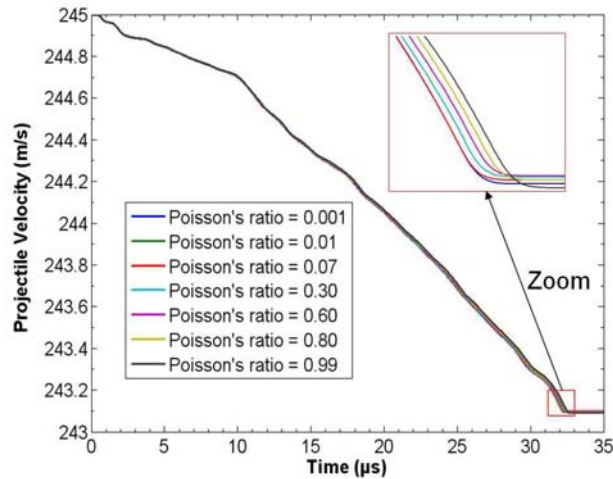


**Figure 7:** Evolution of projectile velocity during impact on a single bundle with varying Poisson's ratio

In the impact case on a complete fabric, globally, all curves are also similar to each other from the beginning of the impact to yarn failure moment (from 0  $\mu\text{s}$  to 20  $\mu\text{s}$  approximately). After 20  $\mu\text{s}$ , yarn failure begins to appear when yarn stress passes over limit. In this period, the element removal is executed and an inevitable calculation perturbation produced a slight difference among curves. Again, we found the fragility of bundles with small Poisson's ratios equal to 0.01 and 0.07. The fabric is early perforated and projectile velocity curve is rapidly horizontal.

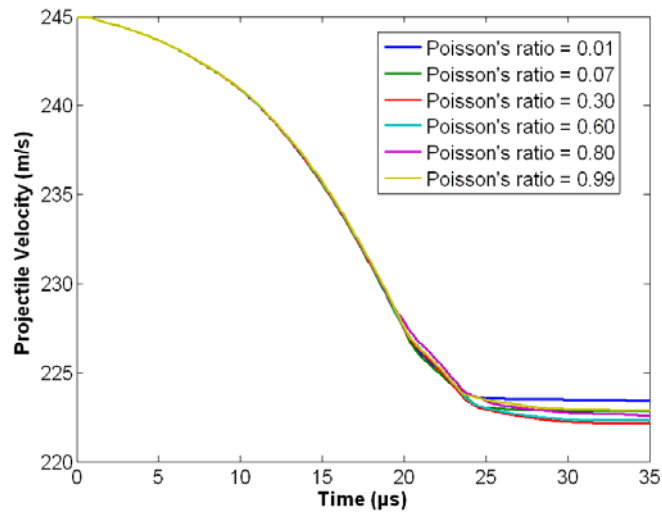


**Figure 8:** Evolution of projectile velocity during impact on a complete fabric with varying Poisson's ratio

### 3.3. Effect of the transverse Young's modulus

Figure 9 shows the evolution of projectile velocity versus time in the impact case on a single bundle. Here, we focus on studying the effect of transverse modulus of bundle by varying its value from 0.01 GPa to 100 GPa. We can observe that in the range from 0.01 to 1.34, the effect of the transverse modulus is considerable. When the transverse modulus decreases in this range, the inclination of curves is getting smaller and curves becomes horizontal later (the failure moment of yarns). It indicates that the bundle seems to be softer with decreasing of transverse modulus. Figure 10a shows premature damages of a single bundle at 18.6  $\mu\text{s}$  in the case of the transverse modulus equal to 0.01 GPa. We also found this phenomenon for the case of transverse modulus equal to 0.06 GPa. However, this phenomenon does not exist for all curves with a transverse modulus superior or equal to 1.34 GPa. For example, figure 10b shows that the single bundle with transverse modulus equal to 2.68 GPa is not damaged at the same moment 18.6  $\mu\text{s}$  regarding to the case of 0.01 GPa. Therefore, we can observe a considerable difference of two curves of 0.01 GPa and 0.06 GPa regarding to the other curves with higher transverse modula in the figure 9. It can indicate that with small values of transverse modulus, bundles are easier to be damaged due to the same charge regarding to the cases superior or equal to 1.34 GPa (experiment value of Cheng et al. 2005 [14]).

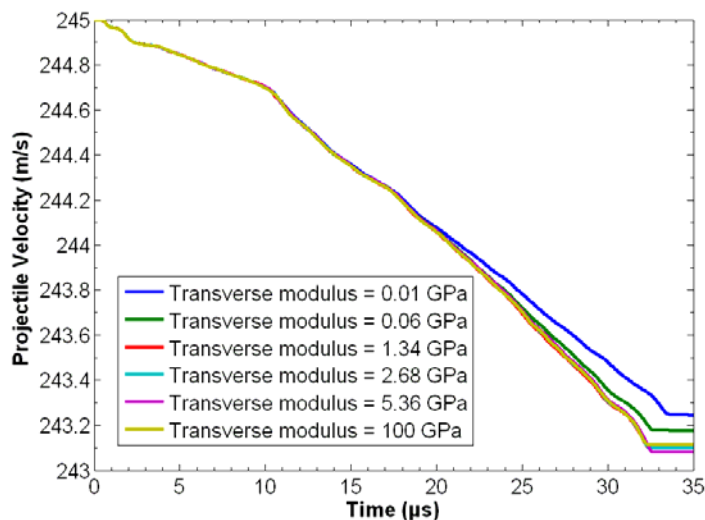


**Figure 9:** Evolution of projectile velocity during impact on a single bundle with varying transverse modulus



**Figure 10:** Comparison on impact behavior of a single bundle in two cases of transverse modulus at 18.6  $\mu$ s: (a)  $E_{22} = 0.01$  GPa; (b)  $E_{22} = 2.68$  GPa

Figure 11 shows the evolution of the projectile velocity in the impact case on a complete 2D fabric with different transverse moduli: 0.06 GPa, 0.62 GPa, 1.34 GPa, 5.36 GPa. Again, we found the effect of transverse modulus at small values from 0.06 GPa to 1.34 GPa on impact behavior of a single bundle in the case of a complete fabric. We can observe in this figure that the transverse modulus increases, projectile velocity during impact event diminishes faster. Therefore, with transverse moduli 0.06 GPa and 0.62 GPa, the ballistic performance of the fabric is low, the fabric is always perforated at higher residual velocities (projectile velocity after perforation) than the cases of 1.34 GPa, 5.36 GPa. The velocity evolution of the projectile seems to be the one with the cases of transverse moduli superior to or equal to 1.34 GPa (Fig. 11). It means that the effect of transverse modulus does not exist in these cases.

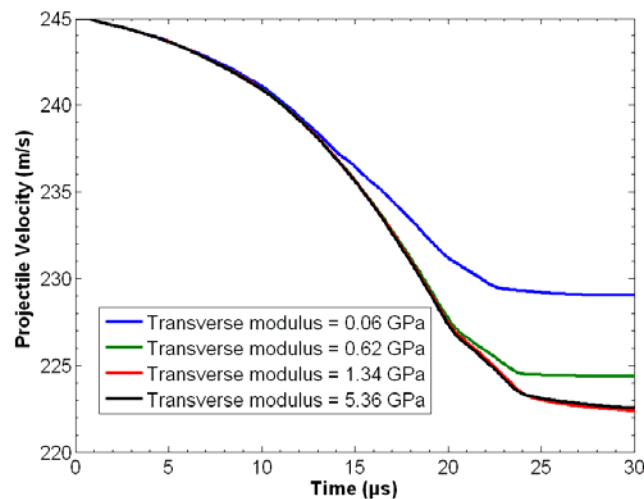


**Figure 11:** Evolution of projectile velocity during impact on a complete fabric with varying transverse modulus

### 3.3. Conclusion

A numerical model is constructed and validated by experiment results. There is a slight softening of single bundles when the Poisson's ratio varies from 0.01 to 0.99. However, globally, the effect of Poisson's ratio is not significant for both impact behaviors of a single bundle and a complete fabric. When the transverse modulus varies from 0.06 GPa to 100 GPa, bundles always fail early at small values ( $< 1$  GPa) and from 1.34 GPa (experiment value) to 100 GPa, the evolution of projectile velocity is mostly the same. In general, this study indicated that transverse properties of modeled bundles do not affect significantly the result of model. However, it is noted that we should not take so small values of transverse Young's modulus for avoiding an early damage of bundles in the transverse resistance.

## References

- [1] Grujicic M, Arakere G, He T, Bell WC, Cheeseman BA, Yen CF, Scott B. A ballistic material model for cross-plyed unidirectional ultra-high molecular-weight polyethylene fiber-reinforced armor-grade composites. *Mate Sci and Eng* 2008;498(1-2):231-241.
- [2] Barauskas R, Abraitienne A. Computational analysis of impact of a bullet against the multilayer fabrics in LS-DYNA. *Int J Impact Eng* 2007;34(7):1286-1305.
- [3] Miravete A. 3-D textile reinforcements in composite materials. Woodhead publishing limited, 2007.
- [4] Yang C, Kim YK, Qidwai UA, Wilson AR. Related strength properties of 3D fabrics. *Textile Research Journal* 2004;74:634 – 639.
- [5] Taylor D, Seyam AFM, Powell NB. Three-dimensional woven composites for automotive applications. Recent advances in textiles composites: Proceedings of the 9th International Conference on Textile Composites, issue Texcomp9, Suresh G Advani and John W Gillespie, Newark, Delaware, USA, 2008. p.280-287.
- [6] Duan Y, Keefe M, Wetzel ED, Bogetti TA, Powers B, Kirkwood JE, Kirkwood KM. Effects of friction on the ballistic performance of a high-strength fabric structure. *WIT Transactions on Engineering Sciences, Impact Loading of Lightweight Structures*, Alves M, Jones N (Editors) 2005;(49):219-229.
- [7] Duan Y, Keefe M, Bogetti TA, Cheeseman BA. Modeling friction effects on the ballistic behavior of a single-ply high-strength fabric. *Int J Impact Eng* 2005;31(8):996–1012.
- [8] Rao MP, Duan Y, Keefe M, Powers BM, Bogetti TA. Modeling the effects of yarn material properties and friction on the ballistic impact of a plain-weave fabric. *J ComStruc* 2009;89(4):556–566.
- [9] Nandlall D, Williams K, Vaziri R. Numerical simulation of the ballistic response of GRP plates. *Composites Science and Technology* 1997;58(9):1463-1469.
- [10] Tabiei A, Nilakantan G. Ballistic impact of dry woven fabric composites: A review. *Appl Mech Rev* 2008; 61(1):010801(13 pages).
- [11] Talebi H, Wong SV, Hamouda AMS. Finite element evaluation of projectile nose angle effects in ballistic perforation of high strength fabric. *Composite Structures* 2009;87(4):314–320.
- [12] Sevkate E, Liaw B, Delale F, Raju BB. A combined experimental and numerical approach to study ballistic impact response of S2-glass fiber/toughened epoxy composite beams. *Composites Science and Technology* 2009;69(7-8):965–982.
- [13] Rao MP, Nilakantan G, Keefe M, BM Powers, Bogetti TA. Global/local modelling of ballistic impact onto woven fabrics. *J Comp Mater* 2009;43:445 – 467.
- [14] Cheng M, Chen W. Mechanical properties of Kevlar® KM2 single fiber. *Journal of Engineering Materials and Technology* 2005;123:197 – 203.
- [15] RADIOSS Theory version 90 manual, 2008

## TRANSFER OF COPYRIGHT AGREEMENT

Copyright to the article entitled: *Effects of the mechanical transverse properties of bundles on the ballistic impact onto textile fabric: Numerical modeling*

By : *C. Ha-Minh, F. Boussus, T. Karit, D. Crépin, A. Imad*  
All Authors

is hereby transferred to the

**DYMAT Association**

effective when the article is accepted for publication in :

**19<sup>th</sup> DYMAT Technical Meeting**  
(electronic or hardcopy format)

However, the authors reserve the following :

- (1) All proprietary rights other than copyright, such as patent rights.
- (2) The right to use all or part of this article in future works of their own, such as lectures, press releases, reviews, textbooks, or reprint books.

*Third party requests to reprint all or part of the article must be directed to the publisher in order to obtain publisher's written permission.*

To be signed by at least one of the authors (who agrees to inform the others, if any) or, in the case of a "work made for hire", by the employer.

  
\_\_\_\_\_  
Signature

\_\_\_\_\_  
Signature

*Cuong HA-MINH*  
\_\_\_\_\_  
Print Name

\_\_\_\_\_  
Print Name

*PhD student*  
\_\_\_\_\_  
Title, if not Author

\_\_\_\_\_  
Title, if not Author

*EMISAIT*  
\_\_\_\_\_  
Institution or Company

\_\_\_\_\_  
Institution or Company

*17/10/2010*  
\_\_\_\_\_  
Date

\_\_\_\_\_  
Date

The signed statement must be received before  
the manuscript can be accepted for publication.

Return to DYMAT before October 15, 2010 :

DYMAT 19<sup>th</sup> TM 2010 IMFS UDS / 2 rue Boussingault / 67000 Strasbourg / France Fax:  
00 33 (0) 3 68 85 29 36 Email: bahlouli@unistra.fr

# Constitutive behaviour of a polymer-bonded explosive

PJ Gould<sup>1</sup>, P Church<sup>2</sup>, R Pereira<sup>2</sup>

<sup>1</sup> *QinetiQ, B240 Bristol Business Park Bristol BS16 1FJ UK*

<sup>2</sup> *QinetiQ, Fort Halstead, Sevenoaks, Kent TN14 7BP UK*

**Abstract.** The constitutive behaviour of an idealised PBX has been investigated. The mechanical properties of the composite and binder have been measured at low and high rate and over a variety of temperatures from 213K to 343K. Predictions have been made of the properties of the constituents and compared against dynamic mechanical analysis and quasi-static tension and compression. Predictions have been made of the properties of the PBX using simple composite theory. Analysis of the split Hopkinson pressure bar (SHPB) output has been attempted. The binder is found to behave in a classic linear viscoelastic manner at low rate but to have a more complex behaviour at high rate. Group Interaction Modelling is found to give good predictions for the properties of the PBX components. In order to obtain agreement with the properties of the composite it has been found necessary to presume a constraint on the action of the plasticiser. At low temperatures and high rates the composite is found to have a modified response that cannot be explained simply. The material appears not to obey classical time-temperature superposition. It is hypothesised that the plasticiser is having an effect that goes beyond a simple reduction in glass transition temperature.

## 1. INTRODUCTION

In assessing safety of explosives it is found that the mechanical properties of the composite material formed from binder and energetic filler have a significant effect on the violence of a dynamic, but non-shock, event. The cost of gathering information about explosives through mechanical tests is increasingly expensive and material is often not available for testing on the timescales required. A predictive capability is needed that uses only limited information. The mechanical properties of various polymer-bonded explosives (PBX) have been measured in large and small-scale tests and models constructed in order to simulate real events. These models have given only small insight and have not formed the basis of a predictive capability. Theory of composite behaviour is well advanced, although there is still a large amount of research on failure of composites and the evolution and effects of damage. Composite theory, to be useful, requires knowledge of the components and their properties and also any interactions that occur between the components when they form the composite. Dynamic properties may also differ from those measured at quasi-static rates.

Recent advances in polymer theory have allowed predictions of polymer behaviour to be made both at low and high rates. Group Interaction Modelling (GIM) [1] gives good predictions of polymer mechanical properties from chemistry alone and can take into account interactions between components. It has already been used very successfully in the prediction of equations of state [2]. This suggests that the constitutive behaviour of PBX should be able to be predicted without fitting allowing test output to be used as validation.

## 2. COMPONENTS

The polymer-bonded explosive (PBX) material used in this study was formulated as an ideal composite. It consisted of 75% by mass RDX in a HTPB binder plasticised with DOS and cross-linked to just over two crosslinks per polymer chain. Its monomodal particle size was a well-controlled distribution that peaked at 15  $\mu\text{m}$  and had a maximum detectable size of 100  $\mu\text{m}$ . This was designed to be processable but with an adequate particle spacing to avoid particle interactions.

In predicting the properties of PBX materials based upon energetic fillers and rubbery binders, the approach taken to date has been to predict the properties of the components and then use standard composite theory to combine these to predict the PBX properties [2,3]. The properties of the energetic filler need not be known in any great detail as, mechanically, it acts as a strong stiffener; it has no influence on strength beyond this and beyond the lengthscale of the particle spacing. GIM gives the modulus of RDX at room temperature and all rates as:  $K = E = 13 \text{ GPa}$  with Poisson's ratio = 0.33.

The GIM calculation for the plasticised binder is more difficult as one has to take multiple interactions into account. Not only that but cross-linking dominates properties at room temperature due to the plateau modulus effect. Comparisons between DMA and stress-strain are complicated by the existence of liquid-like states in the plasticiser that significantly reduce the small-strain modulus but which play no part in general loading due to the load all being taken by the polymer chains. Young's modulus,  $E$ , should be predicted in tension by the bulk modulus,  $K$ , and cumulative loss tangent,  $\tan\Delta_g$ :

$$\tan \Delta_g = \int_0^T \tan \delta dT \quad E = \frac{K}{[1 + \tan \Delta_g]^2} \quad (1)$$

The complicating factor when comparing with various experimental methods is to understand which mechanical effects give rise to active moduli. This is discussed further in [2]. The measured  $\tan\delta$  vs  $T$  DMA trace is typical of these binders and shows the main glass transition associated with interactions between the HTPB and its plasticiser together with the higher temperature glass transitions associated with interactions between the HTPB and the cross-linking agent. The DMA measurements give  $\tan\Delta_g = 48$ . At room temperature GIM gives  $K = 1.5$  GPa for the binder which gives  $E = 0.6$  MPa. Compression tests at quasi-static rates at room temperature give Young's modulus for the binder  $E = 0.66$  MPa, Figure 1. An estimate of the temperature variation of the bulk modulus can be made from the equation of state [2].

In the compression Hopkinson bar the modulus is seen to increase. Figure 1 shows a comparison between low rate compression and Hopkinson bar compression at room temperature for the binder material. The behaviour of the Hopkinson bar curve is classically linear elastic with a hint of very short time rigidity. The modulus in this high rate test is 2.6 MPa.

At lower temperatures the behaviour of the polymer changes. This is first seen at 213K – as the main glass transition peak is approached – and is seen in Figure 2. The strain rates in the two curves presented here are very similar: 2200/s and 2700/s and yet the stress levels are very different. The main change when compared to Figure 1 is the initial stress jump – a tangent to the main slope of the curves does not go through the origin. This is not a plastic yield in the polymer as there is almost no irreversible deformation in the sample post-test. The implied modulus of this jump is extremely high, though, of the order of 500 GPa as to suggest an initial rigid response.

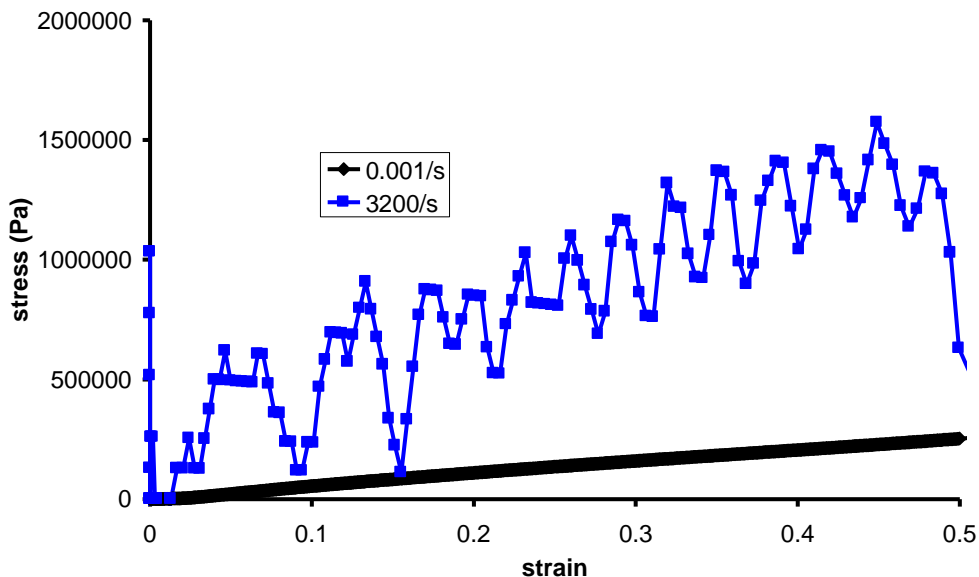


**Figure 1:** Comparison between Hopkinson bar data and low rate compression data for the plasticised binder

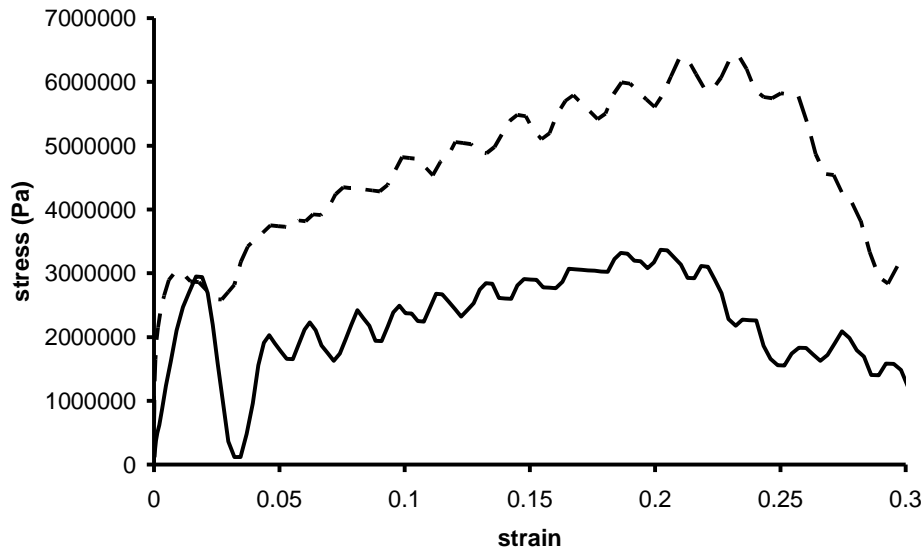


**Figure 2:** Two Hopkinson bar curves for the plasticised binder measured at 213K

In an ideal temperature- and rate-dependent linear elastic material the secant modulus could be measured for each test and plotted for comparison with temperature- and rate-dependence of storage and loss moduli. Unfortunately the secant modulus here changes too much for it to form a valid input to such a discussion. This reflects difficulties in inferring physical mechanisms from Hopkinson bar output. Often a peak stress is used instead but this is not possible here given the linear-elastic response above 213K. If the post-jump tangent modulus is plotted against temperature it can be seen to follow the predicted response for the binder at low rates, Figure 3. This figure also shows some of the difficulties in interpreting time-temperature data for polymers using larger strain data. The high rate data are obviously not only shifted to colder temperatures but have a scale factor; on Figure 3 a scale factor 10 increase and a shift of 5K to lower temperatures is enough to give a good fit to the data. Classical theory would suggest that a temperature shift is the only necessary action but this is obviously not the case here.

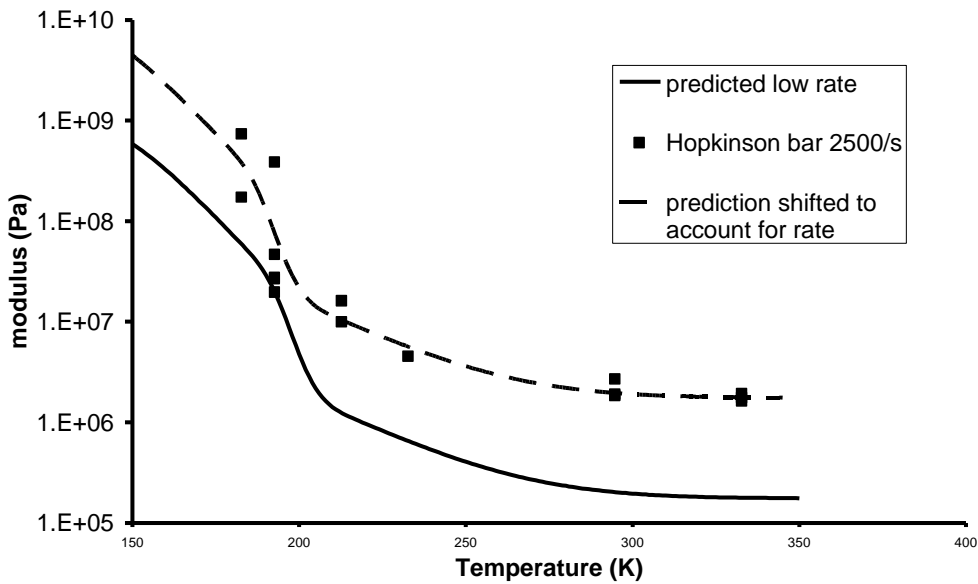


**Figure 3:** Moduli calculated from Hopkinson bar experiments for binder plotted against the prediction for low rate modulus and a shift of that prediction

GIM has shown that the behaviour of polymers is straightforward to predict once all the interactions have been taken into account. There is obviously some other material interaction that is complicating matters. If the behaviour of the plasticiser changed markedly with rate and temperature then this could explain the effects seen here. The freezing point of DOS is 205K but it would be expected that this would change when incorporated into the binder. If the plasticiser froze or crystallised with high rate or at low temperature it would add a further stiffness to the binder as well as a higher overall strength, consistent with the behaviour seen in Figure 3. More data are needed to understand these phenomena and particularly mechanical test data over a range of temperatures on a binder with varying levels of plasticiser. This is particularly important as the plasticiser should affect the binder heat capacity and thus the thermal side of the hazard response as well as the mechanical side. Fully understanding all of the components and their interactions is vital if better compositions are to be designed.

### 3. COMPOSITE

There are various composite theories that predict modulus [3]. The Reuss model is the most simple and should be appropriate given the disparity in moduli of the components in this PBX. The effect of particle-binder interactions needs to be considered. It has been noted [4] that damage to the composite changes not only the modulus of the composite due to loss of stiffening but also the apparent modulus of the binder. This suggests that the particles constrain the polymer chains in some manner. The apparent modulus of the binder when the composite has been fully damaged is equivalent to the predicted modulus of the plasticised binder alone. However, if a prediction is made of the modulus of un-plasticised HTPB then that prediction – approximately 2.6 MPa at room temperature – is equivalent to the apparent modulus of the binder in undamaged composite. This suggests that the constraint nullifies any plasticiser effects.

For the Reuss model,  $E_p$  being the modulus of the particles and  $E_b$  the modulus of the binder, the volume fraction of filler is  $\phi = 0.61$  and so the composite Young's modulus,  $E_c$ , is given by:

$$E_c = \left( \frac{\phi}{E_p} + \frac{1-\phi}{E_b} \right)^{-1} = \left( \frac{0.61}{10000} + \frac{0.39}{2.6} \right)^{-1} = 6.7 \text{ MPa} \quad (2)$$

Another method is that of Halpin and Tsai. This requires calculation of other parameters such as the maximum packing fraction of the filler,  $\phi_m$ , and an Einstein coefficient. The equation is:

$$E_c = E_b \left[ \frac{1 + AB\phi}{1 - B\phi} \right] \quad A = \frac{2.5}{\phi} - 1 \quad B = \frac{\frac{E_p}{E_b} - 1}{\frac{E_p}{E_b} + A} \quad \phi = 1 + \frac{1 - \phi_m}{\phi_m^2} \phi \quad (3)$$

The maximum packing fraction for a monomodal distribution is 0.74. This gives  $E_c = 38.9$  MPa.

The final popular method for determining moduli of composites is the Mori-Tanaka method. For spherical particulate this gives, at room temperature,  $E_c = 14$  MPa. The Young's moduli from a variety of quasi-static mechanical tests are plotted in Figure 4 together with predictions from the composite models described above. Of these methods, the Reuss method appears to be the best predictor but does not do well at low temperatures even given the spread in the data. One possibility is the Reuss model only being accurate if the binder modulus is significantly less than that for the particulate – this becomes increasingly false as the temperature falls. If, however as speculated above, the plasticiser freezes this would add another higher modulus term into the equation and raise the predicted modulus. Of the three models only the Halpin-Tsai contains a parameter that is effectively unknown – the maximum packing fraction – and it could be argued that this could be used as a fitting parameter. Even if this took its maximum possible value of 1, the prediction of the composite modulus would not improve significantly. Should it be shown that the plasticiser has an effect as hypothesised in the previous section the Reuss model would probably be the best predictor at all temperatures. It is worth emphasising that the low rate tests are able to be predicted over a range of temperatures using only the predictions of the component properties. This is vital for further analysis of more complex situations.

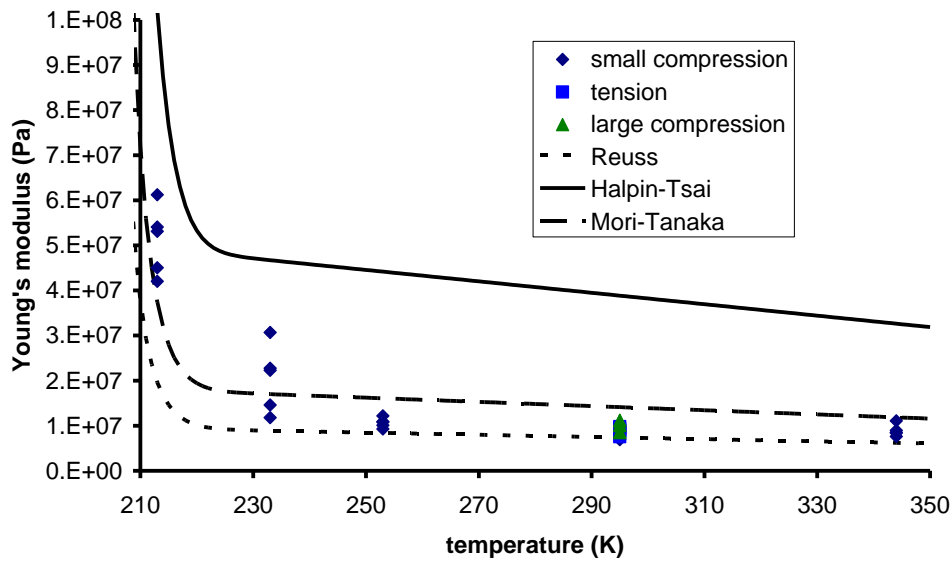


Figure 4: Measured Young's modulus at low rate at several temperatures compared to predictions from various composite models

### 3.1 Hopkinson Bar

When analysing the modulus of the composites in the Hopkinson bar, one first has to ask how that modulus is to be determined from the data available and the one-wave analysis that is usually performed. The issues surrounding this are illustrated by Figure 5 which compares a Hopkinson bar one-wave analysis with the output from a quasi-static compression test on the PBX.

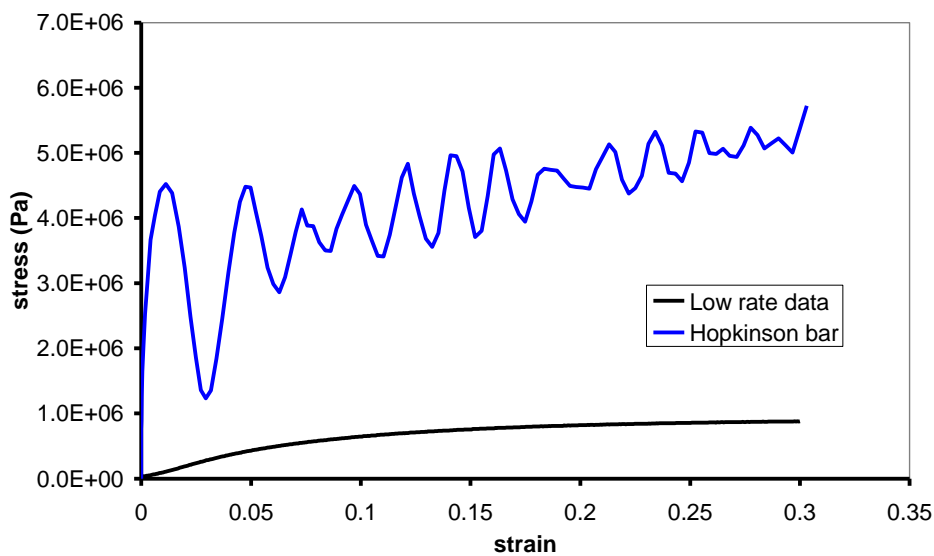


Figure 5: Comparison between the experimental stress-strain response of the PBX at low and high rates.

The stresses in the Hopkinson bar are higher than in the low rate tests. The appearance of the stress-strain response is significantly more like that for the binder at very low temperature with a very short time rise at high modulus followed by a stress rise with approximately linear tangent modulus. The initial secant modulus up to the first peak varies from essentially rigid to around 0.5 GPa – values more relevant to glassy polymers than to rubbers. This is more reminiscent of a stress relaxation test than one that involves strain hardening or softening. One expectation of the form of the output was that the material would damage and this would involve a change in modulus. It can be argued that the constant tangent modulus is indicative of

a degrading secant modulus and that, if there was an unload-reload cycle, linear elastic behaviour with a lower modulus would be seen.

If a modulus is to be reported – and more importantly if a modulus is to be predicted or used to indicate physical mechanisms occurring in the material – a relevant slope needs to be measured. The obvious slope in this test is the constant tangent modulus. This has the same magnitude, 7 MPa, as the initial modulus in the low rate test and, due to the expected strain rate stiffening, suggests that like is not being compared to like. An attempt can be made to predict the modulus of the composite in the Hopkinson bar using composite theory. If the binder modulus at room temperature, as measured in the Hopkinson bar, is used in a Reuss model it predicts a secant modulus of 8 MPa. The actual secant modulus at low strain from Figure 5 – approximately 1 GPa – when used in the Reuss model gives a binder modulus of 400 MPa; this is characteristic of a glass or crystal and not a rubber. At high strains the secant modulus of the PBX in the Hopkinson bar is 16 MPa which, again using the Reuss model, gives a binder modulus of 6 MPa; this is more characteristic of a rubber but the material at these strains will be damaged and damage adds a significant complication. Any effects of extraneous plasticiser interactions only exacerbate the difficulty of analysing the output of this test. This puts a heavier burden on the theory as an interpretive tool and requires a better understanding of these complex materials at intermediate rates and in the Hopkinson bar.

#### **4. CONCLUSIONS**

The properties of the components of a PBX at low rates of loading can be predicted knowing only their chemistry. Interactions not normally accounted for in composite theory appear and need to be included. At high rates the behaviour of the composite changes in ways that are not immediately predictable from theory. There is difficulty in interpreting the output of Hopkinson bar data to learn about the physical mechanisms occurring in the material. This may lead the Hopkinson bar to be used for validation only but a predictive capability is still needed.

#### **Acknowledgments**

The authors would like to acknowledge funding from UK MOD via DTIC and the UK-E consortium

#### **References**

- [1] Porter D., “Group Interaction Modelling of Polymer Properties”, Marcel Dekker, New York 1995.
- [2] Porter D. and Gould P.J., “A General Equation of State for Polymeric Materials”, *J. de Physique IV*, 134 (2006), 373-378
- [3] Nielsen L.E and Landel R.F. “Mechanical Properties of Polymers and Composites 2nd Edition”, Marcel Dekker (1994).
- [4] Cornish R., Porter D., Gould P., Church P., Andrews T., Proud B., Drodge D., Siviour C. “Comparison of Porter-Gould Constitutive Model with Compression Test Data for HTPB/Sugar; SCCM-2007 Hawaii; Elert, M.; Furnish, M.D.; Chau, R.; Holmes, N.; Nguyen, J.; eds.; AIP Conference Proceedings #955; American Institute of Physics; (2007) p777.

- > Final printed area will be of 15 cm x 23 cm. The proceedings will be made of A4 colour prints.
- > Publication limited to 8 pages.
- > Submit 2 electronic files, a .doc file and a .pdf file, along with the copyright agreement form, p. 3 of this file, by October 15, 2010 : bahlouli@unistra.fr

## Dynamic Compressive Properties of Biodegradable Polymer Blend Containing Corn Starch

M. Nishida<sup>1</sup>, Y. Yutani<sup>1</sup>, M. Uemura<sup>2</sup> and E. Ataka<sup>3</sup>

<sup>1</sup> Nagoya Institute of Technology, Gokiso-cho, Showa-ku, Nagoya, Japan

<sup>2</sup> Kumamoto Industrial Research Institute, Higashi-cho, Kumamoto-shi, Japan

<sup>3</sup> Gaia Base Corporation, 4-8-32 Shinhoka, Kumamoto-shi, Japan

**Abstract.** We prepared three polymer blends using different mixing ratios of corn starch, poly(lactic acid) (PLA), and poly(butylene adipate terephthalate) (PBAT) (51:39:10, 51:34:15, and 51:29:20). We observed the cryofractured surfaces of these specimens under a scanning electron microscope before performing experiments on them. We measured the stress–strain curves for the three corn starch/PLA/PBAT specimens using a split Hopkinson pressure bar (Kolsky bar) and a universal testing machine. We determined that the PBAT content affected the stress–strain curves of the specimens. The Young's modulus and yield stress of the specimens also decreased with increasing PBAT content, regardless of the strain rate. However, the effects of the mixing ratio on yield stress reduction were found to depend on the strain rate. In addition, we confirmed the effects of temperature and water absorption on the yield stress of the specimens. We also measured the Izod impact strength of the three polymer blends.

### 1. INTRODUCTION

The increasing use of plastic products worldwide is causing considerable damage to the environment. Therefore, extensive investigations are being conducted on biodegradable plastics (plastics that can decompose in the natural environment) and bio-based plastics (plant-derived or recyclable-resource-based plastics), and new biodegradable and bio-based plastics are continuously being developed.

For our study, Uemura and Ataka developed corn starch/PLA/PBAT blends [1]. Because the main component of the polymer blends is corn starch, they are inexpensive while simultaneously containing a high percentage of plant-derived materials. In order to use corn starch powder in industrial products such as the interior parts of cars and computer cases, a binder composed of thermoplastic polymers is required. Poly(lactic acid) (PLA) is one such bio-based (plant-derived) biodegradable polymer. It has high strength and stiffness, but it is brittle. The problem of brittleness can be overcome by blending PLA with poly(butylene adipate/terephthalate) (PBAT), which is a ductile and biodegradable polymer. We anticipate that PLA/PBAT polymer blends and alloys can potentially exhibit high impact strengths [2], and they can be used as binders. Although the melting point and decomposition temperature of the three components, PLA, PBAT, and corn starch, are different, we were able to successfully prepare the corn starch/PLA/PBAT polymer blends.

We prepared corn starch/PLA/PBAT blends including 51% of corn starch. In the present study, we measured the stress–strain curves of the corn starch/PLA/PBAT blends using a universal testing machine and a split Hopkinson pressure bar (Kolsky bar) system. We examined the effects of the mixing ratio on the Young's modulus and flow stress of the polymer blends. We also confirmed the effects of temperature and water absorption on their yield stresses.

### 2. EXPERIMENTAL METHODS

#### 2.1. Materials

We prepared corn starch/PLA/PBAT blends using corn starch powder (average particle diameter of 10  $\mu\text{m}$ ) obtained from San-ei Sucochemical Co., Ltd.; PLA, from Mitsui Chemicals, Inc. (LACEA); and PBAT, from BASF (Ecoflex). The mixing ratios of corn starch, PLA, and PBAT for the three specimens were 51:39:10, 51:34:15, and 51:29:20. Figure 1 shows scanning electron microscope (SEM) photographs of the cryofractured surfaces of the specimens, captured before the start of the experiments. We observe a sea-island structure consisting of particles (islands) of almost the same size. Figure 2 shows optical microscope

photographs of the specimen surfaces after the specimens were stained using iodine solution. The color of the islands changed from white to dark blue. We believe that the sea–island structure consists of a PLA/PBAT matrix (sea) and corn starch particles (islands). Figure 3 shows a magnified image of Fig. 1(a). The small particles in the PLA/PBAT matrix shown in Fig. 3 are presumed to belong to the PBAT-rich phase; this was deduced from the mixing ratio and deformation behavior of this phase, as discussed later.

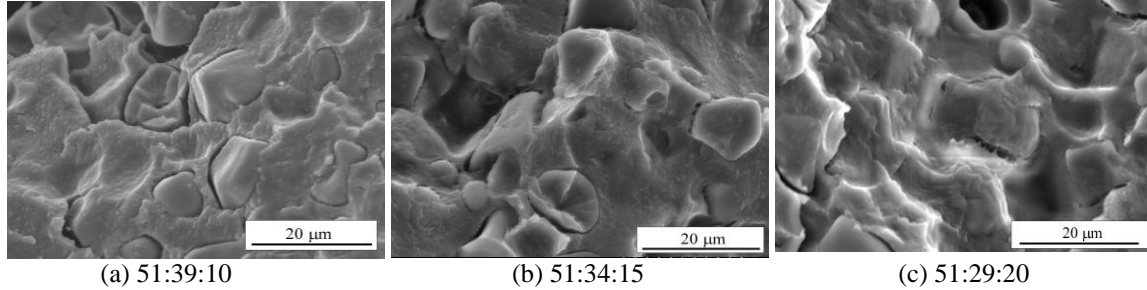


**Figure 1.** SEM photographs of cryofractured surfaces of corn starch/PLA/PBAT.

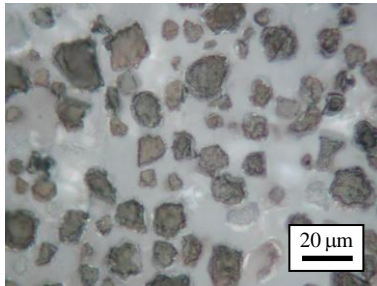


**Figure 2.** Optical microscope photograph of specimen surfaces

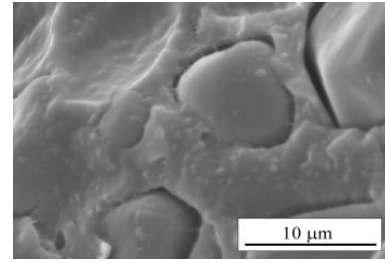


**Figure 3.** Magnified photograph of Figure 1 (a).

## 2.2. Polymer Blend Specimens

Polymer blend specimens for the compressive tests were produced using a lathe, and their end faces were polished and parallelized. The specimens used for the dynamic compressive tests had a diameter of approximately 11.6 mm to enable us to accurately measure the stress–strain curves using our equipment. The specimen thickness was 3.8 mm. In the quasi-static tests based on ASTM D695-02a, we used specimens with a diameter and thickness of 8 mm and 12 mm, respectively. Specimens for the Izod impact tests were prepared using a milling machine. They had dimensions of  $63.5 \times 12.7 \times 5$  mm and an A-type notch. An Izod impact testing machine procured from Toyo Seiki Seisaku-sho, Ltd., was used.

## 2.3. Experimental Setup

Quasi-static compressive tests were conducted at strain rates ranging from  $10^{-4}$  to  $10^{-2} \text{ s}^{-1}$  using a universal testing machine (A&D Co., Ltd., RTM-500). At high strain rates of  $10^2$  to  $10^3 \text{ s}^{-1}$ , the compressive properties of the specimens were examined by the split Hopkinson pressure bar (Kolsky bar) method, as shown in Fig. 4. To employ this method, input and output bars were made of an aluminum alloy (A2024-T4), and they had a diameter of 28 mm and respective lengths of 1900 mm and 1300 mm. Strain gages were placed on both sides of the input and output bars at distances of 950 mm and 300 mm from the specimen, respectively. As the stress histories were almost equal on both the sides of the specimens, the stress and strain of the specimens were calculated from the strain on the bars using eqns. (1) and (2), which are given below. In addition, the strain on the bars was measured using the strain gages [3].

$$\varepsilon(t) = \frac{2c_3}{L} \int_0^t [\varepsilon_I(t) - \varepsilon_T(t)] dt \quad (1)$$

$$\sigma(t) = \frac{AE}{A_S} \varepsilon_T(t) \quad (2)$$

Here,  $\varepsilon_I$  and  $\varepsilon_T$  denote the axial strains induced in the input bar by the incident wave and in the output bar by the transmitted wave, respectively.  $E$  and  $c_3$  respectively denote the Young's modulus of and elastic wave velocity in the input and output bars.  $L$  denotes the specimen thickness.  $A$  and  $A_S$  denote the cross-sectional

areas of the input/output bars and specimens, respectively. The material constants of the aluminum alloy (A2024-T4) bars used in the calculations are listed in Table 1. We used brass strikers with a diameter of 20 mm and lengths of 220–390 mm. The specimens were maintained at a temperature of  $23\pm 2^\circ\text{C}$  using silicone rubber heaters (Heatwell®, Kawai Electric Heater Co., Ltd.), each of length 60 mm. We preserved the specimens in a desiccator at a humidity of 30%–40% until just before use in order to avoid the effect of moisture absorption on the specimens.

**Table 1.** Material constants of input and output bars used in calculations.

Density	Elastic wave velocity in bar, $c_3$	Young's modulus $E$
$2.77 \times 10^3 \text{ kg/m}^3$	5150 m/s	73.6 GPa

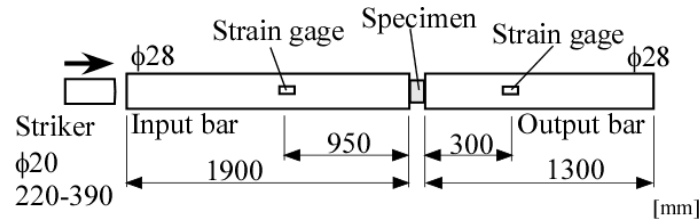


**Figure 4.** Experimental setup for split Hopkinson pressure bar method (Kolsky bar).

### 3. RESULTS AND DISCUSSION

#### 3.1. Results of Izod Impact Tests

The results of the Izod impact tests are shown in Fig. 5. The figure shows the standard deviation of the results and their statistically significant difference. When the mixing ratio of corn starch:PLA:PBAT was 51:29:20, the Izod impact strength was twice that when the mixing ratios were 51:34:15 and 51:39:10. Figure 6 shows SEM photographs of the fractured surfaces of specimens after the Izod impact tests. When the mixing ratio of corn starch:PLA:PBAT was 51:29:20, the PLA/PBAT matrix underwent considerable deformation. We also observe strings in Fig. 6(a)–(c). We believe that they have originated from the PBAT particles because PBAT is ductile and rubber-like. Figure 7 shows photographs of the fractured surfaces after the Izod impact tests. The surface of each specimen is flat.

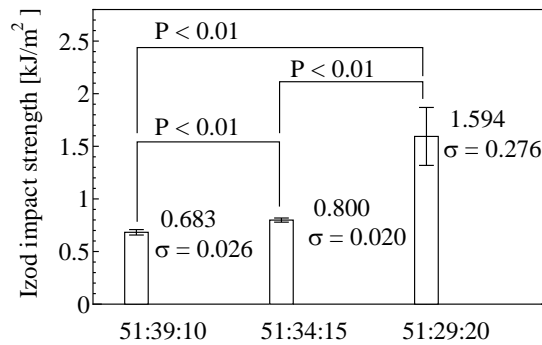
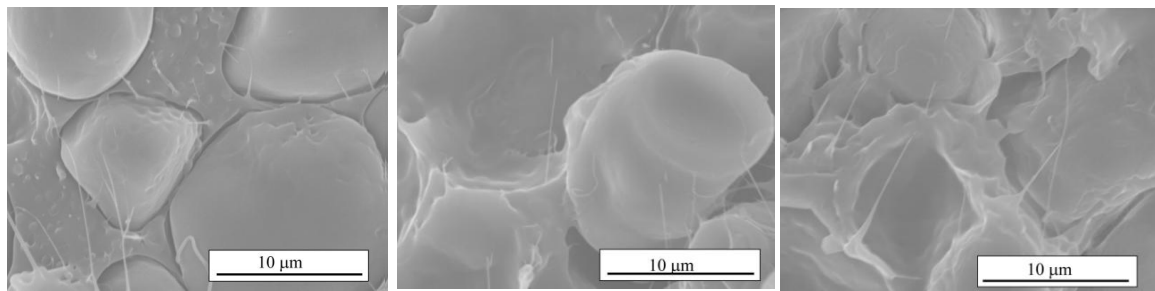


**Figure 5.** Impact resistance of different corn starch/PLA/PBAT blends.



(a) 51:39:10

(b) 51:34:15

(c) 51:29:20

**Figure 6.** SEM photographs of fractured surfaces of specimens.

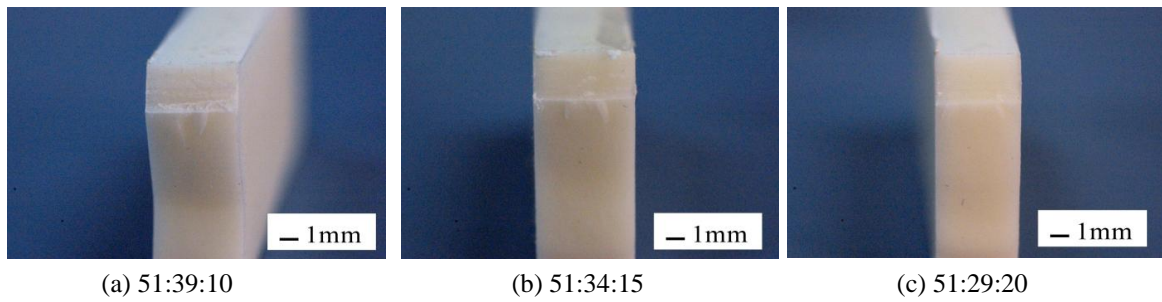
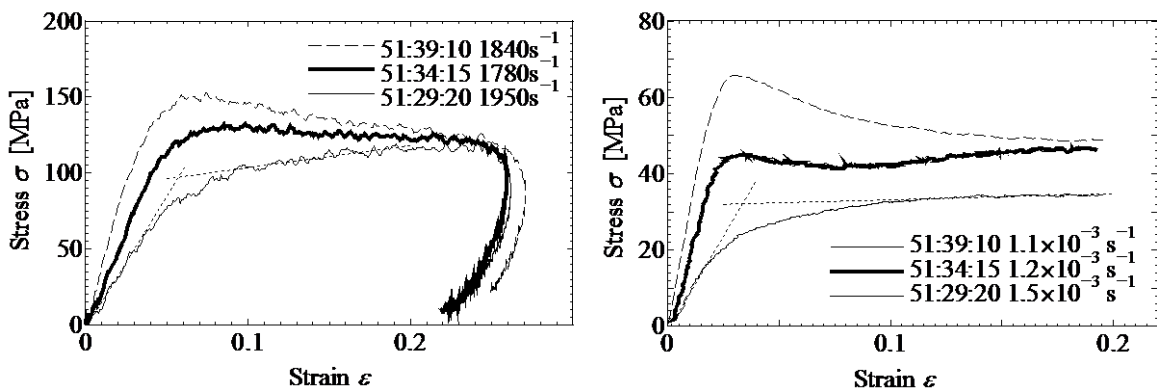


**Figure 7.** Photographs of fractured surfaces of specimens.

### 3.2. Results of Compressive Tests

The effects of the mixing ratio on the dynamic properties of the corn starch/PLA/PBAT specimens were examined by the split Hopkinson pressure bar method. Figure 8(a) shows the nominal stress–nominal strain curves, which were obtained from the strain history and stress history using eqns. (1) and (2), of the corn starch/PLA/PBAT specimens. We determined the average value of the strain rate–strain curve as the strain rate [4]. Figure 8(b) shows the nominal stress–nominal strain curves of the corn starch/PLA/PBAT specimens at strain rates of  $1.1\text{--}1.5 \times 10^{-3} \text{ s}^{-1}$ . Regardless of the strain rate, when corn starch:PLA:PBAT = 51:39:10, the stress–strain curve of the specimen peaked near the elastic limit, and then, the stress decreased gradually with increasing strain (softening). As the PBAT content in the mixing ratio increased, the peak of the stress–strain curve became lower, and the yield stress and Young’s modulus decreased gradually as shown in Fig. 8(a) and (b). When corn starch:PLA:PBAT = 51:34:15, the flow stress remained almost constant. When corn starch:PLA:PBAT = 51:29:20, the flow stress increased slightly (work hardening).

Figure 9 shows the effect of strain rate on the yield stress of the polymer blend specimens. For each polymer blend, the yield stress increased with the strain rate, as is commonly observed among most engineering plastics such as poly(methyl methacrylate) (PMMA) and polycarbonate (PC). As the PBAT content in the mixing ratio increased, the yield stress decreased at high and low strain rates. Here, when corn starch:PLA:PBAT = 51:39:10 and 51:34:15, the yield stress corresponded to the flow stress at the peak near the elastic limit. When corn starch:PLA:PBAT = 51:29:20, the yield stress was determined by the intersection of two asymptotic lines in the strain regions of 0%–1.5% and 10%–20%, as shown by the dashed lines in Fig. 8. Figure 10 shows the effects of the PBAT content on yield stress at each strain rate. On the basis of the results of the yield stress of corn starch:PLA:PBAT = 51:39:10 at each strain rate, all the experimental results were normalized and plotted on a graph. The yield stress of corn starch:PLA:PBAT = 51:29:20 was half of that of corn starch:PLA:PBAT = 51:39:10 in the low strain rate region. At strain rates of  $1750\text{--}1850 \text{ s}^{-1}$ , the yield stress of corn starch:PLA:PBAT = 51:29:20 was approximately 80% of that of corn starch:PLA:PBAT = 51:39:10. The effects of the mixing ratio on yield stress reduction were found to depend on the strain rate.



(a) Strain rates of  $1780\text{--}1950 \text{ s}^{-1}$

(b) Strain rates of  $1.1\text{--}1.5 \times 10^{-3} \text{ s}^{-1}$

**Figure 8.** Effect of PBAT content on stress–strain curves.

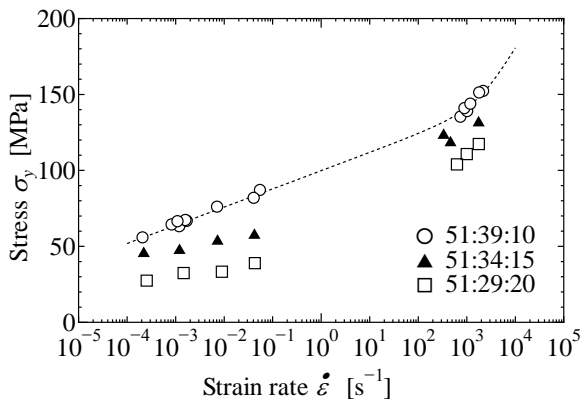


Figure 9. Effect of strain rate on yield stress.

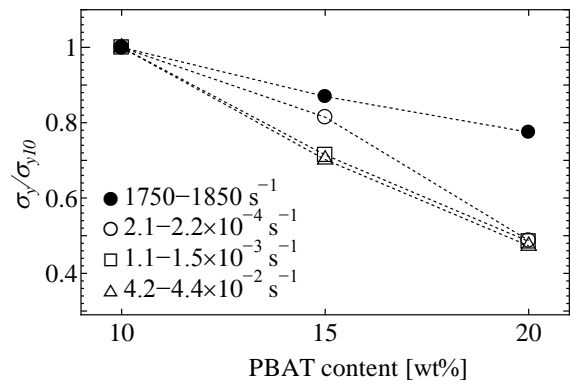


Figure 10. Effect of PBAT content on yield stress.

### 3.3. Effect of Water Absorption on Yield Stress

Water absorption usually affects the compressive properties of polymers. Therefore, for the above experiments, we preserved the polymer blend specimens in a desiccator until just before use in order to avoid the effect of water absorption on the specimens. Here, we specifically examined the effect of water absorption on the compressive properties of the specimens. The specimens were soaked in distilled water (Wako Pure Chemical Industries, Ltd.) at 24 °C. After 40 days, the water absorption of the specimens was 10% by weight, as shown in Fig. 11. Figures 12 and 13 show the stress–strain curves of the water-absorbed specimens at low and high strain rates. The absorption of water by the specimens affected their Young’s modulus and considerably decreased their flow stress and yield stress. The strain rate dependence of yield stress of all the experimental results is shown in Fig. 14. Thus, water absorption affected the strain rate dependence of yield stress in the low and high strain rate regions.

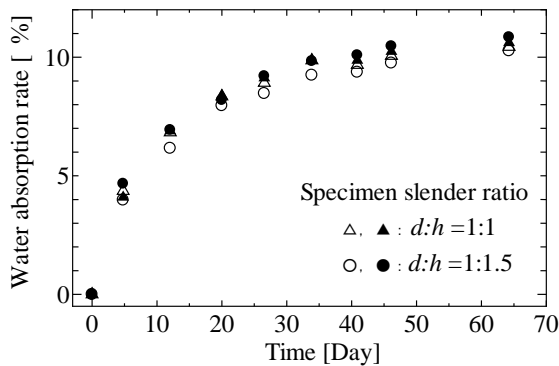


Figure 11. Water absorption.

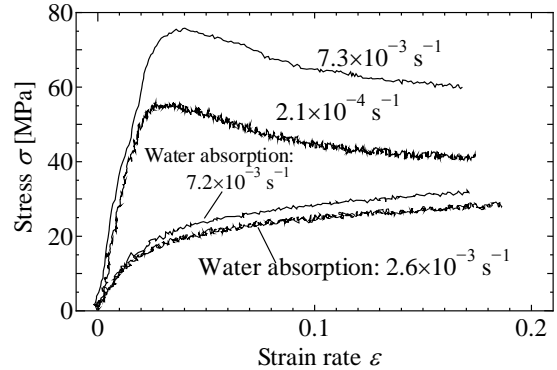


Figure 12. Effect of water absorption on stress–strain curves at low strain rate.

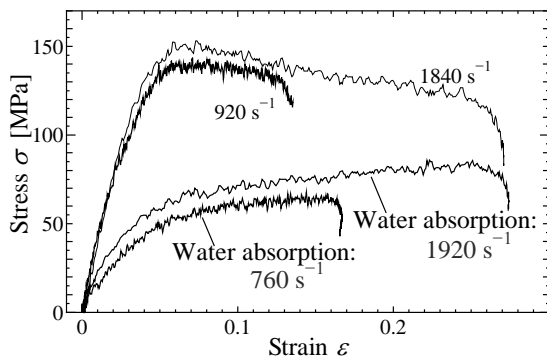


Figure 13. Effect of water absorption on stress–strain curves at high strain rate.

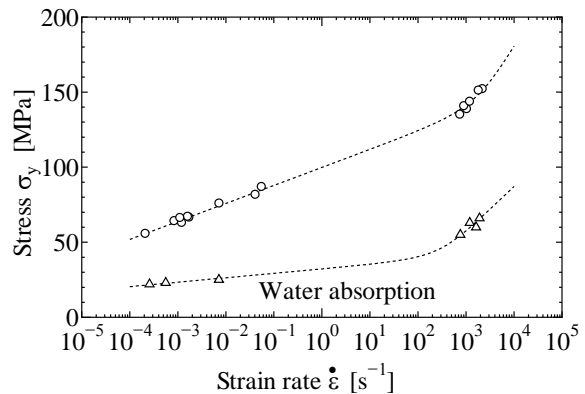
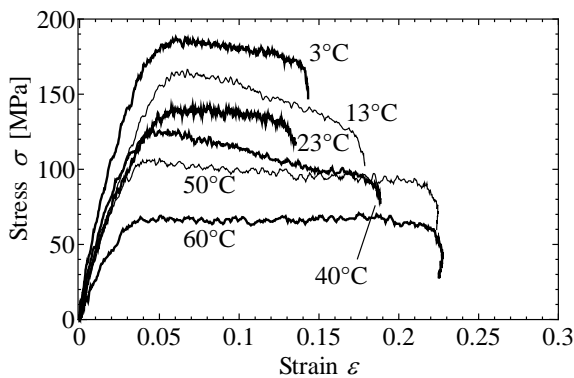


Figure 14. Yield stress and strain rate.

### 3.4. Effect of Temperature on Yield Stress

The compressive properties of polymers are also affected by temperature. Therefore, for the abovementioned experiments, the specimens were maintained at a temperature between 23 °C and 25 °C using silicone rubber heaters during the compression. We examined the effect of temperature on the stress–strain curves at high strain rates of 900–1000 s<sup>-1</sup>. Figure 15 shows that the Young’s modulus and flow stress of the specimens slightly decreased with an increase in temperature; this is commonly observed among most engineering plastics. Figure 16 shows that the yield stress decreased gradually with increasing temperature. The result obtained using a differential scanning calorimeter (DSC) is shown in Fig. 17, according to which the glass transition temperature is 50 °C. The effects of temperature on the yield stress of the specimens were almost the same for both below and above the glass transition temperature.



**Figure 15.** Effect of temperature on stress–strain curves at strain rates of 900–1000 s<sup>-1</sup>.

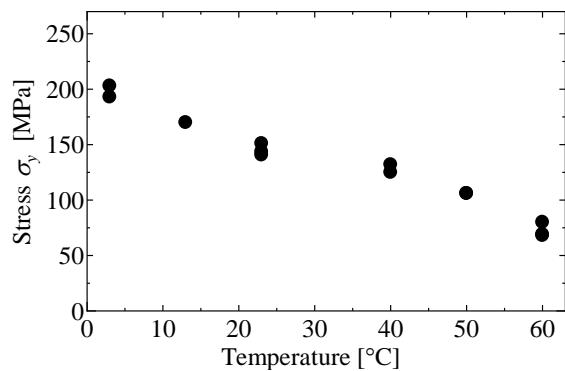


**Figure 16.** Temperature and strain rate.

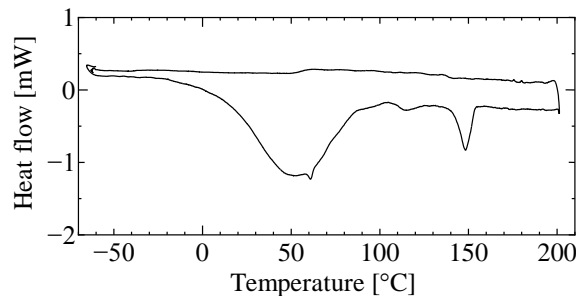


**Figure 17.** Results of differential scanning calorimeter (DSC).

## 4. CONCLUSIONS

We examined polymer blend specimens prepared using different mixing ratios of corn starch/PLA/PBAT. The stress–strain curves of the corn starch/PLA/PBAT specimens were measured using a split Hopkinson pressure bar and a universal testing machine. The PBAT content in the mixing ratios affected the stress–strain curves obtained for the specimens. The Young’s modulus and yield stress of the specimens decreased with increasing PBAT content, regardless of the strain rate. However, the effects of mixing ratio on yield stress reduction were found to depend on the strain rate. An increase in temperature and water absorption led to a decrease in the yield stress of the specimens.

## References

- [1] International patent: PCT/JP2008/057589 (2008).
- [2] Nishida M., Ichihara H. and Fukuda N. Evaluation of Dynamic Compressive Properties of PLA/PBAT Polymer Alloys Using Split Hopkinson Pressure Bar Method, Proc. 7th Int. Symp. on Impact Engineering (2010).
- [3] Gray III G.T. Classic Split Hopkinson Pressure Bar Testing, in ASM Handbook Vol 8, Mechanical Testing and Evaluation, ASM. (2000) 462-476.
- [4] Nakai K. and Yokoyama T., Strain Rate Dependence of Compressive Stress-Strain Loops of Several Polymers, J. of Solid Mechanics and Materials Engineering, 2(4) (2008) 557-566.

# CONSTITUTIVE MODEL FOR THERMOPLASTICS – CALIBRATION AND VALIDATION

Arild Holm Clausen<sup>1,2</sup>, Martin Thuve Hovden<sup>2</sup>, Mario Polanco-Loria<sup>1,3</sup>, Torodd Berstad<sup>1,3</sup> and Odd Sture Hopperstad<sup>1,2</sup>

<sup>1</sup> *Structural Impact Laboratory (SIMLab), Norwegian University of Science and Technology (NTNU), NO-7491 Trondheim, Norway*

<sup>2</sup> *Department of Structural Engineering, NTNU, NO-7491 Trondheim, Norway*

<sup>3</sup> *SINTEF Materials and Chemistry, NO-7465 Trondheim, Norway*

**Abstract.** This paper presents an outline of a constitutive model for thermoplastics. It involves a hyperelastic-viscoplastic response due to intermolecular resistance, and an entropic hyperelastic response due to re-orientation of molecular chains. Both parts are developed within a framework for finite strains. The main constituents are the Neo-Hookean model describing large elastic deformations, the pressure-sensitive Raghava yield function, a non-associated visco-plastic flow potential and Anand's stress-stretch relation representing the intramolecular stiffness. The 11 non-zero coefficients of the model are identified from uniaxial tension and compression tests on two materials; HDPE and PVC. Subsequently, it is employed in numerical simulations of three-point bending tests on the same materials. The model gives satisfactory predictions when compared to experimental behaviour.

## 1. INTRODUCTION

This paper presents a hyperelastic-viscoplastic constitutive model for thermoplastics [1]. It is partly based on a model described by Boyce et al. [2], but with some modifications. The idea of separating the response into inter-molecular and intra-molecular contributions, originally proposed by Haward and Thackray [3], is adopted. In our model, the energy-elastic deformation is represented with a Neo-Hookean model. Further, Raghava's pressure-dependent yield function is introduced [4], and a non-associated flow rule is assumed, applying a Raghava-like plastic potential. The entropy-elastic deformation is modelled with Anand's stress-stretch relation [5]. The model involves 11 non-zero coefficients which can be determined from uniaxial tests in tension and compression.

The next section of this paper provides a brief outline of the constitutive model. Thereafter, material tests on a high-density polyethylene (HDPE) and polyvinylchloride (PVC) are reviewed. The results from these tests are used to calibrate the constitutive model. Finally, the model is employed in numerical simulations of a tension test specimen and a three-point bending test. The predictions are compared with experimental results.

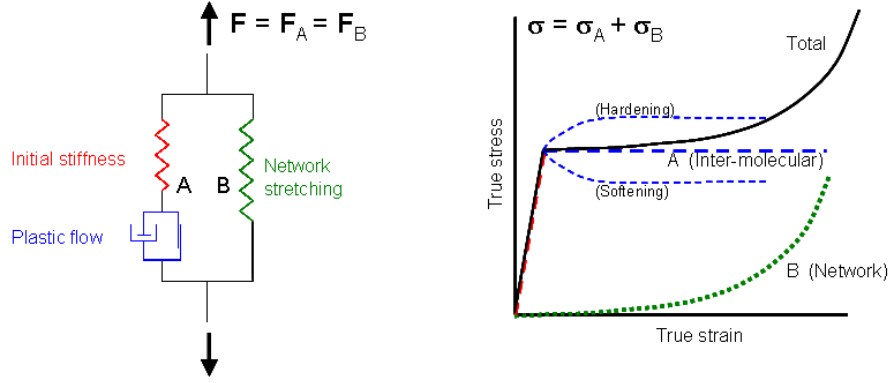
## 2. OUTLINE OF CONSTITUTIVE MODEL

Figure 1 summarises the main constituents of the constitutive model proposed by Polanco-Loria et al. [1]. The material response is assumed to have two resistances A and B, which represent the intermolecular and intramolecular (network) strength, respectively. Parts A and B are kinematically described by the same deformation gradient  $\mathbf{F}$ . The Cauchy stress tensor  $\boldsymbol{\sigma}$  is obtained by summing the contributions of Parts A and B, i.e.  $\boldsymbol{\sigma} = \boldsymbol{\sigma}_A + \boldsymbol{\sigma}_B$ .

The deformation gradient  $\mathbf{F}_A$  is decomposed into elastic and plastic parts, i.e.  $\mathbf{F}_A = \mathbf{F}_A^e \cdot \mathbf{F}_A^p$ . Similarly, the Jacobian  $J_A$  of Part A, representing the volume change, is decomposed as  $J_A = \det \mathbf{F}_A = J_A^e J_A^p = J$ . This decomposition of  $\mathbf{F}_A$  means that the viscoplastic part of the model is formulated on an intermediate configuration  $\bar{\Omega}_A$  defined by  $\mathbf{F}_A^p$  [1]. A compressible Neo-Hookean material is chosen for the elastic part of the deformation, and the Cauchy stress tensor  $\boldsymbol{\sigma}_A$  reads

$$\boldsymbol{\sigma}_A = \frac{1}{J_A^e} \left( \lambda_0 \ln J_A^e \mathbf{I} + \mu_0 [\mathbf{B}_A^e - \mathbf{I}] \right) \quad (1)$$

where  $\lambda_0$  and  $\mu_0$  are the classical Lamé constants of the linearized theory,  $\mathbf{B}_A^e = \mathbf{F}_A^e \cdot (\mathbf{F}_A^e)^T$  is the elastic left Cauchy-Green deformation tensor, and  $\mathbf{I}$  is the second order unit tensor. The coefficients  $\lambda_0$  and  $\mu_0$  may alternatively be expressed as functions of Young's modulus  $E_0$  and Poisson's ratio  $\nu_0$ .



**Figure 1.** Constitutive model with inter-molecular (A) and network (B) contributions.

The yield criterion is assumed in the form

$$f_A = \bar{\sigma}_A - \sigma_T - R(\varepsilon_A^p) = 0 \quad (2)$$

where  $\sigma_T$  is the yield stress in uniaxial tension and  $R(\varepsilon_A^p)$  is a term allowing for hardening or softening. The equivalent stress  $\bar{\sigma}_A$  accounts for the pressure-sensitive behaviour, commonly observed in polymeric materials, and it is defined according to Raghava et al. [4], viz.

$$\bar{\sigma}_A = \frac{(\alpha - 1)I_{1A} + \sqrt{(\alpha - 1)^2 I_{1A}^2 + 12\alpha J_{2A}}}{2\alpha} \quad (3)$$

The material parameter  $\alpha = \sigma_c / \sigma_T \geq 1$  describes the pressure sensitivity, where  $\sigma_c$  is the uniaxial compressive yield strength of the material, and  $I_{1A}$  and  $J_{2A}$  are stress invariants related to respectively the total and the deviatoric Mandel stress tensor  $\bar{\Sigma}_A$  operating on the intermediate configuration  $\bar{\Omega}_A$ . More details, including relations between the different stress measures, are provided by Polanco-Loria et al. [1]. It is noted that the equivalent stress  $\bar{\sigma}_A$  is equal to the von Mises – equivalent stress  $\bar{\sigma} = \sqrt{3J_2}$  when  $\alpha = 1$ , i.e.  $\sigma_c = \sigma_T$ .

The term  $R(\varepsilon_A^p)$  in Equation (2) reads

$$R(\varepsilon_A^p) = (\sigma_s - \sigma_T) \left[ 1 - \exp(-H \varepsilon_A^p) \right] \quad (4)$$

where  $\sigma_s$  is the saturated stress level of Part A, and the decay coefficient  $H$  is used to provide an optimum fit of the stress-strain curve between  $\sigma_T$  and  $\sigma_s$ . Clearly, Equation (4) represents hardening when  $R(\varepsilon_A^p)$  is positive, while softening is obtained by selecting  $\sigma_s < \sigma_T$ .

It turned out that an associated flow rule predicts unrealistic large volumetric plastic strains. In order to control the plastic dilatation, a non-associated flow rule is introduced, applying a Raghava-like plastic potential function

$$g_A = \frac{(\beta-1)I_{1A} + \sqrt{(\beta-1)^2 I_{1A}^2 + 12\beta J_{2A}}}{2\beta} \geq 0 \quad (5)$$

where the material parameter  $\beta \geq 1$  controls the volumetric plastic strain. Isochoric plastic behaviour is obtained in the special case of  $\beta = 1$ .

Finally, the plastic rate-of-deformation tensor is  $\bar{\mathbf{D}}_A^p = \dot{\bar{\boldsymbol{\varepsilon}}}_A^p / \partial \bar{\boldsymbol{\Sigma}}_A$ . The equivalent plastic strain rate  $\dot{\bar{\boldsymbol{\varepsilon}}}_A^p$  is chosen as

$$\dot{\bar{\boldsymbol{\varepsilon}}}_A^p = \begin{cases} 0 & \text{if } f_A \leq 0 \\ \dot{\varepsilon}_{0A} \left\{ \exp \left[ \frac{1}{C} \left( \frac{\bar{\sigma}_A}{\sigma_T + R} - 1 \right) \right] - 1 \right\} & \text{if } f_A > 0 \end{cases} \quad (6)$$

where  $R$  is the hardening term defined in Equation (4). The two coefficients  $C$  and  $\dot{\varepsilon}_{0A}$  are easy to identify from uniaxial strain-rate tests.

The deformation gradient  $\mathbf{F}_B$  of Part B, see Figure 1, represents the network orientation and it is assumed that the network resistance is hyperelastic. Following Anand [5], the Cauchy stress-stretch relation is given as

$$\boldsymbol{\sigma}_B = \frac{1}{J} \left[ \frac{C_R}{3} \frac{\bar{\lambda}_L}{\bar{\lambda}} L^{-1} \left( \frac{\bar{\lambda}}{\bar{\lambda}_L} \right) (\mathbf{B}_B^* - \bar{\lambda}^2 \mathbf{I}) + \kappa (\ln J) \mathbf{I} \right] \quad (7)$$

where the Jacobian  $J = J_B = \det \mathbf{F}$ , and  $L^{-1}$  is the inverse function of the Langevin function defined as  $L(\beta) = \coth \beta - 1/\beta$ . The effective distortional stretch is  $\bar{\lambda} = \sqrt{\text{tr}(\mathbf{B}_B^*)}/3$ , where  $\mathbf{B}_B^* = \mathbf{F}_B^* \cdot (\mathbf{F}_B^*)^T$  is the distortional left Cauchy-Green deformation tensor, and  $\mathbf{F}_B^* = J_B^{-1/3} \mathbf{F}_B$  denotes the distortional part of  $\mathbf{F}_B$ . There are three constitutive parameters describing the intra-molecular resistance:  $C_R$  is the initial elastic modulus of Part B;  $\bar{\lambda}_L$  is the locking stretch; and  $\kappa$  is a bulk modulus. The coefficient  $\kappa$  is fixed to the value 0 in the work presented herein, thereby ensuring that the stress state of Part B is deviatoric. By omitting Part A, however, the remaining Part B with  $\kappa \neq 0$  may be applied for rubber modelling.

The model is implemented as a user-defined model in LS-DYNA [6], so far working for brick elements. A set of numerical verification tests has been carried out [1], showing that the model is able to capture pressure dependency, volumetric plastic strain, strain rate sensitivity, and induced strain anisotropy.

### 3. MATERIAL TESTS

Two thermoplastics were acquired as large extruded plates with thickness 10mm for application in this study: A semi-crystalline high-density polyethylene (HDPE), and an amorphous polyvinylchloride (PVC). The material test coupons as well as specimens for the validation tests were machined from these plates. Material tests on these materials have already been reported by Moura et al. [7]. New tests were now performed, however, to incorporate any possible effects of storage time, and with a different design of test samples.

The material tests were carried out in uniaxial tension and compression. All specimens, see Figure 2, were taken in the extrusion direction. Unlike the previous study [7], there was not machined any imperfection in the gauge part of the tension sample, and cylinder-shaped coupons were applied instead of cubes in the compression tests.

The tests were carried out in a servo-hydraulic testing machine under displacement control. The applied velocity and hence the nominal strain-rate  $\dot{\varepsilon}$  were constant in each test, and the applied rates were  $10^{-3}$ ,

$10^{-2}$  and  $10^{-1} \text{ s}^{-1}$  in both loading modes. In general, two parallel tests were performed in each case, and the scatter between these replicates was small.

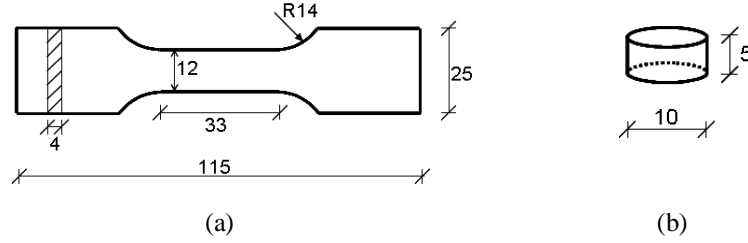


**Figure 2.** (a) Tension test specimen. (b) Compression test specimen.

The acquisition system of the machine provided measurements of the cross-head displacement and force. The capacity of the load cell was 20 kN. Moreover, each test was monitored with a camera taking digital photos for a subsequent determination of the full-field in-plane deformations applying digital image correlation (DIC). This system facilitates the determination of true longitudinal and transverse strains, respectively  $\varepsilon_1$  and  $\varepsilon_2$ , at the surface of the coupon facing the camera. Moura et al. [7] provide a more thorough description of the processing of the photos.

As shown by Hovden [8] and also by Moura et al. [7], the transverse deformation of both materials is close to isotropic, i.e.  $\varepsilon_2 = \varepsilon_3$ . The true stress in the tension samples can therefore be calculated from

$$\sigma = \frac{F}{A} = \frac{F}{w_0 \exp(\varepsilon_2) \cdot t_0 \exp(\varepsilon_3)} = \frac{F}{A_0 \cdot \exp(2\varepsilon_2)} \quad (8)$$

where  $F$  is the force measured during the test, and  $A_0 = w_0 t_0$  is the initial cross-section area of the sample. A digital sliding calliper provided the exact measures of  $w_0$  and  $t_0$  for each specimen. The true stress was calculated in the section experiencing the initial localization.

The DIC software was not applied in the compression tests. Similar to the tension specimens, the initial height  $h_0$  and diameter  $d_0$  were measured prior to each test. Assuming homogeneous deformation over the length of the sample, the longitudinal strain was found from the relation  $\varepsilon_1 = \ln(h/h_0) = \ln(1 - \Delta h/h_0)$ , where  $\Delta h$  is the shortening as measured by the servo-hydraulic machine. The digital pictures were employed in the determination of the transverse deformation, as they provided a measure of the diameter increase  $\Delta d$  during the test. The transverse strain  $\varepsilon_2$  is thus  $\varepsilon_2 = \ln(d/d_0) = \ln(1 + \Delta d/d_0)$ . The current diameter  $d$  turned out to be the same over the height of the sample until  $\varepsilon_1 \approx 0.5$ , implying that rather large deformations were possible before any barrelling effect was present [8]. The last equality of Equation (8) was used for calculation of the true stress in the compression tests as well, setting  $A_0 = (\pi/4)d_0^2$ .

Representative stress-strain curves obtained at different nominal strain-rates in tension are shown in Figure 3, while compression data are presented in Figure 4. A significant strain-rate effect is present for both materials and loading modes. PVC experiences also a softening effect after yielding. Both materials are to some degree pressure dependent. PVC has higher yield strength in compression than in tension. The situation for HDPE is slightly more complicated. Without any local maximum point neither for the nominal nor the true stress-strain curves, the yield stress is conveniently determined from the classical Considère construction. It turns out that the yield stress is almost identical in tension and compression for HDPE. On the other hand, the evolution of hardening between true strains of 0.1 and 0.5 differs. Although not shown here, the full-field strain measurements also revealed that the deformation of HDPE is rather isochoric (volume preserving), while PVC dilates (volume increases) in tension [8].

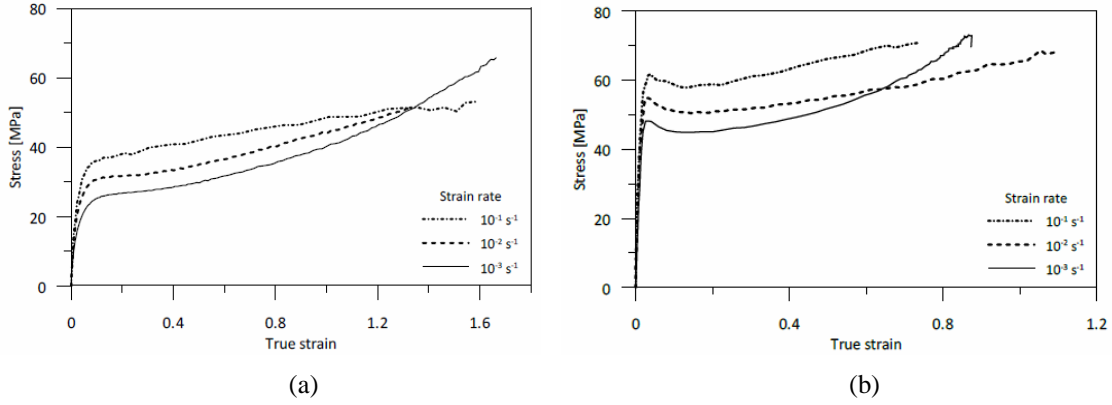


**Figure 3.** True stress-strain curves in tension [8]. (a) HDPE. (b) PVC.

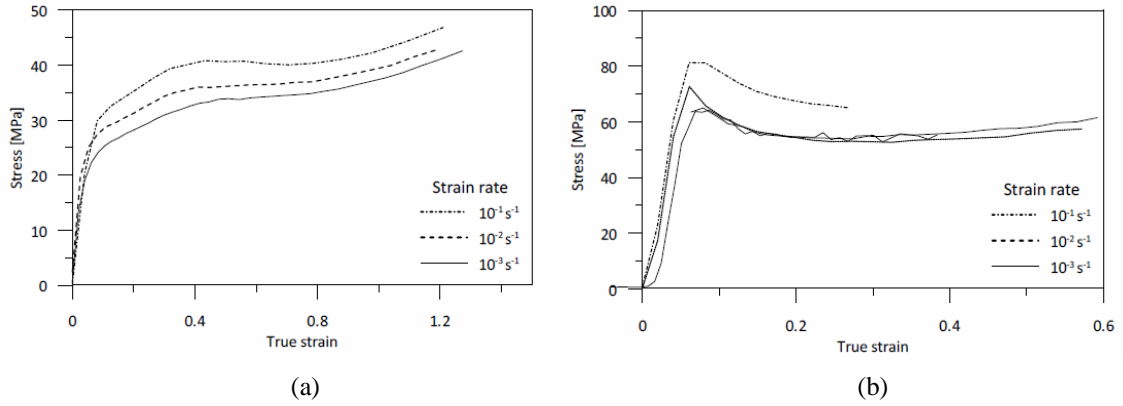


**Figure 4.** True stress-strain curves in compression [8]. (a) HDPE. (b) PVC.

#### 4. CALIBRATION OF CONSTITUTIVE MODEL

The constitutive model depicted in Figure 1 involves 11 non-zero coefficients.

- Spring A: Two elastic coefficients  $E_0$  (Young's modulus) and  $\nu_0$  (Poisson's ratio).
- Friction element A: The yield criterion applies the yield stress in tension  $\sigma_T$ , the ratio  $\alpha = \sigma_C / \sigma_T$ , and the hardening/softening parameters  $\sigma_s$  and  $H$ . Moreover, the coefficient  $\beta$  is employed to control the plastic dilatation.
- Dashpot A: Two strain-rate sensitivity parameters  $C$  and  $\dot{\epsilon}_{0A}$ .
- Spring B: Two coefficients  $C_R$  (initial elastic modulus) and  $\bar{\lambda}_L$  (locking stretch).

Details on the calibration procedure are provided by Hovden [8], and only a brief survey is given here. The measurements of transverse and longitudinal strains in tension give the parameters  $\nu_0$  and  $\beta$ . Further, one of the tension tests at the lowest strain-rate ( $10^{-3} \text{ s}^{-1}$ ) serves as the baseline case, wherefrom most of the remaining coefficients are identified. The local strain rate at yielding is taken as  $\dot{\epsilon}_{0A}$ . The shape of the true stress-strain curve determines whether the hardening (HDPE) or softening (PVC) option of Equation (4) is to be adopted. Next, a plot of yield stresses in tension as function of the logarithm of strain-rate determines  $C$ . To obtain an optimum curve fit, the physical yield stress is assigned to  $\sigma_T$  for PVC, and to  $\sigma_s$  for HDPE, and the values of these coefficients are found from the plot by extrapolation of the linear regression curve to zero strain-rate. Thereafter  $E_0$  and  $H$  are determined together with the remaining coefficients  $\sigma_T$  and  $\sigma_s$ . The Part B parameters  $C_R$  and  $\bar{\lambda}_L$  require some calculation efforts. Part A as defined by the coefficients identified so far is subtracted from the baseline stress-strain curve,

yet also recognizing that Part B does not represent any uniaxial rather a deviatoric stress state. Finally,  $\alpha$  is the ratio between the yield stress in compression and tension. All parameters are gathered in Table 1.

**Table 1.** Coefficients for HDPE and PVC [8].

	$E_0$ (MPa)	$\nu_0$	$\sigma_T$ (MPa)	$\sigma_s$ (MPa)	$H$	$\alpha$	$\beta$	$\dot{\epsilon}_{0A}$ (s <sup>-1</sup> )	$C$	$C_R$ (MPa)	$\bar{\lambda}_L$
HDPE	800	0.40	13.0	23.9	39.6	1.00	1.04	.0007	0.108	1.74	7.75
PVC	3000	0.30	46.8	37.8	15.0	1.30	1.27	.001	0.070	5.50	1.92

## 5. VALIDATION OF CONSTITUTIVE MODEL

As a first step in the validation process, the tension test sample was modelled in LS-DYNA, applying 1084 eight-node brick elements [8] and the coefficients of Table 1. Considering the baseline test at strain rate  $10^{-3} \text{ s}^{-1}$ , Figure 5 shows comparisons between the force-displacement curves found from the tests and with LS-DYNA. Applying the digital pictures, the displacement was determined by considering how the distance between two defined points evolved during the test. Thus, these points served as an optical extensometer. The same points were selected in the numerical simulations. The agreement in Figure 5 is excellent, and, although not shown here, the model predicts also the necking of the sample in an adequate way.

Formally, a validation should apply other tests than those involved in the calibration, yet it is important for the subsequent numerical modelling that the validation tests are well-defined. Three-point bending tests are suitable for this purpose. The experimental set-up is shown in Figure 6. The rollers ensure that no bending moments are transferred to the supports. Four different plate thicknesses  $t = \{4\text{mm}, 6\text{mm}, 8\text{mm}, 10\text{mm}\}$  and two punch nose radii  $R = \{3\text{mm}, 6\text{mm}\}$  were applied. The bending tests were carried out in the same machine as was used in the material tests, and the cross-head velocity was 0.1 mm/s in all tests. Some of the tests with plate thickness 8mm and 10mm were painted with a speckled pattern and instrumented with a digital camera, facilitating determination of the strain field at the surface by means of DIC.

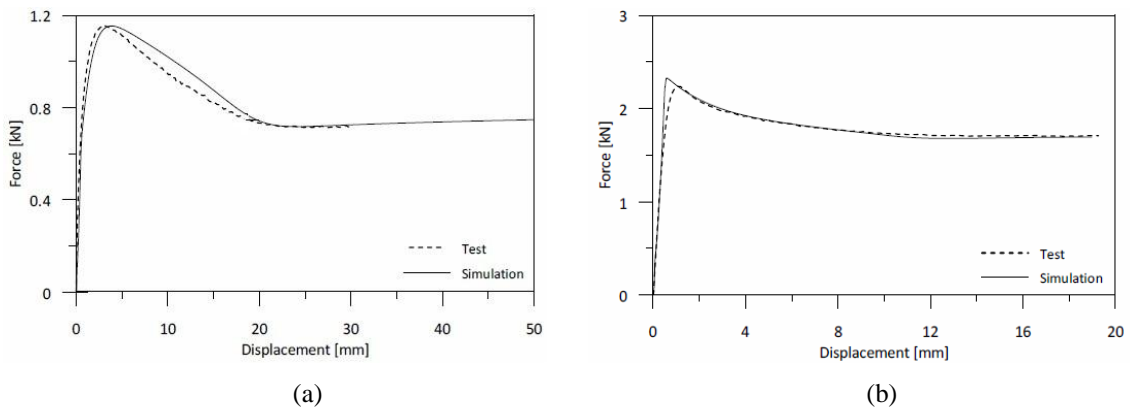


**Figure 5.** Force-displacement curves in tension at  $10^{-3} \text{ s}^{-1}$ . Comparison of laboratory tests and numerical simulations [8]. (a) HDPE. (b) PVC.

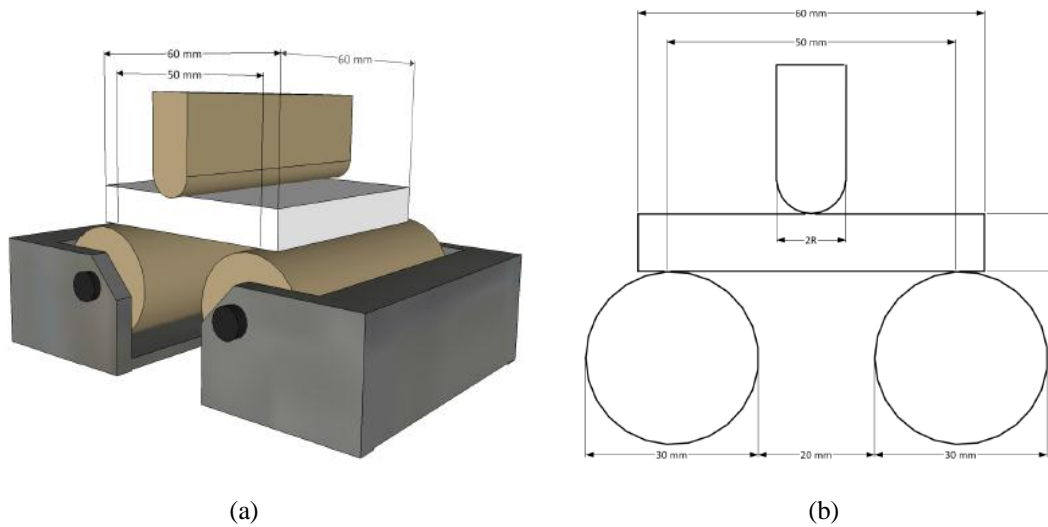
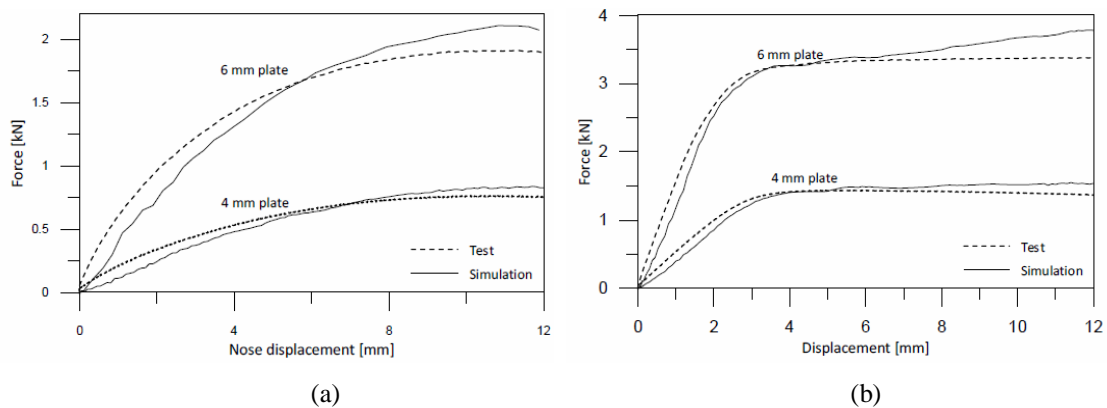


**Figure 6.** Set-up for three-point bending tests [8]. (a) 3D sketch. (b) Drawing with dimensions.

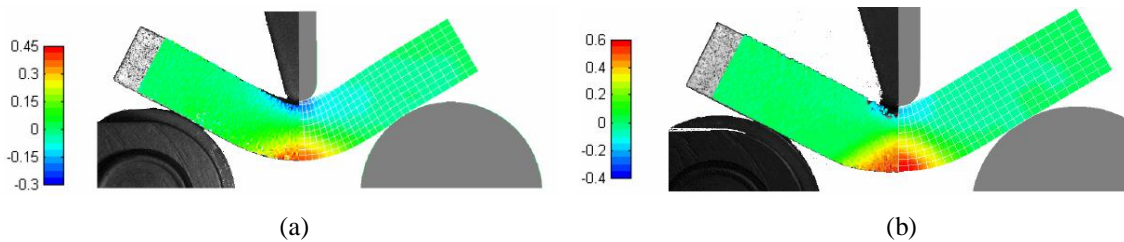
Utilising the two symmetry planes,  $\frac{1}{4}$  of the plate was modelled with brick elements in LS-DYNA, applying 9 elements over the thickness and 25 elements in each of the in-plane directions. The coefficient of friction between the plate and steel parts was set to 0.1. Increasing the coefficient to 0.2 or lowering it to 0.01 did not give any significant difference in the results.

Figure 7 shows a comparison between the force-displacement curves found in the experiments and the numerical simulations for a nose radius of  $R = 3\text{ mm}$ . The thinnest plates, having thickness 4 mm and 6 mm, are addressed in this figure. The agreement is satisfactory, although some discrepancy is present at large deformations. The constitutive model assumes that the stress-strain curves have the same shape in both loading modes and at all strain-rates. It appears from Figures 3 and 4 that this is not the case. In particular, the hardening effect at compression strains between 0.1 and 0.5 is not captured by the model. Another shortcoming of the model is the choice of plastic potential, see Equation (5). The Raghava function predicts dilation at all pressure states except for the special case of  $\beta = 1$ , where the plastic deformation is incompressible. On the other hand, experimental evidence shows a contraction effect for PVC in plastic compression, while HDPE behaves close to isochoric, i.e. no change of volume.

Finally, Figure 8 compares the longitudinal normal strains in the tests and simulations, now addressing a 10 mm thick specimen with DIC instrumentation. Again, the agreement is acceptable. Figure 8 indicates that the tension strains have a larger absolute value than the compression strains, and a more closely look at the data reveals that 75% of the middle section is in tension.



**Figure 7.** Force-displacement curves from bending tests with  $R = 3\text{ mm}$  [8]. (a) HDPE. (b) PVC.



**Figure 8.** Strain field from DIC measurements (left-hand part) and simulations (right-hand part) at 10mm deformation. Nose radius  $R = 3\text{mm}$  and plate thickness 10mm [8]. (a) HDPE. (b) PVC.

The choice of the Raghava-like plastic potential is not the optimal one for all materials and loading situations. Therefore, it is likely that the model will be improved by introducing another potential. As PVC and also some PP materials experience a significant void growth process during plastic deformation in tension, see Delhaye et al. [9], an option might be to employ a potential which is function of the damage in the material. Yet, the capabilities of the present version of the model at biaxial stress states are further explored by Ognedal et al. [10]

## 6. CONCLUSION

This paper outlined a new hyperelastic-viscoplastic constitutive model for thermoplastics. The model consists of two fractions sharing the same deformation gradient, and accounting in turn for the intermolecular resistance by pressure-dependent, non-associated hyperelastic-viscoplasticity, and the network resistance by hyperelasticity for compressible rubber-like materials. The constitutive relation is implemented as a user-defined model in LS-DYNA, currently working for brick elements.

The 11 non-zero parameters of the proposed model were determined for two materials, HDPE and PVC, applying data from uniaxial tension and compression tests at different strain rates. The experimental set-up included a digital camera, facilitating the determination of true stress-strain curves. Both materials exhibit significant strain-rate sensitivity. PVC has also a strong pressure-dependent response.

The calibrated model was employed in numerical simulations of a tension test coupon and three-point bending tests. The force-displacement curve and the strain field as found in the experimental test were rather well captured in the simulations.

## REFERENCES

- [1] Polanco-Loria M, Clausen AH, Berstad T and Hopperstad OS, Constitutive model for thermo-plastics with structural applications, *International Journal of Impact Engineering* **37** (2010) 1207-1219.
- [2] Boyce MC, Socrate C and Llana PG, Constitutive model for the finite deformation stress-strain behavior of poly(ethylene terephthalate) above the glass transition, *Polymer* **41** (2000) 2183-2201.
- [3] Haward RN and Thackray G, The use of a mathematical model to describe isothermal stress-strain curves in glassy thermoplastics, *Proceedings of the Royal Society of London Series A (Mathematical and Physical Sciences)* **302** (1968) 453-472.
- [4] Raghava R, Caddell RM and Yeh GSY, The macroscopic yield behaviour of polymers, *Journal of Materials Science* **8** (1973) 225-232.
- [5] Anand L, A constitutive model for compressible elastomeric solids, *Computational Mechanics* **18** (1996) 339-355.
- [6] Livermore Software Technology Corporation, LS-DYNA Keyword User's Manual. Version 971 (2007).
- [7] Moura RT, Clausen AH, Fagerholt E, Alves M and Langseth M, Impact on PEHD and PVC plates – Experimental tests and numerical simulations, *International Journal of Impact Engineering* **37** (2010) 580-598.
- [8] Hovden MT, Tests and numerical simulations of polymer components, MSc thesis, Dept. of Structural Engineering, NTNU (2010).
- [9] Delhaye V, Clausen AH, Hopperstad OS, Moussy F, Othman R, Nesa D, Behaviour and modelling of a rubber-modified polypropylene, *19<sup>th</sup> DYMAT Technical Meeting*, Strasbourg, France (2010).
- [10] Ognedal AS, Clausen AH, Hopperstad OS, Polanco-Loria M, Benallal A, Raka B, Biaxial tension of PVC and HDPE, *19<sup>th</sup> DYMAT Technical Meeting*, Strasbourg, France (2010).

- > Final printed area will be of 15 cm x 23 cm. The proceedings will be made of A4 colour prints.
- > Publication limited to 8 pages.
- > Submit 2 electronic files, a .doc file and a .pdf file, along with the copyright agreement form, p. 3 of this file, by July 18, 2008 to : 18dymat@nexter-group.fr

## Numerical approach for modelling and simulating ballistic impact onto 3D dry fabric – Meso-macro models hybrid method

K. THORAL-PIERRE<sup>1</sup> and B. LANGRAND<sup>2</sup>

<sup>1</sup> CEDREM, Ecoparc, Domaine de Villemorant, 41210 Neung sur Beuvron, France

<sup>2</sup> ONERA, Centre de Lille, Lille, France

**Abstract.** The paper aims at developing numerical methods to model/optimize ballistic impact onto bullet proof vest. The multi-scale nature of the structural problem prevents the use of complex detailed FE models (refined mesh) to analyse the resistance of dry weave 2D or 3D. A method based on multi-scale/multi-level approach is developed to simulate huge and complete structure with standard computers. The proposed approach to address this issue is based on: (1) a meso-scale model in the impact area to study the damage of the dry textile and the penetration of the impactor; and (2) a macro-scale model outside the impact area to simulate the mechanical behaviour of the dry textile. The meso-scale is related to the characteristic length of the multifilament yarn and the textile architecture; and the macro-scale is related to the characteristic length of the structure subjected to the impact. Another aspect of the problem deals with the communication or the data transfers (hybrid theory) between both meso-scale and macro-scale models. The meso-scale model simulates the dry textile behaviour in the local impact area using a detailed FE mesh of the complex architecture of the fabric. A specific tool developed in the hypermesh software to generate/produce meso scale finite element models of textiles is first presented. Several models of textiles structures including geometry and meshing are described in this study. Yarns modelled using thick shell or solid FE are developed to simulate damage surrounding the impactor contact area and during ballistic impact. Based on a literature review, relevant material models and failure criteria are implemented within the explicit FE code to deal the mechanical behaviour and the rupture of the multifilament yarn. It is also proposed to investigate the influence of contact friction properties between the yarns and/or between the textile and the impactor (supposed to be rigid). The macro-scale model will allow determining the parameters of a homogeneous material model based on the architecture of the dry textile. The homogenous model is developed for the part of the structure far enough of the local impact. It is supposed that the homogenous media is only subjected to elastic transformation. (Non linear transformations are addressed by the meso-scale models.) The mechanical behaviour of the homogeneous media is supposed to be elastic and the influence of the strain rate on the material behaviour is omitted for the same reason. The originality and the interest of the proposed approach are to take in the homogeneous model the influence of the contact and the friction between the yarns into account. In such problem, contact and friction have both a real influence of the stiffness of the material. It is then proposed to study how to establish the connection between both the local meso-scale FE model and the macro-scale FE model. Different types of connections between two corresponding meshes maybe indeed defined using specific interfaces.

### 1. INTRODUCTION

The aims of this paper are to study personal armour protective systems face to ballistic impact. The multi-scale nature of the structural problem prevents the use of complex detailed FE models (refined mesh) to analyse the resistance of soft individual protections. The approach proposed is based on: (1) a meso-scale model in the impact area to study the damage of the dry textile and the penetration of the bullet; and (2) a macro-scale model outside the impact area to simulate the mechanical behaviour of the dry textile. The meso-scale is related to the characteristic length of the multifilament yarn and the textile architecture; and the macro-scale is related to the characteristic length of the structure subjected to the ballistic impact. Another aspect of the problem deals with the communication or the data transfers (hybrid theory) between both meso-scale and macro-scale models. The method proposed to simulate ballistic impacts onto soft individual protection.

In the first section, the influence of several parameters on the ballistic impact onto composites materials is discussed based on a literature review. The second part of the work aims at presenting the numerical approach developed to simulate ballistic impacts based on meso-scale FE models. The last part presents the homogeneous method developed to characterise mechanical properties of fabrics to be used in the macro-scale model. Both methods (meso and homogeneous) are illustrated with applications and the influence of numerical parameters (friction, material data) are analysed.

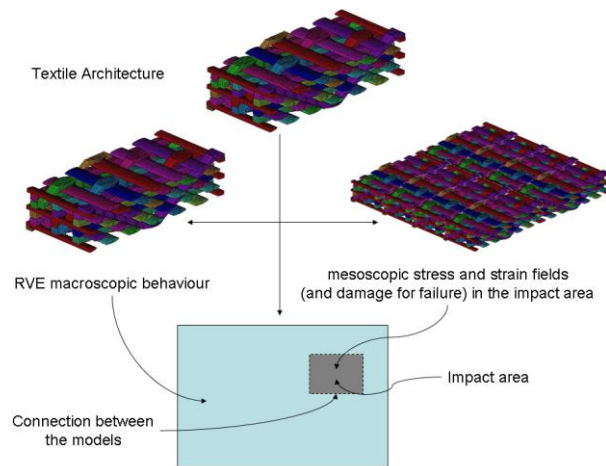


**Figure 1: Mesoscopic and macroscopic approach proposed to simulate ballistic impact onto dry textile**

## 2. Literature review

Cheeseman and Bogetti have studied the influence of several parameters on the ballistic impact onto composites materials. Among them, the following parameters were found to have an influence in term of penetrating ability of the bullet into the structure:

- the material properties of the fabric,
- the architecture of the textile,
- the projectile geometry,
- the impact displacement rate,
- the boundary conditions applied to the protective system, and
- the friction properties between both the bullet and the composite ; and the yarns.

Mechanical properties may be found in the open literature for fibres made of Aramid Twaron (i.e., CT709, K129), Zylon, Kevlar KM2, carbon T300 and glass. Many authors have produced data for 2D balanced fabrics considering different fibre dimensions and surfacic density. Some results concern the influence of three-dimensional braided composites under ballistic penetration using finite element modelling.

Many type of bullets are also found (spherical, STANAG, etc.). Other studies deal with the perforation of plain weave fabric by projectiles having a flat, hemispherical, ogival and conical head. The geometry of a projectile influences its ability to perforate a fabric. Montgomery investigated different projectile geometries on the ballistic performance of one, two and three layers of Kevlar 49. It is found that pointed bullets had the ability to wedge through fabric and were not decelerated as quickly as blunt bullets. Similar results have been reported by Bazhenov. Recently Tan has studied the perforation of a single ply of Twaron CT 716 plain weave fabric by projectiles having a flat, hemispherical, ogival and conical head. He found fabric creasing and perforation mechanisms highly dependent on the shape of the projectile. The conical and ogival projectiles perforated the fabric with least amount of yarn pull-out, indicating these projectiles were able to slip through the weave.

The impact velocity of a projectile will affect the performance of fabrics and compliant laminates. Most of results are given for impact velocities from 200m/s to 800m/s. With low-impact velocities, the yarns do not fail during the initial stress rise; therefore, the transverse deflection of the fabric has time to propagate to the edges of the panel, which allows the fabric to absorb more energy. With a high-velocity impact, the damage is localized and the yarns fail before significant transverse deflection can develop. A great number of experiments have been performed impacting multiple plies of ballistic textiles. When testing fabric or compliant armor systems for ballistic impact, the size of the specimen and the means of fixturing (far-field boundary conditions) it during the impact event is important.

Friction has been shown to play a role, both directly and indirectly, on the impact performance of textiles. Yarn pull-out may be directly responsible for absorbing energy during a non-perforating impact event. However, friction between the projectile and the yarns and the yarns themselves may also be responsible for how much energy is absorbed during an impact event.

### 3. MESO-SCALE MODEL

#### Model Description

This section deals with the FE modelling of the dry textile to simulate the projectile penetration and the fabric rupture in the impact area using a detailed FE model (local or meso-scale) based on the architecture of the fabric. Based on a literature review, relevant material models and failure criterion will be implemented in an explicit FE code to represent the mechanical behaviour and the rupture of the multifilament yarn (e.g., Figure 2). The model parameters will be identified using available data found in the open literature or experimental data produced within the EPIDARM project. It is also proposed to investigate the influence of contact friction between the yarns and/or between the textile and the bullet. The bullet is supposed to be rigid.

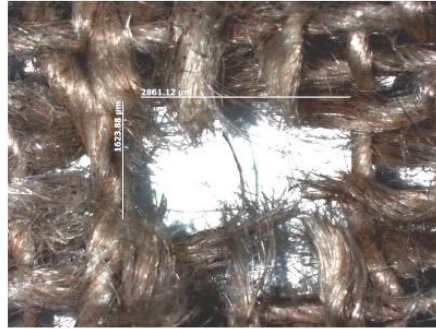


**Figure 2 : Failure of the first layers of flax fabrics by shearing (“ EPIDARM” program)**

A commercially available explicit nonlinear FEA code, Radioss, is used to model the ballistic impact of a projectile onto a fabric. The mesh of the fabric is developed using Hypermesh software. Figure 3 presents an example of FE meshes developed for the fabric. In the case of FE model made of shell elements, each yarn is split into several sets of elements having different thicknesses. The interest of the FE presented in Figure 3 is that the direction 1 of each element local frame matches to the yarn direction. Different material properties may be considered for the warp and weft yarns in the fabric.

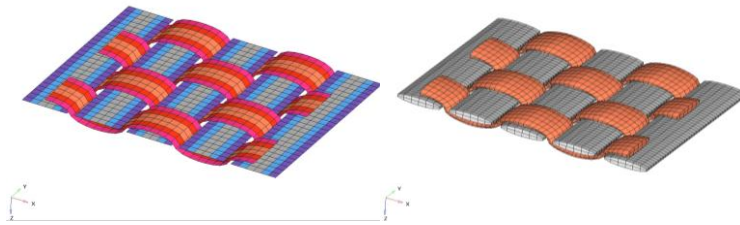


**Figure 3 - Example of plain weave meshes (left: shell elements; right: solid elements)**

The projectile is modelled using solid finite elements. More simple projectiles, such spherical bullet or fragment simulator projectile (FSP), can be modelled using analytical surface (no mesh). In that case, the mechanical behaviour of the projectile is rigid.

In the study, the material behaviour of the yarns of the fabric is assumed orthotropic elastic. A material is orthotropic if its behaviour is symmetrical with respect to two orthogonal plans. More complex material behaviour (e.g., non-linear, damage, strain rate effects) may be introduced in the model if material data are available.

**Table 1.** Material properties (orthotropic elasticity) considered in FE simulations (aramid Twaron CT709).

$\rho$ g/mm <sup>3</sup>	$E_{11}$ MPa	$E_{22}$ MPa	$E_{33}$ MPa	$G_{12}$ MPa
0.00144	100000	200	300	100
$G_{23}$ MPa	$G_{31}$ MPa	$\nu_{12}$ -	$\nu_{23}$ -	$\nu_{31}$ -
200	200	0.05	0.3	0.05

Material failure may be considered in the FE impact simulations. Failure model considered in the impact simulations for fabrics is based on Hashin's theory. This theory enables to describe the complete loss of load carrying capacity of the material. Four different modes of failure are taken into account in the model: fibre rupture in tension and shear, fibre rupture in compression and crush, matrix rupture in shear and When a failure criterion is reached, the stresses are decreased by using an exponential function to avoid numerical instabilities. A relaxation technique by decreasing the stress gradually is used. This failure criterion is available for both shell and solid element used in this study. It is supposed that the yarns of the fabrics fail only in fibre tension mode.

Many solutions are implemented in the FE code Radioss to model friction between shell and/or solid elements. The most complexes need specific tests to identify friction properties. The Coulomb friction model will be implemented in the contact interface used in this study. This model enables to vary the normal/tangential loading ratio depending on a single parameter. The friction property will be taken from the open literature.

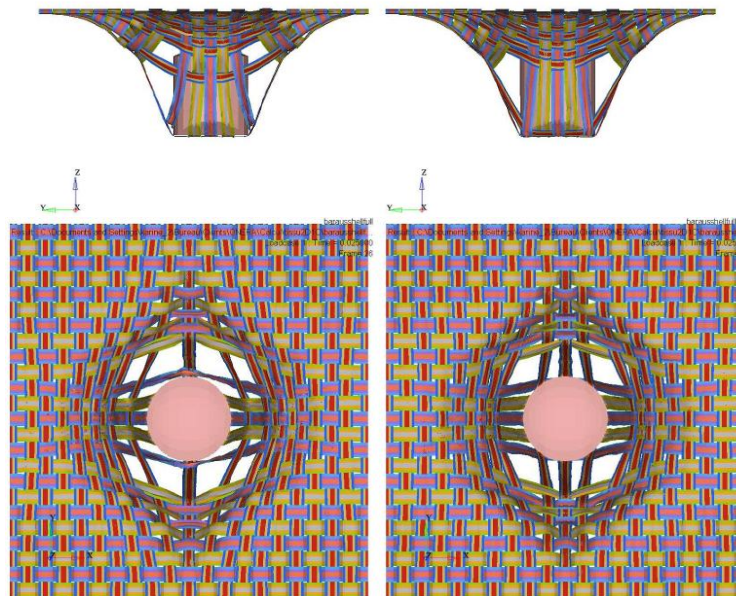
A contact interface is implemented between the yarns themselves and between the fabric and the projectile. The contact interface avoids interpenetrations using penalty method. A node to surface and edge to edge interface type is selected for both contacts implemented in the FE model. The initial interface gap is computed by the solver (e.g., average thickness in the case of shell contacts).

#### **Application : 1 layer of plain weave fabric**

The FE modelling technique presented in previous sub-sections are applied to a single layer of 2D fabric (1 ply Plain Weave). The geometrical characteristics of the fabric are taken from a paper from Barauska and Abraitiene. The dimension of the fabric is about 25mm×25mm. The material properties have been previously presented (Tables 1). The fabric is modelled using shell element.

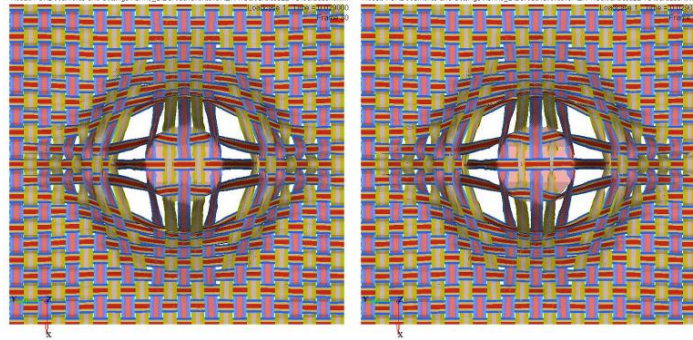
In the computations friction parameter was set to 0 (no tangential loads with respect to normal pressure), in the following ones it is now set to 0.2.

Figure 4 compares the deformed shape of the fabric for both configurations for friction (model of a yarn composed of shell elements). Friction parameter has a weak influence on the deep of penetration. Without friction the deep of penetration increases a little. More yarns remain in contact with the projectile when friction parameter defers from 0 because the transverse displacements slow down. The more the number of yarns in contact with the projectile, the more the projectile displacement rate is reduced. The dimension of the crater is a little influenced by friction.



**Figure 3: Influence of friction properties in the contact interface (left:  $f=0$ ; right:  $f=0.2$ )**

The failure properties considered in the impact computation will have a real influence on the perforation of the fabric. The failure properties will be calibrated when experimental data will be available. It has been already assessed that taking failure into account does not induced additional numerical problems due to the element elimination. An example of such computation is given in Figure 4.



**Figure 4: Influence of failure properties (left:  $\sigma_1^t = 3600 \text{ MPa}$  ; right:  $\sigma_1^t = 3000 \text{ MPa}$  )**

#### 4. MACRO-SCALE MODEL

This section deals with a homogeneous method to analyse the parameters of macro-scale material model. The homogenous model is for the part of the structure far enough of the local impact (the impact problem is modelled using the meso-scale approach). The homogeneous model is based on a RVE of the architecture of the dry textile (that is taken from the previous meso-scale FE model). In this study, the mechanical behaviour of the homogeneous media is supposed to be elastic. (The material non-linear and damage behaviour are addressed by the meso-scale model in the impact area.) In the macro-scale approach, it is supposed that the influence of the strain rate on the material behaviour is negligible for the same reason. The originality and the interest of the proposed approach are to take in the homogeneous model the influence of the contact and the friction between the yarns into account. Other parameters are studied by the method, such the influence of the twist applied onto the yarn.

##### Homogenisation method

Homogenisation is the basic method to obtain from the numerical treatment of the so-called Representative Volume Element (RVE), both the homogenised responses to any macroscopic loading and the corresponding local fields. Under an homogenised macroscopic loading, for a known and period structure, the method can be considered as exact provided the solution is obtained with a sufficient fine discretisation (in time and space). Using homogenisation techniques the average elastic material properties of an RVE can be determined. This technique uses the so-called average operator  $\langle \cdot \rangle$  to calculate the average quantity  $\langle T \rangle$  of a tensor field  $T(x)$  in a certain volume  $\Omega$ . The expression of average stress and strain tensor fields is given by relations (1).

$$\Sigma = \langle \sigma \rangle = \frac{1}{V_\Omega} \int_{V_\Omega} \sigma(x) dV_\Omega \quad \text{and} \quad E = \langle \varepsilon \rangle = \frac{1}{V_\Omega} \int_{V_\Omega} \varepsilon(x) dV_\Omega \quad (1)$$

with  $V_\Omega$  the RVE overall volume

Periodic homogenisation based analysis can be realised using finite element technique. The RVE is subdivided into several local sub-volumes,  $r$ , such that each consists of a mono-phase material (stress and strain fields are assumed to be uniform in each sub-volume). Using FE environment each finite element is considered as a sub-volume of the RVE. The FE computation of the RVE enables to solve the local stress and strain fields in each sub-volume  $r$  and at several loading increments  $t$ :  $\sigma_{ij}(r,t)$  and  $\varepsilon_{ij}(r,t)$ . The integrals in equation (10) are then approximated within the FE environment by numerical Gaussian integration; the average quantities being expressed by relations (2).

$$\Sigma = \langle \sigma \rangle = \sum_r c_r \sigma(r) \quad \text{and} \quad E = \langle \varepsilon \rangle = \sum_r c_r \varepsilon(r) \quad \text{with} \quad c_r = \frac{V_r}{V_\Omega} \quad (2)$$

with  $c_r$  the volume fraction of sub-volume  $r$  and  $V_r$  the volume of sub-volume  $r$ .

By varying the macroscopic loading direction applied on the boundaries of the RVE (Figure 5), a set of macroscopic stress and strain responses are obtained to analyse a macro-scale material model. Periodical conditions are considered in addition to each elementary load applied at the boundary of the RVE. If  $S_n^+$

and  $S_n^-$  are two surfaces with normal  $\vec{n}^+$  and  $\vec{n}^-$ , and if  $M^+$  and  $M^-$  are two opposite points of  $S_n^+$  and  $S_n^-$  (Figure 22), then  $S_n^+$  and  $S_n^-$  are linked by periodical conditions given by relation (3).

$$u_i(M^+) = u_i(M^-) \quad (3)$$

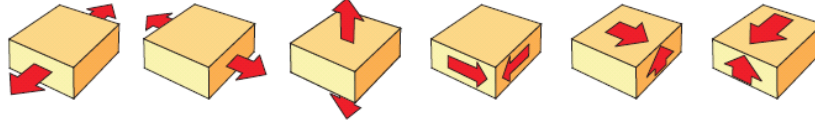


Figure 5 : load cases to compute homogenise properties of an RVE

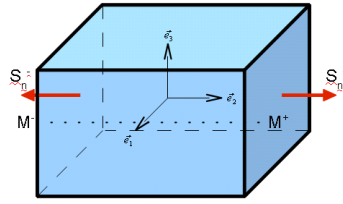


Figure 6 : Periodical conditions applied at the boundary of the RVE

Using the FE environment, the loading is modelled with imposed displacement time history noted  $\tilde{u}_i(t)$ . If the loading is applied in direction  $\vec{e}_i$  to surfaces with normal  $\vec{i}^+$  ( $+\tilde{u}_i(t)$ ) and  $\vec{i}^-$  ( $-\tilde{u}_i(t)$ ), then the macro-strain corresponds to an elongation following direction  $\vec{e}_i$  ( $E_{ii}$  or  $E_i$ ). For surfaces  $S_i^+$  and  $S_i^-$ , the periodical conditions are expressed then such as:  $u_j(M^+) = u_j(M^-)$  with  $j \neq i$  (Figure 23). If the loading is applied in  $\vec{e}_j$  to surfaces with normal  $\vec{i}^+$  ( $+\tilde{u}_j(t)$ ) and  $\vec{i}^-$  ( $-\tilde{u}_j(t)$ ), then the macro-strain corresponds to a shear ( $E_{ij}$ ) state in the surface ( $\vec{e}_i$ ,  $\vec{e}_j$ ). For surfaces  $S_i^+$  and  $S_i^-$ , the periodical conditions are expressed then such as:  $u_k(M^+) = u_k(M^-)$  with  $k \neq j$  (Figure 23). The macro-strain  $E_{ij}$  is then given by relation (4).

$$E = \frac{1}{2} \left( (\nabla \tilde{u})^t + \nabla \tilde{u} \right) \quad (4)$$

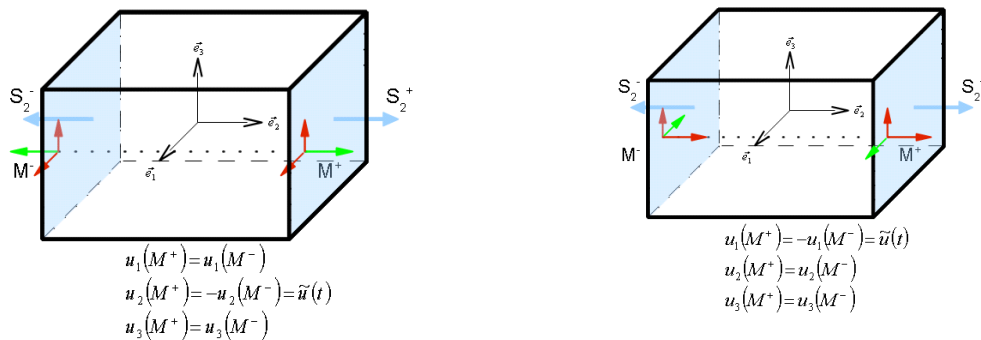


Figure 7 - Loading and periodical conditions: left elongation; right: shear

The FE problem is solved for each increment of loading, given the local stress field  $\sigma_{ij}(r, t)$ . Then, the macroscopic stress  $\Sigma_{ij}$  is analysed applying relation (2). Finally, this numerical procedure makes it possible to establish a relation between macro-strains and macro-stresses. In the proposed approach, the influence of material constants of the sub-volumes that composed the RVE and of contact friction

parameters between the yarns is studied regarding the macroscopic fields relation. (Local stress and strain fields will be influenced by material constants of the sub-volumes that composed the RVE and by contact friction parameters between the yarns.) The influence of the twist that has been observed during the experiments performed by Onéra, will be modelled in the homogenised model by varying the elastic constants of the yarns.

In the following applications, the material behaviour of the yarns is orthotropic elastic (the constitutive model has been already presented in section 3) with the material constants given in Table 1. The contact between the yarns is controlled using the same previous interface types with the same friction law.

### 5 Connection between the local meso-scale FE model and the macro-scale FE

The perspective in the study deals with the development of a numerical hybrid method to establish the connection between the local meso-scale FE model and the macro-scale FE model. Different types of connections between two corresponding meshes may be defined using specific interfaces. The type of interface will depend on the type of elements to connect. For example, Such Dual method may be used to link shell element meshes (Figure 35) by means of Lagrange multipliers. The meshes may be compatible or incompatible and the interfaces may be open or closed. Based on the type of element chosen for both the macroscopic and mesoscopic models, specific interface will be tested.



Figure 8 : of shell to shell connection (left) and articial skin (right)

It is also possible to compute contact between domains by using the rad2rad (Radioss numerical tool) connection. This approach is based on the “artificial skin” method. The part of the slave domain concerned by the contact must be duplicated in the master domain with a void material having the same density and young modulus. That’s what we will call artificial skin. The contact is then treated normally by RADIOSS inside the master domain and a node to node connection is applied between the nodes of the artificial skin and the corresponding nodes or the slave domain.

Data transfers are mass and nodal stiffness are transferred by rad2rad from the slave domain to the artificial skin. Therefore modifications of mass and nodal time step may be observed in the master domain at the beginning of the computation. If kinematic constrains are applied on the part of the slave domain that is duplicated in the master domain, they must be duplicated as well.

### 6 Conclusion

The multi-scale method to model ballistic impact onto fabric is presented in this report. The approach proposed in the project to address this issue is based on: (1) a meso-scale model in the impact area to study the damage of the dry textile and the penetration of the bullet; and (2) a macro-scale model outside the impact area to simulate the mechanical behaviour of the dry textile.

In the method developed for the meso-scale model, layers are meshed using yarns of shell or solid finite elements. The material behaviour is supposed orthotropic elastic. Failure properties may be taken into account. Failure model considered in the impact simulations for fabrics is based on Hashin’s theory. It’s assumed that failure was mainly triggered by an ultimate tensile stress. A FE model is also developed for a fragment simulator projectile. Other more simple projectile (e.g., spherical) may be also modelled using analytical surface. Yarn-to-yarn, layer-to-layer and layer-to-projectile contact interfaces can be implemented in the computation depending on the fabric (1 or more layers). Solid element to model the yarns has introduced numerical instability due the elastic stiffness of the material in the thickness direction, and to the under-integration rule considered in the computations. This type of element leads to very expensive the computation cost (limitation for optimisation purpose). Friction parameter appears to influence the projectile deep of penetration and the shape of the crater.

The homogeneous approach to model macro-scale behaviour of fabric is presented. The RVE of fabric is taken from previous meso-scale FE models developed to simulate ballistic impacts. The material behaviour of the yarns is supposed orthotropic elastic. The same material constants are considered for the macro and meso-scale FE models, as well as the contact interface properties. The homogeneous method is applied for 1 layer of Plain Weave fabric. The RVE is subjected to three types of macro-strain loads in order to analyse the parameters of a macro-scale constitutive model. The influence of contact friction and of the Young's modulus in the yarns fibre direction is studied using the homogeneous approach. It is shown that the most influent parameter is the Young's modulus of the yarns fibre.

The parameters values to be determined by comparing the computed results against the experimental ones are: the yarn-to-yarn friction coefficient and projectile-to-yarn friction coefficient (between the layer and the surface of the impactor). Material elastic properties and failure properties considered in both meso-scale and macro-scale models will have a real influence on the perforation of the fabric and the deformation mode of the fabric outside the impact area. The failure properties will be calibrated when experimental data will be available.

Both models are connected with Rad2Rad tool developed in Radioss software. This tool allows to transfer data between both models.

### Acknowledgments

The authors are grateful to the European Defence Agency for their financial support.

### References

- [1] Barauskas R., Vilkaustas A., *Finite Element Analysis of ballistic properties of a multilayer textile package in LSDYNA*, Proceedings of the nordic LS-DYNA users' conference.
- [2] Barauskas R., and Abraitiene, A., *Computational analysis of impact of a bullet against the multilayer fabrics in LS-DYNA*, Int. J. of Impact Engineering, Vol. 34, 2007, pp.1286-1305.
- [3] Briscoe B.J, Motamedi F., *The ballistic impact characteristics of aramid fabrics: the influence of interface friction*, Wear, Vol. 158(1-2), 1992, pp.229-47.
- [4] Cheeseman B.A., Bogetti T.A., *Ballistic impact fabric and compliant composite laminates*, Composite Structures, Vol. 61(1-2), 2003, pp.161-173.
- [5] Chocron Benloulo I.S., Rodriguez J., Martinez M.A. and Sanchez Galvez V., *Dynamic tensile testing of aramid and polyethylene fiber composites*, Int. J. of Impact Engineering, Vol.19(2), 1997, pp.135-146.
- [6] Dong Z., Sun C.T., *Testing and modeling of yarn pull-out in plain woven kevlar fabrics*, Composites Part A: Applied Science and Manufacturing, Vol. 40(12), 2009, pp.1863-1869.
- [7] Duan Y., Keefe M., Bogetti T.A., Cheeseman B.A., *Modeling the role of friction during ballistic impact of a high-strength plain-weave fabric*, Composite Structures, Vol. 68(3), 2005, pp.331-337.
- [8] Duan Y., Keefe M., Bogetti T.A., Cheeseman B.A., Powers B., *A numerical investigation of the influence of friction on energy absorption by a high-strength fabric subjected to ballistic impact*, Int. J. of Impact Engineering, Vol. 32(8), 2006, pp.1299-1312.
- [9] Gasser A., Boisse P., Hanklar S., *Mechanical behaviour of dry fabric reinforcements, 3D simulations versus biaxial tests*, Computational Materials Science, Vol. 17(1), 2000, pp.7-20.
- [10] Gu B., *Ballistic penetration of conically cylindrical steel projectile into plain-wave fabric target – a finite element simulation*, Journal of Composite Materials, Vol. 38(22), 2004, pp.2049-2074.
- [11] Gu B., Ding X., *A refined quasi-microstructure model for finite element analysis of three-dimensional braided composites under ballistic penetration*, Journal of Composite Materials, Vol. 39(8), 2005, pp.685-710.
- [12] Larsson F., Svensson L., *Carbon, polyethylene and PBO hybrid fibre composites for structural lightweight armour*, Composites Part A: applied science and manufacturing, Vol. 33(2), 2002, pp.221-231.
- [13] Lim C.T, Tan V.B.C, Cheong C.H., *Perforation of high-strength double-ply fabric system by varying shaped projectiles*, Int. J. of Impact Engineering, Vol. 37(6), 2002, pp.577-591.

- [14] Altair Engineering, Radioss Theory Manual, Version 10.0, September 2009.
- [15] Rao M.P., Duan Y., Keefe M., Powers B.M., Bogetti T.A. Modeling the effects of yarn material properties and friction on the ballistic impact of a plain-weave fabric, Composite Structures, Vol. 89(4), 2009, pp. 556-566.

# Glass-fibre reinforced unsaturated polyesters: Towards a compromise between high mechanical behaviours and improved fire performance?

Jérémy Ciret<sup>1</sup>, Michel Dorget<sup>1</sup>

Centre de Transfert de Technologies du Mans, 20 Rue Thalès de Milet, 72000 Le Mans, France

**Abstract:** The use of flame retardants in materials is becoming a key part of the development and applications of new materials. Unsaturated polyester composites are not an exception, a fortiori when we focus on their extreme versatility and their intrinsic high flammability and poor fire resistance. Nevertheless, flame retardant additives act not only on fire properties of the composite but also on the processability of the resin and the mechanical properties of the material. The purpose of this study is to observe the effect of different flame retardants on unsaturated polyester materials by taking into account these three aspects. Changes of viscosity are plotted versus weight content of additives to qualify the processability. Furthermore the thermal stability and the fire performance of the formulation are investigated. Finally, all the results are balanced against the consequence on the mechanical properties in order to obtain an optimised material with a great compromise.

## 1. INTRODUCTION

Unsaturated polyester resins (UP) are extremely versatile in terms of their properties and applications and have been a popular thermosetting resin for glass-fibre reinforced materials [1]. Among all of these properties, unsaturated polyester resins reinforced by glass-fibre are a composite material with an excellent ease of processability, an outstanding chemical resistance, a high flexural moduli and moreover low cost. That is why they are increasingly becoming common for industrial applications looking for the highest strength-to-weight ratios such as railway, automotive, marine and offshore applications [2, 3]. However, unsaturated polyester resins have both very poor resistances to fire associated to high smoke densities during burning because of their intrinsic chemical composition and molecular structures [4, 5].

Hence, additions of flame retardant or smoke suppressant additives are required to pass national or international standards of flammability [6, 7, 8] and to be used in industrial applications. The most used additive in current commercial formulations is aluminium trihydroxide (ATH). It improves greatly flammability but the first acceptable improvements are viewable only with a very high quantities (>30wt.-%). Moreover, flame retardant additives may adversely affect the intrinsic properties of the materials and notably sacrificing the mechanical behaviour of the resultant reinforced composite materials. This effect is even more important at high content [9, 10, 11]. Consequently, new alternative fire retardant additives must be considered and these should be used at lower content or without modifying the viscosity of the formulations. One of them could be phosphorus components (ammonium polyphosphate, melamine phosphate...) [5, 9] those combine indeed the fire retardant functions of nitrogen and phosphorus and can exhibit synergism of both.

So, this study consists in evaluating several flame retardants among these usual additives: ATH and phosphorus components are investigated. Furthermore, the effect of nano-clays is observed in partial substitution of the phosphorus and potential synergism between nano-clays and phosphorus compounds are studied. All the consequences on the fire, mechanical, and thermal properties of glass fibre reinforced polyester composites are shown thanks to Limiting Oxygen Index test (LOI), thermogravimetric analysis (TGA), flexural test and viscosity determination. The results should allow us to propose a material with good compromise between fire resistance and mechanical properties without neglecting the processability of the formulation.

## 2. EXPERIMENTAL DETAILS

### 2.1. Materials

In this study, unsaturated polyester resin (UP) Enydyne N50-1912 AI is purchased from Cray Valley and is used as matrix system. This grade of resin is specially developed to be processed by infusion thanks to a very low viscosity.

Fibre reinforcements is biaxial (0°/90°) E-glass woven roving fabrics with a weight of 300g/m<sup>2</sup> and is purchased from Sicomin. Ten mats of fibres have added on materials.

The different fillers added in the formulation to improve the fire performance of the composite materials are:

- Aluminium trihydroxide Apyral 40CD (ATH) from Nabaltec with a specific surface area of 3.5m<sup>2</sup>/g,
- Ammonium polyphosphate AP422 (AP422) from Clariant that is a fine-gained white powder with great intumescent flame retardant effect in many applications,
- Melamine phosphate MP200/70 (MP) from Ciba.

Nano-clays are also used to improve the fire resistance, two grades of montmorillonite clays have been chosen among the products purchased by Southern Clay Products:

- Cloisite 10A (CI10A) that is a natural organophilic montmorillonite modified with a quaternary ammonium salt (high steric hindrance),
- Cloisite 30B (CI30B) that is a natural organophilic montmorillonite modified with a quaternary ammonium salt (low steric hindrance).

Details of the different formulations studied are summarized on the Table 1 and the accurate compositions will be determined thanks to viscosity measurements.

**Table 1** : Composition of the formulations (accurate ratios are determined thanks to viscosity measurements)

	UP	ATH	AP422	MP200/70	CI10A	CI30B
FR0	X					
FR1	X	X				
FR2	X		X			
FR3	X			X		
FR2A	X		X		X	
FR2B	X		X			X
FR3A	X			X	X	
FR3B	X			X		X

The different formulations are prepared in two steps prior to curing. In a first step, UP resin and fillers have been mechanically mixed for 15 minutes, then hardener has added at room temperature.

Even if the properties of the resin allow a process by infusion, the samples have been processed by casting on a rectangular mould where ten plies of glass fibre are laid on. The fibre ratio is so roughly 60wt.-%. Curing lasts 20h at room temperature and 2h at 70°C, adequate sized samples are then sawed through the rectangular plate.

## 2.2. Analysis and characterization

### 1.1.1. Viscosity testing

The Brookfield viscosities of the uncured resin mixtures are measured using a Brookfield DV II Pro Digital Viscometer. The samples were tested at 25°C using a RV-1 Spindle at 50rpm according to the ISO Standard 2555.

### 1.1.2. Fire testing

The Limited Oxygen Index (LOI; i.e., minimum oxygen concentration to support candle-like combustion of plastics) is measured with a Fire Testing Technology instrument on sheets (100x10x3 mm<sup>3</sup>) according to the standard “oxygen index” test (ISO 4589). It measures the minimum concentration of oxygen in a nitrogen/oxygen mixture required to just support combustion (ignition time between 0 and 180s) of a test sample under specified test conditions in a vertical position (the top of the test sample is ignited with a burner).

### 1.1.3. Thermal analysis

Thermogravimetric analyses (TGA) are conducted on 10mg samples at heating rate 10°C/min between ambient temperature to 900°C in nitrogen (100mL/min) using a Perkin Elmer Pyris TGA. Thermogravimetric analysis (TGA), which measures weight changes in materials as a function of temperature, provides a simple and fast alternative to the screening standards methods used to determine burning characteristics or burning rate.

By monitoring the TG curves of different formulations and of the ingredients separately, the burning characteristics of different material formulations can be compared. Interactions between the compounds of a mixture can be revealed by comparing the experimental TG curve ( $W_{exp}$ ) with a “theoretical” TG curve ( $W_{theo}$ ), calculated as a linear combination of the TG curves of the mixture ingredients weighted by their contents (1):

$$W_{theo}(T) = \sum_i x_i W_i(T) \quad (1)$$

where  $x_i$  is the content of compound I and  $W_i$  is the TG curve of the compound i.

To determine the potential interactions between the two components and their further effects on the thermal stability of the systems, the curves of weight differences between experimental and theoretical TG curves were computed as follows (2):

$$\Delta W(T) = W_{exp}(T) - W_{theo}(T) \quad (2)$$

where  $\Delta W(T)$  is the curve of weight difference and  $W_{exp}(T)$  is the experimental TG curve of the formulation.

### 1.1.4. Three point bending test

Flexural tests are performed according to ASTM D790 on an MTS Dy 25C at a rate of 5mm/min at 50% relative humidity and 23°C. Flexural test samples are cut into a large panel to obtain sheets (80x10x4 mm<sup>3</sup>). The bars are loaded to failure. The flexural moduli  $E_f$  is determined from the slope of a stress-strain curve while the flexural strength  $\sigma_r$  is calculated from the following standard relation (3):

$$\sigma_r = \frac{3PL}{2bd^2} \quad (3)$$

where  $P$  is the load to break,  $b$  and  $d$  are the width and the thickness of the specimen, respectively,  $L$  is the length between supports.

Five samples is used for each formulation.

## 3. RESULTS AND DISCUSSION

### 3.1. Effect of fillers on viscosity and determination of the weight content of formulations

Unsaturated polyester resin compositions are well-known to be customized with numerous fillers to reduce the cost of the finished product and to improve its properties (surface appearance, water resistance, flame resistance). However, addition of the levels of filler needed to accomplish these results also increases the viscosity of the filled polyester composition rendering it more difficult to process. That is why it is necessary to follow the viscosity change caused by the addition of fillers and to fix the maximum ratio of fillers that can be mixed in the formulation.

The first filler used to provide fire retardant properties is aluminium trihydroxide, widely known to dilute the amount of fuel available by replacing part of the resin and to release water at high temperatures, which limits the oxygen available for combustion [11]. ATH causes progressive increase of the formulation viscosity up to reach a critical value. Empirically after several processes to make reinforced polyester composite, we have fixed this value at 250cP, knowing that the initial viscosity of the resin is to 110cP. Hence, results exposed in Figure 1 show an exponential trend about the viscosity increase and limit the amount of ATH added. The accurate composition of FR1 is so fixed with 80wt.-% of UP and 20wt.-% of ATH because we observe a viscosity of 248cP when 20wt.-% of ATH is added.

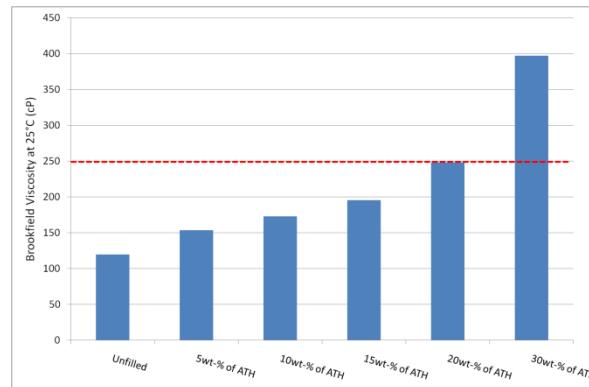


Figure 1 : Viscosity change of FR1 versus weight content of ATH

Similar value and similar method have been used with formulations based on ammonium polyphosphate and on melamine phosphate. Consequently, results exposed on Figure 2 and Figure 3 allow to accurate the formulations FR2 and FR3. These two additives cause more important changes on viscosity and only 15wt.-% of additives can be added before reaching 250cP. The accurate composition of FR2 and FR3 is so fixed respectively with 85wt.-% of UP and 15wt.-% of AP422 and with 85 wt.-% of UP and 15 wt.-% of MP.

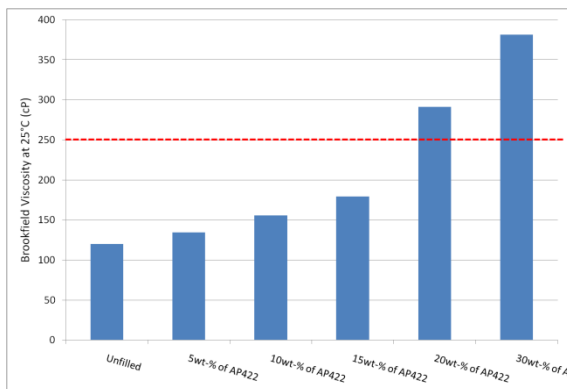


Figure 2 : Viscosity change of FR2 versus weight content of AP422

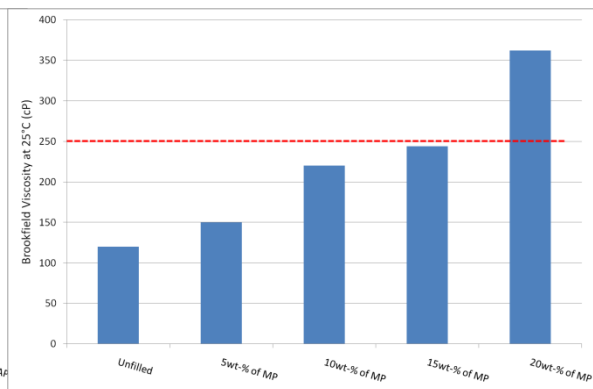


Figure 3 : Viscosity change of FR2 versus weight content of MP

The four additional formulations with three components are deduced from FR2 and FR3. AP422 and MP are partially substituted by two different grades of nano-fillers, C110A or C130B:

- FR2A = 80wt.-% of UP + 10wt.-% of AP422 + 5wt.-% of C110A and FR2B = 80wt.-% of UP + 10wt.-% of AP422 + 5wt.-% of C130B
- FR3A = 80wt.-% of UP + 10wt.-% of MP + 5wt.-% of C110A and FR3B = 80wt.-% of UP + 10wt.-% of MP + 5wt.-% of C130B

Finally to sum up the eight formulations studied in this study, we find out the accurate composition in Table 2.

Table 2 : Maximum weight content of fire retardant additives to maintain formulations processable

	UP	ATH	AP422	MP200/70	C110A	C130B
FR0	100					
FR1	80	20				
FR2	85		15			
FR3	85			15		
FR2A	85		10		5	
FR2B	85		10			5
FR3A	85			10	5	
FR3B	85			10		5

### 3.2. Fire performance of composite formulations

Limiting Oxygen Index (LOI) is widely used for the determination of the relative flammability of polymeric materials. A material has fire retardant performances of interest if its LOI value is higher than 21% which represents the concentration of oxygen in the air. The higher this value is, the better the flame retardant properties of the material are. The LOI values of the composites samples are shown in Figure 4 and Figure 5. Figure 4 compares the LOI results of FR0, FR1, FR2, FR2A and FR2B. Unfilled material shows an important combustion at very low oxygen concentration while the benefits of 20wt.-% of ATH (FR1) and 15wt.-% of AP422 (FR2) are easily viewable. Addition of these fire retardants allows materials become auto-extinguishable in air. Furthermore, use of nano-fillers as synergist agent with AP422 in FR2A and FR2B does not provide clear improvement of the fire performance of the materials.

Then Figure 5 compares the LOI results of FR0, FR1, FR3, FR3A and FR3B. At similar weight content (15wt.-%), MP causes a better improvement of fire performance than AP422. With this additive, the composite material is widely auto-extinguishable (LOI=26). The improvement provided by MP to polyester prevents the materials from burning and being destructed in free air. Nevertheless, in spite of a promising result, the substitution of MP by nano-fillers in FR3 (FR3A and FR3B) does not improve the fire properties.

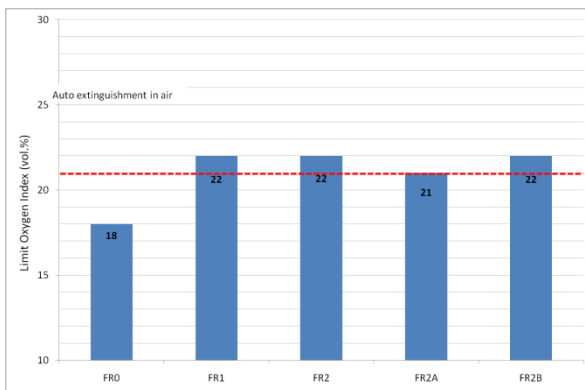


Figure 4 : LOI results of FR0, FR1, FR2, FR2A and FR2B

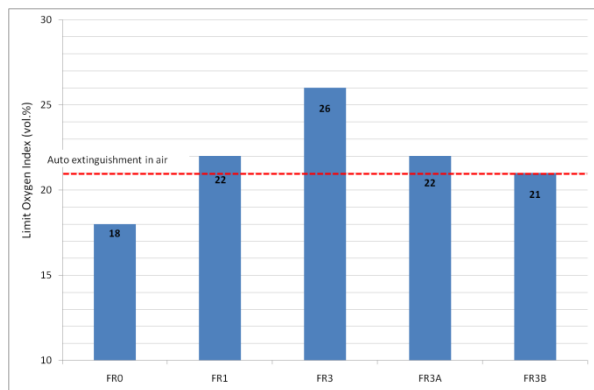


Figure 5 : LOI results of FR0, FR1, FR3, FR3A and FR3B

With this easy-to-handle test and the determination of the LOI values, we have underlined the effect of different usual fire retardant additives in polyester composites. It appears that melamine phosphate is the more efficient additive to improve the fire behaviour of the material without increasing dramatically the viscosity.

### 3.3. Thermal analysis

To examine the effect of fire retardants on the thermal stability and degradation, TGA data in nitrogen were determined and analysed. Before exposing results, it must be noted that phenomena highlighted by the two experiments are quite different and can underlined dissimilar results. If the LOI values give qualitative information about the abilities of the materials to limit the superficial burning, TGA in pyrolysis conditions indicates the role played by flame retardant into the decomposition and the potential benefit into thermally stability (increase of the residual mass). The LOI evaluation traduces a behaviour facing to flame in oxidative conditions while TGA represent s the resistance in temperature in pyrolysis conditions (oxygen depletion).

Figure 6 compares the thermal stability of FR0, FR1, FR2 and FR3. It appears that all the additives provide an increase of the residual weight up to 450 °C, in agreement with the addition of thermally stable ingredients (respectively ATH, AP422 or MP). By comparing experimental and theoretical curves (Figure 7), it appears that ATH has an opposite effect to AP422 or MP. Indeed, positive interactions are observable for FR1 between 250 and 700°C while for FR2 and FR3 their interactions are detrimental between 320 and respectively 900°C and 500°C. This effect at lower temperature can be explained by the

mechanism of action of ATH that releases water over this broad temperature range. In the other hand, action of MP and AP422 is later and potential stabilization occurs up to 500°C for FR3.

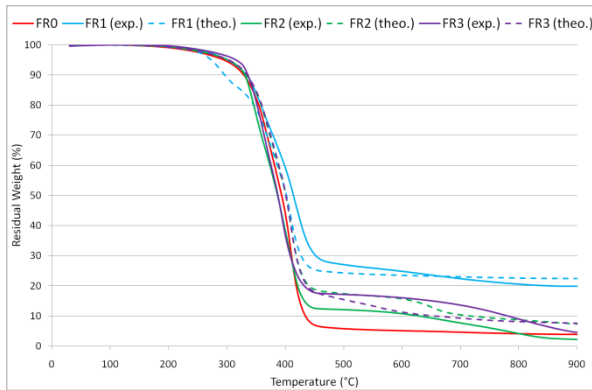


Figure 6 : Experimental and theoretical TG curves of FR0, FR1, FR2 and FR3

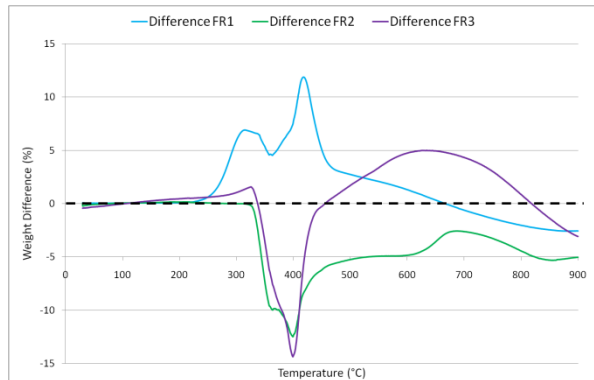


Figure 7 : Experimental and theoretical weight differences for FR1, FR2 and FR3

Similar experiments and analysis have been carried out with formulations based on AP422 (FR2A and FR2B) comparing with FR2 to observe effect of nano-fillers. Figure 8 shows that nano-fillers improve the stability of the materials up to 450 °C. This improvement is in agreement with the substitution of AP422 by nano-fillers and the better stability of this last. About the potential interactions between UP+AP422 and nano-fillers (Figure 9), it is detrimental in a first narrow temperature range [300-450°C], then up to 450°C the effect provided by nano-fillers is benefit but limited.

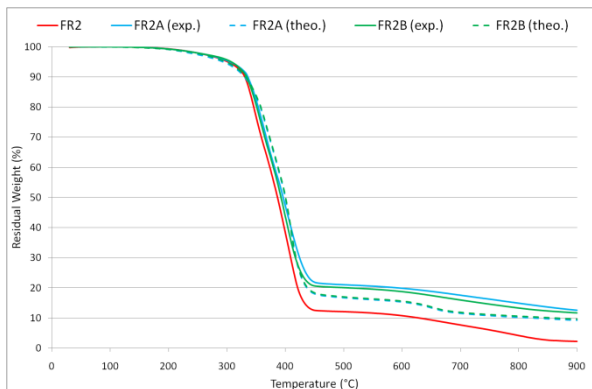


Figure 8 : Experimental and theoretical TG curves of FR2, FR2A and FR2B

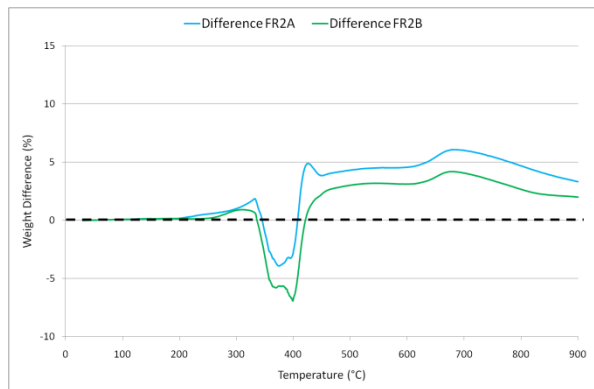


Figure 9 : Experimental and theoretical weight differences for FR2A and FR2B

Finally, experiments and analysis on formulations based on MP (FR3A and FR3B) and compared to FR3 are exposed on Figure 10 and Figure 11. Figure 10 shows that nano-fillers do not significantly modify the behaviour of the materials based on MP. Consequently, the variation observed between theoretical and experimental TG curves are limited (Figure 11), slightly detrimental between 350 and 450°C and then benefit up to 500°C whatever the grade of montmorillonite used.

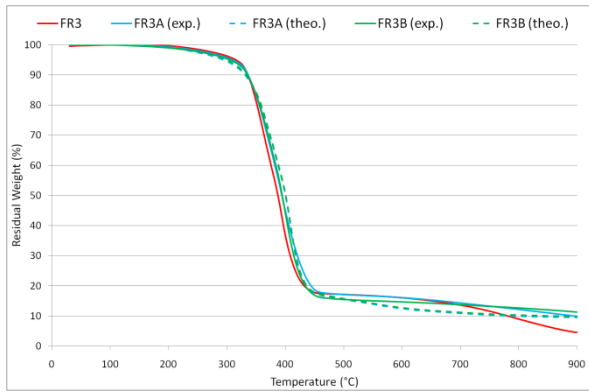


Figure 10 : Experimental and theoretical TG curves of FR3, FR3A and FR3B

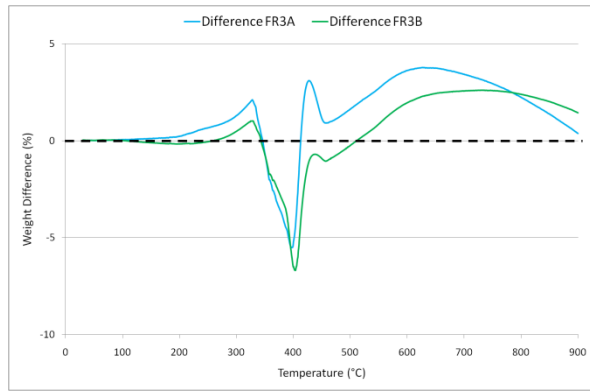


Figure 11 : Experimental and theoretical weight differences for FR3A and FR3B

So, except FR1 that shows a thermal stability improved by ATH between 250 and 450°C, the contribution of each additive to the stability of materials is limited and cannot be significant to explain fire behaviours exposed with LOI results.

### 3.4. Effect of the fire retardant additives on mechanical properties

As enounced in the introduction, addition of flame retardant can modify dramatically the mechanical behaviour of the composite materials and above all the flexural properties [10, 11, 12]. Figure 12 and Figure 13 show the flexural modulus and the flexural strength of the different materials. A clear tendency can be observed in these figures, the neat UP presents both higher flexural strength and ultimate strain, compared to the filled composites. The worst consequence is observed when both MP and Cloisite 10A are added on UP (FR3A): flexural modulus is decreased of 60wt.-% while flexural strength is decreased of 50wt.-%. On the contrary, for FR2 and FR3 the effect is minor and we could consider it as negligible.

These results are in agreement with other studies. Previously, Demirel et al. [10] or Jang et al. [12] have found similar results concerning the effect of flame retardant on flexural properties of composites. This behaviour can be due to the existence of defects in the structure created by a poor additives–matrix interaction. This behaviour hinders the stress transfer from the matrix to the additive, producing lower mechanical resistance in the composites. The worst behaviour of formulations containing nano-clays can also be explained thanks to this bad interaction, this trend was observed in other works for nano-clay/UP nano-composites [13, 14].

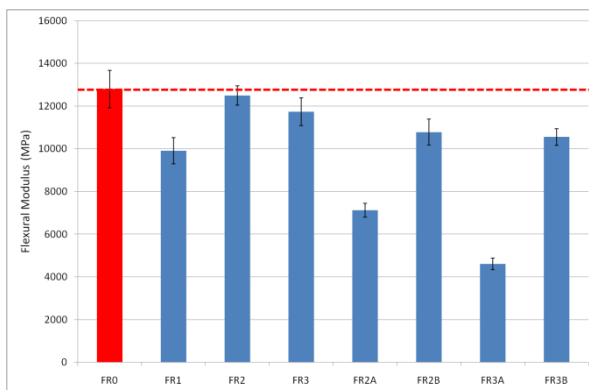


Figure 12 : Flexural modulus of the different formulations - Effect of the fillers

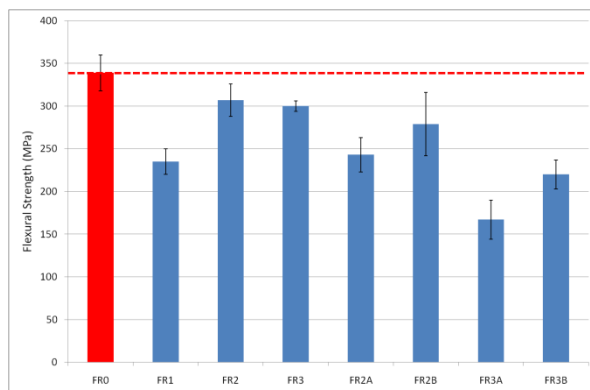


Figure 13 : Flexural strength of the different formulations - Effect of the fillers

## 4. CONCLUSIONS

In this work, evaluation of flame retardant formulations based on unsaturated polyester was carried out and consequence of flame retardant addition was investigated on process ability and mechanical properties. From the results obtained, the main conclusions are:

- First of all, the amount of flame retardant is widely restricted because of their effect on formulation viscosity. Indeed, the most filled formulation (FR1) contains 20wt.-% of ATH while AP422 and MP are limited to 15wt.-% respectively in FR2 and FR3.

- Nevertheless, the addition of whatever these additives allows composite materials to become self-extinguishable in a free air. Among them MP appears as the most efficient flame retardant for the glass fibre reinforced polyester composites with a LOI value of 26 (+8 compared to unfilled materials).
- The comparison between theoretical and experimental TG curves shows an increase in thermal stability for formulations with ATH, AP422 or MP in agreement with the addition of thermally stable compounds.
- Finally, neither AP422 (causing an improvement of 4 points in LOI) nor MP (+8 in LOI) cause dramatically decrease of the flexural properties.

All these results highlight the intrinsic worst flammability of UP resins and the improvement provided to materials by a few amount of fire retardant additives. Nevertheless, the compatibility between matrix and additives seems to be not enough to reach important flame retardant properties (LOI > 30) without destroying the mechanical behaviour of the composites. Indeed, addition of phosphorus compounds and nano-fillers causes weakness on material even at low weight content. This drawback is not major for some formulations studied but other results let think a bad interaction between components. This new aspect should be taken into account in a next study and responses should be provided in order to enhance the compatibility between matrix and additives and maintain the flexural properties of the flame retarded materials.

### References

- [1] Heger F. J. and Sharff P. A.: Buildings: Plastics and composites. in '*Encyclopaedia of materials: Science and technology*' (eds.: Buschow K. H. J., Cahn R., Flemings M. C., Ilshner B., Kramer E. J., Mahajan S., Veyssiere P.) Pergamon Press, Oxford, 833–841 (2001).
- [2] Xu, L., and Lee, L. J. *Polymer* 45.21 (2004) 7325-7334
- [3] Chiu, H. T., Chiu, S. H., Jeng, R. E. and Chung, J.-S. *Polymer Degradation and Stability*, 70.3 (2000) 505-514.
- [4] Nazaré, S., Kandola, B. K. and Horrocks, A. R. *Polymers for Advanced Technologies*, 17.4 (2006) 294-303.
- [5] Penczek, P., Czub, P. and Pielichowski, J. *Advances in Polymer Science*, 184 (2005) 1-95.
- [6] NF F 16-101 Matériel roulant ferroviaire – Comportement au feu – Choix des matériaux (1988).
- [7] NF F 16-102 Matériel roulant ferroviaire – Comportement au feu – Choix des matériaux, application aux équipements électriques (1992).
- [8] FMVSS 302 Federal Motor Vehicle Safety Standards – Flammability of Materials used in the occupant compartments of motor vehicles.
- [9] Hörold, S. *Polymer Degradation and Stability*, 64.3 (1999) 427-431.
- [10] Demirel, M., Pamuk, V. and Dilsiz, N. *Journal of Applied Polymer Science*, 115.5 (2010) 2550-2555.
- [11] Hapuarachchi, T.D. and Peijs, T. *Express Polymer Letters* 3.11 (2009) 743-751.
- [12] Jang, J., Chung, H., Kim, M. and Sung, H. *Polym Test* 19.3 (2000) 269-79.
- [13] Inceoglu, A. and Yilmazer, U. *Polym Eng Sci* 43.3 (2003) 661-669.
- [14] Kornmann, X., Berglund, L. A., Sterte, J. and Giannelis, E. P. *Polym Eng Sci*, 38.8. (2008) 1351-1358.

## TRANSFER OF COPYRIGHT AGREEMENT

Copyright to the article entitled: Glass-fibre reinforced unsaturated polyesters: Towards a compromise between high mechanical behaviours and improved fire performance?

By: Jérémy Ciret and Michel Dorget

All Authors

is hereby transferred to the

**DYMAT Association**

effective when the article is accepted for publication in :

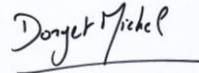
**19<sup>th</sup> DYMAT Technical Meeting**  
(electronic or hardcopy format)

However, the authors reserve the following:

- (1) All proprietary rights other than copyright, such as patent rights.
- (2) The right to use all or part of this article in future works of their own, such as lectures, press releases, reviews, textbooks, or reprint books.

*Third party requests to reprint all or part of the article must be directed to the publisher in order to obtain publisher's written permission.*

To be signed by at least one of the authors (who agrees to inform the others, if any) or, in the case of a "work made for hire", by the employer.

Signature		Signature	
Print Name	CIRET	Print Name	DORGET
Title, if not Author		Title, if not Author	
Institution or Company	CTTM	Institution or Company	CTTM
Date	01/10/2010	Date	01/10/2010

The signed statement must be received before the manuscript can be accepted for publication.

Return to DYMAT before October 15, 2010:

DYMAT 19<sup>th</sup> TM 2010 IMFS UDS / 2 rue Boussingault / 67000 Strasbourg / France  
Fax: 00 33 (0) 3 68 85 29 36      Email: bahlouli@unistra.fr

# Dynamic Deformation of PBXs and their simulants

D. R. Drodge<sup>1</sup>, D. M. Williamson and W. G. Proud

*Cavendish Laboratory, University of Cambridge, JJ Thomson Avenue, Cambridge CB3 0HE, UK*

**Abstract.** The study of polymer bonded explosives has been a long-running research theme at the Cavendish Laboratory. Here we present a broad overview of recent experimental results. An investigation was conducted into the effect of filler particle size and fill-fraction: for this purpose a family of explosive simulants was produced and imaged using X-ray tomography. Simple composite theory and a strain-energy activated damage model were found to describe their behaviour. Finally, we carried out a novel series of damage-characterisation experiments on a set of model explosives. Dynamic modulus, thermal conductivity, density and mechanical response were measured as a function of damage energy. The fine-particle compositions were found to be most resilient. All experiments performed can offer valuable validation data for modellers.

## 1. INTRODUCTION

A PBX (polymer bonded explosive) must fulfil functions beyond simple explosive power: mechanical resilience and structural integrity are also important. PBXs are often placed in situations presenting risk of thermal or mechanical insult, which may cause deterioration in mechanical properties and sensitivity. Quantification of this effect is important in establishing design limitations of devices that employ PBXs and similar materials as components.

Unlike other composites such as fibre-reinforced polymers or concrete, most PBXs are not designed with structural properties foremost in mind, as their function is to produce an explosion when required and remain safe at all other times. Of course, some rigidity is required for PBXs used in geometry-sensitive applications, such as explosive cutting, welding or lensing, and in the latter application precision machining of the PBX billet is required. Mechanical properties, however, govern the storage and dissipation of energy when a PBX is subjected to dynamic loading. With increased priority given to developing insensitive munitions, understanding the effect of PBX formulation on mechanical properties has become as important as understanding its effect on explosive output.

Constitutive models that account for failure are numerous and complex and the range of PBX materials studied under dynamic loading is largely confined to end-product formulations and their simulants. To allow for thorough validation of models, a more diverse range of composites can be produced with a focus solely on experimental testing. Here we present two examples of this from recent projects performed in the Fracture and Shock Physics Group at the Cavendish Laboratory.

## 2. EFFECT OF SIZE AND SEPARATION

The effect of particle size on PBX strength was studied as part of a wider investigation by Balzer and colleagues [1]. Several ammonium perchlorate / HTPB composites, of equal fill-fraction but varying particle size were tested in compression. These materials exhibited an inverse square-root dependency of flow stress on particle size, which was termed a pseudo-Hall-Petch relationship. Because the fill-fraction of all materials was constant, the same relationship can be asserted to hold between flow stress and the interparticle separation.

Suggested mechanisms behind this relationship are presented by Siviour et al. [2]: a consideration of fracture energy produces the required dependence, as does a similarly derived result by Gent and Park [3]. Both mechanisms have particle size as the sole important parameter. The inverse relationship results from balancing surface fracture energy with strain energy density in the vicinity of a particle, the larger of which

---

<sup>1</sup> *Correspondance address : Dept of Engineering Science, Parks Rd, Oxford OX1 3PJ, UK*

requires more energy to debond (scaling as  $r^2$ ) but has a larger local volume from which strain energy is drawn (scaling as  $r^3$ ).

This local failure phenomenon translates to a bulk strain-softening of the composite as debonded particles are unable to support tensile or shear stresses. Siviour et al describe the degradation as a strain energy-activated Arrhenius process, with the activation energy expressed in terms of an activation strain  $\epsilon_a$ . With additional mechanical response data on representative composite materials, these and other models can be assessed, and the ambiguity inherent in Balzer's result, resolved.

Eleven composites were produced to achieve this goal: five with varying particle separation and fixed particle size, and six with varying particle size and fixed particle separation. Their mechanical and microstructural properties were measured as part of a wider investigation into energetic composites [4].

## 2.1. Production of PBX Simulants

Specimens of PBX materials present a hazard in the production, storage and testing phases of an investigation. Production and storage of energetic materials is limited by safety protocol, and testing may introduce risks by virtue of the very damage that one intends to study. So-called inert simulants, also referred to as "mock" explosives (and anecdotally, in one case, "sham" explosives) contain unreactive substitute materials in place of the energetic components, and otherwise follow the same formulation as the PBX being simulated. Examples are PBS9501 [5] and EDC1037 [6]. For this investigation, inert-type materials were used to avoid safety issues, although no explosive equivalent exists.

Crystalline sucrose is used as a replacement for HMX and RDX due to similarity in bonding, crystal structure and mechanical strength [7]. Crystals with a broad, monomodal particle size distribution were obtained in the form of caster sugar, which has a modal particle size of around 200  $\mu\text{m}$ . This was sieved to produce eight particle size fractions, ranging from 125-150  $\mu\text{m}$  to 425-600  $\mu\text{m}$ . Crystals in the 300-425  $\mu\text{m}$  fraction were the most abundant, so this range was used to produce several simulants of fixed particle size and varying particle separation.

HTPB resin was supplied by Sartomer Europe. Catalyst (dibutyl tin dilaurate) and antioxidant (Calco 2246) were added in weight ratios 0.02% and 1% respectively. The sugar and HTPB were mixed by hand with the curing agent, isophorone diisocyanate (IPDI), which was added in the quantity required to give an agent to resin activity ratio of 1.1:1. A rough vacuum was applied to de-aerate the mixture. The composites were cast into slab moulds and cured in an oven at 70°C. To prevent sedimentation of the crystals, the composites were rotated slowly about a horizontal axis during cure.

To produce composites with variation in particle separation and size, the ratio of sugar to HTPB must be varied. A simple model was used to generate the desired trends. Crystals were assumed to be cubes of side  $a$ , suspended in a regular array separated by binder layers of thickness  $s$ . This produces a simple relationship between  $a$ ,  $s$  and volume fill-fraction,  $f$ , given in Equation 1 below. The model is not particularly realistic given that crystals will tend to be randomly aligned, have a range of sizes and are extremely unlikely to co-ordinate their positions. It is used solely to prescribe mixing ratios and not for analytical purposes.

$$f = \left( \frac{a}{a+s} \right)^3 \quad (1)$$

An upper limit to  $f$  is inevitable for a monomodal composite, unless perfect tessellation occurs. Preliminary studies indicated that fill-fractions above 50% become difficult to de-aerate, so this was selected as an upper limit. For the fixed separation materials, a constant separation of 130  $\mu\text{m}$  was selected, which can be achieved across the whole range of particle sizes, requiring  $f = 51\%$  for the 425-600  $\mu\text{m}$  fraction and lower values for smaller particles. The fixed particle-size materials were designed to range in separation from 94 to 234  $\mu\text{m}$  in 35  $\mu\text{m}$  increments. Calculation of the required fill-fraction was performed using the median of the sieve range. The compositions, as prescribed, are shown in Table 1.

**Table 1.** Prescribed compositions of the composites.

Composite	Sieve Range / $\mu\text{m}$	$f$	$s$ / $\mu\text{m}$
F1	300-425	0.224	94.4
F2	300-425	0.269	94.4
F3	300-425	0.326	94.4
F4	300-425	0.400	94.4
F5	300-425	0.499	94.4
PXX	125-150	0.137	94.4
PX	150-180	0.176	94.4
P1	180-212	0.218	94.4
P2	212-250	0.263	94.4
P3	250-300	0.314	94.4
P5	425-600	0.509	94.4

## 2.2. Characterisation of Microstructure

The eleven composites described above were inspected using X-ray micro-tomography, the principles and application of which are described well in the review by Stock [8]. The technique allows small specimens to be imaged in 3D using X-ray absorption. The resulting image set allows internal structure to be visualized, provided there is sufficient resolution and density contrast between features. We employed a Skyscan 1072, with resolution  $3.2\mu\text{m}$ , allowing it to detect most particles in the composites.

Specimens were cut from the composites using a hollow punch, and assembled into stacks to allow several to be scanned at once. Three X-ray transmission images of exposure time 1.1s were taken and averaged at 1600 intervals of rotation. The beam power was 10 W, and the voltage was 51 kV. These images were processed using Skyscan's NRecon reconstruction program. Sections of the composite are shown in Figure 1 below.

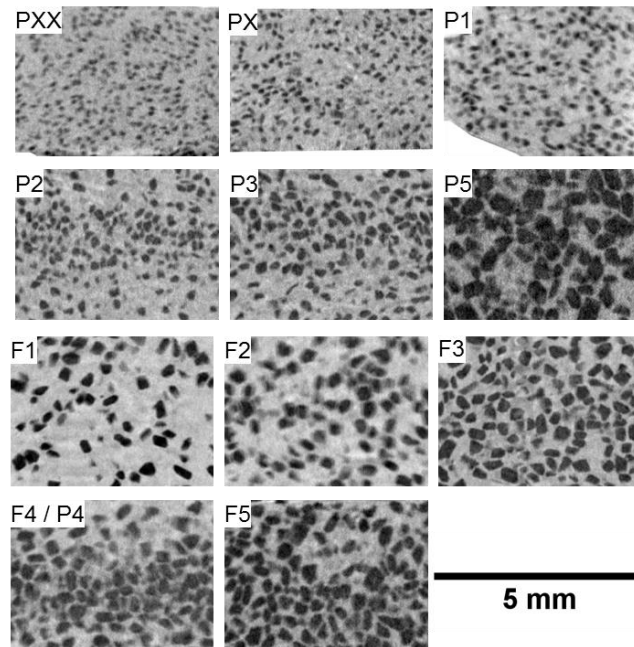


**Figure 1.** Cross-sectional images from X-ray tomography scans, for the eleven composites.

Image analysis of these composites was performed using *ImageJ* [9]. Fill fraction was computed from binary threshold images as a function of depth through the specimen. A particle size distribution was computed using a 3D object counting routine, and a particle separation distribution was estimated from measurements of the local thickness of the binder structure. Local thickness is described mathematically by

Hildebrand & Rügsegger [10] and is calculated using an *ImageJ* subroutine [11]. The measurements for each composite are summarized in table 2 below.

**Table 2.** Microstructural parameters, obtained from tomography images.

Composite	$\bar{f}$	$\sigma_f$	$\bar{a} / \mu\text{m}$	$\sigma_a / \mu\text{m}$	$\bar{s} / \mu\text{m}$	$\sigma_s / \mu\text{m}$
F1	23	3	314	35	401	150
F2	28	4	299	53	362	122
F3	34	7	308	45	216	99
F4	33	14	314	52	259	138
F5	45	7	259	74	162	74
PXX	10.5	0.9	150	27	160	59
PX	15.9	1.4	157	31	189	67
P1	9.7	1.5	161	29	277	83
P2	20	6	209	27	207	94
P3	29	5	249	39	207	84
P5	52.0	0.9	512.5*	87.5*	122	61

### 2.3. Mechanical Properties

Dynamic and quasi-static compressive strength were measured for all eleven composites using an Instron and a Hopkinson Bar system. Nominal strain rates were  $2 \times 10^{-2}$  and  $2 \times 10^3 \text{ s}^{-1}$ . The Instron was instrumented with a clip gauge and videography system to measure strain, and a 20N load-cell to measure stress. The Hopkinson Bars used were 12.7mm diameter Magnesium AZM rods with semiconductor strain-gauges. Both sets of experiments used paraffin wax lubricant. Three specimens of each material were compressed in each piece of apparatus, and the averaged stress-strain plots are shown in figures 2(a) – (d) below.

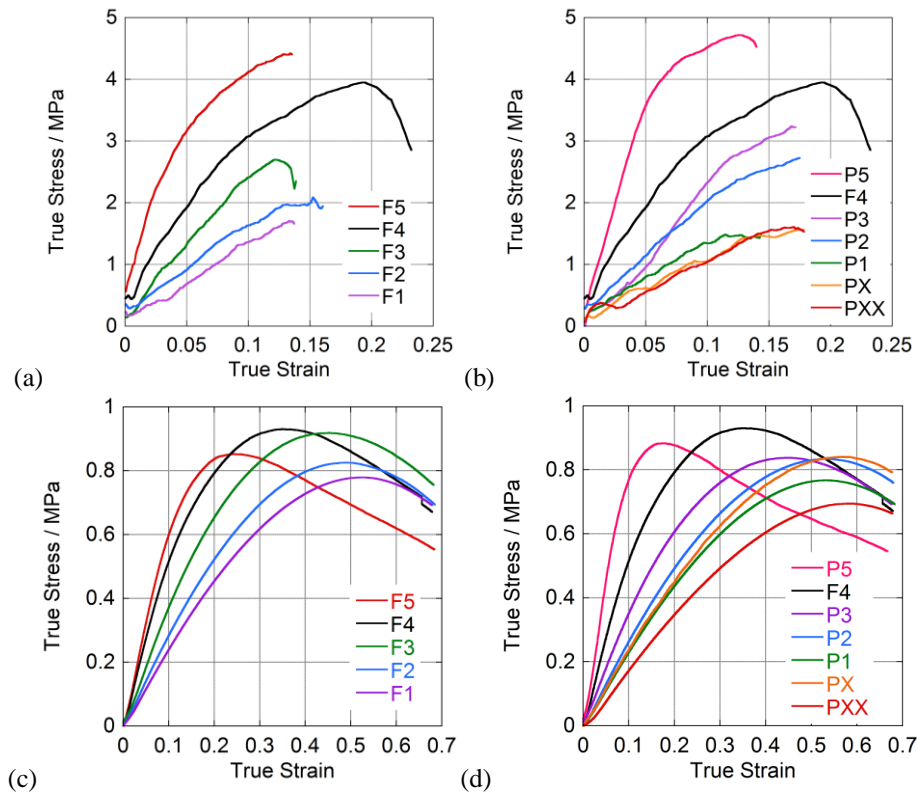


**Figure 2.** Compressive true stress - true strain plots: (a) SHPB results for varying particle-size composites; (b) SHPB results for varying particle separation composites; (c) Instron results for varying particle-size composites; (d) Instron results for varying particle separation composites

## 2.4. Discussion

Young's modulus, calculated from the Instron stress-strain measurements, follows an expected trend of increasing with increasing fill-fraction. A Halpin-Tsai based model, such as that of Nielsen [12], can be used to describe the relationship quite well. This increase appears to be independent of particle size. Similarly, the peak stresses of the materials show no correlation with particle size, but are dominated by the fill-fraction. The consistent fill-fraction used by Balzer and colleagues allowed the inverse-root relationship to manifest, and particle size rather than separation is responsible.

SHPB stresses are about four times higher than those recorded using the Instron alone. This is expected for polymeric systems and has been observed before. A point of note is that the peak stresses in the Instron are within a narrow range for all composites, whereas those in the SHPB increase for increasing fill-fraction. The low strains reached by the SHPB prevent us from locating a peak stress for many specimens but those that do see some softening (PX, F3, F4 and F5) do follow this trend.

Whilst this set of experiments has answered the question posed by the result of Balzer et al., it also provides a range of well-characterised composites which can be used for model validation. This is currently ongoing. Tomographic measurements of particle sizes, separations and fill-fraction can clearly provide a more reliable measure of true microstructural parameters than assumptions based solely on PBX formulation.

## 3. DAMAGE MEASUREMENT IN PBXS

A concurrent investigation was conducted into the effects of compressively-induced damage on the mechanical and thermal transport properties of PBX materials [13]. For these investigations, three PBXs of varying particle size composition were provided by QinetiQ of Fort Halstead. These were designated QRX214 (fine), QRX217 (coarse) and QRX221 (bimodal). These consist of HTPB-bound RDX crystals, the formulations for which are given in table 3. The constituent crystals were drawn from coarse and fine batches of RDX, whose modal particle sizes were 200  $\mu\text{m}$  and 12  $\mu\text{m}$  respectively.

**Table 3.** Compositions of PBX materials, by volume fraction of filler

Material	Coarse RDX	Fine RDX
QRX214 (fine)	-	0.54
QRX217 (coarse)	0.60	-
QRX221 (bimodal)	0.47	0.20

### 3.1 Experimental Methodology

The scheme of experiments is shown in figure 3. Three specimens of each of the three materials are subjected to four levels of damage (including zero damage). These specimens then have four properties measured: dynamic modulus, quasi-static stress-strain response, density and thermal conductivity. In total 144 experiments are required.

Damage is applied using a Drop-weight or a Direct Impact Hopkinson bar system, with strain-protection rings to limit the final compressed length. Larger specimens, such as those required for DMA and thermal measurements, used the drop-weight. The impact velocity of the Hopkinson bar was approximately 8  $\text{ms}^{-1}$ , and of the drop-weight was approximately 4.5  $\text{ms}^{-1}$ .

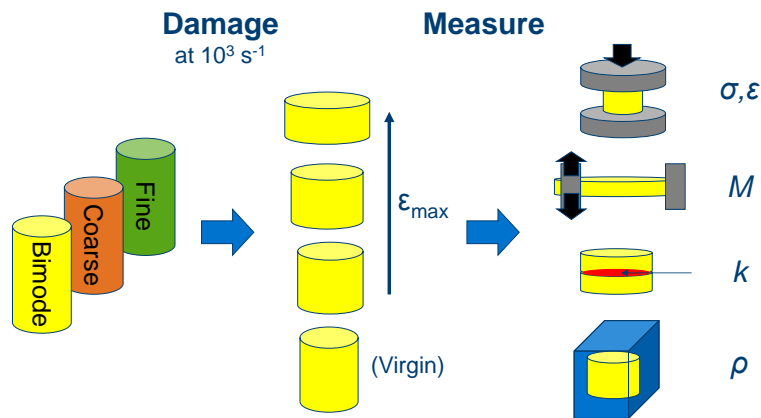


**Figure 3.** Schematic of the damage measurement process. Each experiment is repeated three times.

Density is measured using an immersion technique; quasi-static response using an Instron as described above for the Simulant specimens; dynamic modulus was measured using a TA Instruments Q800 DMA device in cantilever-bending mode; and thermal conductivity was measured using a Hot Disc Thermal Analyser [14]. The resulting trends are plotted as a function of damage strain in figure 4 below, and the stress-strain curves are plotted in figure 5.

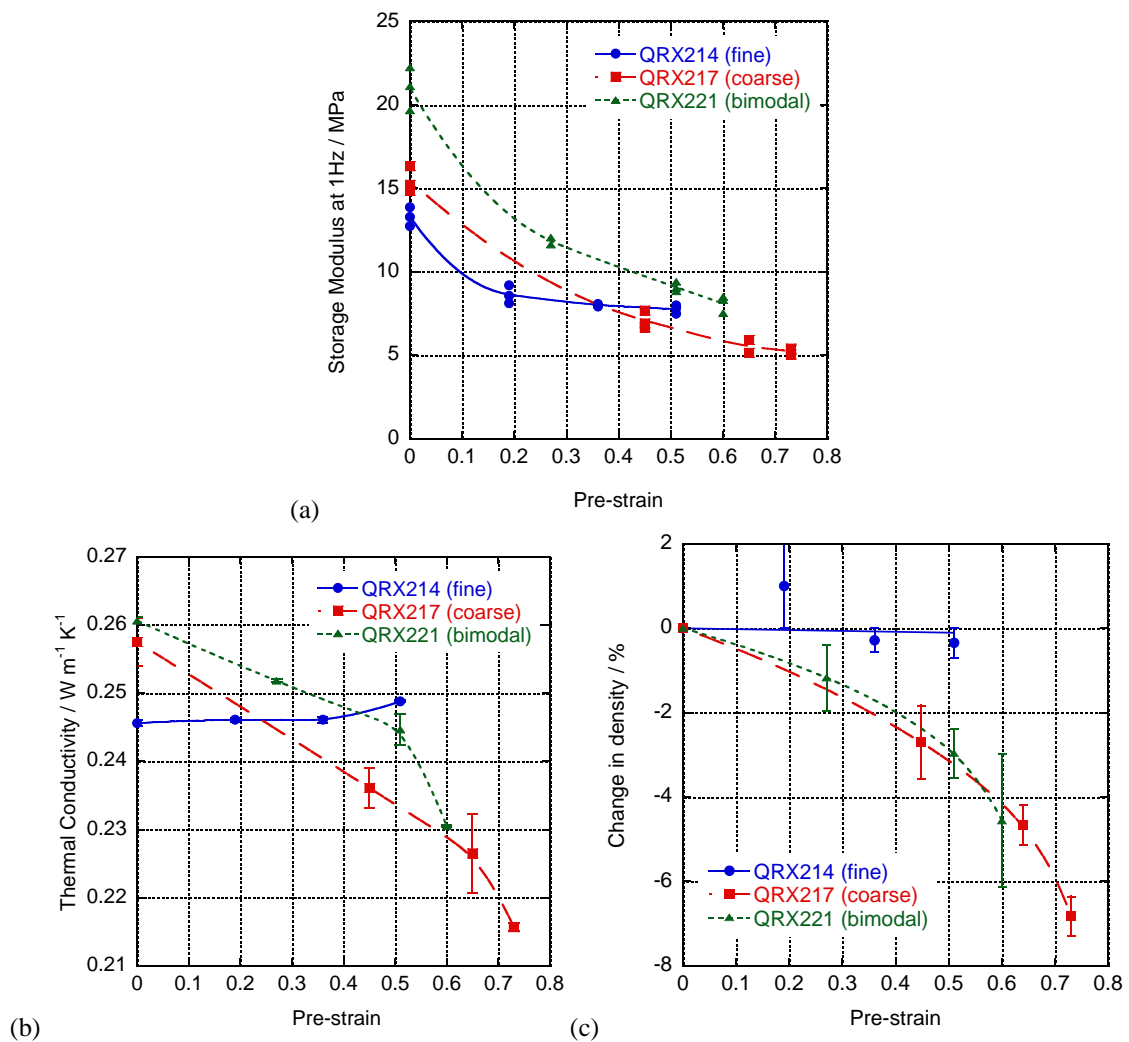


**Figure 4.** Mechanical and thermal properties as a function of pre-strain damage.

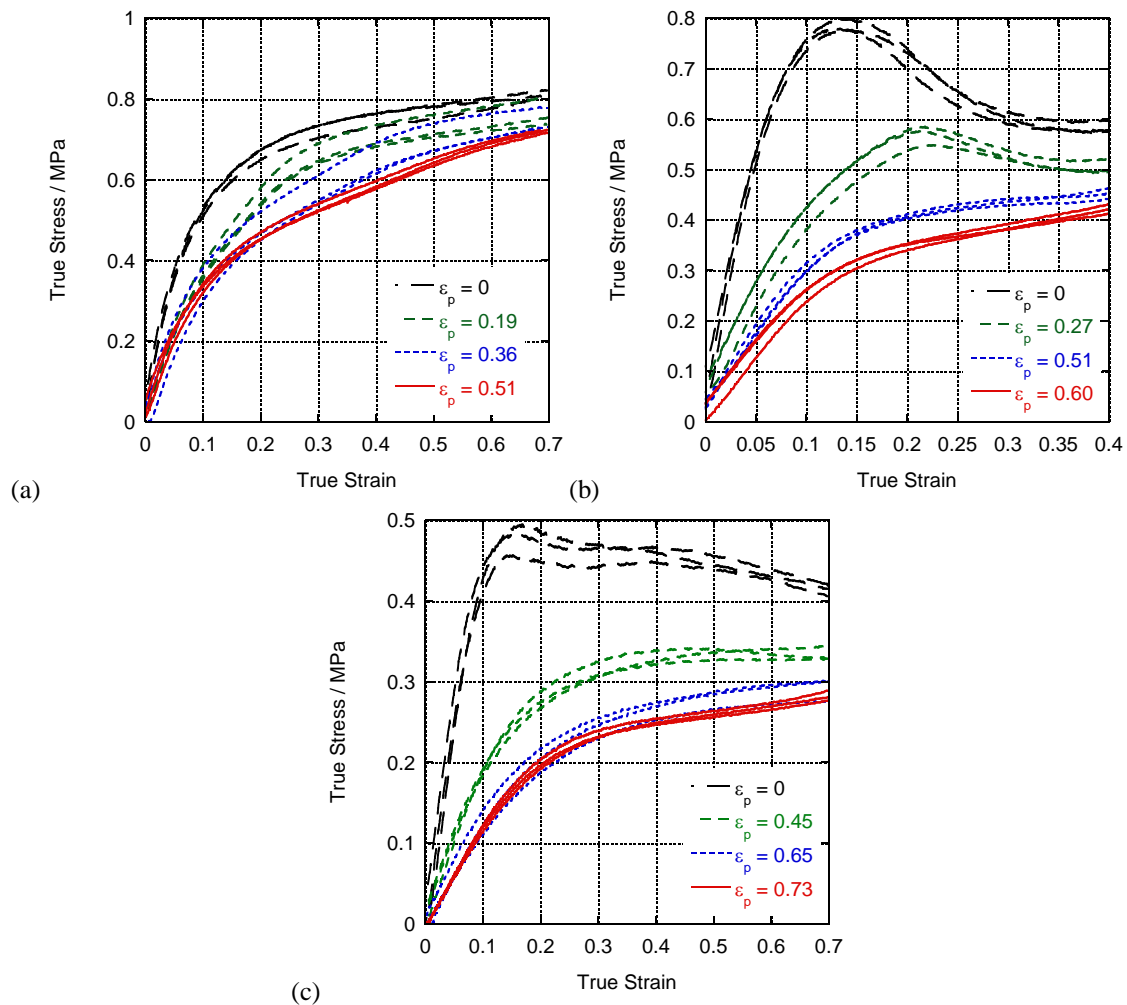


**Figure 5.** Instron stress-strain curves for (a) QRX214 (fine); (b) QRX217 (coarse); (c) QRX221 (bimodal)

### 3.2 Discussion

The expected trend for composites is that mechanical strength and moduli deteriorate with increasing damage. Figures 4a and 5 indicate that deterioration occurs for all materials. Examining the details of the stress-strain curves, it can be noted that the decrease in strength (taken as peak stress) is more extreme for the coarser-grained materials. The stress-strain curves for the coarser composites appear to become more like that of the fine-grained composite as damage increases. This is due to the debonding of coarse particles to leave a fine-grained (or binder-only) network.

The damage in the fine-grained composite is not sufficient to promote any measurable decline in thermal conductivity or density, although the deterioration in mechanical response is clear. It is assumed that this is because these measurements cannot distinguish a specimen containing closed cracks from an undamaged specimen, as both will have identical densities and thermal transport properties. The coarse-grained materials by contrast have noticeable density and conductivity decreases, as they appear to be unable to recover their original geometries, perhaps due to rotation of the debonded grains.

The implication for PBX design and safety is that propellants and composites with coarse-grained microstructure are more susceptible to damage. However, fine-grained composites also accrue damage but it may not be detectable using passive techniques which rely on irrecoverable void formation when cracking occurs. Further studies are required to determine the extent to which closed cracks affect burn rate in fine composites.

## 4. CONCLUSIONS

The studies described here have emphasised some general trends in PBX behavior under mechanical insult: microstructure affects both immediate response and also long-term damage susceptibility. Larger filler particles will debond at lower stresses, and more highly-filled materials will be stiffer, and can reach this point at lower strains. The use of non-invasive imaging techniques such as X-ray tomography can be used to inspect and quantify microstructure, but damaged PBXs may contain closed crack surfaces, which will mask their corresponding deterioration in mechanical properties. More invasive damage probing techniques, measuring modulus degradation, are thus advised for future studies of damage evolution.

## Acknowledgments

Daniel Drodge and David Williamson thank AWE for financial and scientific support. We are grateful for the help and advice of Peter Laity and Rob Cornell at the University of Cambridge Department of Materials Science and Metallurgy, Stewart Palmer and the Mott Workshop at the Cavendish Laboratory and Sally Gaulter at Cranfield University. The damage characterisation research was performed as part of the UK-Energetics HAZARD research programme, funded by the Defence Technology and Innovation Centre, UK MoD.

## References

- [1] Balzer, J. E.; Siviour, C. R.; Walley, S. M.; Proud, W. G. & Field, J. E. Behaviour of ammonium perchlorate-based propellants and a polymer-bonded explosive under impact loading *Proc. R. Soc. London, Ser. A*, 2004, 460, 781-806
- [2] Siviour, C.; Laity, P. R.; Proud, W. G.; Field, J. E.; Porter, D.; Church, P. D.; Gould, P. & Huntingdon-Thresher, W. High strain rate properties of a polymer-bonded sugar: their dependence on applied and internal constraints *Proc. R. Soc. London, Ser. A*, 2008, 464, 1229-1255
- [3] Gent, A. N. & Park, B. Failure processes in elastomers at or near a rigid spherical inclusion *J. Mat. Sci.*, 1984, 19, 1947-1956
- [4] Drodge, D. R. Mechanical Properties of Energetic Composites. PhD Thesis, University of Cambridge, 2009
- [5] Idar, D. J.; Peterson, P. D.; Scott, P. D. & Funk, D. J. Low strain rate compression measurements of PBXN-9, PBX9501, and Mock 9501. *Proceedings of the 10<sup>th</sup> APS Topical Conference on Shock Compression of Condensed Matter*, 1997, 587-590
- [6] Williamson, D. M., Palmer, S. J. P. & Proud, W. G. Fracture studies of PBX simulant materials. *Proceedings of the 14<sup>th</sup> APS Topical Conference on Shock Compression of Condensed Matter*, 2005, 829-832
- [7] Sheffield, S. A.; Gustavsen, R. L. & Alcon, R. R. Porous HMX initiation studies - sugar as an inert simulant *Proceedings of the 10<sup>th</sup> APS Topical Conference on Shock Compression of Condensed Matter*, 1997, 575-578
- [8] Stock, S. R. Recent advances in X-ray microtomography applied to materials *Int. Mater. Rev.*, 2008, 53, 129-181
- [9] Abramoff, M. D.; Magelhaes, P. J. & Ram, S. J. Image Processing with ImageJ *Biophotonics International*, 2003, 11, 36-42
- [10] Hildebrand, T. & Rüeggsegger, P. A new method for the model-independent assessment of thickness in three-dimensional images. *J. Microsc.*, 1997, 185, 67
- [11] Dougherty, R. & Kunzelmann, K. Computing Local Thickness of 3D Structures with ImageJ *Microsc. Microanal.*, Cambridge University Press, 2007, 13, 1678-1679
- [12] Nielsen, L. E. Generalized equation for the elastic moduli of composite materials *J. Appl. Phys.*, 1970, 41, 4626-4627
- [13] Williamson, D. M., Drodge, D. R., Cullis, I. G., Gould, P. J. & Church, P. D. Towards a Fundamental Understanding of the Thermomechanical Response of Damaged Polymer Bonded Energetic Materials, *Proceedings of the 14<sup>th</sup> International Symposium on Detonation*, Coeur d'Alene, ID, 2010
- [14] Gustafsson, S. E. Transient plane source techniques for thermal conductivity and thermal diffusivity measurements of solid materials *Rev. Sci. Instrum.*, 1991, 62, 797-804

- > Final printed area will be of 15 cm x 23 cm. The proceedings will be made of A4 colour prints.
- > Publication limited to 8 pages.
- > Submit 2 electronic files, a .doc file and a .pdf file, along with the copyright agreement form, p. 3 of this file, by October 15, 2010 : bahlouli@unistra.fr

## Effect of strain rate and temperature on the compression yielding of polypropylene and polypropylene copolymer

T. Gómez-del Río and J. Rodríguez

<sup>1</sup> Dpto. Ciencia e Ingeniería de Materiales. ESCET. Universidad Rey Juan Carlos. C/Tulipán s/n 28933 Móstoles (Madrid), España

**Abstract.** The mechanical behaviour of solid amorphous and semi-crystalline polymers is greatly affected by strain rate and temperature. There are many studies on the yielding behaviour of these materials but most of them are only validated for amorphous polymers and at low and medium strain rates. In this work, uniaxial compression tests were carried out on homopolymer polypropylene and copolymer of polypropylene with 9% of polyethylene. The experiments were performed at a wide range of strain rates ( $10^{-4}$ - $10^3$  s<sup>-1</sup>) and temperatures (25-100 °C). A split-Hopkinson pressure bar was used for high strain rate tests. The yield stress is found to increase with decreasing temperature and with increasing strain rate. This increment is much more significant for high strain rates. The strain rate/temperature superposition principle was assumed and a new formulation based on the cooperative model was used to fit the experimental data of the compressive yield stress. Experimental data were fitted to equations based on the Ree-Eyring and cooperative models for semicrystalline polymers.

### 1. INTRODUCTION

The increased application of polymers for light-weight structures has led to renewed interest in the study of mechanical behaviour at different loading rates and temperatures. Many molecular theories have been proposed for the prediction of the yield stress of polymers. These models consider the yield behaviour to be thermally activated and take into account strain rate and temperature influences. The first model known is the Eyring theory [1]. Although this theory was developed for shear induced in viscous fluid, it has been successfully used to describe the yielding process of solid polymers. Macroscopic deformation is assumed to be the result of basic processes and yielding consists of jumps of macromolecular segments from one equilibrium position to another with a potential energy barrier of height  $\Delta H$ . According to Ree-Eyring model [2] several processes may be required to obtain a good description in a wide range of temperatures and strain rates for non-Newtonian polymers. For many amorphous polymers, Bauwens-Crowet et al. [3-4] have shown that at least two rheological processes,  $\alpha$  and  $\beta$ , are necessary for the modelling of yield stress. The equation for the Ree-Eyring model is then given by:

$$\frac{\sigma_y}{T} = \frac{k}{V_\alpha} \left[ \ln \left( \frac{2\dot{\epsilon}}{\dot{\epsilon}_{0\alpha}} \right) + \left( \frac{\Delta H_\alpha}{kT} \right) \right] + \frac{k}{V_\beta} \sinh^{-1} \left( \frac{\dot{\epsilon}}{\dot{\epsilon}_{0\beta} \exp \left( -\frac{\Delta H_\beta}{kT} \right)} \right) \quad (1)$$

where  $k$  is the Boltzmann's constant,  $\sigma_y$  is the yield stress under uniaxial loading,  $T$  is the absolute temperature,  $\dot{\epsilon}$  is the strain rate,  $\Delta H_\alpha$  and  $\Delta H_\beta$  are activation energies for the processes  $\alpha$  and  $\beta$ , respectively,  $V_\alpha$ ,  $V_\beta$  are the two activation volumes and  $\dot{\epsilon}_{0\alpha}$  and  $\dot{\epsilon}_{0\beta}$  are pre-exponential factors that must be obtained by fitting of experimental data. Moreover the two processes acting in parallel also permits to successfully model the yield stress of semi-crystalline polymers [5], although the activation process of the crystalline part is different from those of the amorphous part of the polymer [6].

In the last years, many authors have shown the two Ree-Eyring process model can be substituted with the cooperative model of Fotheringham and Cherry [7] for the description of yield stress of both amorphous [8-

9], and semi-crystalline [10] polymer over a wide range of strain rates and temperatures. The cooperative model considers only one activation process, and postulated this process is enough to model the yielding of polymers if a new term of internal stress,  $\sigma_0$ , is also included. This internal stress is due to the elastic recovery process and depicts the past thermal history. The effect of this extra stress term will be to cause a vertical shift to the curves of the applied stress. It has also been noted that the co-operative movement of a number of polymer segments would be necessary to allow significant flow in solid polymers. If it is necessary for  $n$  segments to move co-operatively during yielding process, the equation of the cooperative model will be given by:

$$\frac{\sigma_y}{T} = \frac{\sigma_0}{T} + \frac{2k}{V} \sinh^{-1} \left[ \frac{\dot{\epsilon}}{\dot{\epsilon}_0 \exp\left(-\frac{\Delta H}{kT}\right)} \right]^{1/n} \quad (2)$$

In the recent years, Richeton et al. [11] developed a formulation of the cooperative model identifying the activation energy as the energy of the  $\beta$  relaxation and extended the cooperative model to amorphous polymers above the glass transition temperature. Richeton et al. [12] validated this model for three amorphous polymers (PC, PMMA and PVC) for temperatures ranging from -40 °C to temperatures above the glass transition temperature and in a range of strain rate from  $10^{-4}$  to impact strain rates.

Based on the Richeton model, Gueguen et al. [13] considered that semi-crystalline polymers, unlike amorphous ones, are less sensitive to wide variations of stiffness above the glass transition and below the melt temperature. As a consequence, they used the classical form of the cooperative model with the Arrhenius' law for temperatures above the glass transition in semi-crystalline polymers.

$$\frac{\sigma_y}{T} = \frac{\sigma_i(0) - mT}{T} + \frac{2k}{V_{eff}} \sinh^{-1} \left[ \frac{\dot{\epsilon}}{\dot{\epsilon}_0 \exp\left(-\frac{\Delta H_{eff}}{kT}\right)} \right]^{1/n} \quad (3)$$

where  $\Delta H_{eff}$  and  $V_{eff}$  are the effective activation energy and activation volume, respectively. This parameters are obtained as a combination of activation parameters of the amorphous phase,  $\Delta H_\beta$  and  $V_\beta$ , an of the crystalline phase,  $\Delta H_c$  and  $V_c$ .

The yield stress of semi-crystalline polymers was also adequately described by a model combining thermal nucleation of dislocations in the crystals with Ree-Eyring dependence for yielding in the amorphous phase, all with reasonable parameter values [14]. Scogna et al. validated the model for low-density polyethylene and five ethylene-methacrylic acid copolymers of varying MAA content. By simple addition of the crystalline and amorphous contributions to yield, the final equation proposed was:

$$\frac{\sigma_y}{T} = \underbrace{\frac{1}{T} \frac{K(T)B}{\pi r_o} \exp\left[\frac{2\pi\Delta G^*(\dot{\epsilon})}{K(T)B^2 l_c} - 1\right]}_{\text{crystal slip contribution } \sigma_c} + \underbrace{\sum_i \frac{k}{V_i} \sinh^{-1} \left[ \frac{\dot{\epsilon}}{\dot{\epsilon}_{0,i}} \exp\left(\frac{\Delta H_i}{kT}\right) \right]}_{\text{amorphous contribution}} \quad (4)$$

where  $K(T)$  is the temperature-dependent shear modulus of the slip plane,  $B$  is the magnitude of the Burgers vector,  $r_o$  is the dislocation core radius,  $l_c$  is the crystal thickness and  $\Delta G^*$  is the energy barrier for the nucleation event, for the crystalline phase. For the amorphous phase, a Ree-Eyring like model was chosen and the subindex "i" appears taking into account different relaxation processes.

To the authors' knowledge, works on yielding behaviour of polypropylenes studied only the strain rate dependence at low strain rates. The Eyring model can fit well the response of the polymers in this range but it can not reproduce the huge increase of yielding stress observed at high strain rates. In this work, the compression behavior of two semi-crystalline polypropylenes, a homopolymer and an ethylene-propylene block copolymer, is analyzed in a wide range of strain rates ( $10^{-3}$ - $10^3$  s $^{-1}$ ), and above the glass transition temperature (20-100 °C). The applicability of the previously described models will be evaluated in the light

of the general acceptance of the strain rate-temperature superposition principle. Finally, the data has been fitted using different models, obtaining all the material parameters involved and comparing the results.

## 2. MATERIALS AND CHARACTERIZATION

### 2.1. Materials

The materials under study were an isotactic polypropylene homopolymer (PP) and an ethylene-propylene block copolymer (PB), supplied by REPSOL in the form of rectangular plates of size 150 x 25 x 6 mm<sup>3</sup>. The PP homopolymer is characterized as having high isotacticity (90%) and the copolymer PB a nominal ethylene content of 9% wt.

A Mettler Toledo balance, with  $\pm 0.001$  mg, equipped with a density determination kit by means of the buoyancy technique, was used to measure the density of the polypropylenes. Table 1 collects the data obtained.

**Table 1.** Densities obtained from water and ethanol immersion for polypropylene homopolymer (PP) and copolymer ethylene-propylene (PB).

	Density (g/cm <sup>3</sup> )	
	water	ethanol
PP	0.884 $\pm$ 0.001	0.8948 $\pm$ 0.0003
PB	0.875 $\pm$ 0.001	0.8875 $\pm$ 0.0006

Dynamic mechanical properties were determined with a TA Instrument DMTA Q800 operating in single cantilever mode with three oscillation frequencies. The apparent melting temperature,  $T_m$ , the crystallinity temperature,  $T_c$ , and the crystallinity index,  $\lambda$ , of the two samples were measured via differential scanning calorimetry (DSC) using a Mettler-Toledo (model DSC822) equipment. Table 2 collects the data obtained from the DSC and DMTA measurements. The block copolymer presents two values of these properties, first corresponding to propylene and second of ethylene. All the measured values are in accordance with data reported in the literature [15, 16].

**Table 2.** Thermal and morphological parameters obtained from DSC, DMTA and XRD measurements.

	DSC					DMTA						
	$T_m$ (°C)		$T_c$ (°C)		$\lambda_{PP}$	$\lambda_{PE}$	$\Delta H_m$ (J/g)	$T_g$ (°C)	$\Delta H_\beta$ (kJ/mol)			
PP	167		113		47.3	--	89.9	12	384.2			
PB	169	115	38.5	1.1	38.5	1.1	73.1	3.2	-46	12	406.4	276.2

### 2.2 Low strain rate compression tests

Quasi-static tests were carried out in a MTS universal testing machine with a load frame of 100 kN. The high temperature test was conducted placing the load train (hinges, compression plates and sample) inside an environmental chamber (MTS 651.06-03).

Samples were tested at three different temperatures: 20, 50 and 100 °C (all above the polypropylene glass transition temperature), and at different strain rates ranging from 10<sup>-3</sup> s<sup>-1</sup> to 10<sup>-1</sup> s<sup>-1</sup>. Right cylinders were machined with dimensions of 6 mm in thickness and 12 mm in diameter. Molybdenum disulphide grease was spread on the specimen surface in contact with the compression plates to minimize friction.

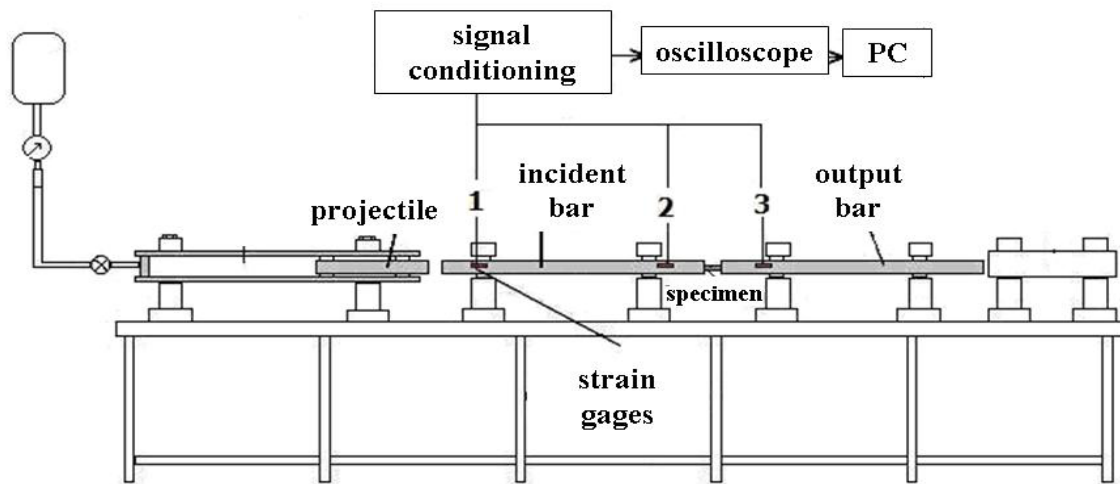
### 2.3 High strain rate compression tests

Dynamic uniaxial compression tests were conducted at high strain rates of about 1000-4000 s<sup>-1</sup> using a split-Hopkinson pressure bar (SHPB) setup and at room temperature, 50 °C and 100 °C. The length (l) to

sample diameter ( $d$ ) ratio used in high strain rate tests must be carefully chosen to ensure that stress equilibrium is achieved in the loading of the sample. The sample geometry at low and high strain rate tests is equal in order to avoid possible changes due to size effects. The length to diameter ratio,  $l/d$ , of the specimens must be carefully chosen to ensure that stress equilibrium is achieved during the loading stage of the sample. To minimize friction, the specimen's surfaces in contact with the compression bars were lubricated before mechanical loading.

The SPHB device consists of a gas gun, an input bar and an output bar, the supports, and the data acquisition system. Both bars are made of steel, 20 mm in diameter and lengths of 1.2 m and 0.8 m for the input and output bars, respectively. The air gun impels a third bar of approximately 0.3 m in length against the input bar where, as a consequence of the impact, a compression pulse is generated. It travels along the input bar up to the specimen, where is partially reflected and partially transmitted to the output bar. To measure the incident, reflected and transmitted pulses, strain gauges (VISHAY J2A-06-S047K-350) are attached to the bars. The strain gage signals are recorded using a VISHAY 2200 conditioner together with a TEKTRONIX TDS 420A digital oscilloscope. A diagram of the dynamic device is shown in Figure 1.

Figure 1. Schematic representation of the SHPB setup.



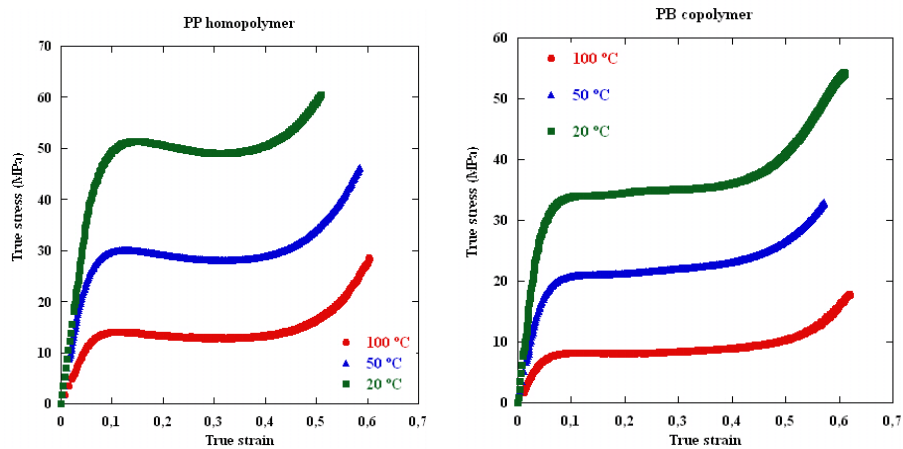
For the high temperatures, a new heating device was developed consisting in a heater ring, connected to a temperature controller and a thermocouple. The ring was located around the bars without touching them avoiding possible friction effects.

### 3. RESULTS

Experimental results can be classified according the influence of strain rate, temperature and ethylene content. Concerning the strain rate of the tests, an increase of yield stress with increasing strain rate can be observed for both materials. Many authors [11, 13, 17-23] believe the increase with strain rate is due to a decrease in the molecular mobility of the polymer chains by making the chains stiffer due to secondary molecular processes. A similar increase of yield stress would be observed at low temperatures, where the yield stress increases dramatically as temperature goes down near the secondary relaxation temperature,  $T_{\beta}$ .

Regarding the stress-strain curves, both polymers exhibit a similar mechanical response, at least at low strain rates: an initial elastic region followed by yielding, then a decrease in the stress level associated with softening and, finally, a marked strain hardening. This last stage can not be appreciated in the high strain rates curves, possibly because the compressive pulse is not long enough. The compression stress-strain curves at a constant strain rate of  $0.0018 \text{ s}^{-1}$  for various temperatures are given in Figure 2.

**Figure 2.** Uniaxial compression true stress-strain curves for the PP and PB materials at strain rate of  $0.0018 \text{ s}^{-1}$  over the range of temperatures (20-100°C).



The yield stress and the Young's modulus are found to decrease with increasing temperature for both polymers. This decrease is a bit more marked in the PP homopolymer. Both polymers show strain hardening at all the temperatures. In the case of the homopolymer the strain hardening comes after a small softening, but in the copolymer, this softening has almost vanished.

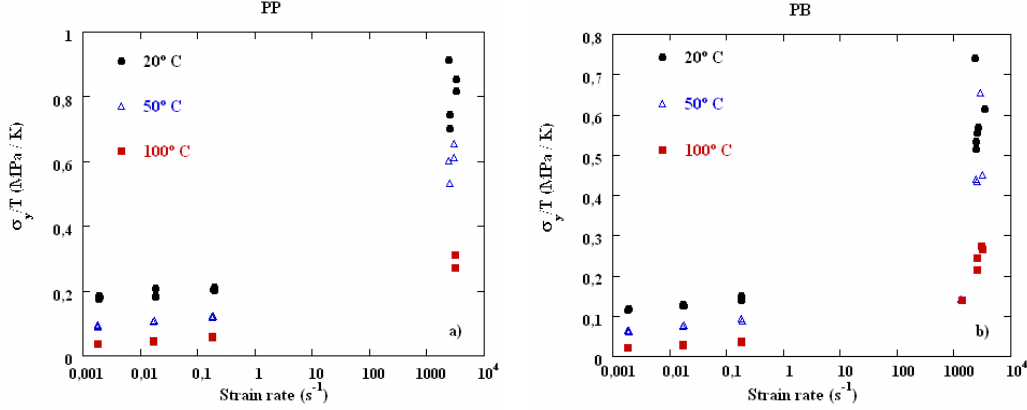
The effect of the ethylene content can be determined comparing stress-strain curves of compression tests for the copolymer and polypropylene homopolymer. PP is stiffer and has a high yield stress than the copolymer. Additionally, homopolymer is also more affected by temperature and strain rate variations.

#### 4. MODELLING THE YIELD STRESS

The experimental data of yield stress for PP and PB were normalized by the absolute temperature and plotted against the strain rate in a logarithmic scale. The results are shown in Figure 3. There appear to be two asymptotes: one at low strain rates and one at high strain rates. This supports the notion that two microstructural processes are relevant over the range of conditions studied. The behavior of the copolymer is similar to that of the homopolymer: at lower strain rates (or, equivalently, higher temperatures), there exists a low-slope regime while, at higher rates (or lower temperatures), the slope increases dramatically.

As shown, PP and PB are strain rate and temperature sensitive materials. Assuming that they verify the well known strain rate-temperature superposition principle, i. e., an increase in temperature will have the same effect on the yield stress as a decrease in strain rate, the Eyring plots shown in Figure 3 can be horizontal and vertical shifted to create a master curve for a reference temperature chosen as  $T_{ref}=20 \text{ °C}$ . Then, the master curve should be used to adjust the values to different Ree-Eyring based models which need several parameters.

**Figure 3.** Eyring plots at different temperatures: (a) PP and (b) PB.



The expression of these shift factors,  $s_x$  and  $s_y$ , for the Ree-Eyring, Scogna and Gueguen models are given by equation 5, respectively. In fact all the shifts follow a linearized Arrhenius law as Bauwens-Crowet et al. [3] proposed, except for the vertical shift in the Scogna model where  $\sigma_c$  depends on the temperature. In fact, the three models are very similar although each one gives different meaning to the parameters in their equations. The shifts equations can be expressed for each model as:

$$s_x = \underbrace{\left( \frac{\Delta H}{\beta} \right) \left( \frac{1}{T} - \frac{1}{T_{ref}} \right)}_{\text{Ree-Eyring}} = \underbrace{\left( \frac{\Delta H_{eff}}{\ln(10)R} \right) \left( \frac{1}{T} - \frac{1}{T_{ref}} \right)}_{\text{Gueguen}} = \underbrace{\left( \frac{\Delta H}{\ln(10)R} \right) \left( \frac{1}{T} - \frac{1}{T_{ref}} \right)}_{\text{Scogna}} \quad (5)$$

$$s_y = - \underbrace{\left( \frac{\Delta H_{\alpha} - \Delta H_{\beta}}{V_a} \right) \left( \frac{1}{T} - \frac{1}{T_{ref}} \right)}_{\text{Ree-Eyring}} = - \underbrace{\sigma_i(0) \left( \frac{1}{T} - \frac{1}{T_{ref}} \right)}_{\text{Gueguen}} = - \underbrace{\left( \frac{\sigma_c(T)}{T} - \frac{\sigma_c(T_{ref})}{T_{ref}} \right)}_{\text{Scogna}}$$

All the parameters in these shifts have been defined previously. For the Scogna model, only one Eyring process has been assumed for the polymers studied and so, the subscript “1” in equation 4 has been omitted for clarity. In the Scogna model, values of some parameters have been taken from polyethylene data [14]. B the burgers vector is assumed to be equal to the polyethylene c-axis dimensions of 0.154 nm and the dislocation core radius  $r_0$  is equal to 1 nm. The shear modulus, K has been considered constant in the range of temperatures studied, 1.52 GPa.

In Figure 4 the master curve created at the reference temperature 20 °C, using both horizontal and vertical shifts is shown. The values of the horizontal and vertical shifts, and so those of the model parameters ( $V_a$ ,  $\Delta H_{\alpha}$  and  $\Delta H_{\beta}$ ,  $\Delta H_{eff}$  and  $\sigma_i(0)$ , and B, K,  $r_0$ ,  $l_c$  and  $\Delta H$ ) were finally selected to provide the best fit of the experimental data (Table 3). An acceptable agreement between experiments and the three models considered is achieved (Figure 4).

**Figure 4.** Master curve built at room temperature for polypropylene homopolymer (PP) and the 9wt.% ethylene copolymer (PB).

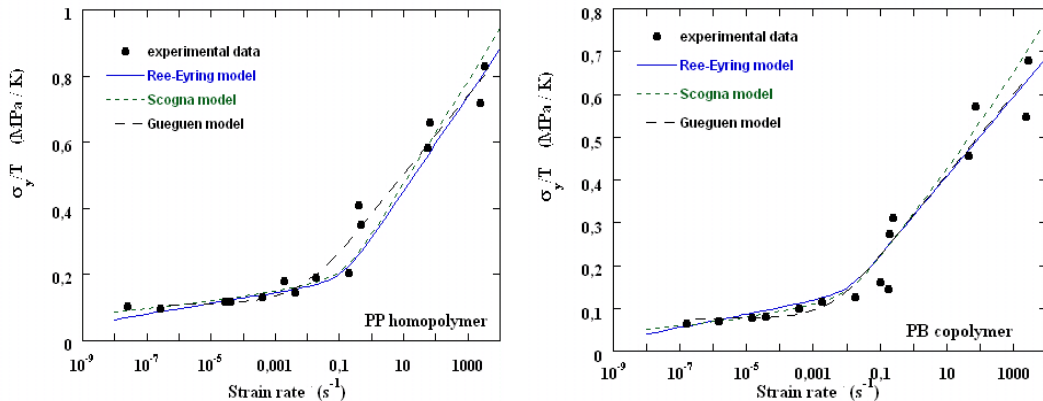


Table 3 shows the model parameters obtained for materials under study, PP and PB. They are in the same order of magnitude than those found in bibliography for other thermoplastics, such as PET and polyethylene [13, 14]. The parameter  $n$  is related to the number of segments involved in the plastic deformation. Previous works suggested that higher crystalline percentage implies more cooperative segmental motion [24], and this agrees with the smaller value of  $n$  for PB. The activation volume,  $V_{\text{eff}}$ , is in the order of  $10^{-29} \text{ m}^3$ , the same order as Dasari and Misra [25] for activation volumes calculated using Eyring model. The pre-exponential strain rate  $\dot{\epsilon}_0$  is roughly in the same order of magnitude as the Debye frequency ( $10^{14}$ - $10^{17}$  Hz). The activation energies in the models are smaller than those obtained for the  $\beta$  activation energy by DMTA (Table 2), but they are in the same order of magnitude. The values are also in the same order of those obtained by Vu-Khanh and El Majdoubi [26] for polypropylenes with different crystalline percentage. The values of the parameters  $\sigma_i(0)$  and  $m$  are consistent with the relationship predicted by Rault [6] for semi-crystalline polymers.

**Table 3.** Summary of the models parameters.

Gueguen model			Ree-Eyring model			Scogna model		
Parameter	PP	PB	Parameter	PP	PB	Parameter	PP	PB
$n$	2.27	1.69	$V_\alpha \text{ (nm}^3\text{)}$	1.97	2.04	$\dot{\epsilon}_c \text{ (s}^{-1}\text{)}$	$2.1 \cdot 10^1$	$3.5 \cdot 10^1$
$V_{\text{eff}} \text{ (nm}^3\text{)}$	0.23 4	0.40 2	$\dot{\epsilon}_{0\alpha} \text{ (s}^{-1}\text{)}$	$9.64 \cdot 10^2$	$3.22 \cdot 10^2$	$l_c \text{ (nm)}$	3.01	2.18
$\sigma_i(0) \text{ (MPa)}$	80	60	$\Delta H_\alpha \text{ (kJ mol}^{-1}\text{)}$	194	184	$\Delta H \text{ (kJ mol}^{-1}\text{)}$	100	110
$m \text{ (MPa/K)}$	0.165	0.129	$V_\beta \text{ (nm}^3\text{)}$	0.251	0.412			
$\dot{\epsilon}_0 \text{ (s}^{-1}\text{)}$	$1.68 \cdot 10^1$	$3.46 \cdot 10^1$	$\dot{\epsilon}_{0\beta} \text{ (s}^{-1}\text{)}$	$1.96 \cdot 10^1$	$8.83 \cdot 10^1$			
$\Delta H_{\text{eff}} \text{ (kJ mol}^{-1}\text{)}$	100	110	$\Delta H_\beta \text{ (kJ mol}^{-1}\text{)}$	100	110			

## 5. CONCLUSIONS

Compression tests at different temperatures, ranging from room temperature to 100 °C, (all above the glass transition temperature) and strain rates ( $10^{-3}$ - $10^3 \text{ s}^{-1}$ ) have been carried out in two polypropylenes, a homopolymer and an ethylene-propylene block copolymer. From the experimental results the following conclusions can be ascertained:

- Polypropylenes under study show a significant increase of their compression yield stress with strain rates. This increase is accentuated at very high rates of strain, such as those characteristic of Hopkinson bar experiments. Temperature produced, as expected, the opposite tendency in a new verification of the time – temperature superposition principle.
- Under all conditions analyzed, the ethylene-propylene block copolymer, PB, presents lower values of compression yield stress than the polypropylene homopolymer, PP. Nevertheless, its sensibility to strain rate and temperature is also inferior.
- Several models describing the yield stress of semi-crystalline polymers and its dependence on temperature and strain rate were compared. Although the physical meaning of parameters and equations are different, the shape of the final curve is roughly similar.

## References

- [1] Eyring H. “Theory of non-Newtonian flow. I. Solid plastic system.” J Chem Phys 4 (1936), 283-291.
- [2] Ree T, Eyring H. “Viscosity, plasticity and diffusion as examples of absolute reaction rates”. J Appl Phys 26 (1955) 793-800.

- [3] Bauwens–Crowet C, Bauwens JC, Homès G. “Tensile yield-stress behavior of glassy polymers”. *J Polym Sci A2*, 7 (1969) 735-742.
- [4] Bauwens–Crowet C, Bauwens JC, Homès G. “Tensile yield-stress behavior of poly(vinyl chloride) and polycarbonate in the glass transition region”. *J Polym Sci A2*; 7 (1969) 1745-1754.
- [5] Truss R.W., Clarke P.L., Duckett R.A. “The dependence of yield behavior on temperature, pressure, and strain rate for linear polyethylenes of different molecular weight and morphology”. *J Polym Sci, Polym Phys* 22 (1984) 191-209.
- [6] Rault J. “Yielding in amorphous and semi-crystalline polymers: the compensation law”. *J of non-crystalline solids* 235-237 (1998) 737-741.
- [7] Fotheringham D, Cherry BW. “The role of recovery forces in the deformation of linear polyethylene”. *J Mater Sci* 13 (1978) 951-964
- [8] Povolo F., Hermida E.B. “Phenomenological description of strain rate and temperature-dependent yield stress of PMMA”. *J Appl Polym Sci* 58 (1995) 55-68.
- [9] Povolo F., Schwartz G., Hermida E.B. “Temperature and strain rate dependence of the tensile yield stress of PVC”. *J Appl Polym Sci* 61 (1996) 109-117.
- [10] Brooks N.W.J., Duckett R.A., Ward I.M. “Modeling of Double Yield Points in Polyethylene - Temperature and Strain-rate Dependence”, *J Rheol* 39 (1995) 425-436.
- [11] Richeton J, Ahzi S, Daridon L, Rémond Y. “A formulation of the cooperative model for the yield stress of amorphous polymers for a wide range of strain rates and temperatures”. *Polymer* 46 (2005) 6035-6043.
- [12] Richeton J, Ahzi S, Vecchio KS, Jiang FC, Adharapurapu RR. “Influence of temperature and strain rate on the mechanical behavior of three amorphous polymers: Characterization and modeling of the compressive yield stress”. *Int J of Solids and Structures* 43 (2006) 2318-2335.
- [13] Gueguen O, Richeton J, Ahzi S and Makradi A. “Micromechanically based formulation of the cooperative model for the yield behaviour of semi-crystalline polymers”. *Acta Materialia* 56 (2008) 1650-1655.
- [14] Scogna R.C. and Register R.A. “Rate-dependence of yielding in ethylene-methacrylic acid copolymers”. *Polymer* 49 (2008) 992-998.
- [15] Moore EP Jr.: *Polypropylene Handbook*; Hanser Publications, Vienna, 1996.
- [16] Karger-Kocsis, J. *Polypropylene: an A-Z reference*; Kluwer Academic Publishers, Dordrecht, 1999.
- [17] Bauwens J.C. “Yield condition and propagation of Lüder’s lines in tension–torsion experiments on poly(vinyl chloride)” *Journal of Polymer Science: Part A-2* 8 (1970) 893–901.
- [18] Bauwens-Crowet, C. “The compression yield behaviour of polymethyl methacrylate over a wide range of temperatures and strain-rates” *Journal of Materials Science* 8 (1973) 968–979.
- [19] Rietsch F. and Bouette B. “The compression yield behaviour of polycarbonate over a wide range of strain rates and temperatures” *European Polymer Journal* 26 (1990) 1071–1075.
- [20] Xiao C., Jho J.Y. and Yee A.F. “Correlation between the shear yielding behaviour and secondary relaxations of bisphenol A polycarbonate and related copolymers” *Macromolecules* 27 (1994) 2761–2768.
- [21] Chen L.P., Yee A.F. and Moskala E.J. “The molecular basis for the relationship between the secondary and mechanical properties of a series of polyester copolymer glasses”, *Macromolecules* 32 (1999) 5944–5955.
- [22] Brulé B., Halary J.L. and Monnerie L. “Molecular analysis of the plastic deformation of amorphous semi-aromatic polyamides”, *Polymer* 42 (2001) 9073–9083.
- [23] Rana D., Sauvant V. and Halary J.L. “Molecular analysis of yielding in pure and antiplasticized epoxy-amine thermosets”, *Journal of Materials Science* 37 (2002) 5267–5274.
- [24] Mallick PK, Zhou Y, “Yield and fatigue behaviour of polypropylene and polyamide-6 nanocomposites”. *J Mater Sci* 38 (2003) 3183-3190.
- [25] Dasari A., Misra R.D.K., “On the strain rate sensitivity of high density polyethylene and polypropylenes”. *Mater Sci Eng A* 358 (2003) 356-371.
- [26] Vu-Khank T., El Majdoubi M., “Entropy change with yielding and fracture of polypropylene”. *Theor Appl Fract Mech* 51 (2009) 111-116.

## BEHAVIOUR AND RUPTURE MODELS FOR POLYPROPYLENE IN DYNAMIC.

F.Lauro<sup>1, 2, 3</sup>, B. Bennani<sup>1, 2, 3</sup> and A. F. Epee<sup>1, 2, 3</sup>

<sup>1</sup> Univ Lille Nord de France, F-59000 Lille, France

<sup>2</sup> UVHC, LAMIH, F-59313 Valenciennes, France

<sup>3</sup> CNRS, FRE 3304, F-59313 Valenciennes, France

**Abstract.** This paper deals with a viscoelastic-viscoplastic model for semi-crystalline polymers in crash application. A polymer behaviour model is implemented in the commercial PAM CRASH © code thanks to a user material card. Global variables (load, displacement) and local variables (strain) are validated on notched tensile specimens by comparing the numerical responses with data obtained by digital image correlation. An experimental fracture criterion is determined by means of the correlation image techniques for different stress states and strain rates.

### 1. INTRODUCTION

Crashworthiness simulation is a major factor that has enabled automotive manufacturers to achieve a 30 to 50% reduction in development time and costs over the past decade. Today, this technology is a mature and proven design tool for the development of conventional 'ductile' automotive steel where the predominant energy absorption mechanisms are plastic bending and collapse. However, demand for greater weight savings and occupant protection has necessitated new design concepts and the use of lightweight materials that often have high ductility and a complex failure. The polymer materials are good candidates to reach such objectives. There have been many studies on polymer in recent years, especially in quasi static states, two approaches are generally used. A phenomenological one, based on the models previously developed for metals to introduce the viscoplasticity [1-4] and physical ones where the strain hardening of a semi-crystalline polymer is interpreted as entropic forces needed to orient the macromolecular chains connected by cross-links [5-7]. Nevertheless, the isochoric deformation is basically the main assumption used by the previous authors due to the difficulty of obtaining experimental data by classical extensometry with specimens which present an early necking. To take the pressure dependency of the polymer matrix into account, some studies have been done by introducing damage models to overcome this problem. The main model used for damage is the Gurson model [8, 9] which describes the growth of spherical cavities under hydrostatic stress [10-12]. This introduction results in very complex models in which parameters are difficult to identify for automotive application, like the length of the macromolecular chain, the number of rigid links per chain, the initial porosity, etc. The phenomenological approach is therefore more suitable if the non isochoric deformation is taken into account and if a new technique is used to identify behaviour laws at constant strain rates for a large strain rate range [13]. In this work, the behaviour of a semi-crystalline polypropylene to which talc particles are added (20% of the volume) is modeled by a non linear viscoelasticity model until a plasticity criterion which is pressure dependent and a viscoplastic model which represents the structural hardening. During the plastic deformation, the non isochoric deformation is introduced by means of a non associative return on the yield surface. All these models are implemented in a commercial explicit finite element code PAM CRASH c and are used for a polypropylene under various dynamic loadings from 0.01 to 260 s<sup>-1</sup>. In this paper, the different models representing the complete behaviour of a semi-crystalline polymer are presented. The parameters of a polypropylene material are identified by means of the SEË method [13] and the global (force) and local (total strain) variables are compared experimentally and numerically in the case of a non homogeneous strain field obtained with a notched tensile specimen under dynamic loading. Very good correlations are obtained for both variables. The aim of this work is also to provide a new failure criterion which depends on the triaxiality stress ratio and also of the strain rate. This criterion is identified on bulk specimen tests. These tests are realized on a large range of strain rate and for different triaxiality stress ratio so as to be used for various conditions. The triaxiality stress ratio range is achieved by realizing tensile, notched tensile, shear and compressive tests.

Identification of equivalent failure strain is realized by new measurement techniques like 2D and 3D digital image correlation.

## 2. MATERIAL MODEL FOR POLYPROPYLENE

During dynamic strain loading, the semi-crystalline polymer shows an elastic behaviour phase which depends on strain rate, and a non isochoric viscoplastic behaviour. A elastic plastic transition limit, different under tensile and compressive loadings, splits the two phases.

### 2.1. Material behaviour model

The viscoelastic behaviour law is described by

$$\sigma_{ij} = \frac{E(\dot{\bar{\epsilon}})}{(1+\nu)} \epsilon_{ij} + \frac{E(\dot{\bar{\epsilon}})\nu}{(1+\nu)(1-2\nu)} \epsilon_{kk} \delta_{ij} \quad (1)$$

With

$$E = (E_0 + \eta \dot{\bar{\epsilon}}^k) \quad (2)$$

where  $E_0$  is the quasi-static elastic modulus,  $\eta$  is the consistency parameter,  $k$  is the material coefficient,  $\epsilon_{ij}$  are the strain tensor components and  $\dot{\bar{\epsilon}}$  is the equivalent strain rate. The viscoplastic part of the behaviour law is described by the following modified G'Sell stress

$$\sigma_M = \sigma_y + k_p \left( 1 - \exp\left(-w \bar{\epsilon}^p\right) \right) * (h_1 \bar{\epsilon}^p + h_2 \bar{\epsilon}^{pn}) * (\dot{\bar{\epsilon}}^p)^m \quad (3)$$

with  $\sigma_y$  the elastic yield stress,  $k_p$  the consistency of the material,  $\bar{\epsilon}^p$  the equivalent plastic strain,  $w$  the sensitivity of tangent modulus after yield stress,  $h_1$ ,  $h_2$  and  $n$  the parameters characterizing hardening stress,  $\dot{\bar{\epsilon}}^p$  the equivalent plastic strain rate and  $m$  the coefficient of sensitivity to strain rate.

### 2.2. Constitutive law

To represent the asymmetry of the elastic plastic transition phase under tensile and compressive loadings, the following Drucker-Pragger yield criterion is used:

$$f = \alpha I_1 + \sqrt{J_2} - \sigma_y = 0 \quad (4)$$

in which  $I_1$  and  $J_2$  are the first and second stress tensor invariants,  $\sigma_y$  is the elastic yield stress and  $\alpha$  is the coefficient describing the difference under tensile and compressive loadings by

$$\alpha = \sqrt{\frac{1}{3}} \left( \frac{\sigma_c - \sigma_t}{\sigma_c + \sigma_t} \right) \quad (5)$$

Where  $\sigma_t$  and  $\sigma_c$  are respectively the elastic yield stress in tension and compression. The elastic to plastic transition limit is then predicted as follows

- if  $f < 0$  then the behaviour is elastic,
- if  $f = 0$  then the behaviour is plastic,
- if  $f > 0$  then the elastic stress is overestimated and a return to the following viscoplastic potential has to be performed.

The viscoplastic potential is defined by

$$\Omega = \bar{\sigma} - \sigma_M \quad (6)$$

in which  $\sigma_M$  is the modified G'Sell stress defined in equation 3 and  $\bar{\sigma}$  is the Drucker-Pragger equivalent stress defined by

$$\bar{\sigma} = \frac{\beta \sqrt{3} I_1 + \sqrt{3} J_2}{\beta \sqrt{3} + 1} \quad (7)$$

in which the coefficient  $\beta$  is equal to  $\alpha$ . In this case, the viscoplastic potential is called  $\Omega_\alpha$ . For the semi-crystalline polymer in this study, the coefficient  $\beta$  has to be identified by inverse technique with regards to experimental measurements to correctly predict the volume variation. The computation of the plastic strain

is performed with an identified coefficient  $\beta$  different to  $\alpha$  by using a non associative return to the viscoplastic potential. The viscoplastic potential is then called  $\Omega_\beta$ .

### 3. THE SEE METHOD

The identification of viscoplastic model for polymer is always depending on the early necking appearance. Then the strain rate and strain states are heterogeneous in the tensile specimen which leads to identification problems for the behaviour after the necking point.

#### 3.1. Material behaviour law

The viscoplastic behaviour is defined by modified G'sell's stress expressed in equation 3. It is an additive formulation of the stress value starting with elastic yield stress. The second term describes the hook at the beginning of the plasticity and the hardening of the macromolecule stretch in function of the strain rate. For polymers, the necking appears very early in the process of deformation, around the peak of the stress in the hook of the behaviour law. This strain localization leads to non uniform strain and strain rate fields on the tensile specimen and the behaviour law obtained by classical measurement techniques is therefore not accurate enough because the behaviour laws are not obtained for constant strain rates. To overcome this problem, a specific method called SEE method is used [13]. The idea is to measure, throughout the test, the evolution of the local total strain, local total strain rate and local uniaxial stress in different areas of a tensile specimen without controlling the speed of the machine. Some hypothesis must then be made in order to exploit these results. First of all, the digital image correlation measures the displacement field occurring on the surface of the specimen between two pictures, either by studying the natural observed texture of the material or by using the artificial one obtained by painting the top surface of the specimen with black and white colours in order to obtain different grey scale levels.

The picture is defined by a matrix in which each cell represents a pixel of the video. The accuracy of the displacement measurement depends on the quality of the grey scale pattern. The picture is defined by a matrix in which each cell represents a pixel of the video CCD or CMOS digitizers and its value varies from 0 (white color) to 255 (black color) in the case of 8-Bits code. The repetitiveness of the painting application has to be checked to avoid dispersions due to grey scale patterns. The specimen is divided in the DIC analysis in square areas which are called ZOI (Zone Of Interest). The Green Lagrange in-plane strain tensor ( $\epsilon$ ) is deduced from the displacement fields of the Zone Of Interest (ZOI).

The strain field at the fracture initiation and propagation can be computed if the frame per second of the video enables one to observe the fracture phenomena. A hypothesis on the material behaviour (incompressibility, transverse isotropy) has to be made to calculate the through thickness strain  $\epsilon_{33}$  in order to deduce the tensile stress  $\sigma_{11}$  in each ZOI by using

$$\sigma_{11} = \frac{F}{S_0} e^{\epsilon_{22} + \epsilon_{33}} \quad (8)$$

in which  $F$  is the force through the ZOI transverse section,  $S_0$  is the initial transverse section,  $\epsilon_{22}$  is obtained by digital image correlation and  $\epsilon_{33}$  is the transverse strain obtained by calculation hypothesis ( $\epsilon_{11} + \epsilon_{22} + \epsilon_{33} = 0$  in case of incompressibility or  $\epsilon_{22} = \epsilon_{33}$  in case of transverse isotropy). The current section of the specimen throughout the test is then calculated by the sum of the section of each ZOI along the cross section. For strain rate sensitive material, the equivalent plastic strain rate is calculated by backward finite difference. For each ZOI, the triple point  $\epsilon_{11}$ ,  $\sigma_{11}$ ,  $\dot{\epsilon}_{11}$  is plotted in the space of stress, plastic strain and plastic strain rate to form the SEE (Sigma, Epsilon, Epsilon dot) material behaviour surface (Figure 1a). The material behaviour laws are deduced by cutting the material behaviour surface at the desired plastic strain rates. The results obtained by this cutting are a set of curves defining the behaviour of the material for a large plastic strain rate range as well as for a large plastic strain range particularly after necking (Figure 1b).

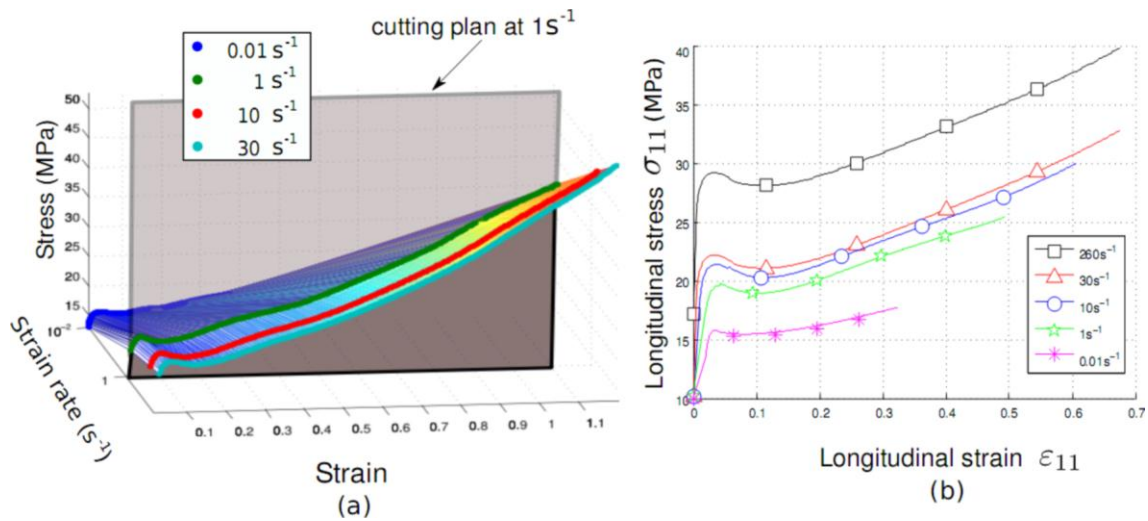


**Figure 1.** a) material behaviour surface and b) the material behaviour laws at constant strain rate.

The material parameters of the viscoplastic behaviour law (Equation 3) are then determined by using an optimization loop (Table 1). Based on the results found previously, a direct identification is made by means of a minimization of a least square function and gives an analytical model which describes the behaviour laws of the polymer for large strains and strain rates.

**Table 1.** Material parameters of the viscoplastic behaviour law.

$K_p$ (Mpa)	w	h1	h2	n	m
9.95	187	-30.8	31.95	1.026	0.118

#### 4. DYNAMIC TENSILE TEST WITH NOTCHED SPECIMEN

A notched specimen presented in figure 2, for which the material model has been identified by the SEÉ method, is modelled in the part out of grips of the tensile machine, tested at 0.25 m/s and studied by DIC (Figure 2).

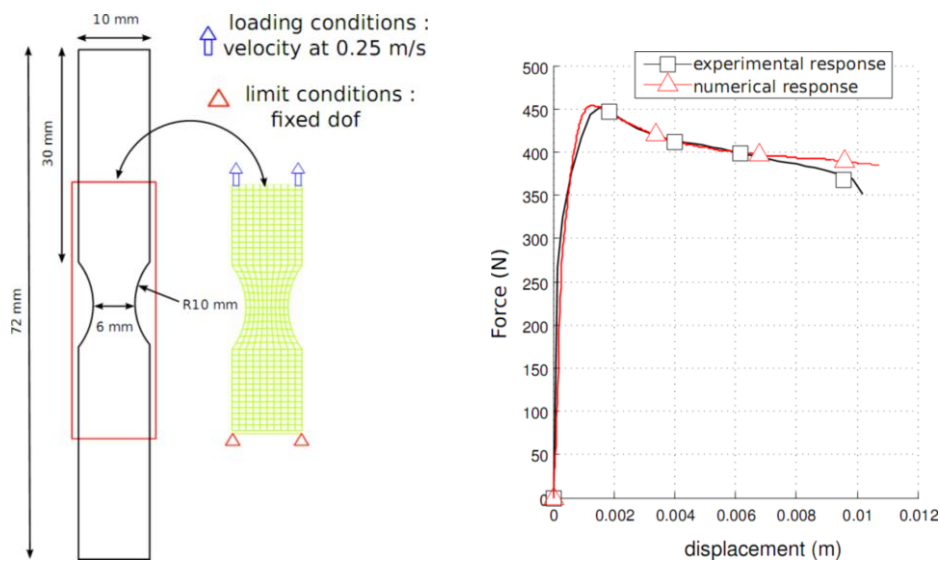


**Figure 2.** Experimental and numerical test conditions and results

The experimental force displacement response is compared to the numerical result. The strain fields and strain rate fields involved along the specimen are rather different due to the notch effect. Once again,

different behaviour laws are used during the computation for all the elements and the result is very close to the experimental data in terms of force-displacement (Figure 2). The experimental curve decreasing at the end of the elongation is due to the damage by cavity growing until failure. This effect has not yet been taken into account in the implemented model.

Concerning the strain fields, the digital image correlation gives information in the longitudinal and transversal direction of the notched specimen. Figure 3 show the comparison between DIC and FEM strain fields at the middle of the tensile test. One notes that, there is a good correlation for both longitudinal and transversal strains in terms of quality (form of the strain fields) and quantity (strain values). These results highlight the correct choice of the Drucker- Prager model as plasticity criterion and also the non associative return schema. The apparent surface (volume) observed by means of the digital image correlation in the notched area is well represented by the numerical simulation.

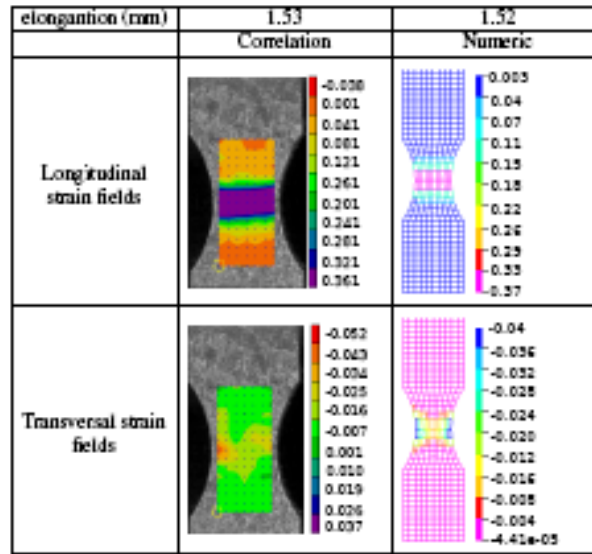


**Figure 3.** Strain fields obtained by DIC and FEM on notched specimen at 1.5 mm elongation.

## 5. RUPTURE MODEL

For the failure strain based criterion, two models are mainly used. The first one is extracted from Johnson and al works [14], this criterion gives a good description of strain rate dependency of equivalent failure strain but the triaxiality stress ratio is only managed by a monotonic function. The second model comes from Wierzbicki and al works [15]. This criterion gives a fine description of dependence on the triaxiality stress ratio of the failure strain but does not include strain rate effects.

In this paper, the shape of the future fracture criterion is defined by using various experimental tests in which the stress triaxiality ratio is different and with different speed loadings. Then, classic tensile specimens, notched specimens are used for stress triaxiality ratios over 0.33. Arcan specimens with various angles are used for stress triaxiality ratios between 0. and 0.33 and cylinder specimens are used for stress triaxiality ratios under 0. [16]. For all the tests, the true equivalent failure strain is computed in the center of the specimen so as to avoid edge effects. The true equivalent failure strain rate  $\dot{\bar{\epsilon}}_f$  is computed by back finite difference according to the two last frames, before apparent failure, obtained by digital image correlation. With all the tests, an equivalent fracture strain surface is then obtained in the space of the stress triaxiality ratio, the strain rate and the equivalent fracture strain (Figure 4). The failure criterion must be stress triaxiality dependent as presented in figure 5 but also strain rate dependent. Based on the previous models available in the literature, a new model is proposed which could take all these observations into account. The equivalent fracture strain value is divided into a strain rate function  $f_1$  and a stress triaxiality ratio function  $f_2$ , which comes from the work of Johnson and al [14], and it is defined by

$$\bar{\epsilon}_f = f_1(\dot{\bar{\epsilon}}) + f_2(\eta) \quad \text{with} \quad (9)$$

$$f_2(\eta) = C_1 \exp(C_2 \eta) \quad (10)$$

$$f_1(\dot{\epsilon}) = A_1 * (1 - e^{A_2 * \dot{\epsilon}^{A_3}})(A_4 - A_5 \dot{\epsilon}). \quad (11)$$

Parameters  $A_i$  and  $C_i$  are material parameters determined directly with the equivalent fracture strain surface.

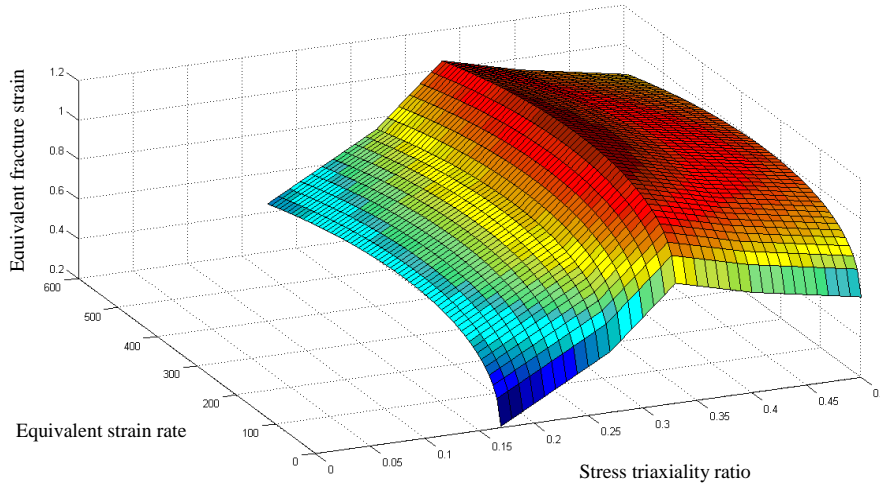


**Figure 4.** Equivalent fracture strain surface.

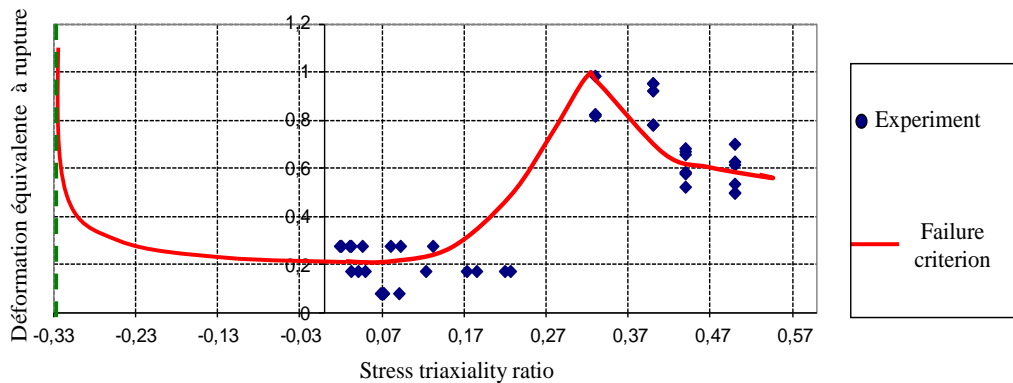


**Figure 5.** Failure criterion at constant strain rate.

## 6. CONCLUSIONS

In this paper, a behaviour model for polypropylene is proposed to cover a large range of plastic strain rate. A non-linear viscoelasticity model until a plasticity criterion which is pressure dependent and a viscoplastic model which represents the structural hardening are used to describe the complete behaviour of the polymer. The compressibility is also introduced by means of non-associative potential. The parameters of a polypropylene material are identified by means of the SE $\dot{\epsilon}$  method and the global (force) and local (total strain) variables are compared experimentally and numerically in the case of a non homogeneous strain field obtained with a notched tensile specimen under dynamic loading. Very good correlations are obtained for both variables. To obtain good prediction of behaviour and failure of structures, pertinent and realistic failure models are needed. For that, this work gives the definition of a new failure criterion which depends on triaxiality stress ratio and strain rate.

## Acknowledgments

The present research work has been supported by International Campus on Safety and Intermodality in Transportation, the Region Nord Pas de Calais, the European Community, the Délégation Régionale à la

Recherche et à la Technologie, the Ministère de l'Enseignement Supérieur et de la Recherche, and the Centre National de la Recherche Scientifique: the authors gratefully acknowledge the support of these institutions.

## References

- [1] O. van der Sluis, P. J. G. Schreurs, H. E. H. Meijer, "Homogenisation of structure elastoviscoplastic solids at finite strains", *Mechanics of Materials* 33 (9) (2001) 499–522.
- [2] K. Ho, E. Krempl, "Extension of the viscoplasticity theory based on overstress (VBO) to capture non-standard rate dependence in solids", *International Journal of Plasticity* 18 (7) (2002) 851–872.
- [3] O. U. Colak, N. Dusunceli, "Modeling viscoelastic and viscoplastic behavior of high density polyethylene (HDPE)", *Journal of Engineering Materials and Technology* 128 (4) (2006) 572–578.
- [4] C. G'Sell, J. M. Hiver, A. Dahoun, "Experimental characterization of deformation damage in solid polymers under tension, and its interrelation with necking", *International Journal of Solids and Structures* 39 (13-14) (2002) 3857–3872.
- [5] M. C. Boyce, E. M. Arruda, "An experimental and analytical investigation of the large strain compressive and tensile response of glassy polymers", *Polymer Engineering & Science* 30 (20) (1990) 1288–1298.
- [6] E. M. Arruda, M. C. Boyce, R. Jayachandran, "Effects of strain rate, temperature and thermomechanical coupling on the finite strain deformation of glassy polymers", *Mechanics of Materials* 19 (2-3) (1995) 193–212.
- [7] P. D. Wu, E. van der Giessen, "On neck propagation in amorphous glassy polymers under plane strain tension", *International Journal of Plasticity* 11 (3) (1995) 211–235.
- [8] A. Gurson, "Continuum theory of ductile rupture by void growth: part i yield criteria and flow rules for porous ductile media", *Journal of Engineering Materials and Technology* (1977) 2–15.
- [9] F. Lauro, B. Bennani, P. Drazetic, J. Oudin, X. Ni, "Ductile damage and fracture finite element modelling of elasto-viscoplastic voided materials", *Computational Materials Science* 7 (3) (1997) 295–307.
- [10] T. F. Guo, L. Cheng, "Modeling vapor pressure effects on void rupture and crack growth resistance", *Acta Materialia* 50 (13) (2002) 3487–3500.
- [11] M. Imanaka, Y. Nakamura, A. Nishimura, T. Iida, "Fracture toughness of rubbermodified epoxy adhesives: effect of plastic deformability of the matrix phase", *Composites Science and Technology* 63 (1) (2003) 41–51.
- [12] F. Zaïri, M. Naït-Abdelaziz, J. Gloaguen, J. Lefebvre, "Modelling of the elastoviscoplastic damage behaviour of glassy polymers", *International Journal of Plasticity* 24 (6) (2008) 945–965.
- [13] F. Lauro, B. Bennani, D. Morin, A. Epee, "The SEĒ method for determination of behaviour laws for strain rate dependent material: Application to polymer material", *International Journal of Impact Engineering* 37 (6) (2010) 715–722.
- [14] G. R. Johnson, W. H. Cook, "Fracture characteristics of three metals subjected to various strains, strain rates, temperatures and pressures", *Engineering fracture mechanics*, 21, (1985) 31-48.
- [15] T. Wierzbicki T, L. Xue, "On the effect of the third invariant of the stress deviator on ductile fracture", *Impact and Crashworthiness Lab Report*, 136, (2005).
- [16] D. Morin, G. Haugou, B. Bennani, F. Lauro, "Experimental characterization of a toughened epoxy adhesive under a large range of strain rates", *Journal of adhesion science and technology*, (2010), DOI:10.1163/016942410X524417.

# **Propagation rapide de fissure dans des matériaux viscoplastiques, comment un matériau peut-il être à la fois ductile et fragile.**

**Christophe Fond**

Institut de Mécanique des Fluides et des Solides, Université de Strasbourg, 2 rue Boussingault, F67000 Strasbourg.

## **Résumé**

Un dispositif expérimental basé sur la géométrie de l'éprouvette en bande a été utilisé pour étudier le comportement fragile en fissuration rapide des polymères. Ce dispositif permet d'obtenir un régime permanent de propagation sur une dizaine de centimètres et de mesurer précisément la vitesse de propagation de la fissure. Pour un PMMA "choc", on observe que la vitesse de la fissure est quasiment constante tout au long de l'essai, qu'il y ait ou non branchement ou arrêt de fissure. En effet, contrairement aux matériaux testés jusqu'à présent, le PMMA "choc" présente la particularité de consommer une énergie de rupture décroissante avec la vitesse de fissure dans le régime dynamique. A la vitesse de branchement macroscopique, on observe que la valeur macroscopique mesurée de l'énergie de rupture ainsi que la rugosité de la surface de rupture ne sont pas uniques dans le PMMA "choc". On constate que l'énergie de rupture macroscopique croît avec la quantité d'instabilités ou "micro-branchements frustrés". La célérité de la fissure ne pouvant dépasser la vitesse de branchement, elle se stabilise donc à environ 0.6 fois la vitesse des ondes de Rayleigh. Cette vitesse correspond à l'instabilité de branchement liée aux effets inertiels. L'énergie consommée par la propagation de la fissure s'ajuste donc à l'énergie disponible en multipliant des micro-branchements frustrés.

Ce type de comportement, constaté dans d'autres polymères tels que le PE ou le PA est typique des matériaux viscoplastiques. On montre donc qu'il existe deux grandes classes de matériaux dans le régime de propagation rapide et que la notion de ductilité peut-être versatile.

# EXPERIMENTAL AND NUMERICAL INVESTIGATION OF COMPOSITE BEHAVIOUR AT HIGH STRAIN RATE.

E. Gay<sup>1\*</sup>, L. Berthe<sup>1</sup>, M. Boustie<sup>2</sup>, M. Arrigoni<sup>3</sup>, A. Johnston<sup>4</sup>, R. Cole<sup>4</sup>, J. Barroeta<sup>4</sup>, E. Buzaud<sup>5</sup>.

<sup>1</sup> *Laboratoire Procédés et Ingénierie en Mécanique et Matériaux (CNRS), Arts et Métiers ParisTech, 151 bd de l'Hôpital, 75013 Paris, France*

<sup>2</sup> *Institut Pprime (CNRS), Département Physique et Mécanique des Matériaux, ENSMA, 1 av Clément Ader, 86960 Futuroscope Cedex, France*

<sup>3</sup> *Laboratoire Brestois de Mécanique et des Systèmes EA 4325, ENSIETA, 2 rue François Verny, 29806 Brest Cedex 9, France*

<sup>4</sup> *Institute for Aerospace Research (CNRC), 1200 chemin de Montréal, Ottawa, Ontario, Canada, K1A 0R6*

<sup>5</sup> *CEA Gramat, 46500 Gramat, France*

**Abstract.** Ultra-high strain-rate loading is induced by a nanosecond laser pulse. By internal wave propagation, this short duration loading generates a local tensile stress within the sample which can damage the material when intense enough. The induced damage, termed spallation, occurs near the free surface of a specimen and can be detected and quantified by means of real-time free surface velocity measurement or cross-sectional microscopy. As composite materials become more widespread in the aerospace industry as substitutes for metal alloys, the spallation technique is applied to these strongly anisotropic materials. The final aim of this work is development of an industrial adhesion test for bonded composite material assemblies employing the LASAT (LAsER Shock Adhesion Test) principle. This paper focuses on the behaviour of 4 ply unidirectional carbon epoxy laminates shocked with a laser intensity leading to traction levels near the material delamination threshold. Numerical simulations are carried out to understand shock waves propagation mechanisms within these complex multilayer materials and the results compared with experimental results.

## 1. INTRODUCTION

The LAsER Shock Adhesion Test (whose abbreviation LASAT will be used herein) is a non-destructive non-intrusive technique based on laser induced shock waves produced by a pulsed laser to evaluate bond strength. This technique has been studied for the measurement of the bond strength of coated material [1] and bonded assemblies [2]. It has the potential to be used to assess the bond strength of composite material assemblies, a key industrial problem [3]. As a first step, the behaviour of single composite laminate is studied under laser induced shocks (ns, < GPa) [4-6]. LASAT also has the potential to evaluate the strength of a laminate in the transverse direction (i.e. between plies) by identifying the damage threshold at a good ply-to-ply interface.

Inducing damage in a selected place within this multilayer structure and understanding the mechanisms of shock wave propagation are scientific challenges. In this context, this paper describes the principles of the LASAT technique as applied to a stud of a 4-ply composite laminate to shock at ultra-high strain rate (about  $\dot{\epsilon} = 10^7 \text{ s}^{-1}$ ). Results at different densities of power near the damage threshold are shown along with numerical simulations performed with the SHYLAC code of a simplified multi layered structure under shock.

## 2. EXPERIMENTAL CONFIGURATION

At high power density ( $\approx \text{GW.cm}^{-2}$ ), a laser pulse generates a plasma during a period of few ns, producing a sharp loading pressure, followed by an unloading wave that relaxes the material to its initial state. The addition of a transparent condensed layer (water, glass,...) on the irradiated face retains the plasma expansion, it has the global effect of doubling the pulse duration [7] from 10 to about 20 ns at Full Width Half Maximum (FWHM). A time history of equivalent pressure pulse in a constrained case is shown in Figure 1-a.

This compressive pulse, whose pressure reaches the level of GPa, propagates through the sample and is reflected at the rear free surface as a tensile wave. The maximum tensile stress is located at a distance of approximately  $C_0 \cdot \tau / 2$  from the back surface ( $C_0$  is the bulk sound velocity of the specimen and  $\tau$  is the shock wave duration at FWHM) in the area where the reflection of the incident shock wave crosses the release wave.

Shock wave propagation is illustrated in Figure 1-b by a space-time diagram, representing the shock wave evolution within a homogeneous plate under uni-axial deformation; red and blue areas represent respectively the compressive and the tensile waves. The propagation of shock wave will be somewhat more complex in multi-layered structures as each interface modifies the amplitude of the transmitted and reflected shock waves [8] depending on the impedance mismatch at the interface.

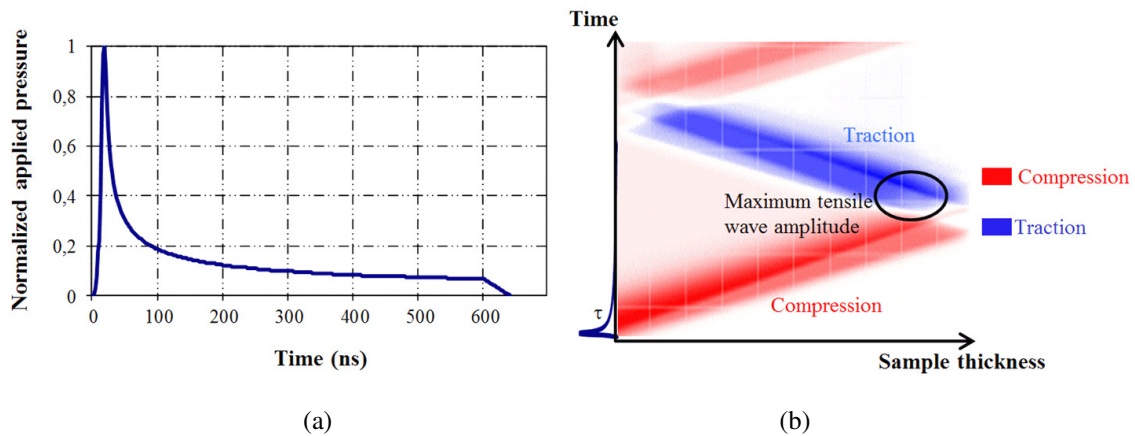


**Figure 1.** Description of shock sharpening and propagation (a) Normalized time history of the pressure pulse equivalent to laser shock (under a constrained regime) and (b) Space-time diagram of shock wave propagation within a homogeneous plate, with pulse duration  $\tau$  (SHYLAC code [9]).

If it is of sufficient magnitude, the created internal tensile stresses can induce damage in a small area near the point of maximum stress. This damage can be detected in real time by using a VISAR interferometer to measure Rear Free Surface Velocity (RFSV), performed by a VISAR interferometer, based on a Doppler shift in light reflected from the free surface [10].

Real-time RFSV signals can even be used to characterize the damage extent by studying signal shape [11]. Using this method, it is then possible to identify a delamination damage threshold by incrementing the laser incident energy until delamination is induced. A key benefit of the LASAT technique is its ability to test strength locally while allowing most of the samples to be retained for analysis by other (e.g. destructive) means.

**Experimental Conditions:** Experiments were performed on a high power Continuum© pulsed laser, with a maximum energy of  $E = 1,5 \text{ J}$  at  $\lambda = 532 \text{ nm}$  wavelength, delivering pulses of about  $\tau = 8\text{-}10 \text{ ns}$  duration at FWHM. This allows a maximum power density of  $\phi = 3 \text{ GW.cm}^{-2}$ , defined by  $\phi = E/\tau \cdot S$ , where  $E$  is the incident energy provided by the laser (J),  $\tau$  is the pulse duration (ns) and  $S$  is the irradiated surface upon which the laser beam is focussed ( $\text{cm}^2$ ). The spot diameter was adjusted to about 2.7 mm in order to avoid edge effects resulting from the crossing of release waves around the impact area. Since the spot diameter is at least two to three times as large as the sample thickness, wave propagation through the target can be considered one-dimensional [12].

Impact faces of samples are covered with black paint that fully absorbs the deposited laser energy and limits thermal effects on the composite laminate.

### 3. PRESENTATION OF STUDIED MATERIALS

In a context of light weight structures, composite materials are commonly used in the aerospace industry, especially unidirectional carbon fibre reinforced epoxy plies stacked in laminates, e.g.  $[0^\circ/90^\circ]_S$  for a 4 ply laminate. Figure 2 shows an SEM cross section of a 600  $\mu\text{m}$  thick composite showing the laminate plies (130-140  $\mu\text{m}$  of carbon fibres embedded in epoxy), the relatively homogeneous interply epoxy layers (roughly 15-20  $\mu\text{m}$  thick), as well as thin unreinforced epoxy layers on the sample top and bottom surfaces.

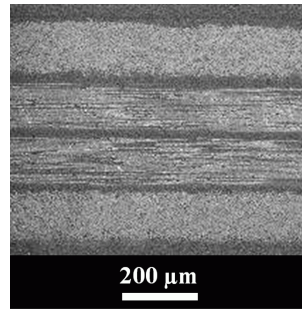


**Figure 2.** SEM micrograph of a 4 ply composite laminate cross section.

Based on the experimental results and a ply homogenisation technique, dynamic properties of the carbon / epoxy plies and the pure epoxy interply region are given in Table 1 and 2 [Cytec Engineered Materials database ; 13]. As the behaviour of unidirectional plies are transversely isotropic, the table presents properties in the direction normal to the plies, i.e. through-thickness, since this corresponds to the shock propagation direction.

**Table 1.** Physical and mechanical properties of carbon fibre / epoxy plies and the epoxy interply (through-thickness direction).

	Density ( $\text{kg.m}^{-3}$ )	Young's modulus (GPa)	Poisson ratio	Tensile strength (MPa)
Epoxy interply	1 260	5.5	0.34	110
Carbon/epoxy ply	1 630	10.6	0.30	120

**Table 2.** Acoustic properties of carbon fibre / epoxy plies and the epoxy interply (through-thickness direction).

	Hugoniot slope parameter	Mie Grüneisen coef.	Sound velocity ( $\text{m.s}^{-1}$ )	Impedance ( $\text{MPa.s.m}^{-1}$ )
Epoxy interply	1.4	0.87	2 600	3.3
Carbon/epoxy ply	1.22	2	3 000	4.8

### 4. EXPERIMENTAL RESULTS

The experimental results given in Figure 3 show real-time RFSV versus time for two different laser power densities. The light grey signal corresponding to shot A at  $\phi = 0,51 \text{ GW.cm}^{-2}$  is a signature for undamaged material whereas the dark grey curve for shot B indicates delamination after a  $\phi = 1.03 \text{ GW.cm}^{-2}$  impact. For both signals the first sharp velocity peak at 200 ns (referred 1 on figure 3) identifies the time at which the compressive wave reaches the back surface and accelerates it; immediately followed by a reduction of the velocity due to rarefaction.

The velocity peaks for signal A identified as 2 and 3, respectively 600 ns and 1.05  $\mu\text{s}$  after the impact, correspond to this wave after it has propagated through the undamaged specimen three and five times. Time required for a back and forth across the whole material (time between peak 1 and 2, or 2 and 3) is almost 400 ns, meaning that wave propagation across the 600  $\mu\text{m}$  of the laminate requires about 200 ns.

The wave propagation velocity is experimentally determined to be  $3\,000\text{ m}\cdot\text{s}^{-1}$ , which corresponds to the composite material bulk sound velocity (transverse direction).

This result means that the compressive wave propagates in the material elastic regime. The maximum stress level is below the Hugoniot Elastic Limit since no elastic precursor is visible and the stress generated is moderated. The solicitation is thus non-invasive, as far as the material will not be affected by an elastic solicitation, all the more that composite behaviour is fully elastic at high strain rate [14].

The small velocity variations between the principal peaks (e.g. 1a, 1b and 1c in Figure 3, but also noticeable between the two principle peaks 2 and 3) are due to wave reflections at the interfaces between the plies and interply layers (see these reflections on a space-time diagram in Figure 6). Thus, the main wave is split and it induces a loss of energy.

As all the plies and interply layers have very similar thicknesses, these smaller velocity peaks are very regular, occurring about every 100 ns. This corresponds to the time of wave propagation within a single ply and its interply (a total of about  $150\text{ }\mu\text{m}$  thickness).

The dark grey signal measured after a  $1.03\text{ GW}\cdot\text{cm}^{-2}$  irradiation (sample B) shows a typical signature of delamination, identified by small oscillations with a constant period following the initial wave rebounds within the debonded ply and its interply, followed by a slow deceleration as the shock is attenuated. This signal enables to identify the damage threshold at about  $0.9\text{ GW}\cdot\text{cm}^{-2}$ .

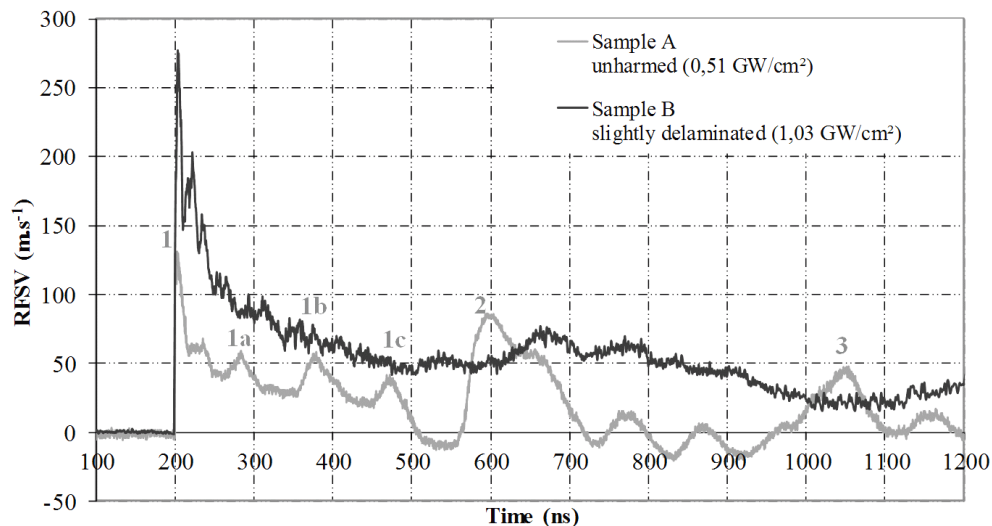


**Figure 3.** 4 ply RFSV measured following shock loading near the delamination threshold.

The presence or absence of delamination was confirmed by post-testing SEM images of sample cross-sections. Figure 4 shows images for samples A and B and a specimen subjected to a higher laser power density.

This figure shows that there is no observable damage below the delamination threshold (sample A, Figure 4-a). Sample B, shocked at  $1.03\text{ GW}\cdot\text{cm}^{-2}$  shows an incipient micrometer scale crack in the interply layer between the last and the second-to-last ply (Figure 4-b). It can be seen that the fracture is mainly adhesive and thus, shows that the method is sensing the adhesion at the fiber/resine interface. The severity of the induced damage was proportional to the incident power density: at higher power density ( $\Phi = 2\text{ GW}\cdot\text{cm}^{-2}$  for Figure 4-c), delamination occurred within both the interply layer and the matrix of the last ply with evidence of minor vertical intra-laminar cracks caused by flexural loading that occurred following the removal of the last ply.

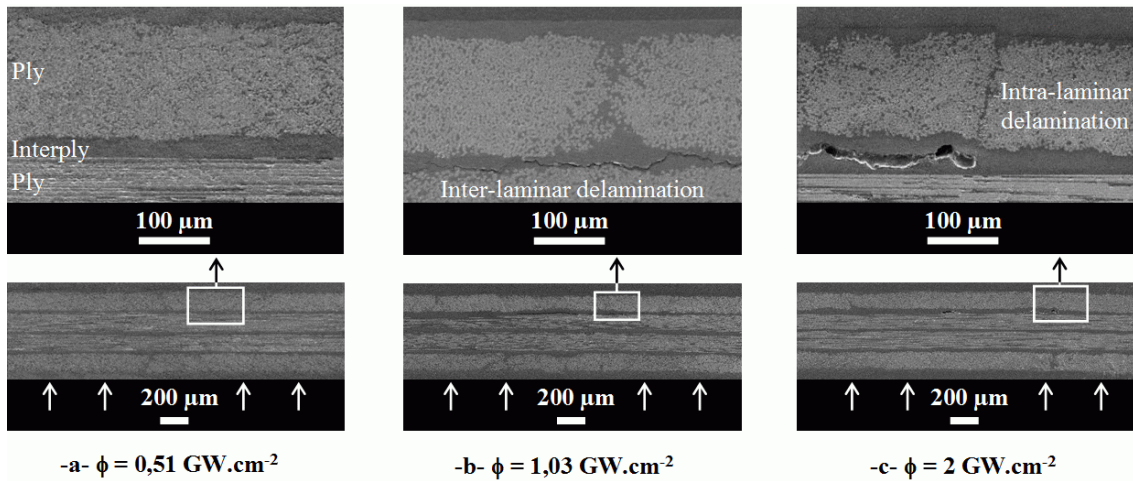


**Figure 4.** Microscopic transverse observations of 4 ply composite laminates after shock at different laser power densities. Laser impact is indicated by white arrows.

## 5. NUMERICAL MODELS

A numerical model of the experiments was carried out using the SHYLAC code under the assumption of one-dimensional shock wave propagation. Dynamic response was simulated using hydrodynamic elastic model under adiabatic conditions, with shock attenuation.

Based on the description of the material given in §3 and properties given in Table 1, the composite laminates were simulated as a sandwich of stacked isotropic layers, whose thickness was adjusted based on SEM post-mortem measurements. Impact parameters such as pressure time history (see Figure 1) are set in accordance with the experimental configuration of sample A. The inverse approach reveals that the loading amplitude was estimated to be 0.35 GPa to fit with RFSV curves, as presented in Figure 5.

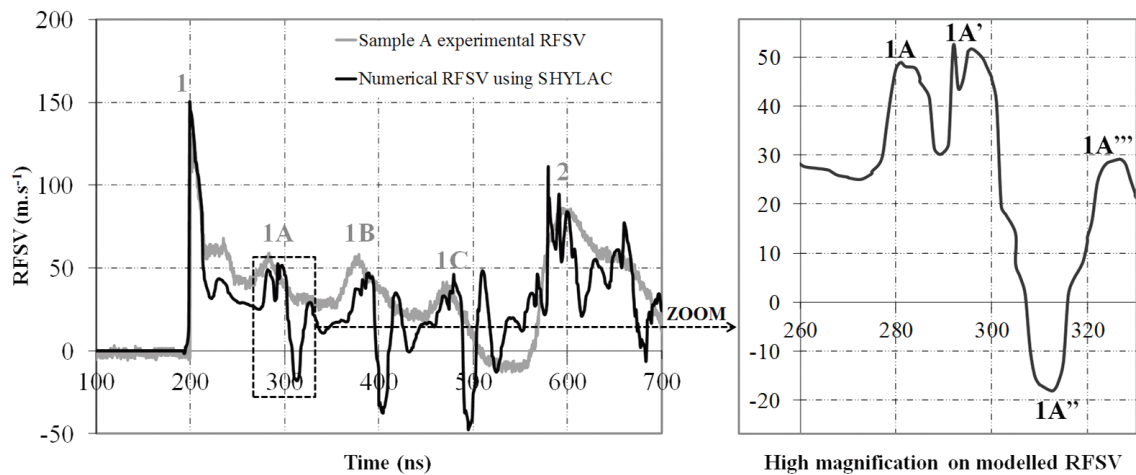


**Figure 5.** Comparison between experimental and numerical RFSV signal for a 4 ply composite laminate during a shock below the delamination threshold.

Measured principal velocity peaks 1 and 2 as well as the small echoes 1A, 1B and 1C correlate in good agreement with those shown in the model, leading us to believe that the values assumed for bulk sound velocity and the layer thickness measurements are correct.

On the other hand, the impedance ratios for the ply and the interply regions do not seem entirely appropriate, based on significant differences in the velocity amplitudes.

The appropriateness of the material density values used is of particular concern since the bulk sound velocity was validated experimentally is matched well by the model.

This could be explained by local variations in the proportion of carbon fibres, both within a ply and between plies. Therefore, actual local ply density may be different from that used in the model, which was calculated from a ply homogenization technique assuming uniform distribution.

Differences between the experimental RFSV signal and the model may also be attributable to other simplifying assumptions, particularly the one-dimensional model used for shock propagation as flexural stresses are evidenced by the post mortem analysis. The complexity of the real composite material is also an issue, as the thickness of each layer is not constant within the sample.

The presence of additional peaks observed in the magnified zone of the theoretical velocity versus time curve (referred to as 1A, 1A', 1A'' and 1A''') is explained using space-time diagram.

Figure 6 shows wave propagation within a multilayered 4 ply laminate obtained with the SHYLAC code, representing shot A. After the compressive wave propagates a few times within the sample, the global amplitude of the main wave attenuates so this graph was truncated after a couple of propagations through the sample.

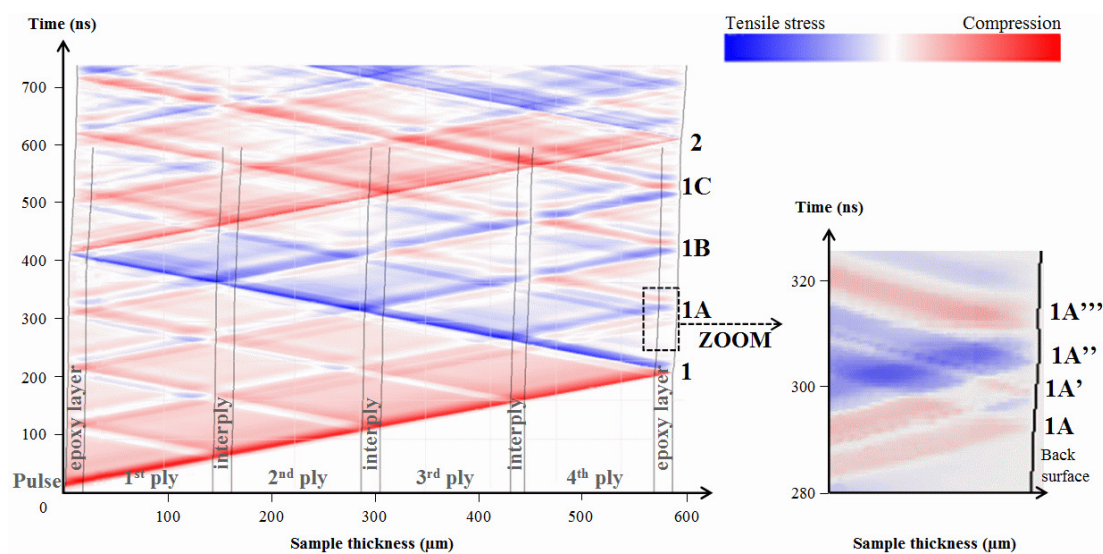


**Figure 6.** Space-time diagram of the shock wave propagation within a multilayered 4 ply laminate (sample A) obtained with the SHYLAC code. Compression is represented by red, tensile stress by blue.

The main shock wave is reflected at the free surface 200 ns after the applied shock, resulting in tensile stress areas that propagate throughout the whole material with tensile stress peak at each ply / interply interfaces due to the numerous wave reflections at the interfaces. That is why damage appears in the interply zone, since its tensile strength is a bit lower than the ply one.

A compressive wave at the back surface accelerates it, and conversely the arrival of a tensile wave at the rear free surface induces deceleration. This is why a sharp velocity decrease is observed just after the first peak (referred to as point 1 in Figure 5), as a tensile stress arrived at the back surface. A tensile wave is also observed 305 ns after impact inverting the theoretical velocity (see reference 1A'' in figure 5 and figure 6). In the experimental signal, this is traduced by only a strong decrease because of the flexure effects that are not taken into account in the simulation.

Table 3 synthesizes the correspondences between the theoretical RFSV presented in Figure 5 and the observed acoustic phenomena, depending on shock wave reflection and transmission.

**Table 3. Shock waves arriving at the laminate back surface and their effects.**

Ref	Time after impact (ns)	Acoustic phenomenon	Nature of the shock	Influence on RFSV
1	200	Arrival of the main compressive wave after propagating through the thickness.	Compressive	Acceleration
1A	280	Reflection of incident wave within the first ply near the incident surface at the interface between the first ply and the associated interface, then propagating through the whole sample thickness.	Compressive	Acceleration
1A'	295	The preceding wave is reflected and arrives at the rear free surface after a back and forth within the back thin epoxy layer, in addition to the other wave that made a round trip within an epoxy layer.	Compressive	Acceleration
1A''	305	This corresponds to the back and forth of the reflection of the incident wave within the whole last ply near the back surface, enhancing tension at the back surface.	Tensile	Strong deceleration
1A'''	315	Following two back and forth within the interply layer, the secondary waves arrives at the back surface.	Compressive	Acceleration
2	615	Back and forth of the main wave within the material after its first arrival. The reflected tensile wave was reflected again at the incident surface as a compressive wave that accelerated the back surface when reaching it	Compressive	Acceleration

This whole phenomenon is reiterated in a more complex way for velocity peaks 1B and 1C, with an amplification of the simultaneous superposition of waves reflected at the different interfaces, arriving almost at the same time at the back surface.

We point out that arrivals of waves are almost synchronous as the layers have similar thicknesses. In reality, all secondary waves from the reflection at the different interfaces are added as they arrived at very similar time for peaks 1A; 1B and 1C. This phenomena, added to flexural effects, explains why no sharp variation of experimental velocity was observed and thus the differences between experimental and numerical velocity signals.

A parametric theoretical study will help to understand the interaction of shock waves within the different layers with modifying their thickness: desynchronization of shock waves will clarify the influence of each interface in shock propagation and its results in terms of RFSV. Moreover, Fourier analysis will give more information about frequencies hidden in the signal and may confirm delamination [2].

## 6. CONCLUSION.

Using shock waves from a high power laser impact provides local tensile stress able to induce delamination. In addition, it can be detected in real-time by laser Doppler interferometry.

The numerical analysis of waves propagation into a simplified model of the composite material helps understanding the main features observed in the pattern of time resolved free surface velocity measurements. However, some major discrepancies between numerical simulations and experimental data clearly indicate the need for a much better constitutive law combined with damage modelling for these materials under dynamic loading. In effort to achieve a better fit to the experiments, more accurate ply densities will be used which consider carbon fibre proportions measured from SEM images. Other perspectives for numerical models include consideration of material anisotropy and impact of edge effects by modelling with 3D software.

Meanwhile we highlight the potential of the LASAT technique for testing adherence between plies and study composite behaviour at high strain rate. The perspective of this study is the optimization of the test parameters to provide maximum tensile stress at the interface to be assessed, with the help of simulation as a predictive tool.

## Acknowledgments

This work was undertaken in the framework of the project SATAC (Shock Adhesion Test for Adhesively bonded Composites) between French CNRS and Canadian NRC. We are grateful to M. Nivard for her technical support in operating the laser facility. We also thank the French General Delegation for Armament (DGA) for its funding.

## References

- [1] M. Arrigoni, Propagation des chocs laser dans des systèmes revêtus, Editions universitaires européennes (2010).
- [2] M. Arrigoni, S. E. Kruger, A. Blouin, D. Lévesque, B. Arsenault, J.-P. Monchalain, M. Boustie, L. Berthe, Adhesive bond testing by laser induced shock waves, Proceedings of the 17th World Conference on Non-destructive Testing, Shanghai, China (2008).
- [3] R. Bossi, K. Housen, C. Walters, Laser bond inspection device for composites: Has the holy grail been found?, Non-destructive Testing Information Analysis Centre Newsletter, Vol. 30, n°2 (2005).
- [4] I. Gilath, S. Eliezer, S. Shkolnik, Spall behaviour of carbon epoxy unidirectional composites as compared to aluminum and iron, Journal of composite materials, Vol. 24, n° 11, 1138-1151 (1990).
- [5] E. Gay, L. Berthe, M. Boustie, M. Arrigoni, J.-P. Monchalain, M. Perton, A. Blouin, A. Johnston, R. Cole, J. Barroeta, E. Buzaud, Experimental investigation of a composite behaviour under short laser-short loading, Proceeding of the 24th International Conference on Surface Modification Technologies (SMT 24), September 7 – 9 in Dresden, Germany (2010).
- [6] M. Boustie, E. Gay, L. Berthe, M. Arrigoni, J. Radhakrishnan, T. De Résséguier, A. Blouin, J.P. Monchalain, A. Perton, A. Johnston, R. Cole, E. Buzaud, Laser Shock Adhesion Test (LASAT) of composite materials for aerospace industry, Proceedings of the 23<sup>rd</sup> International Conference on Surface Modification Technologies (SMT23), Madras, India (2009).
- [7] L. Berthe, R. Fabbro, P.Peyre, Shock waves from a water-confined laser-generated plasma, Journal of Applied Physics, Vol. 82, n° 6, 2826-2832 (1997).
- [8] S. K. Datta, Wave propagation in composite plates and shells, Comprehensive Composite Materials, Vol.1, 511-558 (2000).
- [9] L. Marty, Etude numérique et expérimentale d'une onde de choc induite par impact laser dans une cible solide, Thèse de l'Université de Poitiers (1988).
- [10] L.M. Barker, R.E. Hollenbach, Laser interferometer for measuring high velocities of any reflecting surface, Journal of Applied Physics, Vol.43, n° 11, 4669-4675 (1972).
- [11] L. Tollier, R. Fabbro, Study of the laser-driven spallation process by the VISAR interferometry technique. II. Experiment and simulation of the spallation process, Journal of Applied Physics, Vol. 83, n° 3, 1231-1237 (1997).
- [12] D. Salzman, I. Gilath, B. Arad, Experimental measurements of the conditions for the planarity of laser-driven shock waves, Applied Physic Letter, Vol. 52, n°14, 1128-1129 (1988).
- [13] A. Yu, V. Gupta, Measurement of in situ fibre/matrix interface strength in graphite/epoxy composites, Composites Science and Technology, Vol. 58, n°11, 1827-1837 (1998).
- [14] M. Perton, A. Blouin, Z. Gu, J.-P. Monchalain, E. Gay, L. Berthe, M. Boustie, M. Arrigoni, Laser shock waves for adhesive bond testing, Proceedings of the Society for the Advancement of Material and Process Engineering (2009).

# HIGH STRAIN RATE TESTS ON POLYPROPYLENE MATERIALS

M. Zrida<sup>1,2</sup>, H. Laurent<sup>2</sup>, V. Grolleau<sup>2</sup>, G. Rio<sup>2</sup>, M. Khlif<sup>1</sup>, D. Guines<sup>3</sup>, N. Masmoudi<sup>1</sup> and C. Bradai<sup>1</sup>

<sup>1</sup>Laboratoire des Systemes ÉlectroMécaniques, Ecole Nationale d'Ingénieurs de Sfax, TUNISIE

<sup>2</sup>Laboratoire d'Ingénierie des MATériaux de Bretagne (LIMATB), Université de Bretagne Sud, France

<sup>3</sup>Laboratoire de Génie Civil et Génie Mécanique (LGCGM), Université Européenne de Bretagne, France

**ABSTRACT.** The mechanical behaviour of a polypropylene material was studied under high strain rate tensile conditions. The mechanical tensile tests were performed from  $10^{-1} \text{ s}^{-1}$  to  $200 \text{ s}^{-1}$  using a servo-hydraulic machine [1]. A special original grip system was used in order to maintain the specimen on the machine and to accurately measure the load during the test. The local strain of the specimen was determined using strain gages glued onto the specimen. The experimental results show that, with this new device, the strain rate sensitivity is accurately captured.

Next, an Hyperelasto-Visco-Hysteresis (HVH) model [2] was used to describe the strain rate dependence of polypropylene. The material parameters of the HVH model were identified for several strain rates. Experimental results were compared to numerical results. Viscous parameters are modified for each strain rate to take into account the strain rate effects.

## 1. INTRODUCTION

Polymer materials are used in sensitive applications, such as automotive, packaging, aeronautic, etc. The stress-strain responses of polymers show a considerable rate dependence due to their viscoelastic properties.

The properties of materials subjected to high strain rates can be studied experimentally using several test methods, such as those involving the use of servo-hydraulic machines, impact methods and the Split Hopkinson Pressure Bar (SHPB) method [3–5]. The high strain rate servo-hydraulic testing machine provides another means of investigating the mechanical behaviour of polymer materials [5, 6].

In this paper, a copolymer polypropylene material is tested on a high strain rate servo-hydraulic machine. An experimental device is designed to perform high-speed tensile tests with this machine. Finally, the material parameters of an Hyperelasto-Visco- Hysteresis model (HVH) are identified at various strain rates.

## 2. MATERIAL AND METHODS

### 2.1. Material

Supplied by the society Total-Petrochemicals, an heterophasic copolymer polypropylene (named PPC7712) is used. The PPC7712 combines good fluidity and mechanical properties. It is characterized by excellent impact resistance. These parameters with other mechanical parameters, given by the manufacturer data, are presented in table 1.

**Table 1.** Thermo-mechanical properties of the PPC7712.

Characteristics	Method	value
Melt flow index MFI (g/10 min)	ISO 1133	13
Molecular weight $M_w$ (g/mol)	-	229527
Crystallinity ratio $\chi_c$ (%)	[7]	34.2
Tensile modulus (MP a)	ISO 527-2	1280
Charpy impact strenght (notched) (kJ/m <sup>2</sup> )	ISO 179	7
Yield stress (MP a)	ISO 527-2	19

The NF ISO 8256 specimen is used (Figure 1) though there is not yet a valid standard execution procedure for the high-speed tensile tests for polymer materials. These specimens are obtained via injection moulding.

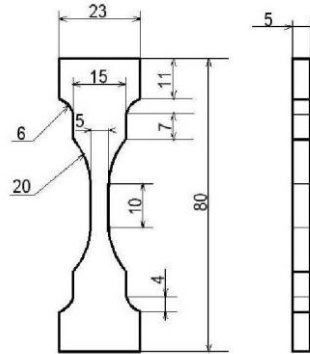


**Figure 1.** NF ISO 8256 specimen dimensions (thickness=5 mm).

## 2.2. Instrumentation

In this study, the investigations are achieved with a DELTALAB servo-hydraulic testing machine. A schematic representation of the new experimental device implemented in this machine is shown in Figure 2.

If the experimental set-up is not carefully designed in order to avoid any resonance phenomena, the reliability of the test is not ensured. According to this point, during the test, the piston rod and the specimen are not directly coupled, unlike the quasi-static tensile test. The specimen clamping system, presented in Figure 3, is composed of upper and lower grips and a specially designed mooring system. This clamping system is placed at the beginning of the test on the mooring system of the machine. A slack is managed between the lower mooring and the lower grip system (zoom in Figure 2). At the beginning of the test, the piston accelerates and reaches a constant speed, then the slack is compensated and the tensile test begins.

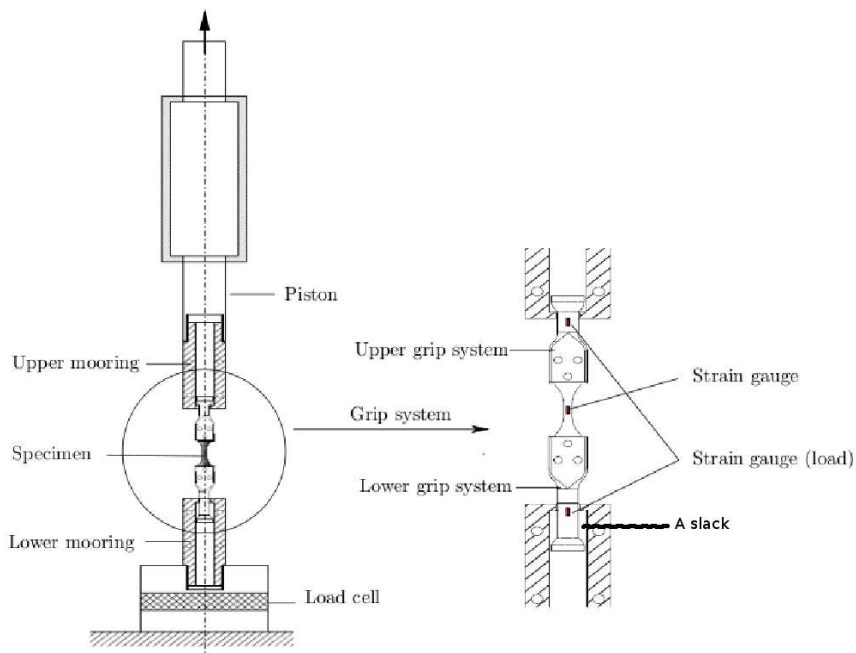


**Figure 2.** Schematic representation of the new high speed tensile test experimental device.

The measurements provided by the load cell and the piston LVDT are perturbed by spurious oscillations. Thus, to minimize this problem the measures were done, for the load as closely as possible to the sample, and for the strain directly on the sample, using gauges. The local strain of the specimen is measured in the tensile direction using quarter bridge mounted KYOWA KFEL-5 strain gauges (5 mm gage length), glued on to the middle of the specimen. The load is calculated on each grip, with a pair of diametrically opposite KYOWA KFG-5 strain gauges (gauge length: 5mm) embedded in a half tensile bridge circuit.

### 2.3. Results

Figure 4 shows Cauchy stress/Almansi strain curves at strain rates ranging from  $10^{-3} \text{ s}^{-1}$  to  $200 \text{ s}^{-1}$ . The stress-strain curves present small oscillations due to the impact-like loading for the high strain rates. Spurious oscillations are only obtained at a strain rate of  $200 \text{ s}^{-1}$ . The comparison of the curves shows a continuous increase of the stress at a given longitudinal strain, and an increase of the Young's modulus with respect to the strain rate.

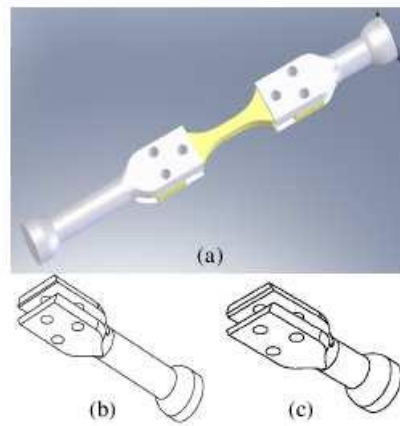


Figure 3. Specimen grip system.

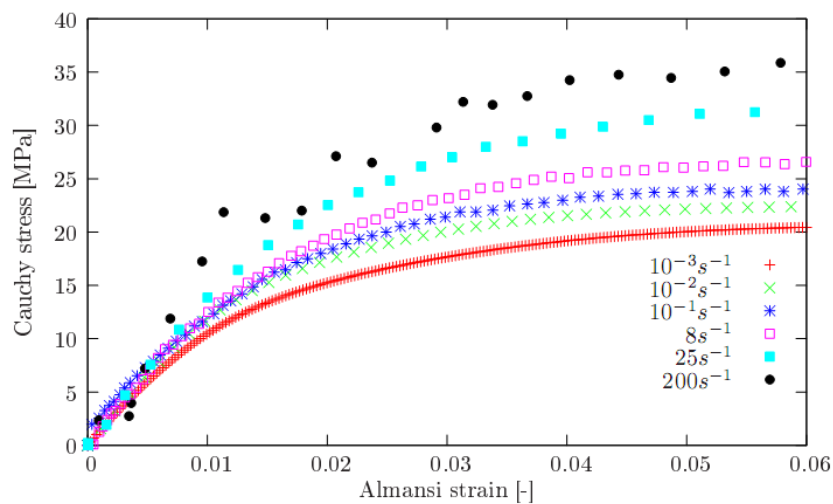
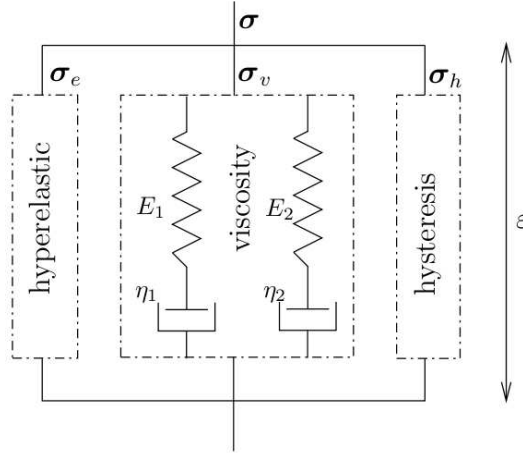


Figure 4. Influence of the strain rate in the experimental tensile stress-strain curves.

### 3. HYPERELASTO-VISCO-HYSTERESIS MODEL

To reproduce the mechanical behaviour of the polymer materials, it is necessary to define a model which is able to take into account the response of polymers to the various mechanical loadings, as well as the strain rate dependence. The present model is based on the partition of the various stress contributions [8]. This approach has already been used successfully to reproduce the mechanical behavior of shape memory alloys [9, 10], ferroelectrical and ferromagnetical materials and the solid polymer PA66 [11].

A simple rheological representation of the new Hyperelasto-Visco-Hysteresis (HVH) model is presented in Figure 5.



**Figure 5.** Rheological representation of the Hyperelasto-Visco-Hysteresis model.

The HVH model is composed from an hyperelastic  $\sigma_e$ , viscoelastic  $\sigma_v$  and pure hysteresis  $\sigma_h$  stress contributions:

$$\sigma = \sigma_e + \sigma_v + \sigma_h \quad (1)$$

$$P_{int} = P_e + P_v + P_h = \text{tr}(-\sigma_e \cdot D) + \text{tr}(-\sigma_v \cdot D) + \text{tr}(-\sigma_h \cdot D) \quad (2)$$

where,

- $P_{int}$  is the power of the internal efforts,
- $D$  is the strain rate tensor,
- $\sigma_e$  and  $P_e$  are the stress and internal power associated with the hyperelastic behaviour,
- $\sigma_v$  and  $P_v$  are associated with the viscous behaviour,
- $\sigma_h$  and  $P_h$  are associated with the irreversible hysteretic behaviour.

10 parameters appears on the HVH model: 3 hyperelastic parameters ( $Q_{0r}$ ,  $\mu_0$ ,  $\mu_\infty$ ), 4 Maxwell viscoelastic parameters ( $E_1$ ,  $\mu_1$ ,  $E_2$ ,  $\mu_2$ ) and 3 hysteretic parameters ( $\eta_p$ ,  $\mu_h$ ,  $Q_0$ ). These different contributions have been already presented in a previous paper [2].

#### 4. IDENTIFICATION OF THE HVH MODEL PARAMETERS

The material parameters of the HVH model presented in the previous section were identified in this part. The hyperelastic and hysteretic parameters are identified in using a simple tensile test at a strain rate of  $8 \cdot 10^{-3} \text{ s}^{-1}$ . In changing only the viscous parameters of the two Maxwell contributions, these parameters have been identified with the high-speed tensile tests for strain rates of  $8 \text{ s}^{-1}$  to  $200 \text{ s}^{-1}$ . The obtained parameters are presented in table 2 and the Cauchy stress/Almansi strain curves are described in Figure 6. During the identification procedure, the optimization software program SiDoLo [12] joined with the finite element code HERZHZ++ are used [2].

The obtained results show a good correlation between experimental data and model prediction. The viscous modulus ( $E_1$  and  $E_2$ ) increase, whereas the viscous parameters ( $\mu_1$  and  $\mu_2$ ) decrease in increasing the strain rate. This result is explained in characteristic times ( $\tau_i = \mu_i / E_i$ ) in Figure 7.

**Table 2.** Obtained parameters for each strain rate in simple tensile test.

Constant coefficients	Hyperelastic parameters			Hysteretic parameters		
	$Q_{0r} = 5.6 \text{ MPa}$			$n_p = 0.94$		
	$\mu_0 = 237 \text{ MPa}$			$\mu_h = 200 \text{ MPa}$		
	$\mu_\infty = 0.1 \text{ MPa}$			$Q_0 = 5.5 \text{ MPa}$		
Viscous parameters						
$\dot{\epsilon} [\text{s}^{-1}]$	$10^{-3}$	$10^{-2}$	0.8	8	25	200
$E_1 [\text{MPa}]$	140	280	412	681	650	750
$\eta_1 [\text{MPa}\cdot\text{s}^{-1}]$	2123	225	45	1.9	1.82	0.14
$E_2 [\text{MPa}]$	87	236	276	193	200	250
$\eta_2 [\text{MPa}\cdot\text{s}^{-1}]$	17536	581	31	1.1	0.56	0.04

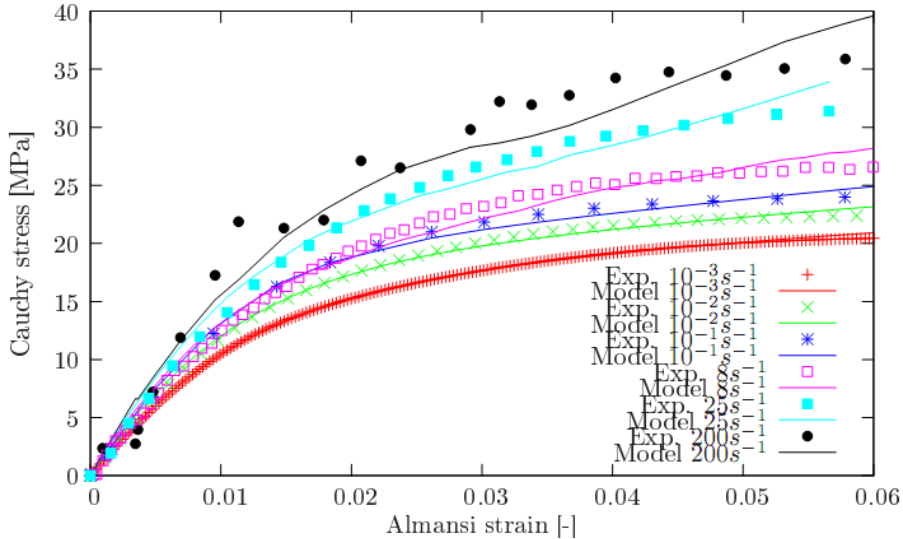


**Figure 6.** Comparison between experimental data/identification results for a strain rates range from  $10^{-3} \text{ s}^{-1}$  to  $200 \text{ s}^{-1}$ .

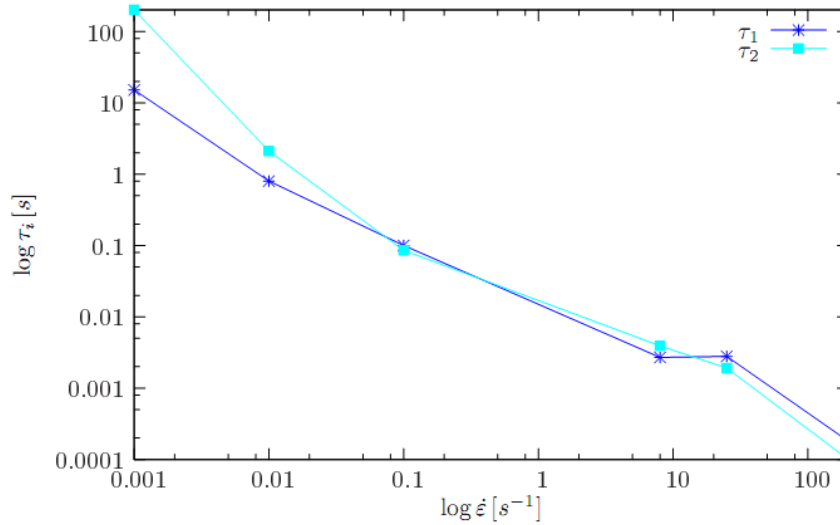


**Figure 7.** Evolution of the characteristic times in both Maxwell branches according to the strain rate.

## 5. NUMERICAL SIMULATION

To analyze the relevance of the HVH model, a numerical simulation is realized using the finite element software program HEREZH++ [13] on a high-speed tensile test for a strain rate of  $8 \text{ s}^{-1}$ . The symmetry conditions of the specimen are considered to reduce the computational times. The specimen is meshed with 3D linear hexaedral elements (Figure 8.a).

Figures 8.b) and 8.c) shows, respectively, the deformed mesh and the Von Mises stresses distribution in the specimen. The experimental and numerical results are compared in Figure 9. A good reproduction of the experimental curve and a correct simulation of this high-speed tensile test can be observed.

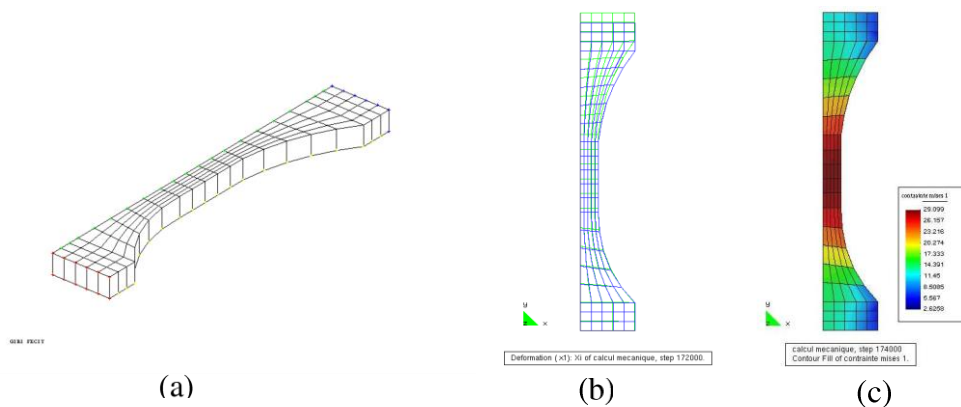


**Figure 8.** (a) Mesh used for the simple tensile test simulation, (b) Deformed mesh obtained after simple tensile test, (c) Von-Mises distribution.

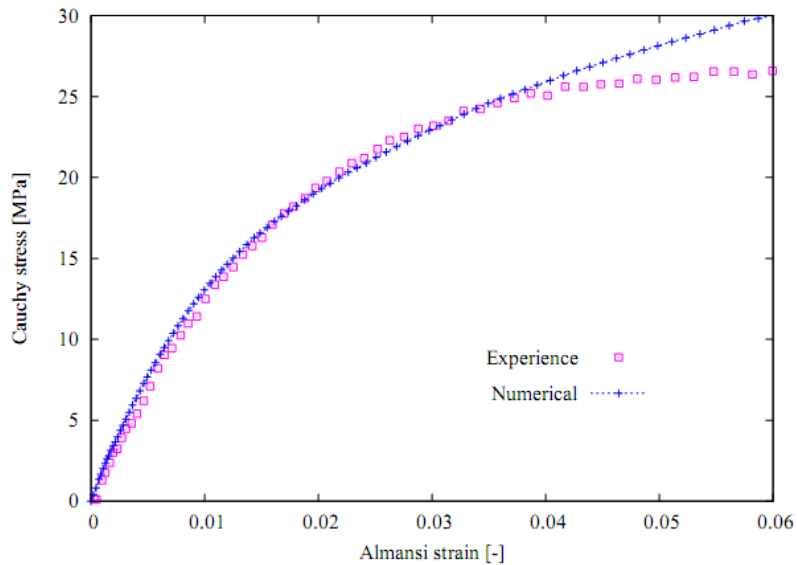


**Figure 9.** Comparison between the experimental data and numerical result in the case of simple tensile test at  $8s^{-1}$ .

## 6. CONCLUSION

Dynamic tensile tests were carried out on polypropylene specimens by using a servo-hydraulic machine. In order to minimize any resonance phenomena, a new technique was proposed. It was based on the use of a strain gauge on the center of the specimen for the determination of the local strain and two strain gages on the mooring for the measurement of the load. Next, an optimization method was proposed to identify the HVH model parameters. Numerical simulations using this model show results in accordance with the experimental data.

## Acknowledgments

The authors thank the Brittany Region for financial support and the Laboratory of Civil Engineering and Mechanical Engineering (LGCGM) for the use of the servo-hydraulic machine.

## References

- [1] M. Zrida, H. Laurent, V. Grolleau, G. Rio, M. Khelif, D. Guines, N. Masmoudi, and C. Bradai. High-speed tensile tests on a polypropylene material. *Polymer Testing*, 29 (2010) 685–692.
- [2] M. Zrida, H. Laurent, G. Rio, S. Pimbert, V. Grolleau, N. Masmoudi, and C. Bradai. Experimental and numerical study of polypropylene behavior using an hyper-visco-hysteresis constitutive law. *Computational Materials Science*, 45 (2009) 516–527.
- [3] S. M. Walley, J. E. Field, P. H. Pope, and N. A. Safford. *Philosophical Transactions of the Royal Society of London. Series A, Mathematical and Physical Sciences*, 328 (1989) 1–33.
- [4] A. M. S. Hamouda and M. S. J. Hashmi. Testing of composite materials at high rates of strain: advances and challenges. *Journal of Material Processing Technology*, 77 (1998) 327–336.
- [5] X. Xiao. Dynamic tensile testing of plastic materials. *Polymer Testing*, 27 (2008) 164–178.
- [6] M. A. Meyers. *Dynamic Behavior of Materials*. John Wiley & Sons, Inc., New York, 1994.
- [7] S. D. W. Van Krevelen. *Properties of polymer*. Elsevier, 1976.
- [8] P. Guélin. Remarques sur l’hystérésis mécanique. *J. Mécanique Théorique et Appliquée*, 19(2) (1980) 217–247.
- [9] P. Y. Manach, D. Favier, and G. Rio. Finite element simulations of internal stresses generated during the pseudoelastic deformation of niti bodies. *J. de Physique*, 1(6) (1996) 244–253.

- [10] G. Rio, P. Y. Manach, and D. Favier. Finite element simulation of shell and 3d mechanical behaviour of NiTi shape memory alloys. *Archives of Mechanics*, 47(3) (1995) 537–556.
- [11] G. Blès, S.P. Gadaj, W.K. Nowacki, and A. Tourabi. Experimental study of a PA66 solid polymer in the case of shear cyclic loading. *Archives of Mechanics*, 54(2) (2002) 155–174.
- [12] SiDoLo. *P. Pilvin*. <http://web.univ-ubs.fr/lg2m/~pilvin/>, Université de Bretagne-Sud, Lorient, France, user's manual in french - edition, 2007.
- [13] G. Rio. *Herezh++*. Certification IDDN-FR-010-0106078-000-R-P-2006-035-20600, <http://www-lg2m.univ-ubs.fr/rio>.

# Development of a multiscale analysis tool, the sDEMA “synchronized Electro-Mechanical Analysis”, for understanding the non-linear behavior of filled polymers and elastomers

Tarek Fathallah, Patrice Mélé, Lionel Flandin  
 LMOPS UMR 5041, CNRS Université de Savoie, Chambéry France;  
 Email: [Tarek.Fathallah@univ-savoie.fr](mailto:Tarek.Fathallah@univ-savoie.fr)

The Dynamic Mechanical Analysis (DMA) is a very common tool to investigate mechanical properties of a large materials range. Filled elastomers exhibit appreciable changes in their mechanical properties under deformation, characterized by an elastic properties drop with increasing deformation amplitude, characteristic of their non linear mechanical behavior. This result, measured at the macroscopic scale, is related in the literature to either filler / filler interactions or fillers / polymer interactions<sup>1</sup>. To separate these origins, additional techniques, such as electrical measurements, can be useful. Surprisingly, *in situ* measurements of electrical properties on a sample submitted to a dynamic mechanical solicitation have rarely been studied<sup>2,3</sup>.

The purpose of this study is to develop a new experimental *apparatus*, (named *synchronized* Dynamic Electro-Mechanical Analysis sDEMA) that “probe” the microstructure of the composite at two different scales: the mechanical properties will give information on the dynamics of polymer chains whereas the electrical properties will probe the microstructure changes at the fillers scale.

When a filled elastomer is subject to a dynamic shear on sDEMA in the DC mode, the temporal change of the resistivity is periodic but present variations at a double frequency than those of the mechanical signals (in shear mode). For high amplitudes deformation, a specific electrical signal inversion is moreover observed (Figure 1a).

A specific method had thus been developed to decompose the electrical signal into a sum of harmonics, with the help of fast Fourier Transform (FFT). New electrical parameters are then defined (e.g. average Resistivity  $\rho_m$ , harmonic amplitude  $A_{Hi}$  and phase angle  $\delta_{Hi}$ ). In a shear mode, harmonic  $H_2$  relative amplitude  $A_{H2rel}$  and the phase angle  $\delta_{H2}$  exhibit some particular evolutions at a critical amplitude deformation corresponding to the electrical signal inversion (Figure 1b). A spectacular  $\pi$  radians evolution of  $\delta_{H2}$  is observed in this region, whereas the variations of the mechanical phase angle,  $\tan\delta$ , don't exceed 0.1 radians.

The development of this apparatus, in the AC mode, has confirmed the extreme sensibility of the electrical parameters to changes in microstructure of filled elastomers under deformation, and allowed to complete our knowledge of the role played by the different phases (and interfaces) on the non linear mechanical behavior of reinforced elastomers.

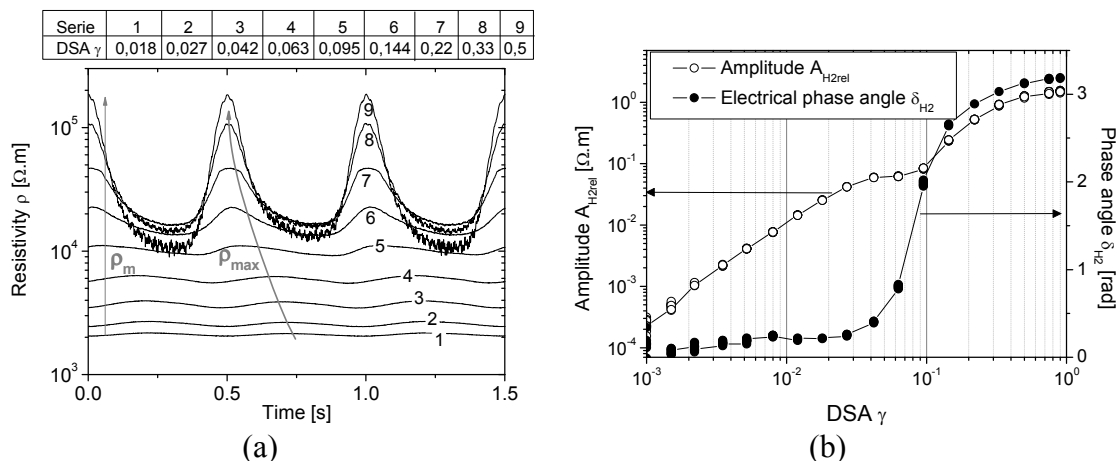


Figure 1: Experimental results with sDEMA for a filled SBR CB filled subjected to a dynamic shear dynamic deformation. (a) Bulk electrical results for increased amplitudes deformations. (b) Relative amplitude  $A_{2rel}$  and phase angle  $\delta_{H2}$  vs. double strain amplitude deformation (DSA).

<sup>1</sup> A. I. Medalia, Rubber Chemistry and Technology, **1973**, 46, pp. 877

<sup>2</sup> A. Voet and F. R. Cook, Rubber Chemistry and Technologie, **1968**, 40, pp. 1207

<sup>3</sup> A. R. Payne J. of Applied Polymer Science, **1965**, 9, pp. 1073-1082

# MECHANICAL CHARACTERIZATION OF OIL-BASED MODELING CLAY FROM DROP-TEST USING INVERSE PROBLEMS

C. Hernandez<sup>1</sup>, A. Maranon<sup>1</sup>, I. A. Ashcroft<sup>2</sup>, J. P. Casas-Rodriguez<sup>1</sup>

<sup>1</sup>*Mechanical Engineering Department, Universidad de los Andes, Cr 1este 19A-40, Bogota, Colombia*

<sup>2</sup>*Wolfson School of Mechanical and Manufacturing Engineering, Loughborough University, Loughborough LE11 3TU, UK*

**Abstract.** Modeling clay is a material often used in impact applications either as backing material or as simulation of soft body impactors. It displays pressure-dependent behavior, where at lower pressures the material behaves as isotropic elasto-plastic and at high pressures as a hydrodynamic material. Thus, the power law plasticity model, which is able to represent this behavior, is selected to model this kind of materials, though the material constants are difficult to measure. This paper presents the formulation and solution of a first class inverse problem for the identification of plasticine material parameters for the power law plasticity equation from a single drop-test. The inverse problem is formulated as an optimization procedure for the determination of the optimal set of the material parameters. The input parameter for the procedure is the depth of the indentation made in the modeling clay by the drop-test. The output parameters are the material model constants, which are determined by fitting the final shape and depth of a numerically simulated drop-test to the final shape and depth of experimental test. This optimization procedure is performed by a real-coded genetic algorithm. This paper includes a numerical example of the characterization procedure for oil-based modeling clay, Roma Plastilina No.1, from a drop-test using a steel sphere of 63.5mm of diameter and 1043g of weight dropped at a height of 2m into the modeling clay. This simulation demonstrates the performance of the algorithm and the ability to estimate the material model constants for the power law plasticity model.

## 1. INTRODUCTION

Oil based modeling clay, also known as Roma Plastilina and plasticine, is widely used as backing material in the ballistic resistance testing of body armors [1]. Plasticine, which replicates the human torso tissue, is used to characterize, as a depth projection, the possible injury suffered by a person as a consequence of a ballistic impact. This measurement, known as Backface Signature (BFS), is used in many body armor standards from a number of countries to determine the potential trauma produced during a non-penetrating round impact [2-4]. Modeling clay plays an important role in the performance evaluation of body armor, thus its mechanical characterization is essential for the development of numerical models of the ballistic impact.

Plasticine is a malleable material made from oils, waxes and minerals that shows an elasto-viscoplastic behavior. Progress has been made to characterize the response of the modeling clay when subjected to different load conditions. Adams et al. [5] described a viscoplastic formulation to model the behavior of the plasticine. The constitutive relationship used was the generalized Herschel-Bulkley model and the material parameters were determined from tensile and ram extrusion measurements. The resulting material model was implemented in a finite element simulation of squeeze flow, obtaining satisfactory agreement for compressive forces. Sofuoglu and Rasty [6] used compressive tests to determine the material parameters of various types (colors) of plasticine using a strain-hardening model, specifically the power law equation. They found that the material parameters vary significantly among modeling clay colors commercially available. Another method to characterize modeling clay was proposed by Huang et al. [7]. They used spherical and conical indentation measurements to determine the material parameters for two models: Herschel-Bulkley and power law. Finite

elements simulations of the indentation process were made to evaluate the performance of the material models. In both cases, a close correlation was obtained. Munusamy and Barton [8] developed a numerical simulation of Roma Plastilina under projectile impact. The model selected to represent the behavior of the clay was the Drucker-Prager material model. The material parameters were determined by performing quasi-static compression tests. The simulation of blunt headed projectiles on clay was compared with experimental data and showed good agreement.

Although, there are a number of characterization procedures for modeling clay in the literature, no characterization methods for modeling clay at high strain rates are available. Hence, this paper presents a novel technique for the dynamic characterization of oil-based modeling clay from a single drop-test. The characterization procedure consists of the formulation and solution of a first class inverse problem [9] to determine the material parameters for the power law plasticity model. The input parameter is the indentation depth measurement from the drop-test. The output parameters are the material constants required for the implementation of dynamic numerical simulation of modeling clay. This optimization procedure is developed by a real-coded genetic algorithm.

## 2. DROP-TEST

The drop-test is used in ballistic resistance standards as a validation procedure of the modeling clay stiffness, when used as backing material. The validation procedure consists of a free release onto the clay of a steel ball of 1043 g and 63.5 mm in diameter from 2.0 m height. The standard states that, after five drops, the arithmetic mean of the indentation depth measurements shall be  $19 \text{ mm} \pm 2 \text{ mm}$ . This proposed calibration procedure is used in this paper as input for the characterization process. Using the calibration procedure as input data to the modeling clay characterization process, better agreement should be expected between the experimental and numerical simulations of ballistic resistance tests.

## 3. POWER LAW PLASTICITY MODEL

Power law is a strain rate dependent plasticity model used to describe the mechanical behavior of materials that show strain rate hardening [10]. The material model is based on the Ramberg-Osgood [11] constitutive relation. The yield strength  $\sigma_y$  is written in the form:

$$\sigma_y = K\dot{\epsilon}^n \quad (1)$$

where  $K$  is the material constant,  $n$  the strain rate sensitivity coefficient and  $\dot{\epsilon}$  the strain rate. In addition to these two constants, it is necessary to determine the Young's modulus  $E$  to implement the material model in a finite element simulation.

## 4. FORMULATION OF MATERIAL CHARACTERIZATION AS AN INVERSE PROBLEM

In the scope of this paper, material characterization is defined as the use of experimental techniques to determine the material parameters associated with a given material model, which define its mechanical behavior. The proposed characterization procedure uses the indentation depth measurement from drop-tests to find the optimal set of material constants for the power law material model by the formulation and solution of a first class inverse problem.

Consider the indentation depth measurement after a drop-test from a specific height ( $H$ ), of a steel sphere, with specific mass and diameter ( $m, D$ ). The sphere is considered rigid and the material parameters for the modeling clay are unknown. Let  $\mathbf{h}_0(H, m, D)$  represent the indentation depth, and  $\overline{\mathbf{u}}_0(\mathbf{h}_0(H, m, D))$  the geometrical coordinates of the circular segment defined by the indentation depth. Now, consider a finite element model representation of the drop-test with the same initial conditions ( $H, m, D$ ) and a known set of trial material constants:  $\vec{z} = [E, K, n]^T$ . Let  $\overline{\mathbf{u}}(\mathbf{h}(\vec{z}, H, m, D))$  represent the geometrical coordinates of the circular segment defined by the indentation depth of the *computed* drop-test with the same initial conditions and using the trial material parameters.

The inverse problem of material characterization can be formulated as follows. Given  $\overline{\mathbf{u}}_0(\mathbf{h}_0(H, m, D))$  the geometrical coordinates of the circular segment defined by the indentation depth measurement, find  $\vec{z} = [E, K, n]^T$  the optimal set of material parameters for the power law material model. The optimal set of material constants is found when the error function proposed in following equation is minimum.

$$\phi_{err}(\vec{z}) = \left\| \overline{\mathbf{u}}(\mathbf{h}(\vec{z}, H, m, D)) - \overline{\mathbf{u}}_0(\mathbf{h}_0(H, m, D)) \right\| \quad (2)$$

Where  $\|\cdot\|$  is the Euclidian norm of the vector. This error function is very complex i.e. it has many local minima, which is not well suited to gradient-based optimization techniques. For this reason, a derivative-free optimization process based on genetic algorithms is used. The genetic algorithm formulation is explained in the next section.

## 5. METHODOLOGY

The characterization procedure is divided into four basic steps, as shown in Figure 1. (1) A single drop-test is performed on the material to be characterized. (2) The circular segment geometrical moments defined by the indentation depth are computed. (3) A finite element model representation of the drop-test with trial material parameters is solved. (4) A genetic algorithm optimization procedure, to minimize the difference between the computed geometrical moments of the finite element representation with trial parameters and the moments of the measured drop-test, is implemented.

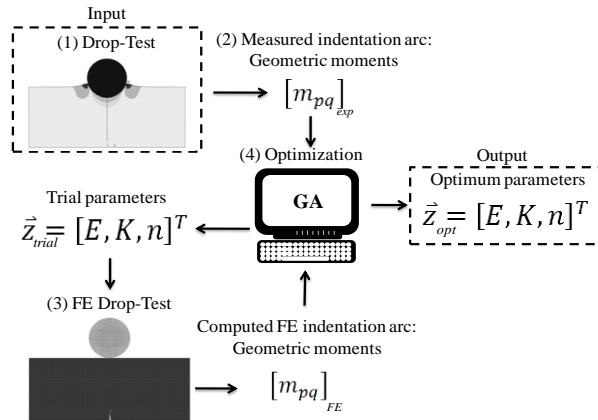


**Figure 1.** Computational procedure for the characterization of modeling clay from a single drop-test.

### 5.1. Finite element model of drop-test

Finite element analysis of the drop-test impact test was implemented using the software ANSYS/LS-DYNA employing an explicit solution scheme. Given the axisymmetric nature of the problem, the event was modeled using explicit 2D structural solid elements with four nodes, six degrees of freedom per node and quadrilateral shape (PLANE162). The material model used for the modeling clay was the power law plasticity model described in previous sections. The impacting sphere was modeled as a rigid body and meshed reasonably fine to maintain the node spacing on the surface finer than the surface of the plasticine to promote proper distribution of contact forces [10]. The contact between the specimen and impacted surface was assumed to be frictionless. In Figure 2 a sketch of the drop-test FE simulation, before and after the impact, is shown.

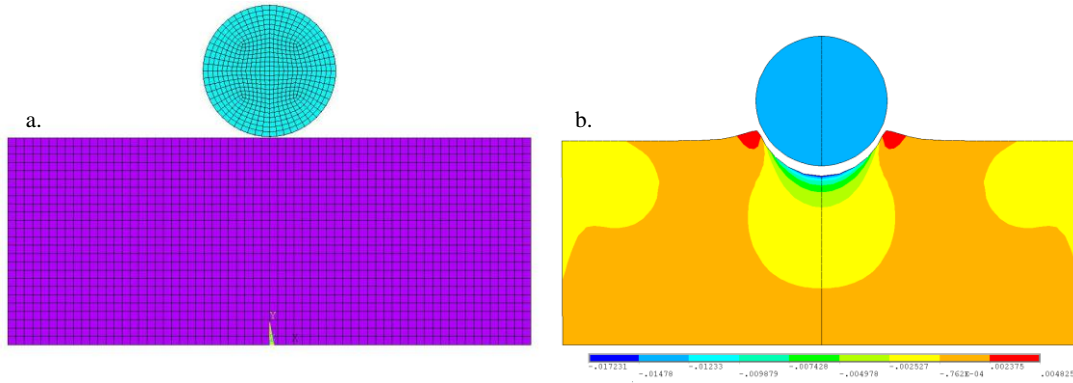


Figure 2. FE simulation of the drop-test (a) before and (b) after the impact (Vertical displacements).

### 5.2. Geometric moments computation

Assuming that the function  $f(x)$  of the indentation silhouette on the modeling clay is discrete, only the position of the center of the elements that forms the contour is known. Then the geometric moments of order  $p+q$  can be approximated by a double summation, as in equation (3). Where  $\Delta x$  and  $\Delta y$  are the element sizes in the  $x$  and  $y$  directions respectively.

$$m_{pq} = \sum_{i=1}^M \sum_{j=1}^N x^p y^q f(x) \Delta x \Delta y \quad (3)$$

### 5.3. Genetic algorithm optimization

Genetic Algorithms (GA) are stochastic optimization techniques based on the concept of natural selection and genetics. GA differ from traditional optimization techniques because they use a fitness function to lead the search instead of differentiation of the objective function. This attribute makes the GA an efficient and robust technique to exploit large, non-linear and highly complex search spaces [12].

The GA consists of five basic operations, as shown in Figure 3. First, an initial population (set of possible solutions) is generated randomly. Then the population evolves by means of five operators: evaluation, selection, crossover, mutation and elitism. The evaluation process determines the fitness of each individual and then in the selection process couples of parents are chosen according to their fitness. The better the fitness, the higher the probability of being selected. During the crossover operation, new offspring are created by combining the parents previously selected. The mutation operator alters the new population by forming new random individuals to maintain the diversity of the population and to prevent locking the optimization

process in a local minimum. The task of the elitism operator is to preserve the best individuals of the previous population in the new generation. The previous steps are repeated until a convergence criterion is reached. In this optimization problem there are three genes or parameters for each individual. The genes  $\vec{z} = [E, K, n]^T$  for each individual represent the material characterization parameters.

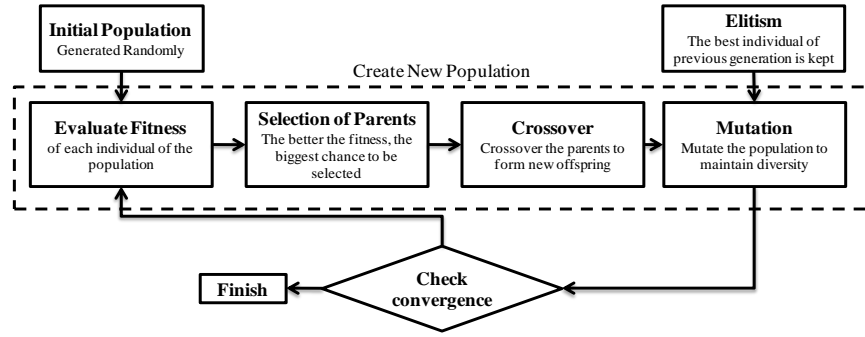


Figure 3. Basic Genetic Algorithm

## 6. NUMERICAL ANALYSIS

To test the performance of the proposed characterization procedure an example was performed. This example consists of the determination of material parameters for Roma Plastilina No.1 used as backing material in ballistic tests. The selected material model to simulate the behavior of the clay, as described above, was the Power Law plasticity model and the corresponding objective parameters, are shown in Table 1. The finite element analysis performed using these objective material constants showed after the simulation of the drop-test an indentation depth of 17.23 mm, which is consistent with experimental measurements that showed an average of 18.31 mm with standard deviation of 1.16 mm.

Table 1. Objective material constants for Roma Plastilina No. 1

Density ( $\rho$ )	Young Modulus (E)	Poisson Ratio ( $\mu$ )	Material Constant (K)	Strain rate sensitivity coefficient (n)
1878 kg/m <sup>3</sup>	14.20 MPa	0.49	0.24 MPa	0.014

This numerical analysis is performed using as input the set of geometrical moments of the computed plasticine surface using the shown material parameters. The optimization genetic algorithm was configured to use a population of 200 individuals and 100 generations. The selection operator used was the roulette wheel, in which the fittest individuals have a better probability of being selected to be the parents for the next generation. For the crossover, three operators were implemented: heuristic, arithmetic and uniform. The mutation operator used was uniform with probability of 80% in order to maintain the diversity of the populations and avoid falling into a local minima. Additionally, the elitism operator was implemented to assure that the best individual was maintained in the next generation. On the other hand, an operator to reduce the search space of each parameter was included. This operator recalculates the search space limits every four generations based on the generation mean and its standard deviation. This operator is not used to recalculate the search space of the parameter  $n$  because the algorithm tends to fall in local minima and narrow the search space around non-optimal results. In the following section the results of the characterization process are shown.

## 7. RESULTS

The characterization procedure of Roma Plastilina No.1 was run three times to evaluate the performance and repeatability of the algorithm. In Table 2 the results of the characterization process are shown, each determined parameter is compared with the expected value. In addition, depth of the indentation produced by the simulation using these parameters is computed and compared with the expected indentation depth. Figure 4 show typical responses of the parameters as the genetic algorithm evolves. These figures show the evolution of each estimated material constant (—), the expected material constant (---), and the search space limits (-·-).

**Table 2.** Roma Plastilina No. 1 material characterization results.

Material Parameters	Young Modulus (E)	Material Constant (K)	Strain rate sensitivity coefficient (n)	Indentation Depth
Objective	14.20 MPa	0.240 MPa	0.0140	17.23 mm
Trial Run1	13.34 MPa	0.236 MPa	0.0144	18.21 mm
Error Run1	6.1%	1.7%	0.3%	3.3%
Trial Run2	14.24 MPa	0.239 MPa	0.0141	17.21 mm
Error Run2	0.3%	0.4%	0.1%	0.1%
Trial Run3	14.28 MPa	0.238 MPa	0.0142	17.14 mm
Error Run3	0.6 %	0.8 %	1.5 %	2.8 %

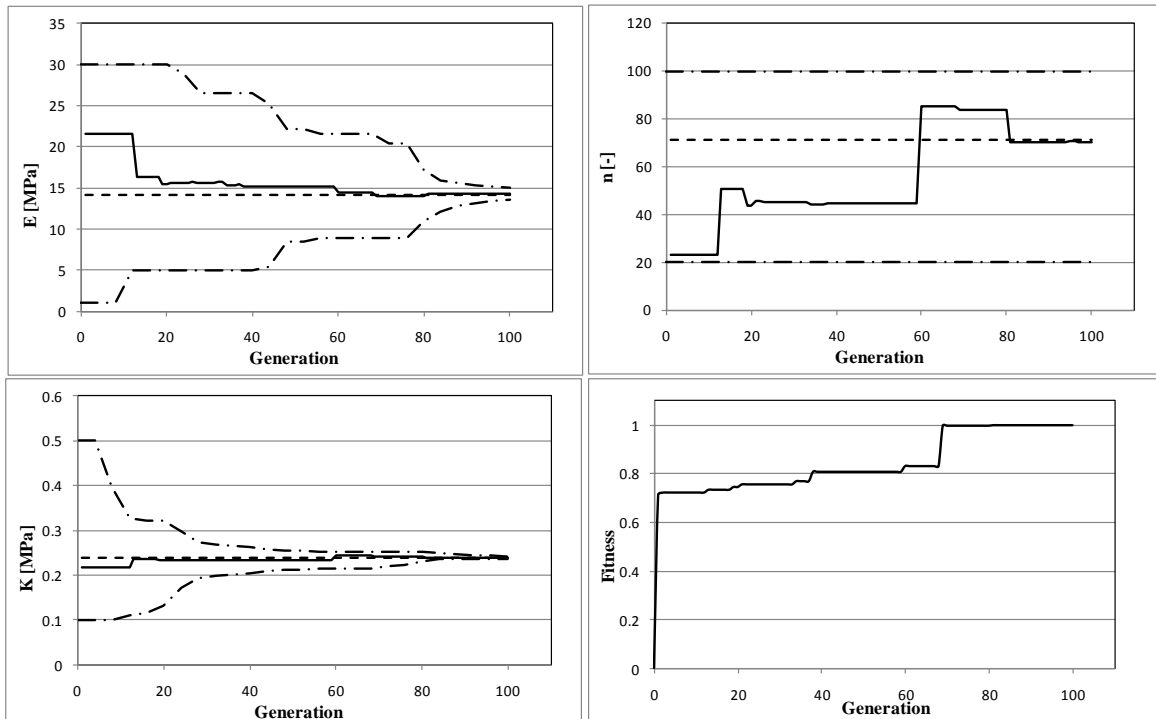


**Figure 4.** Evolution of parameters E, K, n and Fitness for Run1.  
Estimated (—) Objective (---) Search Space Limits (-·-)

It was found that the proposed optimization procedure is capable of determining the material constants. The three material constants,  $E$ ,  $K$ , and  $n$  are determined with excellent accuracy (error less than 6.1% in all

repetitions) and very quickly (30 to 40 generations needed). The strain rate sensitivity parameter  $n$  requires about 80 to 90 generations to converge due to the lower sensitivity of the indentation depth to this coefficient. The computed indentation depths, using the determined material parameters, show good agreement with expected indentation depths. The difference between the computed and the expected depth remain under 3.3%.

## 8. CONCLUSIONS

An inverse formulation for the characterization of Plastilina Roma No.1 was proposed. This formulation is based on a computational methodology to determine the power law material parameters using a single drop-test experiment. The characterization process consists of four basic steps. In the first step, a drop-test on the clay is performed from a known height. During the second step the geometrical moments of the plasticine surface are computed to reduce the amount of data and to compare the shapes in an efficient manner. In the third step a finite element representation of the drop-test with trial material constants is performed. And finally, in the fourth step a real coded genetic algorithm optimization procedure is solved to minimize the difference between the computed geometrical moments of the finite element representation and the moments of the measured clay surface.

Numerical results of the characterization process showed that the algorithm is effective in determining the power law material constants for the Plastilina No.1. The computation of the indentation depth from drop-test using the determined parameters showed good agreement with measured experimental indentation depths. More studies need to be conducted to evaluate the procedure with other materials that exhibit elasto-viscoplasticity.

## 9. REFERENCES

- [1] Office of Law Enforcement Standards, 2008, "Ballistic Resistance of Body Armor NIJ Standard - 0101.06," U.S. National Institute of Justice.
- [2] Croft, J., and Longhurst, D., 2007, "HOSDB Body Armour Standards for UK Police: Part 2: Ballistic Resistance," Police Scientific Development Branch, UK.
- [3] Ministerio de Defensa Nacional (COL), 2010, "NTMD-0225-A3: Resistencia Balística para Chalecos Antibalas," República de Colombia.
- [4] Registro Nacional de Armas (ARG), 2001, "RENAR MA.01: Chalecos Antibalas," Ministerio de Defensa, República Argentina.
- [5] Adams, M. J., Aydin, I., Briscoe, B. J., and Sinha, S. K., 1997, "A finite element analysis of the squeeze flow of an elasto-viscoplastic paste material," *Journal of Non-Newtonian Fluid Mechanics*, 71(1-2), pp. 41-57.
- [6] Sofuoglu, H., and Rasty, J., 2000, "Flow behavior of Plasticine used in physical modeling of metal forming processes," *Tribology International*, 33(8), pp. 523-529.
- [7] Huang, Z., Lucas, M., and Adams, M., 2002, "A numerical and experimental study of the indentation mechanics of plasticine," *The Journal of Strain Analysis for Engineering Design*, 37(2), pp. 141-150.
- [8] Munusamy, R., and Barton, D., C., 2009, "Behaviour of Roma Plastilina upon blunt projectile impact," *DYMAT 2009 - 9th International Conference on the Mechanical and Physical Behaviour of Materials under Dynamic Loading*, pp. 749-755.
- [9] Zabaraz, N., Woodbry, K., and Raynaud, M., 1993, *Inverse Problems in Engineering: Theory and Practice*, The American Society of Mechanical Engineers, New York.
- [10] ANSYS Inc., 2009, "ANSYS LS-DYNA User's Guide: ANSYS release 12.0," Canonsburg, PA.
- [11] Ramberg, W., and Osgood, W. R., 1943, "Description of stress-strain curves by three parameters, Technical Note No. 902," National Advisory Committee for Aeronautics, Washington, D.C.
- [12] Goldberg, D., 1989, *Genetic Algorithms in Search, Optimization, and Machine Learning*, Addison-Wesley Professional.

# Experimental Analysis of Impact Behaviour of Composite Sandwich Panels: Cork Core and jute/epoxy skins

B. Hachemane<sup>1,2</sup>, R. Zitoune<sup>1</sup>, C. Bouvet<sup>3</sup> and B. Bezzazi<sup>2</sup>

<sup>1</sup> *Université de Toulouse, UPS ; Institut Clément Ader ; 133 av. de Ranguel, F-31077 Toulouse, France*

<sup>2</sup> *U. R. Matériaux, Procédés et Environnement ; 1 av. de l'indépendance, 35000 Boumerdès, Algérie*

<sup>3</sup> *Université de Toulouse ; ISAE; Institut Clément Ader ; 10 av. Edouard Belin, F-31077 Toulouse, France*

**Abstract.** In order to better exploit the natural resources available in Algeria, an experimental characterization of impact behaviour by falling mass of a new jute-epoxy/cork sandwich material has been undertaken. To determinate the impact energy and the cork density effect in the sandwich mechanical behaviour and in the damage size, an instrumented dynamic test was carried out. The results shows that, the first damage force, the maximum force as well as the damage size supported by the sandwich panel are more influenced by the cork density and the impact energy. The sandwich material obtained by a heavy cork is characterized with a 72 % elastic energy greater than the sandwich with lighter cork. This difference can be explained by the fact that, during the manufacturing process by infusion, the resin infiltrates the pores of the agglomerated cork, which leads into a change of the local stiffness of the material.

## 1. INTRODUCTION

The use of natural fibres in the reinforcement of composites is growing constantly, mainly due to environmental and economic concerns. Composite materials with natural fibres are considered as potential products to substitute composites with not renewable synthetic fibres. The most current natural fibres are straw, flax, hemp and jute fibre. Among all of them, jute fibre provides, in addition to its mechanical properties, the advantage to be easier to weave [1].

Even if the mechanical performances of composites with natural fibres offer new perspectives for the structures design (low densities, acceptable mechanical properties), the disparity of their properties, the variability of their behaviour as well as the misunderstanding of these materials make them difficult to use [1-2]. In addition, at being a natural material, the reproducibility of their properties is not easy to assure because its dependency on diverse parameters such as the origin of the grains of plants, the type of ground on which they were planted, the weather conditions, etc. Several studies have shown that these materials are sensitive to humidity and to the heat [3]. When these materials are heat up at various temperature levels, we observe a notorious decrement of the tensile, bending and shock failure strengths. For example, the tensile tests carried out on jute fabric at various temperatures have shown that the failure stress decrease of 43 % when the jute fabric is heat up to 180 °C [1].

With the economic and environment facts that represent a better exploit of the natural resources available in Algeria, the aim of this research is to lighten the buildings construction by replacing nowadays existing solutions, such as wall insulation bricks, plaster or Siporex, by sandwich panels based on epoxy-jute fibres skin and cork core fabricated by infusion process. Nonetheless, the sandwich plates are clamped to this type of material can be subject to accidental damage like a falling object (ex: hammer, screwdriver, etc.), and therefore, it is necessary to characterize these sandwich panels during impact dynamic solicitation at low energies.

Few works have focused on the analysis of the behaviour of jute fibre reinforced laminates subjected to impact loading by falling weight. In one of these researches, an experimental study was conducted in order to show the influence of hybridization of glass fibres (jute-glass hybrid composites) on low velocity impact response, damage resistance and damage tolerance capability of woven jute fabric reinforced isothalic polyester composites [4]. The results show that the jute composites have better energy absorption capacity compared to jute-glass hybrid laminates. However, the hybrid laminate with 16 % glass fibre weight is the most optimum combination of jute and glass fibre with minimum deflection, maximum peak load, better damage tolerance, and costlier than hybrids laminates with 25.2 % and 8.2 % glass fibre weight.

Thanks to the acoustic emission and thermoelastic stress analysis, cyclic post-impact three-point bending tests were carried out on plain woven jute fabric/polyester plates [5]. This research showed that damage in natural fibre reinforced laminates progresses as far as the defects present in the laminate reach a critical energy that allow them to grow.

The impact of sandwich cork core and carbon/epoxy skins has also received little attention. A comparison between the mechanical behaviour during impact of sandwich plates in foam core and those in cork core has shown that the last ones have a maximum impact force larger than the first panels. The minimum difference observed is about 25 %. In addition, the sandwiches with cork core have a more important capacity to absorb the impact energy with lower depth damage [6]. Finally, recent works show the thermal protection influence on impacted damaged composites structures used for launcher's fairing. Experimental tests were conducted on cork shielded and unshielded panels [7]. The results showed that for a T300/914 unidirectional laminate, the delamination onset energy is about 3 times greater when the cork thickness is 3.5 mm and about 7 times greater when the thickness is 6.5 mm.

With the mentioned background, this work deals with the mechanical behaviour of sandwiches panels made of jute/epoxy skins and cork core under low energy impact. The main goal is to develop a full factorial experimental study in order to determine the influence of impact energy and cork density, by means of the force - displacement curves and the damage size.

## 2. EXPERIMENTAL PROCEDURE

### 2.1. Material

The employed material is a sandwich composed of jute-epoxy skins and cork core, manufactured by one-shot infusion method. In this case, the jute woven skins and the cork core are infused in only one step, as shown in figure 1. The skins are layed-up with a  $[0^\circ]_s$  stacking sequence. The skin mechanical properties are given in table 1 [1]. Three cork densities are studied with the following values 160, 270 and 310  $\text{Kg/m}^3$ . This values corresponding to a 4-16, 3-5 and 1-2 granulate size respectively. The employed epoxy resin is referenced as LY5052, associated to its HY5052 hardener. When the infusion is completed, the obtained sandwich is polymerised in an incubator at 80 °C during 12 hours. The table 2 gives the sandwich specimen's final dimension confectioned with the mentioned materials.



**Figure 1.** Manufacturing process by infusion of sandwich panels.

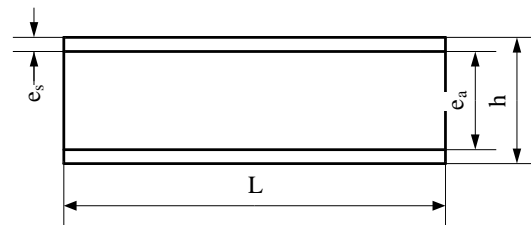


**Figure 2.** Geometry of sandwich panel.

**Table 1.** Means mechanicals properties of composite jute/epoxy [1].

Density ( $\text{Kg/m}^3$ )	$E_t$ (GPa)	$E_f$ (GPa)	G (GPa)	$\nu_{lt}$	$\nu_{tl}$	$\sigma_t$ rupture (MPa)	$\sigma_f$ rupture (MPa)	$\tau_{rupture}$ (MPa)
$1.165 \pm 0.01$	$4.5 \pm 0.6$	$3.2 \pm 0.2$	1.45	0.24	0.27	$38 \pm 6$	$80 \pm 8$	23

**Table 2.** Means geometrical parameters of sandwich specimens.

Sandwich reference	Cork density ( $\text{Kg/m}^3$ )	b (mm)	$e_a$ (mm)	h (mm)	L (mm)	$e_s$ (mm)
SD 160	160	$100.22 \pm 0.4$	$10.48 \pm 0.8$	$13.32 \pm 0.5$	150	$1.42 \pm 0.15$
SD 270	270	$100.5 \pm 0.21$	$12.04 \pm 0.67$	$14.86 \pm 0.49$	//	$1.41 \pm 0.09$
SD 310	310	$100.37 \pm 0.42$	$11.13 \pm 0.37$	$14.61 \pm 0.17$	//	$1.74 \pm 0.1$

## 2.2. Impact tests

The experimental equipment used for the impact tests is illustrated in figure 3. It is mainly composed by a guide column supporting a Kistler force sensor equipped with an impactor. Two lasers sensor and an oscilloscope are the measuring devices. A rigid table with a 125 x 75 mm<sup>2</sup> window holding system, where the sandwich plates are clamped to, complete the parts of the equipment.

The impactor is composed by a 2 Kg free falling main block coupled with a 10 KN force sensor and a 12.7 mm diameter hemispherical tip. The first laser sensor allows calculating the starting contact velocity; meanwhile the second gives the displacement of the non-impacted side. The sensor's signals are synchronized by the oscilloscope.

The impact force,  $F_{impact}$ , between the impactor and the specimen is determinate from the sensor measured force,  $F_{measured}$ , by the equation (1):

$$F_{impact} = \frac{m_{impactor}}{m_{impactor} - m_{tip}} F_{measured} \quad (1)$$

where  $m_{impactor}$  and  $m_{tip}$  are respectively the impactor total mass (2.056 Kg) and the mass of hemispherical tip (0.176 Kg).

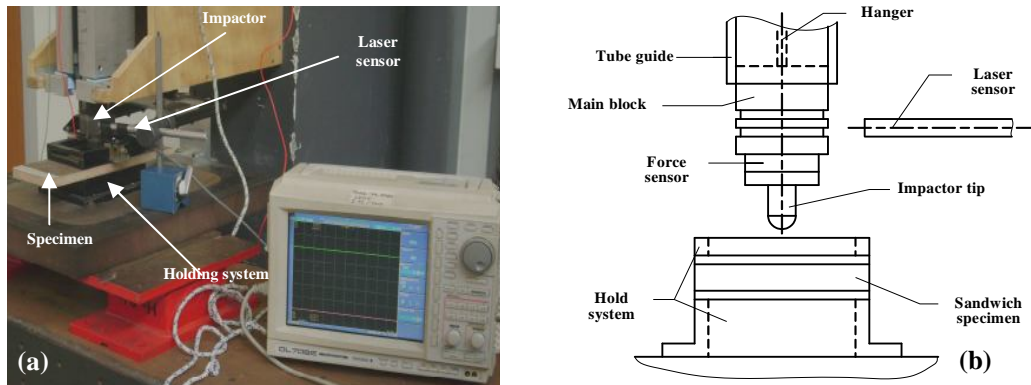


**Figure 3.** Impact equipment.  
(a) Experimental device with recording system, (b) device scheme



**Figure 4.** Three-dimensional measuring machine « MC 1200C».

As a consequence of the absence of a specific standard impact test method for sandwich structures, impact tests were performed following the recommendations of ASTM D1736/D1736M-05, which suggests the equations (2), (3) and (4) for obtaining the main testing results:

$$E_i = \frac{m_{impactor}}{2} V_i^2 \quad (2)$$

$$\delta(t) = \delta_i + V_i t + \frac{g}{2} t^2 - \int_0^t \left( \int_0^t \frac{F_{\text{impact}}(t)}{m_{\text{impactor}}} dt \right) dt \quad (3)$$

$$E_p(t) = \frac{m_{\text{impactor}}}{2} (V_i^2 - V(t)^2) + m_{\text{impactor}} g \delta(t) \quad (4)$$

where  $E_i$  is the impact energy (J);  $V_i$  is the impact velocity (m/s);  $g$  is the acceleration due to gravity (9.81 m/s<sup>2</sup>);  $V(t)$  is the impactor velocity at time  $t$  (m/s);  $\delta_i$  is the impactor displacement from reference at time  $t = 0$  (m);  $\delta(t)$  is the impactor displacement from reference at time  $t$  (m) and  $E_p(t)$  is the sandwich plate energy at time  $t$  (J).

After the impact test, the depth of the damage area is measured using a three-dimensional measuring machine « MC 1200C », as illustrated in figure 4.

### 3. RESULTS AND DISCUSSION

The results in figure 5 shows the evolution of the impact force versus time for four impact energies, obtained on a SD 310 sandwich plate. It is noticed that for impact energies below 15 J, these curves can be regarded as a sine wave. The impact test performed with a energy of 15 J resulted in a damage of the non-impacted skin. From figure 5, it can be distinguished two critical values, the first one relates the first damage force, denoted as  $F_0$ , the second is the maximum impact force recorded by the force sensor, denoted as  $F_{\text{max}}$ . For a 310 Kg/m<sup>3</sup> cork density, the first damage force increases with impact energy. This growth is about 40 % when the impact energy increases from 5 J to 10 J.

In figure 6, it is illustrated the impact force evolution versus the displacement calculated from equation (3) for a SD 310 sandwich plate. After the appearance of the first damage, a slight drop in the sandwich plate stiffness is registered, denoted as zone A. During a short time, the plate returns to its stiffness with the appearance of several oscillations followed by a gradual increase in the force signal. This can be explained on one side by the numerous damages caused by the impactor penetration into the specimen, and on the other hand, the increment of the cork density due to the compression phase which leads to a compression modulus growth. The compression phenomenon was demonstrated in previous works during quasi-static compression tests on natural cork [8]. Also, during the compression phase, three regions corresponding respectively to the elastic bending, the buckling and the crushing of the cell walls are identified.

From this point of view, the oscillations observed in the figure 6, also can be related to the buckling phenomena. From figure 6, it is noticed that the residual displacement for SD 310 sandwiches increases with the impact energy. This residual displacement increases from 3.3 mm to 5.6 mm when the energy grows from 5 J to 10 J. However, for the SD 160, the residual displacement is more important. In this case, when the impact energy doubles, residual displacement is almost tree times, from 2.32 mm for 5 J to 7.84 mm for 10 J.

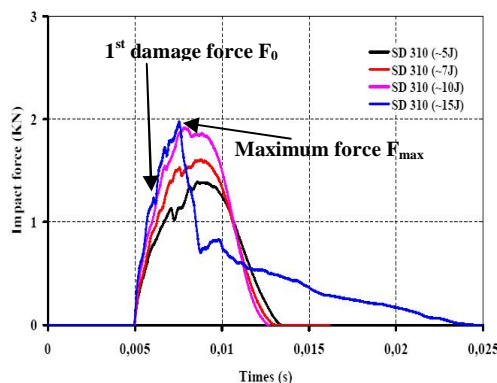


**Figure 5.** Temporal impact force curves for the SD 310 composite sandwich.

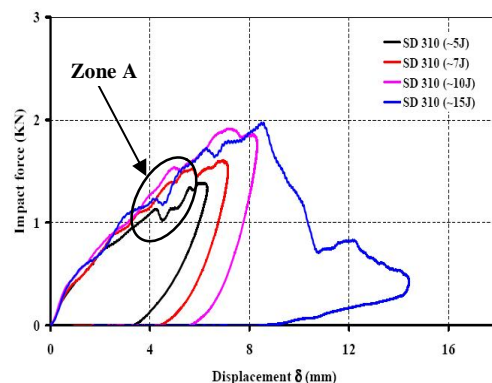


**Figure 6.** Impact force vs. impactor displacement curves for the SD 310 composite sandwich.

The levels of first damage and maximum force recorded by the sensor are strongly influenced by the cork density. As shown in figure 7 and 8, the first damage and maximum force decrease respectively from

1.04 kN to 1.29 kN and from 1.5 kN to 1.65 kN when the cork density increases from 270 to 310  $\text{Kg/m}^3$  for 7 J impact energy. This can be explained by the fact that low cork density increase the grain size which results into a higher porosity. This implies that during the manufacturing of the sandwich plates, the resin infiltrates into the pores increasing the local rigidity of the material, as shown in figure 9. However, for the lowest cork density, SD 160, the force distribution recorded as a function of impact energy shows a random distribution. This distribution may be related to the impactor/target local contact area, which can occur either over a cork grain as shown in figure 9a, or over a cork-resin interface as shown in figure 9b, or totally on a rich zone of resin as shown in figure 9c. Concerning the other densities, this observation is not completely true as seen in figure 9c.

The plot in figure 10 shows the permanent indentation depth evolution for the three sandwiches materials as function of the impact energy. When the impact energy rises from 5 J to 7 J, a significant increase in permanent indentation depth is recorded for all tested densities. It is also noticed that for the impact energies superior to 7 J, the permanent indentation depth varies a few for the SD 270 and SD 310 sandwiches. However, for the SD 160 sandwich, the permanent indentation depth increases significantly until the total specimen rupture. This difference may be related to the difference of energy absorbed by the three materials as well as to the energy dissipation mode.

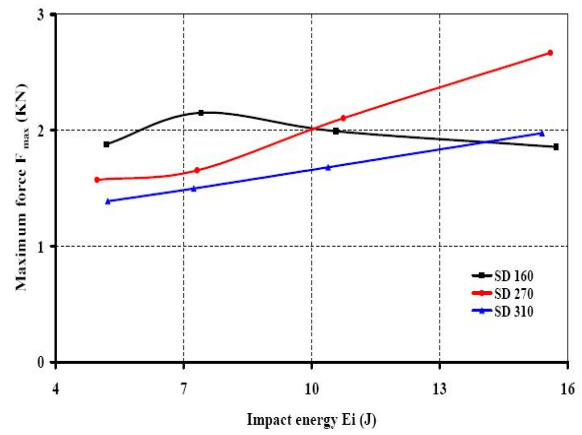
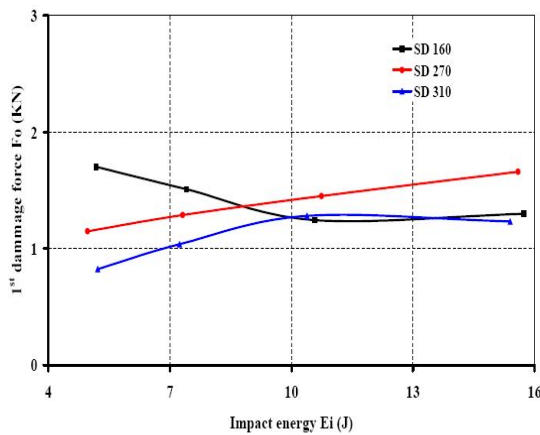


**Figure 7.** Damage initiation force  $F_0$  vs. impact energy. **Figure 8.** Maximum force  $F_{max}$  vs. impact energy.

The results of figure 11 show the cork density influence on the sandwich absorbed energy-impact energy ratio,  $E_d/E_i$ . It is observed that an increase in the cork density causes a decrease of the energies ratio. For 5 J of impact energy, the transition of cork density from 310  $\text{Kg/m}^3$  to 160  $\text{Kg/m}^3$  raises the  $E_d/E_i$  ratio from 76 % to 86 %. If the impact energy grows, this trend is still observed but the difference is less important. As it can be seen, the  $E_d/E_i$  ratio only raises 3.2 % with 7 J of impact energy.

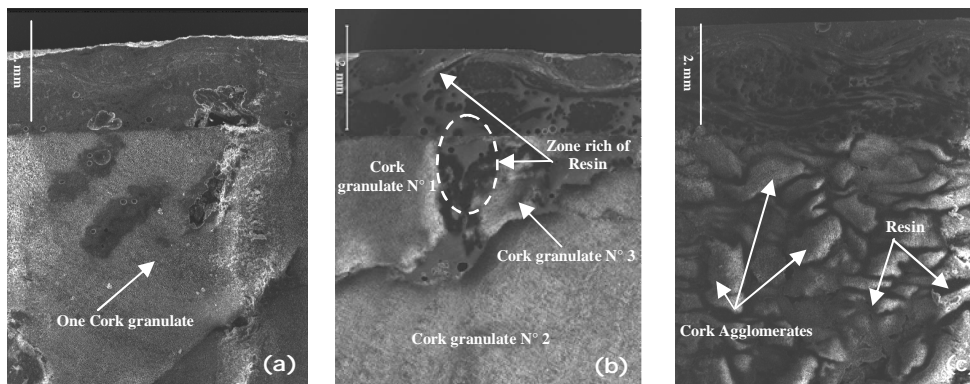


**Figure 9.** SEM observation of sandwiches SD 160 and SD 310. (a) SD160 with one cork agglomerate, (b) SD 160 with 3 cork agglomerates & (c) SD 310 with various cork agglomerates.

The cork density influence on the sandwich elastic energy-impact energy ratio,  $E_e/E_i$ , is shown in figure 12. In contrast with the  $E_d/E_i$  ratio, a growth on the cork density generates an increase in the  $E_e/E_i$ . For 5 J impact energy, when the cork density is changed from 160 to 310 Kg/m<sup>3</sup>, the  $E_e/E_i$  ratio grows from 14 % to 24 %. With increasing the impact energy, this tendency is less important. This difference reduces from 10 % with 5 J of impact energy to 3.2 % at 7 J of impact energy.

With the less dense cork, the resin quantity which infiltrates the pores is more important. Therefore an increment in the resin quantity results in a change of the material proprieties. In this case, the local stiffness is not the same and thus its ability to absorb energy.

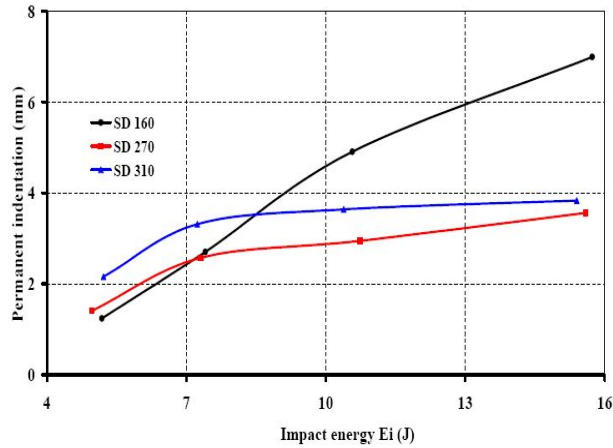


**Figure 10.** Permanent indentation vs impact energy.

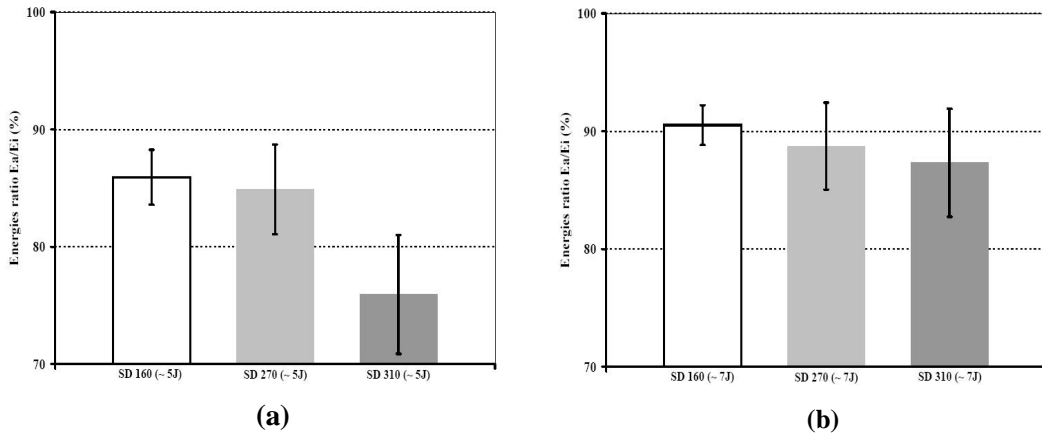


**Figure 11.** Energies ratio  $E_a/E_i$  for the different sandwiches materials. (a) with impact energy  $E_i \approx 5$  J ; (b) with impact energy  $E_i \approx 7$  J

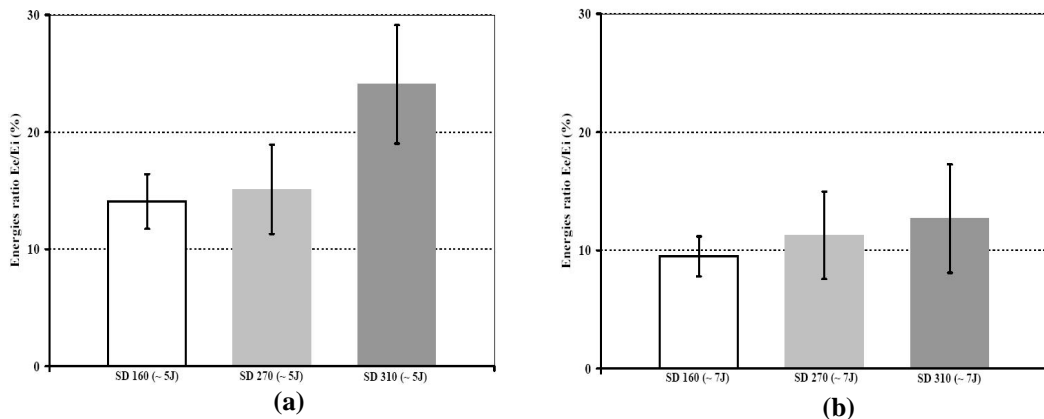


**Figure 12.** Energies ratio  $E_e/E_i$  for the different sandwiches materials. (a) with impact energy  $E_i \approx 5$  J ; (b) with impact energy  $E_i \approx 7$  J

In figure 13, it is shown the post-impact damage state of the sandwiches panels for 7 J of impact energy. The cork damaged areas, for the SD 310 sandwiches, are manifested by the presence of cracks between granulates interfaces, as show in figure 13a. However when the density is lower than 310 kg/m<sup>3</sup>, in addition to interface granulates cracking, cracks through the cork granulates and cork grains broken by compression are observed as well. Concerning the impacted skins, the observed damage is produced by two solicitations types. At the impactor centre, compressive laminate fracture is noticed for all sandwiches panels. However, shear damages are detected near the periphery of the damaged area.

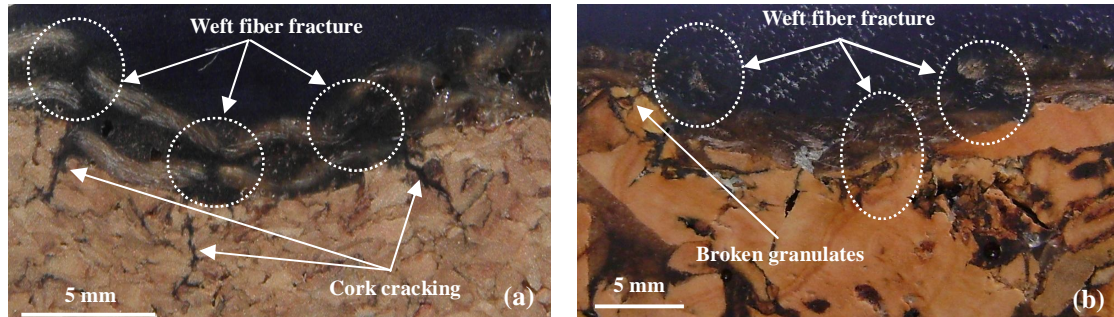


**Figure 13.** Cross section photographs showing the damage state for two sandwiches with 7 J of impact energy. (a) SD 310 sandwich (b) SD 160 sandwich

#### 4. CONCLUSION

The experimental characterization of impact behaviour by falling mass of a new jute-epoxy/cork sandwich material has been undertaken. The results show that the cork density and the impact energy affects noticeably the depth damage, the force responsible of the first damage,  $F_0$ , as well as the maximum force supported by the sandwich panel,  $F_{max}$ .

It is proved that, this force rises with increasing the impact energy and reducing the cork density. When the density increases from 160 Kg/m<sup>3</sup> to 310 Kg/m<sup>3</sup>, the maximum force recorded decreases about 60 %. This difference can be explained by the fact that, during the manufacturing process by infusion, the resin infiltrates the pores of the agglomerated cork, which leads to a change into the local stiffness of the material.

The sandwich panels manufactured with low density cork are characterized by low elastic behaviour and have a better capacity to absorb the energy. The increment of the cork density from 160 Kg/m<sup>3</sup> to 310 Kg/m<sup>3</sup> leads to a reduction on the absorbed energy to 14 % when the impact energy is 5 J.

#### References

- [1] Mir A., Zitoune R., Collombet F. & Bezzazi B., "Study of Mechanical and Thermomechanical Properties of Jute/Epoxy Composite Laminate", *Jour. of Reinf. Plast. and Comp*, 29 (2010) 1669-1680.
- [2] Gassan J. & Bledzki A.K., "Effect of Moisture Content on the Properties of Silanized Jute-Composites", *Polymer Composites*, 18 (1997) 179-184.
- [3] Mukhopadhyay S. & Figueiro R., "Physical Modification of Natural Fibers and Thermoplastic Films for Composites – A Review", *Jour. of Thermoplastic Composite materials*, 22 (2009) 135-162.
- [4] Sabeel Ahmed K., Vijayarangan S. & Kumar A., "Low Velocity Impact Damage Characterization of Woven Jute-Glass Fabric Reinforced Isothalic Polyester Hybrid Composites", *Jour. of Reinf. Plast. and Comp*, 26 (2007) 959-976.
- [5] Santulli C., "Post-impact flexural tests on jute/polyester laminates monitored by acoustic emission", *Jour. of Materials Science* 41 (2006) 1255-1259.
- [6] Castro O., Silva J.M., Devezas T., Silva A. & Gil L., "Cork agglomerates as an ideal core material in lightweight structures", *Materials and Design* 31 (2010) 425-432.
- [7] Petit S., Bouvet C., Bergerot A. & Barrau J.J., "Impact and compression after impact experimental study of a composite laminate with a cork thermal shield", *Composites Science and Technology* 67 (2007) 3286-3299.
- [8] Pereira H., Garcia J. & Baptista C. "The effect of Growth rate on the Structure and Compressive properties of Cork", *IAWA Bulletin*, 13 (1992) 389-396.